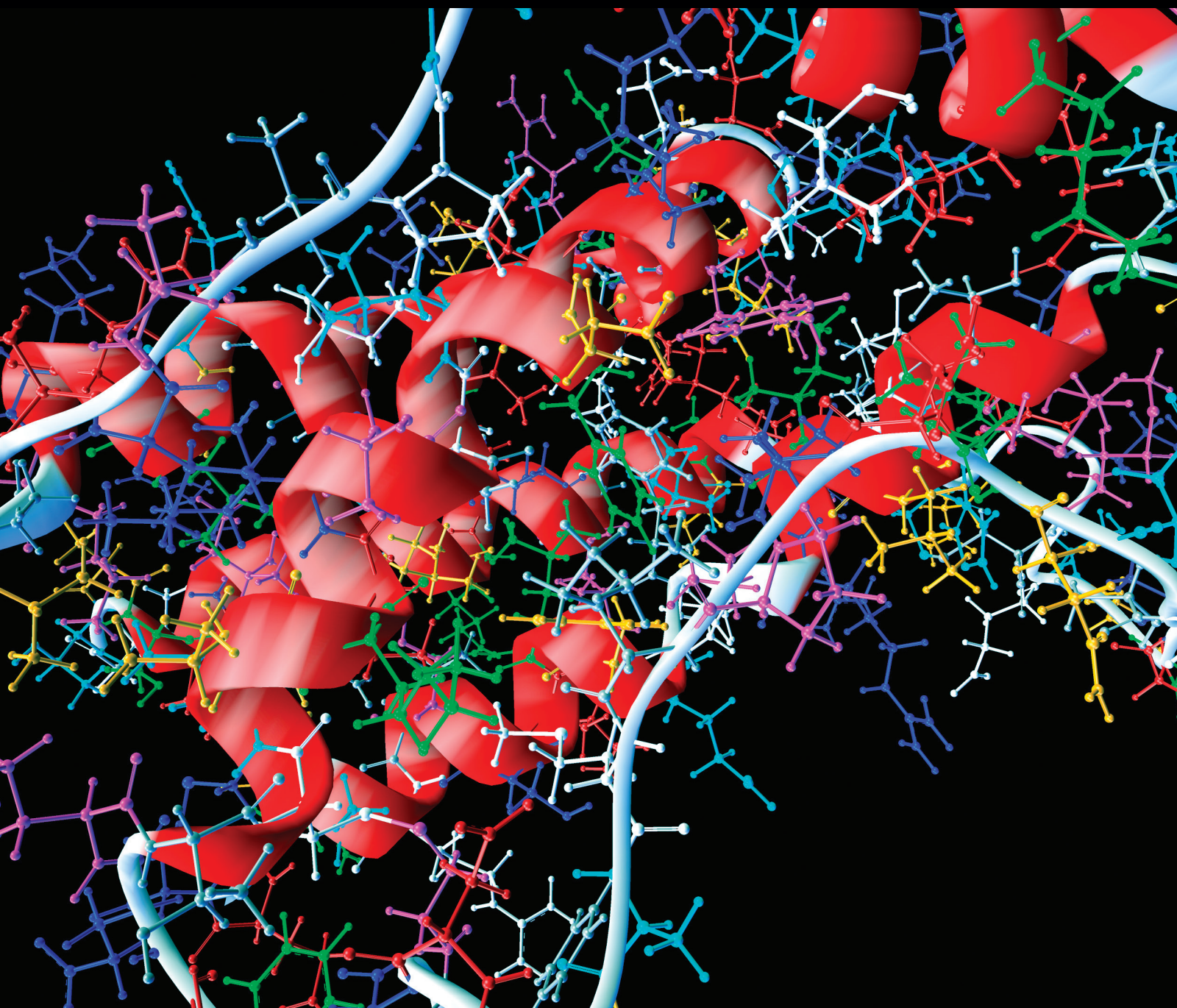


Computational and Mathematical Methods in Medicine

# Numerical Methods and Applications in Biomechanical Modeling 2014

Guest Editors: Eduardo Soudah, Eddie Y. K. Ng, Zhonghua Sun,  
and Spandan Maiti





---

**Numerical Methods and Applications  
in Biomechanical Modeling 2014**

Computational and Mathematical Methods in Medicine

---

**Numerical Methods and Applications  
in Biomechanical Modeling 2014**

Guest Editors: Eduardo Soudah, Eddie Y. K. Ng,  
Zhonghua Sun, and Spandan Maiti



---

Copyright © 2015 Hindawi Publishing Corporation. All rights reserved.

This is a special issue published in “Computational and Mathematical Methods in Medicine.” All articles are open access articles distributed under the Creative Commons Attribution License, which permits unrestricted use, distribution, and reproduction in any medium, provided the original work is properly cited.

## Editorial Board

Emil Alexov, USA  
Georgios Archontis, Cyprus  
Dimos Baltas, Germany  
Chris Bauch, Canada  
Maxim Bazhenov, USA  
Thierry Busso, France  
Carlo Cattani, Italy  
Sheng-yong Chen, China  
William Crum, UK  
Ricardo Femat, Mexico  
Alfonso T. García-Sosa, Estonia  
Damien Hall, Australia

Volkhard Helms, Germany  
Seiya Imoto, Japan  
Lev Klebanov, Czech Republic  
Quan Long, UK  
C-M Charlie Ma, USA  
Reinoud Maex, France  
Michele Migliore, Italy  
Karol Miller, Australia  
Ernst Niebur, USA  
Kazuhisa Nishizawa, Japan  
Hugo Palmans, UK  
David James Sherman, France

Sivabal Sivaloganathan, Canada  
Nestor V. Torres, Spain  
Nelson J. Trujillo-Barreto, Cuba  
Gabriel Turinici, France  
Kutlu O. Ulgen, Turkey  
Edelmira Valero, Spain  
Guang Wu, China  
Huaguang Zhang, China  
Yuhai Zhao, China  
Xiaoqi Zheng, China  
Yunping Zhu, China

# Contents

**Numerical Methods and Applications in Biomechanical Modeling 2014**, Eduardo Soudah, Eddie Y. K. Ng, Zhonghua Sun, and Spandan Maiti  
Volume 2015, Article ID 768652, 2 pages

**Deformation of Soft Tissue and Force Feedback Using the Smoothed Particle Hydrodynamics**, Xuemei Liu, Ruiyi Wang, Yunhua Li, and Dongdong Song  
Volume 2015, Article ID 598415, 10 pages

**Parametric Modeling of Human Gradient Walking for Predicting Minimum Energy Expenditure**, Gerard Saborit and Adrià Casinos  
Volume 2015, Article ID 407156, 6 pages

**Kinematic, Dynamic, and Energy Characteristics of Diastolic Flow in the Left Ventricle**, Seyed Saeid Khalafvand, Tin-Kan Hung, Eddie Yin-Kwee Ng, and Liang Zhong  
Volume 2015, Article ID 701945, 12 pages

**Comparative Sensitivity Analysis of Muscle Activation Dynamics**, Robert Rockenfeller, Michael Günther, Syn Schmitt, and Thomas Götz  
Volume 2015, Article ID 585409, 16 pages

**Bone Mineral Density and Fracture Risk Assessment to Optimize Prosthesis Selection in Total Hip Replacement**, Pröstur Pétursson, Kyle Joseph Edmunds, Magnús Kjartan Gíslason, Benedikt Magnússon, Gígja Magnúsdóttir, Grétar Halldórsson, Halldór Jónsson Jr., and Paolo Gargiulo  
Volume 2015, Article ID 162481, 7 pages

**Assessment of Knee Cartilage Stress Distribution and Deformation Using Motion Capture System and Wearable Sensors for Force Ratio Detection**, N. Mijailovic, R. Vulovic, I. Milankovic, R. Radakovic, N. Filipovic, and A. Peulic  
Volume 2015, Article ID 963746, 8 pages

**Review of Modelling Techniques for *In Vivo* Muscle Force Estimation in the Lower Extremities during Strength Training**, Florian Schellenberg, Katja Oberhofer, William R. Taylor, and Silvio Lorenzetti  
Volume 2015, Article ID 483921, 12 pages

**Vehicular Causation Factors and Conceptual Design Modifications to Reduce Aortic Strain in Numerically Reconstructed Real World Nearside Lateral Automotive Crashes**, Aditya Belwadi and King H. Yang  
Volume 2015, Article ID 269386, 9 pages

**Numerical Study of Turbulent Pulsatile Blood Flow through Stenosed Artery Using Fluid-Solid Interaction**, Mehdi Jahangiri, Mohsen Saghafian, and Mahmood Reza Sadeghi  
Volume 2015, Article ID 515613, 10 pages

**Three-Dimensional Lower Extremity Joint Loading in a Carved Ski and Snowboard Turn: A Pilot Study**, Miriam Klous, Erich Müller, and Hermann Schwameder  
Volume 2014, Article ID 340272, 13 pages

## Editorial

# Numerical Methods and Applications in Biomechanical Modeling 2014

**Eduardo Soudah,<sup>1</sup> Eddie Y. K. Ng,<sup>2</sup> Zhonghua Sun,<sup>3</sup> and Spandan Maiti<sup>4</sup>**

<sup>1</sup>*Centre Internacional de Mètodes Numèrics en Enginyeria (CIMNE), Universitat Politècnica de Catalunya, C/Gran Capitan, s/n, 08034 Barcelona, Spain*

<sup>2</sup>*School of Mechanical and Aerospace Engineering, Nanyang Technological University, Singapore 639798*

<sup>3</sup>*Department of Medical Radiation Sciences, Curtin University, Perth, WA 6102, Australia*

<sup>4</sup>*Department of Bioengineering, University of Pittsburgh, Pittsburgh, PA 15261, USA*

Correspondence should be addressed to Eduardo Soudah; [esoudah@cimne.upc.edu](mailto:esoudah@cimne.upc.edu)

Received 8 June 2015; Accepted 8 June 2015

Copyright © 2015 Eduardo Soudah et al. This is an open access article distributed under the Creative Commons Attribution License, which permits unrestricted use, distribution, and reproduction in any medium, provided the original work is properly cited.

Numerical methods and applications in biomechanical modeling have continued to play increasingly important roles in biomedical research and applications. This special issue, following the very successful one in 2013, provides a snapshot of the emerging biomedical applications and research. The main focus of this special issue was on the interface between numerical methods and biomedical applications especially for cardiovascular dynamics and biomechanics problem in the human body. The goal of this special issue was to bring together experts in related fields of computational biomedical engineering like multiscale flow modeling (3D, 1D, and 0D models), blood flow propagation, boundary conditions, fluid-solid coupling, inverse problems in biomechanics, high-performance computing of multiphysics discretization schemes, cardiovascular biomechanics, and porous media. Then, the details of these papers are summarized as follows.

The work of M. Klous et al. attempts to compare ankle and knee joint loading at the steering leg between carved ski and snowboard turns. The authors showed higher forces along the longitudinal axis in skiing and similar forces for skiing and snowboarding in anterior-posterior and mediolateral direction. This study can help the clinician to improve understanding of how forces are distributed in the ankle and knee joint when these sports are done.

X. Liu et al. present the deformation and haptic feedback of soft tissue in virtual surgery based on a liver model by using a force feedback device. This paper introduces a kind of

mesh-free method for deformation simulation of soft tissue and force computation based on viscoelastic mechanical model and smoothed particle hydrodynamics (SPH). The results reveal that SPH methodology is suitable for simulating soft tissue deformation and force feedback calculation, and SPH based on dynamic local interaction area has a higher computational efficiency significantly compared with the usual SPH.

A. Belwadi and K. H. Yang show an interesting paper about how the occupant-seating position, bumper profile height, and the principal direction of force of impact play a crucial role in the generation of strain and pressure in the aorta and a potential injury mechanism responsible for traumatic rupture of the aorta in automobile crashes. In their study, 16 design of computer experiments were carried out with varying levels of principal direction of force, impact velocity, impact height, and impact position of the bullet vehicle combined with occupant-seating positions in the case vehicle to determine the effects of these factors on aortic injury. Simulation results showed that, in simulated near side left lateral crashes, peak average maximum principal strain mainly took place in the isthmus of the aorta. Their design of computer experiments using finite element vehicle models has identified the key factors responsible for aortic injury.

N. Mijailovic et al. combine within biomechanical model different sensor measurements to determine the knee cartilage deformation ratio and the knee cartilage stress

distribution to predict when it is necessary to perform surgery on a patient. The model includes the impact of ground reaction forces, contact force between femur and tibia, patient body weight, ligaments, and muscle forces. Despite introduction of a new approach and presentation of some preliminary findings, their proposed method shows great potential for preoperative and postoperative surgical planning and treatment of patients with knee injuries.

The paper by M. Jahangiri et al. compares different turbulent models over a stenosed artery considering an elastic wall. The results were compared with those of the laminar flow assumption and the rigid artery wall and show the effects of turbulent blood flow over the velocity profiles.

F. Schellenberg et al. present a review of existing computational techniques to determine muscle forces in the lower limbs during strength exercises *in vivo* and discuss their potential for uptake into sports training and rehabilitation. The review introduces the different computational techniques and outlines their advantages and disadvantages for the informed usage by nonexperts. With sufficient validation and widespread application, muscle force calculations during strength exercises *in vivo* are expected to provide biomechanically based evidence for clinicians and therapists to evaluate and improve 20 training guidelines.

R. Rockenfeller et al. compare two models of mammalian striated muscle activation dynamics proposed by Hatze and Zajac and perform a sensitivity analysis for investigating the influence of model parameters on the solution of the mathematical equations. The authors also used a global sensitivity analysis approach to factor in finite ranges of parameter values. The authors demonstrate that the findings of global sensitivity analysis must be treated with caution because the whole dynamics of a system is condensed to a single average function per whole parameter range.

The work of S. Khalafvand et al. studies the blood flow characteristics in the normal left ventricle. The authors show the vortices produced (generation and growth) and their correlation with flow acceleration and deceleration during the mitral valve opening and closing. This work can help the cardiologist to understand how the vortices are produced in the heart movement, thus contributing to understanding of pathogenesis of cardiac disease.

The objective of the work by Þ. Pétursson et al. describes a novel preliminary methodology for patient evaluation before total hip replacement surgery as a first step towards creating a patient-specific, presurgical application for determining the optimal prosthesis procedure. Ten patients were studied using finite element analysis and bone mineral density to estimate the status of hip before surgery; after that a fracture risk index is defined and compared with the patient's age, sex, and average proximal bone mineral density. Findings of this study showed a high degree of variability between patients grouped according to implant procedure, with age and gender being the poor indicators for determining total hip replacement procedure. Their results could be used as a basis to develop a clinical database for correlating bone mineral density and fracture risk index to total hip replacement patient outcomes.

G. Saborit and A. Casinos present a mathematical model to predict the optimum gradient for a minimum energetic cost. The model focuses on the variation in mechanical energy during gradient walking. The authors show that kinetic energy plays a marginal role in low speed gradient walking. Consequently, the optimal negative gradient depends on the individual step length.

In this special issue, we have provided examples of recent progress in computational and mathematical methods in biomedicine, for the benefit of students, researchers, health-care professionals, and teachers.

## Acknowledgment

We thank the authors of these 10 papers for their contribution to this special issue.

Eduardo Soudah  
Eddie Y. K. Ng  
Zhonghua Sun  
Spandan Maiti

## Research Article

# Deformation of Soft Tissue and Force Feedback Using the Smoothed Particle Hydrodynamics

Xuemei Liu,<sup>1,2</sup> Ruiyi Wang,<sup>1,3</sup> Yunhua Li,<sup>1,2</sup> and Dongdong Song<sup>1</sup>

<sup>1</sup>North China University of Water Resource and Electric Power, Zhengzhou 450011, China

<sup>2</sup>School of Automation Science and Electrical Engineering, Beihang University, Beijing 100191, China

<sup>3</sup>Henan Radio & Television University, Zhengzhou 450011, China

Correspondence should be addressed to Ruiyi Wang; 906505138@qq.com

Received 25 June 2014; Revised 18 October 2014; Accepted 29 October 2014

Academic Editor: Spandan Maiti

Copyright © 2015 Xuemei Liu et al. This is an open access article distributed under the Creative Commons Attribution License, which permits unrestricted use, distribution, and reproduction in any medium, provided the original work is properly cited.

We study the deformation and haptic feedback of soft tissue in virtual surgery based on a liver model by using a force feedback device named PHANTOM OMNI developed by SensAble Company in USA. Although a significant amount of research efforts have been dedicated to simulating the behaviors of soft tissue and implementing force feedback, it is still a challenging problem. This paper introduces a kind of meshfree method for deformation simulation of soft tissue and force computation based on viscoelastic mechanical model and smoothed particle hydrodynamics (SPH). Firstly, viscoelastic model can present the mechanical characteristics of soft tissue which greatly promotes the realism. Secondly, SPH has features of meshless technique and self-adaption, which supply higher precision than methods based on meshes for force feedback computation. Finally, a SPH method based on dynamic interaction area is proposed to improve the real time performance of simulation. The results reveal that SPH methodology is suitable for simulating soft tissue deformation and force feedback calculation, and SPH based on dynamic local interaction area has a higher computational efficiency significantly compared with usual SPH. Our algorithm has a bright prospect in the area of virtual surgery.

## 1. Introduction

Virtual surgery simulation is an important application of virtual reality aiming at establishing vivid virtual surgery environment with all kinds of medical image data so that doctors and trainees can make use of it to do surgical trainings.

Traditionally, the animal model and corpses are considered the most common training model. However, the animal model has fundamental differences in anatomy and tissue consistency compared to human tissue, and the corpses are expensive and cannot be reused. Therefore, it is difficult to reach a proficient skill level for surgeons.

This calls for a more innovative training system for surgical residents. Virtual surgery simulation system can meet it. In such a system, the surgeons would be able to interact with the virtual three-dimensional models of organs using their sense of vision and touch.

In virtual surgery simulation, the deformation model of soft tissue is the decisive factor of visual effect and

accuracy of force feedback and has been widely studied in the computer graphics and computer aided design communities [1]. Currently there are two most widely used physical models of soft tissue. One is Finite Element Models (FEM) [1–5] and the other one is Mass-Spring (M-S) Models [6–9].

A major advantage of FEM is that it uses continuum mechanics and has a solid mathematical foundation. Another advantage is that FEM requires only a few material parameters to describe a physical system's response. However, there are main issues existing in this approach, the first one is the heavy computational load which cannot ensure real-time and the second one is the impact of cutting on the precomputed response. Compared with FEM, M-S does not need parameters of the continuum, so it is easier to implement and handle topological changes at a reduced computational cost. The computation is specifically efficient. However, mass-spring systems are not necessarily accurate which are not built upon elasticity theory. Primarily, most of such systems are not convergent; next, the parameters of every mass and spring in

this model cannot be obtained in the measurement but can often be chosen arbitrarily. Therefore, M-S has low precision and poor stability. The common methods such as M-S and FEM are all built on meshes. Malformation and distortion could arise and they cannot ideally satisfy the needs of real-time virtual surgery simulation and the interaction and attachment between surgery tools and soft tissue must have effect on some specific points when using methods built on meshes. Moreover, we must remesh frequently because of topology changes in cutting and suturing simulations, which leads to expensive computation and bad haptic performance.

In order to overcome these problems, certain meshes should be avoid being used. De et al. [10] developed a point collocation-based method of finite spheres technique to simulate the interaction of surgical tool and soft tissue. Jansson and Vergeest [11] developed a discrete mechanics model for deformation bodies, incorporating behavior such as motion, collision, and deformation. Müller et al. [12] developed a shape matching method for meshless deformations. The meshfree technique is no mesh dependence, strongly self-adaptive, and smoothly continuous. Moreover, it can describe continuum biomechanical characteristics of soft tissue. Meshless method has a broad application prospect in the virtual surgery simulation.

In this paper, we present an application of smoothed particle hydrodynamics (SPH) method to simulate the interaction between virtual surgical tool and soft tissue which is a meshfree technique. In SPH the continuum properties are discredited on smooth particles, the stress-strain governing equations are formulated in a Lagrange frame, and the derivatives are computed by taking the derivatives of the particle kernels. The SPH method can deal with large deformation and be capable of resolving problems with large deformations for both solids and fluids.

In Section 2, we introduce the viscoelastic model used in this paper. In Section 3, we provide a brief introduction to the SPH method. In Section 4, we develop a SPH method based on dynamic local interaction area of performing real time deformation. Finally, in Section 5 simulation results are presented.

## 2. Voigt Viscoelastic Model

The virtual surgery simulation focuses on requirement of (1) reality; (2) real time performance; (3) performance of quantitative deformation; (4) easy calculation for generating the values for force feedback. Requirement (1) depends on the accuracy of the underlying biomechanics models. According to biomechanics literature [9], soft biological tissues exhibit complex viscoelastic in nature. Currently, most of the existing deformation methods are built on an elastic mechanical model, which cannot describe the deformation behavior of soft tissue precisely.

Here, we simulate the biological tissue as a linear viscoelastic solid and use Voigt model to establish the relationship between stress and strain. According to Voigt model, stress tensor of isotropy material can be divided into spherical

tensor and deviator tensor, and strain tensor can be divided into volume deformation and distortion of same volume:

$$\sigma_{\alpha\beta} = S_{\alpha\beta} + \frac{\delta_{\alpha\beta}\sigma_{kk}}{3}, \quad (1)$$

$$\varepsilon_{\alpha\beta} = e_{\alpha\beta} + \frac{\delta_{\alpha\beta}\varepsilon_{kk}}{3}, \quad (2)$$

where  $\alpha, \beta = x, y, z$ ,  $S_{\alpha\beta}$ ,  $\sigma_{kk}$  are the components of the partial stress tensor and spherical stress tensors, respectively,  $e_{\alpha\beta}$ ,  $\varepsilon_{kk}$  are the components of the partial strain tensor and spherical strain tensors, respectively, and  $\delta_{\alpha\beta}$  is the Kronecker symbol.

According to Voigt model, 3D viscoelastic constitutive equations can be described as follows:

$$S_{\alpha\beta} = E \cdot e_{\alpha\beta} + \eta \cdot \frac{de_{\alpha\beta}}{dt}, \quad (3)$$

$$\sigma_{kk} = E \cdot \varepsilon_{kk} + \eta \cdot \frac{d\varepsilon_{kk}}{dt}.$$

Then we establish strain-displacement geometric equation as follows:

$$\begin{aligned} \varepsilon_{xx} &= \frac{\partial u}{\partial x}, & \varepsilon_{xy} &= \frac{\partial u}{\partial y} + \frac{\partial v}{\partial x} \\ \varepsilon_{yy} &= \frac{\partial v}{\partial y}, & \varepsilon_{yz} &= \frac{\partial v}{\partial z} + \frac{\partial w}{\partial y} \\ \varepsilon_{zz} &= \frac{\partial w}{\partial z}, & \varepsilon_{zx} &= \frac{\partial w}{\partial x} + \frac{\partial u}{\partial z}, \end{aligned} \quad (4)$$

where  $u, v, w$  are the components of displacement along the coordinate axis,  $\varepsilon_{xx}, \varepsilon_{yy}, \varepsilon_{zz}$  are the components of normal strain, and  $\varepsilon_{xy}, \varepsilon_{yz}, \varepsilon_{zx}$  are the components of shear strain.

## 3. The Basic Theory of SPH

**3.1. SPH Formulation.** SPH method was firstly put forward by Lucy [13]. It is featured by Lagrangian and particle properties, fully meshless and explicit in coping with those trouble-making nonlinear problems [14]. SPH has been applied to model a wide range of problems [15, 16] such as free surface flows [17, 18], viscous flows [19], and multiphase flows [20].

At the heart of the SPH method is an interpolation technique for evaluating arbitrary field functions. To illustrate this, consider a field function  $f(x)$  in an unbounded domain. The value of the function at a point  $x$  can be obtained by a convolution with the Dirac delta distribution function  $\delta$ :

$$f(x) = \int_{\Omega} f(y) \delta(x-y) dy. \quad (5)$$

Dirac delta function  $\delta$  has the following property:

$$\delta(x-y) = \begin{cases} 1, & x = y \\ 0, & x \neq y. \end{cases} \quad (6)$$

In SPH, the singular Dirac delta function is approximated by a smooth kernel function  $W$  to yield an approximation.

The classical SPH method employs a finite number of particles to discretize the continuum. Each particle located at the position vector  $x$  carries field variables such as mass and density and moves with the material velocity. Therefore, (5) can be transformed to the superposition sum of discretization form of all particles support in the domain:

$$f(x) = \sum_{j=1}^N m_j \frac{f(y)}{\rho_j} W(x-y, h), \quad (7)$$

where  $m_j, \rho_j, y$  are the mass, density, and position of particle  $j$ , respectively, and  $h$  is the smoothing length.

Correspondingly, the derivative of function  $f(x)$  can be introduced in the following form:

$$\nabla f(x) = - \sum_{j=1}^N \frac{m_j}{\rho_j} f(y) \cdot \nabla W(x-y, h) dy. \quad (8)$$

Smooth kernel function strongly affects the stability and accuracy of SPH and plays a very important role. In this paper, the kernel function used in the present investigation is the most widely used cubic spline function [21]:

$$W(R, h) = \frac{3}{2\pi h^3} \times \begin{cases} \frac{2}{3} - R^2 + \left(\frac{1}{2}\right)R^3, & 0 \leq R < 1 \\ \left(\frac{1}{6}\right)(2-R)^3, & 1 \leq R < 2 \\ 0, & R \geq 2, \end{cases} \quad (9)$$

where  $R$  denotes the relative distance between the  $i$ th and the  $j$ th particle at the position of  $x_i, x_j$ ,  $R = r/h = |x_i - x_j|/h$ ,  $r$  is the distance of two particles, and  $h$  is the smoothing length. The derivative of the kernel function is as follow:

$$\frac{\partial W_{ij}}{\partial x^\beta} = \frac{x_i^\beta - x_j^\beta}{u} \cdot \frac{1}{\pi h^4} \times \begin{cases} -3R + 1.25R^2, & 0 \leq R < 1 \\ -0.75(2-R)^2, & 1 \leq R < 2 \\ 0, & R \geq 2. \end{cases} \quad (10)$$

**3.2. Search for the Neighbor Particles.** In order to make the experiment simpler, we set the smoothing length in this paper be a constant, so using the chain table search method is very effective. The basic idea is laying a temporary grid in the problem domain, as shown in Figure 1; the grid cell size is consistent with the size of support domain spatial, when searching particles, for a given particle  $i$ , the neighbor particle only in the same grid or closely neighbor grid. This search method limited the search scope to around the center grid cell so that time is short and search efficiency is high.

**3.3. Momentum Equation of SPH.** In SPH, movement of particles follows the law of conservation of momentum, and any particle conforms to the momentum equation as follows:

$$\frac{dv^\alpha}{dt} = \frac{1}{\rho} \frac{\partial \sigma^{\alpha\beta}}{\partial x^\beta}, \quad (11)$$

where  $v$  is the velocity vector,  $t$  is time,  $\rho$  is the density of particle,  $\sigma$  is stress of particle, and  $x$  is coordinate vector.

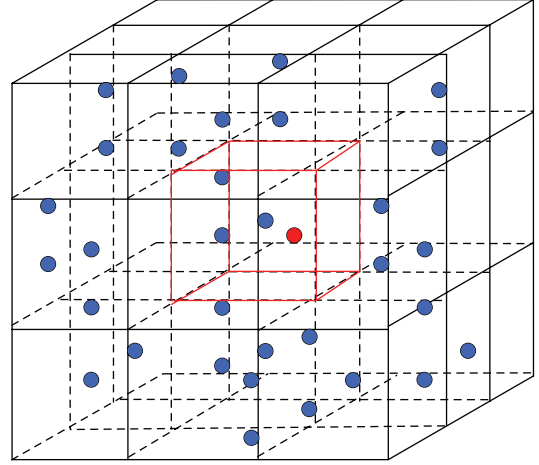


FIGURE 1: 3D grid of cells for searching neighbor particles.

Equation (11) can be transformed as follows using particle approximation method:

$$\frac{dv_i^\alpha}{dt} = \sum_{j=1}^N m_j \frac{\sigma_i^{\alpha\beta} + \sigma_j^{\alpha\beta}}{\rho_i \rho_j} \frac{\partial W_{ij}}{\partial x_i^\beta}. \quad (12)$$

Consider the following equation:

$$\frac{1}{\rho} \frac{\partial \sigma^{\alpha\beta}}{\partial x^\beta} = \frac{\partial}{\partial x^\beta} \left( \frac{\sigma^{\alpha\beta}}{\rho} \right) + \frac{\sigma^{\alpha\beta}}{\rho^2} \frac{\partial \rho}{\partial x^\beta}. \quad (13)$$

Then (12) can be written as

$$\frac{dv_i^\alpha}{dt} = \sum_{j=1}^N m_j \left( \frac{\sigma_i^{\alpha\beta}}{\rho_i^2} + \frac{\sigma_j^{\alpha\beta}}{\rho_j^2} \right) \frac{\partial W_{ij}}{\partial x_i^\beta}. \quad (14)$$

Here, the density of each particle can be computed as

$$\rho_i = \sum_{j=1}^N m_j W_{ij}. \quad (15)$$

Finally, we convert (4) with SPH:

$$\varepsilon_i^{xx} = \frac{\partial u_i}{\partial x} = \sum_{j=1}^N \frac{m_j}{\rho_j} \cdot u_j \cdot \frac{\partial W_{ij}}{\partial x},$$

$$\varepsilon_i^{yy} = \frac{\partial v_i}{\partial y} = \sum_{j=1}^N \frac{m_j}{\rho_j} \cdot v_j \cdot \frac{\partial W_{ij}}{\partial y},$$

$$\varepsilon_i^{zz} = \frac{\partial w_i}{\partial z} = \sum_{j=1}^N \frac{m_j}{\rho_j} \cdot w_j \cdot \frac{\partial W_{ij}}{\partial z},$$

$$\varepsilon_i^{xy} = \frac{\partial u_i}{\partial y} + \frac{\partial v_i}{\partial x} = \sum_{j=1}^N \frac{m_j}{\rho_j} \cdot u_j \cdot \frac{\partial W_{ij}}{\partial y} + \sum_{j=1}^N \frac{m_j}{\rho_j} \cdot v_j \cdot \frac{\partial W_{ij}}{\partial x},$$

$$\begin{aligned}\varepsilon_i^{yz} &= \frac{\partial v_i}{\partial z} + \frac{\partial w_i}{\partial y} = \sum_{j=1}^N \frac{m_j}{\rho_j} \cdot v_j \cdot \frac{\partial W_{ij}}{\partial z} + \sum_{j=1}^N \frac{m_j}{\rho_j} \cdot w_j \cdot \frac{\partial W_{ij}}{\partial y}, \\ \varepsilon_i^{zx} &= \frac{\partial w_i}{\partial x} + \frac{\partial u_i}{\partial z} = \sum_{j=1}^N \frac{m_j}{\rho_j} \cdot w_j \cdot \frac{\partial W_{ij}}{\partial x} + \sum_{j=1}^N \frac{m_j}{\rho_j} \cdot u_j \cdot \frac{\partial W_{ij}}{\partial z}.\end{aligned}\quad (16)$$

#### 4. SPH Method Based on Dynamic Local Interaction Area

**4.1. Fundamental.** SPH is computationally costly. When the number of particles in the model becomes larger, the computing will be multiplied, and real-time performance will be poor with no steady and continuous feedback force output. In order to improve the computational efficiency, we consider that when the node receives external force from the surgical instruments, the internal force will be decaying gradually with the increase of transmission distance and be just a smaller propagation beyond a certain distance, which can be neglected according to Saint-Venant principle. Therefore, we propose a SPH method based on dynamic local interaction area to perform the deformation simulation and the calculation of force feedback, which maintains high touch frame and improves the accuracy of haptic interaction at the same time.

The purpose of employing the SPH based on dynamic local interaction area to compute the deformation process is improving the computational efficiency by reducing the number of particles participating in the computation, and its basic idea is to divide the model into deformation area and nondeformation area and assume that the deformation is only affected by nodes in the deformation area, and the nodes in nondeformation area will remain still. Deformation area contains two parts, namely, interaction area and transmission area. Interaction area is the region greatly influenced by the surgical instruments, in which the SPH method is adopted to do accurate calculation of particles; transmission area is the effective propagation range of force, in which the physical quantities of all particles are obtained by decaying physical quantities of the force points.

In this paper, the transmission number is set to be two. Figure 2 illustrates the conceptual schematic of SPH based on dynamic local interaction area.

The surgical instrument contacted the model by the red point at the contact point. Define the  $Dr$  as interaction area radius and  $Tr1$ ,  $Tr2$  as transmission radius, respectively. Once the contact is detected, the algorithm calculates the relative distance between the force point and other points of the model. If the distance is less than  $Dr$ , we incorporate the points into the computation model and render the deformation, using SPH method to solve the motion equations and calculate the stress and strain. If the distance is between  $Dr$  and  $Tr1$ , to get the acceleration of particles, we multiply the force point acceleration by a weighting factor directly and then calculate the position vectors in terms of Newton's Second Law. Calculate the velocity and position vector of the particles in other transmission layers in the same way until

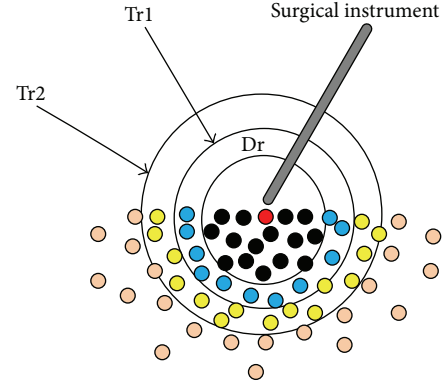


FIGURE 2: Schematic of SPH based on dynamic local interaction area.

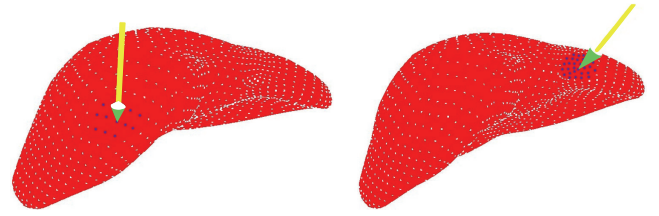


FIGURE 3: Dynamic division of interaction area.

the acceleration becomes zero. At this point, the weighting factor is zero, implying that the particles are located in the nondeformation area and will not be calculated any more.

**4.2. Determination of the Interaction Area.** The interaction area is determined by two factors: the force point and the applied load. Force point determines the location of interaction area, and the load applied on the model influences the scope of force.

**4.2.1. Determine the Location of Interaction Area Dynamically according to the Force Point.** We manipulate the force feedback device to roam in the virtual environment and apply the force to any point of the model, so the interaction area can be determined dynamically depending on the force point location, as shown in Figure 3.

**4.2.2. Determine the Scope of the Interaction Area Dynamically according to the Load.** In the SPH method, the influence domain of any particle is associated with its smooth radius  $h$ ; therefore, we define interaction area radius  $Dr$  to be a linear function of  $h$ . Once being defined,  $Dr$  will remain constant throughout the computation. Similarly, we also define transmission radius  $Tri$  to be a linear function of  $h$ , where  $i$  indicates the  $i$ th level of propagation. The computation formulas of  $Dr$  and  $Tri$  are as follows:

$$\begin{aligned}Dr &= k_1 h, \\ Tri &= k_1 h + k_2 h.\end{aligned}\quad (17)$$

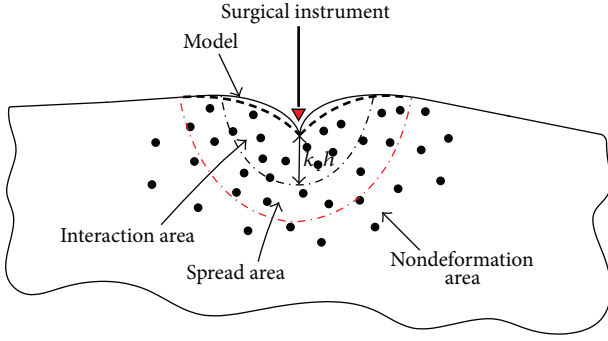


FIGURE 4: The division for deformation area and nondeformation area.

When an external force  $f_{\text{ext}}$  is applied to the model, the larger  $f_{\text{ext}}$  is, the wider influence range will become, so the greater interaction area and transmission area are. Therefore, the parameter  $k_1$  in (17) is related to  $f_{\text{ext}}$ . We define  $k_1$  as follows:

$$k_1 = \frac{f_{\text{ext}}}{2}. \quad (18)$$

So (17) can be converted as

$$\begin{aligned} \text{Dr} &= \frac{f_{\text{ext}}}{2} h \\ \text{Tr}_1 &= \frac{f_{\text{ext}}}{2} h + k_2 h. \end{aligned} \quad (19)$$

Here, the parameter  $k_2$  can be computed as

$$k_2 = \frac{1}{2} i, \quad (20)$$

where  $i$  indicates the  $i$ th level of propagation.

Equation (17) can divide the model into interaction area and influence area dynamically according to the load. So the algorithm is self-adaptive.

The division of deformation area and nondeformation is shown in Figure 4.

**4.3. Weighting Factor.** When the model is on load applied by the surgical instrument, the internal force will decrease with the increase of propagation. But the propagation will no longer increase when the force spreads beyond a certain distance. Therefore, we can set different transmission layers to improve the simulation accuracy.

The particles in different transmission layers have different effect on the deformation of the model. So we set weighting factors to indicate the influence degrees of different transmission layers. The farther transmission layer is, the smaller weighting vector is, meaning that the particles in this layer have less contribution to the deformation.

Assuming that the transmission layer is  $N$ , so the force in  $(N + 1)$ th layer decays to zero. Therefore, the computation formula of weighting vector is

$$w(i) = \frac{N + 1 - i}{N + 1}, \quad (21)$$

where  $i$  indicates the  $i$ th level of propagation. In this paper, we set  $N = 2$ , so the weighting vector can be computed as  $(3 - i)/3$ .

**4.4. Collision Detection.** Collision detection is one of the most important issues in developing a multimodal surgery simulation. It is the prerequisite of soft tissue deformation calculation; fast and accurate collision detection algorithm directly affects the authenticity of the human-computer interaction, in which one needs to ensure that there has indeed been a contact between the surgical instrument and the model in virtual scene. Most collision detection algorithms approximate the models in the scene using bounding volumes such as axis aligned bounding boxes (AABBs) [22–24], oriented bounding boxes (OBBs) [25, 26], spheres [27, 28], and  $k$ -Dop [29].

In this paper, we do experiment based on a liver model. Considering the complexity of liver model's irregularity, the complexity of structuring the bounding box, and the difficulty of the bounding box update after deformation, we use the following collision detection algorithm.

We use a three-dimensional point representing the top of the surgical instrument. We can obtain the position of the virtual instrument by tactile delivery engine in real time, then calculating the distance between the static particle of liver model and surgical instrument successively. When the distance is less than zero, we identify that the collision happened, then returning the vertex sequence number of the particle in collision.

**4.5. Procedure of Deformation Simulation.** The method simulating deformation of soft tissue and calculating the feedback force using the SPH method based on dynamic local interaction area in detail is as follows:

- (1) set up the meshless particle model and initialize each variable as zero;
- (2) build the deformation equations in terms of Vogit viscoelastic model;
- (3) manipulate the force feedback device to stress soft tissue model with external force  $f_{\text{ext}}$ , and return the serial number of contact particle after collision detection; at this time, the internal force  $F_{\text{in}}(t) = 0$ ,  $t = 0$ ;
- (4) calculate each particle as follows:
  - (a) calculate the relative distance  $\text{Dis}$  between the particle and the contact point;
  - (b) if  $\text{Dis}$  is less than  $\text{Dr}$ , calculate the particle's acceleration, strain, and stress by SPH method precisely; if  $\text{Dis}$  is between  $\text{Dr}$  and  $\text{Tr}_1$ , multiply the contact particle's acceleration by weighting factor of the first transmission layer directly to get the particle's acceleration; if  $\text{Dis}$  is between  $\text{Tr}_1$  and  $\text{Tr}_2$ , multiply the contact particle's acceleration by weighting factor of the second transmission layer directly; if  $\text{Dis}$  is larger than  $\text{Tr}_2$ , the particle's acceleration will be set zero;

- (c) calculate the particle's velocity and distance in terms of Newton's Second Law:

$$\begin{aligned} v_i^{t+1} &= v_i^t + \Delta t a_i(t), \\ x_i^{t+1} &= x_i^t + \Delta t v_i^{t+1}; \end{aligned} \quad (22)$$

- (d) draw the state of each particle on the display dynamically using OpenGL functions;

- (5) calculate the out force of contact particle:

$$f_{\text{out}}^i = f_{\text{ext}} + \sigma_{\alpha\beta}^i; \quad (23)$$

- (6) output the force through the feedback device, so the user can feel the tactile feedback with soft tissue.

In step (b), we need to calculate the particle's acceleration, strain, and stress by SPH method precisely. The main procedure is as follows.

- (i) For current particle  $p_i$ , search its neighbor particles  $p_j$  within smooth radius  $h$  in the list; then calculate the smooth nuclear function equation (9) between the current particle and its neighboring particles in support domain.

- (ii) Calculate  $\rho_i$  of the particle by (15).

- (iii) Calculate acceleration  $a_i(t)$ :

$$a_i(t) = -\frac{dv_i(t)}{dt} + \frac{\sigma_i(t)}{m_i} + \frac{F_{\text{ext}}^i}{m_i}, \quad (24)$$

where  $F_{\text{ext}}^i$  is sum of external force at  $p_i$ ,  $\sigma_i$  is the internal force, that is, stress at  $p_i$ ,  $m_i$  is mass of particle  $p_i$ , and  $dv_i(t)/dt$  can be calculated by (14).

- (iv) Calculate the displacement:  $\text{disp}_i(t) = x_i(t) - x_i(t_0)$ .
- (v) Calculate  $\varepsilon_{\alpha\beta}^i$  by previous displacement and state equation (16).
- (vi) Record each particle's current volume strain  $\varepsilon_{kk}^i$  and shape distortion  $e_{\alpha\beta}^i$ , and then use (2) to calculate the new volume strain and shape distortion by previous strain.
- (vii) Calculate each particle's volumetric stress  $\sigma_{kk}^i$  and deviatoric stress  $S_{\alpha\beta}^i$  by (3).
- (viii) Calculate stress state  $\sigma_{\alpha\beta}^i$  of each particle by (1).

## 5. Experiment

In this paper, all experiments were implemented in the same environment, specific as follows: Window XP operating system, AMD Phenom(tm) II X2 3.0 GHz PC with 2.0 GB RAM, Visual Studio 2005, and Open Graphics Library. The haptic feedback device we used is PHANTOM OMNI developed by SensAble Company in USA. It provides a complete API which is fully compatible with the OpenGL API and simplifies



FIGURE 5: Experimental environment based on PHANTOM Omni.

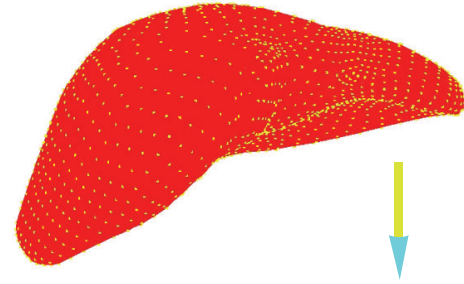


FIGURE 6: The initial state of liver model.

the haptic rendering thread. The experimental environment based on PHANTOM Omni is shown in Figure 5.

We performed simulations of manipulation of a liver model in order to demonstrate the feasibility of the procedure with more realistic organ geometries. The model geometry was obtained from segmented CT data. The initial state of the liver is shown in Figure 6 in which the pencil is representative of the arm of PHANTOM OMNI. The liver is sampled into uniformly distributed 3690 particles carrying the same mass and density. When pull force is applied to the upper part of the liver body, a snapshot of deformation process is shown in Figure 7. When press force is applied to the upper part of the liver body, a snapshot of deformation process is shown in Figure 8.

To verify the accuracy of SPH, we implemented the simulations based on M-S and SPH separately. We can get the displacement of the same node in the model through applying load on liver model with virtual surgery instrument. After fitting them with quadratic curve, we can find they are coherent overall, as shown in Figure 9. De et al. [30] did experiments based on the pig liver in vivo and ex vivo and presented the steady-state force response of pig liver, as shown in Figure 10. Comparing Figure 9 with Figure 10, the results indicate that SPH methodology is suitable for simulating the liver tissue deformation and force feedback calculation.

In this paper, we simulate three liver models of different quantity of particles using mass-spring model and global SPH, respectively; the frame rates of them are indicated in Table 1. Compared to M-S model, SPH method has a heavy computational load and poorer real time though it has higher precision. In virtual surgery simulation, stable tactile feedback required the refreshment rate no less than 300 HZ. The result in Table 1 shows that SPH method does not suit to

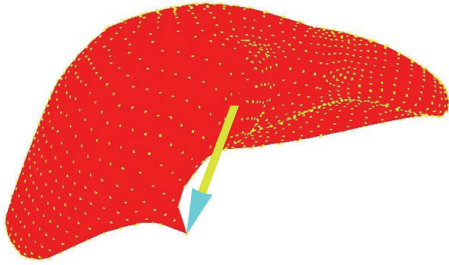


FIGURE 7: Liver deformation under pull force.

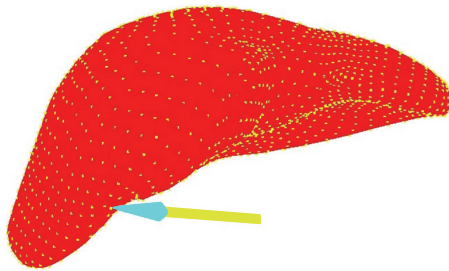


FIGURE 8: Liver deformation under press force.

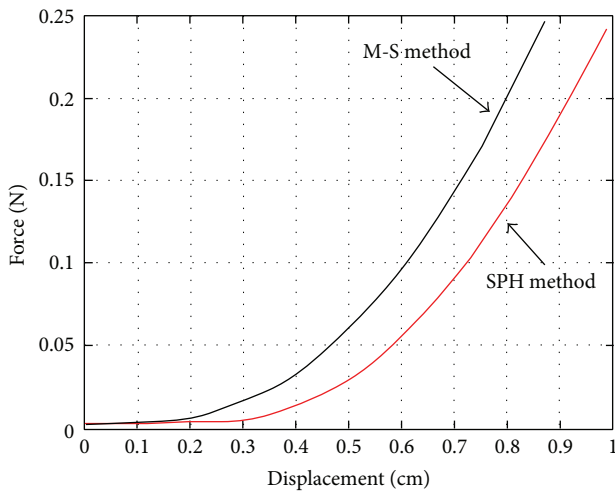


FIGURE 9: The force-displacement curve with M-S model and SPH method.

TABLE 1: Computational efficiency of M-S model and SPH method.

Number of particles	M-S model		SPH method	
	Time (s)	Rate (HZ)	Time (s)	Rate (HZ)
3670	0.00064	1562.50	0.026	38.7
1289	0.00037	2702.70	0.003	333.3
289	0.00007	14285.7	0.00018	5555.6

calculate the feedback force when the number of particles is larger. While the number of particles is around 1300, it could basically achieve a smooth and stable tactile feedback.

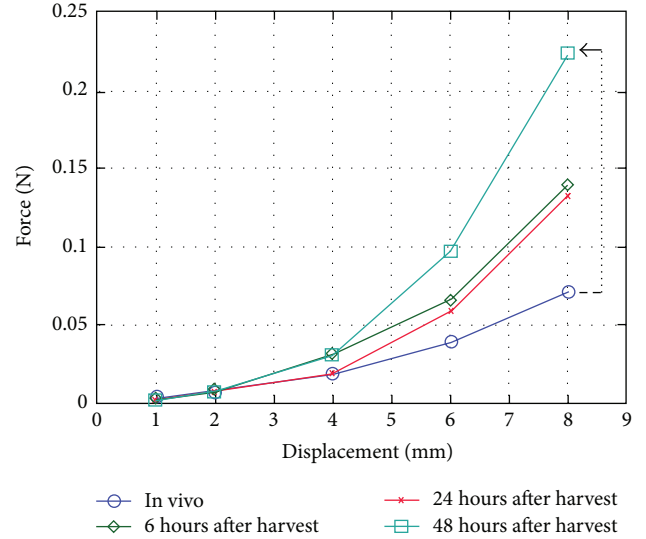


FIGURE 10: Force-displacement curve based on pig liver in vitro and ex vivo [30].

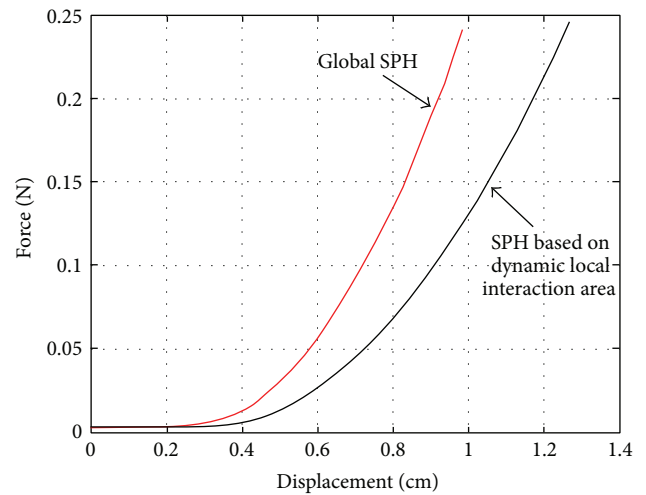


FIGURE 11: Force-displacement curve of two SPH methods.

We implemented the deformation and force feedback using global SPH and SPH based on dynamic local interaction area separately. Applying the same load with same direction and value on the same node in the model, we can get the force-displacement curve, as shown in Figure 11. As can be seen from the figure, the overall trend of the two curves is basically consistent, and the interaction force using SPH based on dynamic local interaction area is smaller than the global SPH method since only part of the domain is discretized and the number of particles involved in the calculation is reduced which result in a local error.

In order to verify the time real performance of SPH based on dynamic local interaction area, we simulated the deformation of five liver models with different numbers of particles using global SPH method and SPH based on dynamic local interaction area, respectively. Since the value of the smooth

TABLE 2: Running time of different models based on global SPH.

Number of particles	Running time			
	$h$			
	$h = 0.3$	$h = 0.5$	$h = 0.6$	$h = 0.8$
3670	0.026	0.089	0.15	0.31
1289	0.003	0.011	0.018	0.04
743	0.0012	0.0054	0.0069	0.12
572	0.0007	0.0022	0.0035	0.0073
289	0.00047	0.00056	0.00063	0.0011

TABLE 3: Running time of different models by SPH based on dynamic local interaction area.

Number of particles	Running time			
	$h$			
	$h = 0.3$	$h = 0.5$	$h = 0.6$	$h = 0.8$
3670	0.0032	0.0056	0.0079	0.02
1289	0.001	0.0014	0.0021	0.0056
743	0.00063	0.00073	0.00097	0.0017
572	0.00047	0.00052	0.00055	0.0012
289	0.00031	0.00033	0.00033	0.0004

radius in the SPH method affects the number of particles involved in the calculation directly which would impact on the computational efficiency, we census the running time of different smooth radiuses. The running time of global SPH is shown in Table 2, and that of SPH based on dynamic local interaction area is shown in Table 3, in which the unit of running time is second.

The following conclusions can be drawn from Tables 2 and 3.

- (1) The running time of SPH based on dynamic local interaction area and global SPH method improves with the increase in the number of particles, but SPH based on dynamic local interaction area has a higher computational efficiency significantly.
- (2) The more particles the model contains, the more effective the SPH based on dynamic local interaction area is. However, the computational efficiency has few gaps for the model containing a small number of particles.
- (3) The value of smooth radius  $h$  has impacted on the computational efficiency directly; while the smooth radius becomes greater, the computational efficiency of process will become lower and timeliness is worse.
- (4) If the model contains a small number of particles, the value of smooth radius impacts on the running time slightly. This is due to the small number of particles distributed sparsely. Setting different smooth radius has little effect on the number of particles involved in calculation. So it almost does not influence the running time of program.

TABLE 4: Calculation efficiency with different local radius.

Interaction radius	$k_1 = 0.5 * f_{ext}$	$k_1 = 0.8 * f_{ext}$	$k_1 = 1.0 * f_{ext}$
Time (s)	0.0027	0.0073	0.02
Rate (HZ)	370.4	137.0	50

TABLE 5: Calculation efficiency with different transmission layer.

Transmission layer	$N = 1$	$N = 2$	$N = 3$	$N = 4$
Time (s)	0.00186	0.0027	0.00357	0.00473
Rate (HZ)	537.6	370.4	280.1	211.4

Refreshment rate of stable tactile feedback should be more than 300 HZ in virtual surgery simulation, so the computing time should be less than 0.0033 s. Comparison of Tables 2 and 3 shows that when smooth radius is set to smaller values such as 0.3, the global SPH would be difficult to meet the requirements of the haptic frame rate with the number of particles over 1289. But SPH based dynamic local interaction area could satisfy tactile frame rate while the number of particles increases to 3670. It greatly improves the simulation in real time compared with global SPH.

The real time performance of SPH based on local dynamic interaction area is related not only with the smooth radius, but also with the interaction region and spread layers. Now we discuss the impact of the different transmission layers and interaction radius to the real time performance of algorithm.

When smooth radius  $h$  is 0.6 and transmission layer is 2, the influence of different interaction area radius on the real time performance of algorithm is shown in Table 4. When smooth radius  $h$  is 0.6 and  $k_1 = 0.5 * f_{ext}$ , the influence of different layers on the real time performance is shown in Table 5, in which  $N$  indicates the propagation layer. It could be concluded from Tables 4 and 5 that as the length of interaction area radius and the number of propagation layers increase, the real time of algorithm becomes worse, and the value of the radius had a greater influence on real time performance. The reason is that when the interaction area radius becomes larger or spread layers increase, the number of particles involved in the calculation will get more which results in an increase in the computational cost. Moreover, the calculation in interaction area is more complex than that in spread region. Therefore, the value of interaction radius has a greater effect on the real time performance.

## 6. Conclusions

In this paper, we adopts Voigt viscoelastic mechanical model to present the characteristics of biomechanics which has strongly physical realism. In the meanwhile we use SPH method as a meshfree technique to solve the deformation process and feedback force which enhances the accuracy of simulation compared with approaches based on meshes.

However, SPH method has a heavy computational load and poorer real time though it has higher precision. In order

to improve the computational efficiency, we proposed a SPH method based on dynamic local interaction area. We divide the model into deformation area and nondeformation area and assume that the deformation is only affected by nodes in the deformation area, and the nodes in nondeformation area will remain still. Deformation area contains two parts, namely, interaction area and transmission area. Interaction area is the region greatly influenced by the surgical instruments, in which the SPH method is adopted to do accurate calculation of particles; transmission area is the effective propagation range of force, in which the physical quantities of all particles are obtained by decaying physical quantities of the force points. The particles in different transmission layers have different effect on the deformation of the model. So we set weighting factors to indicate the influence degrees of different transmission layers.

Experimental results show that SPH methodology is suitable for simulating the liver tissue deformation and force feedback calculation, and SPH based on dynamic local interaction area has a higher computational efficiency significantly compared with usual SPH. SPH based on dynamic local interaction area can ensure 300 HZ frame rate when the number of particles is under certain number which satisfies the need of smooth haptic feedback in virtual surgery. Because the accuracy of SPH method also depends on the arrangement of the particles, when the force loads on some particles in disordered arrangement or topological structure, the result will be unstable. So our next tasks mainly focus on the following.

- (1) Improving the stability of SPH method: during the experiments, particles shocked irregularly when the time step was set to large. In the next work, we will study the factors for stability of SPH, such as smooth radius, kernel function, and the distribution of particles.
- (2) Verifying the accuracy of force feedback: real medical surgery is very strict and does not allow any deviation. Therefore, it must validate the accuracy of force feedback in virtual surgery and make a comprehensive evaluation for authentication methods, for example, joining the deformation time, deformation range, feelings of trainers, and the test of physicians into the evaluation program.

## Conflict of Interests

The authors declare that there is no conflict of interests regarding the publication of this paper.

## Acknowledgments

This research is supported by the Major Program of the National Natural Science Foundation of China (Grant no. 61190121), Program for Innovative Research Team (in Science and Technology) in University of Henan Province (Grant no. 13IRTSTHN023), and Innovation Scientists and Technicians Troop Construction Projects of Zhengzhou City (Grant no. 131PCXTD595).

## References

- [1] D. Terzopoulos and K. Waters, "Physically based facial modeling, analysis and animation," *Journal of Visualization and Computer Animation*, vol. 1, pp. 73–80, 1990.
- [2] H. Kataoka, S. Noda, and H. Yokota, "Simulations of needle insertion by using a eulerian hydrocode FEM and the experimental validations," in *Medical Image Computing and Computer-Assisted Intervention—MICCAI 2008*, vol. 5242 of *Lecture Notes in Computer Science*, pp. 560–568, Springer, Berlin, Germany, 2008.
- [3] M. Nakao, *Cardiac Surgery Simulation with Active Interaction and Adaptive Physics-Based Modeling*, Department of Social Informatics, Graduate School of Informatics, Kyoto University, Kyoto, Japan, 2003.
- [4] D. Marinkovic, M. Zehn, and Z. Marinkovic, "Finite element formulations for effective computations of geometrically nonlinear deformations," *Advances in Engineering Software*, vol. 50, no. 1, pp. 3–11, 2012.
- [5] R. Mafi and S. Sirouspour, "GPU-based acceleration of computations in nonlinear finite element deformation analysis," *International Journal for Numerical Methods in Biomedical Engineering*, vol. 30, no. 3, pp. 365–381, 2014.
- [6] X. G. Tang, Y. S. Xiong, K. Tan, and X. H. Pan, "Soft-tissue finite elements deformation model based on OpenHaptic," *Journal of System Simulation*, vol. 24, no. 7, pp. 1434–1437, 2012.
- [7] R. W. Webster, D. I. Zimmerman, B. J. Mohler, M. G. Melkonian, and R. S. Haluck, "A prototype haptic suturing simulator," *Studies in Health Technology and Informatics*, vol. 81, pp. 567–569, 2001.
- [8] P. E. Hammer, M. S. Sacks, P. J. del Nido, and R. D. Howe, "Mass-spring model for simulation of heart valve tissue mechanical behavior," *Annals of Biomedical Engineering*, vol. 39, no. 6, pp. 1668–1679, 2011.
- [9] X.-M. Liu, R.-Y. Wang, and S. Guo, "Force feedback based on mass-spring volume model and improved Euler algorithm," *Journal of System Simulation*, vol. 25, no. 9, pp. 2234–2238, 2013.
- [10] S. De, J. Kim, Y.-J. Lim, and M. A. Srinivasan, "The point collocation-based method of finite spheres (PCMFSS) for real time surgery simulation," *Computers & Structures*, vol. 83, no. 17–18, pp. 1515–1525, 2005.
- [11] J. Jansson and J. S. M. Vergeest, "A discrete mechanics model for deformable bodies," *Computer Aided Design*, vol. 34, no. 12, pp. 913–928, 2002.
- [12] M. Müller, B. Heidelberger, M. Teschner, and M. Gross, "Meshless deformations based on shape matching," *ACM Transactions on Graphics*, vol. 24, no. 3, pp. 471–478, 2005.
- [13] L. B. Lucy, "A numerical approach to the testing of the fission hypothesis," *The Astronomical Journal*, vol. 82, pp. 1013–1024, 1977.
- [14] F. R. Ming, A. M. Zhang, and X. Y. Cao, "A robust shell element in meshfree SPH method," *Acta Mechanica Sinica*, vol. 29, no. 2, pp. 241–255, 2013.
- [15] J. J. Monaghan, "Smoothed particle hydrodynamics," *Reports on Progress in Physics*, vol. 68, no. 8, pp. 1703–1759, 2005.
- [16] M. B. Liu and G. R. Liu, "Smoothed particle hydrodynamics (SPH): an overview and recent developments," *Archives of Computational Methods in Engineering*, vol. 17, no. 1, pp. 25–76, 2010.
- [17] D. Li, X. Li, and Y. Lin, "Numerical simulation of droplet impacting liquid surface by SPH," *Science China Technological Sciences*, vol. 54, no. 7, pp. 1873–1880, 2011.

- [18] X. Zheng, W. Y. Duan, and Q. W. Ma, "A new scheme for identifying free surface particles in improved SPH," *Science China Physics, Mechanics & Astronomy*, vol. 55, no. 8, pp. 1454–1463, 2012.
- [19] J. Fang, R. G. Owens, L. Tacher, and A. Parriaux, "A numerical study of the SPH method for simulating transient viscoelastic free surface flows," *Journal of Non-Newtonian Fluid Mechanics*, vol. 139, no. 1-2, pp. 68–84, 2006.
- [20] X. Yang and M. Liu, "Numerical modeling of oil spill containment by boom using SPH," *Science China: Physics, Mechanics and Astronomy*, vol. 56, no. 2, pp. 315–321, 2013.
- [21] J. J. Monaghan and J. C. Lattanzio, "A refined particle method for astrophysical problems," *Astronomy & Astrophysics*, vol. 149, no. 1, pp. 135–143, 1985.
- [22] P. Cai, C. Indhumathi, Y. Cai et al., "Collision detection using axis aligned bounding boxes," in *Simulations, Serious Games and Their Applications*, pp. 1–14, Springer, Singapore, 2014.
- [23] L. Yu, T. Wang, H. Song, L. Sun, Z. Wang, and L. Zhao, "Geometric modeling and collision detection based on hybrid bounding box in virtual gallbladder surgery," in *Proceedings of the ICME International Conference on Complex Medical Engineering (CME '13)*, pp. 25–30, Beijing, China, May 2013.
- [24] H. A. Sulaiman, M. A. Othman, M. M. Ismail et al., "Distance computation using Axis Aligned Bounding Box (AABB) parallel distribution of dynamic origin point," in *Proceedings of the Annual International Conference on Emerging Research Areas (AICERA '13) and International Conference on Microelectronics, Communications and Renewable Energy (ICMiCR '13)*, pp. 1–6, June 2013.
- [25] S. Gottschalk, M. C. Lin, and D. Manocha, "OBB-tree: a hierarchical structure for rapid interference detection," in *Proceedings of the Computer Graphics Conference (SIGGRAPH '96)*, pp. 171–180, August 1996.
- [26] X. J. Ding, "Research on collision detection algorithm based on OBB," *Applied Mechanics and Materials*, vol. 433–435, pp. 936–939, 2013.
- [27] F. Ding, *Rapid Cloth Collision Detection Using Bounding Sphere Trees*, 2013.
- [28] H. Berkley, G. Turkiyyah, D. Berg, M. Ganter, and S. Weghorst, "Real-time finite element modeling for surgery simulation: an application to virtual suturing," *IEEE Transactions on Visualization and Computer Graphics*, vol. 10, no. 3, pp. 314–325, 2004.
- [29] J. Z. Zhou, X. P. Xu, Z. C. Zhu et al., "Research and application of K-DOPS algorithm in virtual maintenance training system for diesel engine," *Advanced Materials Research*, vol. 805–806, pp. 1911–1916, 2013.
- [30] S. de, J. Kim, Y. J. Lim, and M. A. Srinivasan, "The point collocation-based method of finite spheres (PCMFS) for real time surgery simulation," *Computers and Structures*, vol. 83, no. 17–18, pp. 1515–1525, 2005.

## Research Article

# Parametric Modeling of Human Gradient Walking for Predicting Minimum Energy Expenditure

**Gerard Saborit and Adrià Casinos**

*Departament de Biologia Animal, Universitat de Barcelona, 08028 Barcelona, Spain*

Correspondence should be addressed to Gerard Saborit; [gsaborit@gmail.com](mailto:gsaborit@gmail.com)

Received 17 December 2014; Revised 2 February 2015; Accepted 3 February 2015

Academic Editor: Zhonghua Sun

Copyright © 2015 G. Saborit and A. Casinos. This is an open access article distributed under the Creative Commons Attribution License, which permits unrestricted use, distribution, and reproduction in any medium, provided the original work is properly cited.

A mathematical model to predict the optimum gradient for a minimum energetic cost is proposed, based on previous results that showed a minimum energetic cost when gradient is  $-10\%$ . The model focuses on the variation in mechanical energy during gradient walking. It is shown that kinetic energy plays a marginal role in low speed gradient walking. Therefore, the model considers only potential energy. A mathematical parameter that depends on step length was introduced, showing that the optimal gradient is a function of that parameter. Consequently, the optimal negative gradient depends on the individual step length. The model explains why recent results do not suggest a single optimal gradient but rather a range around  $-10\%$ .

## 1. Introduction

Human walking requires energy for a variety of reasons. For instance, in level walking, alternate stages of braking and acceleration exist. Although there is a pendulum-like transfer between potential and kinetic energy of the body center of mass, this is only an energy-saving system. Since the transfer is not complete, additional energy must be incorporated into the system in each step (Cavagna et al. [1, 2]).

In gradient walking the situation changes depending on whether walking up- or downhill. In the former case (positive gradient) positive work is needed to provide gravitational potential energy. In downhill walking, the lost potential energy is absorbed by muscles compelled to stretch. Cavagna [3] showed that the lost energy is transformed into heat through negative or braking work. Direct experiments measuring oxygen uptake in subjects walking on different gradients showed that the minimum energetic cost is not accomplished on level ground but on a negative gradient of about  $-10\%$  (Margarita [4]). Further studies (Minetti et al. [5]) demonstrated that minimum energetic cost does not depend on speed and that the optimal path within a positive gradient, considering the vertical cost of transportation, is not always the straight one (Minetti [6]). Further studies (Kamon [7]) showed that oxygen uptake during descent can be about 30% of that required during ascent. Therefore we can deduce that

the process of muscular braking, which involves negative work, is energetically different from positive work due to different efficiency factors [8–11]. A complete mechanical analysis must include both kinetic and potential energies but we can calculate each contribution to determine whether one of these (kinetic or potential) is more dominant or whether both energies contribute equally to the whole energetic cost.

Since walking implies low and rather constant velocity, kinetic energy does not vary greatly during the different walking phases. Supposing standard walking at a speed of  $1.25 \text{ m}\cdot\text{s}^{-1}$ , the total kinetic energy involved in the movement is  $0.78 \text{ J}$  per unit mass. This energy is not supplied at every step since people do not come to a complete standstill between steps. During walking the center of mass moves at almost constant speed. Gottschall and Kram [12] quantified the variation in velocity of the center of mass during different step phases and for different gradients. This variation is about  $0.09 \text{ m}\cdot\text{s}^{-1}$  per step for level walking with a maximum of  $0.18 \text{ m}\cdot\text{s}^{-1}$  per step in some downhill walking situations. During each step one brakes and accelerates about  $0.09 \text{ m}\cdot\text{s}^{-1}$ , leading to a small variation in speed (from  $1.20 \text{ m}\cdot\text{s}^{-1}$  to  $1.30 \text{ m}\cdot\text{s}^{-1}$ ). Calculation of the energy per unit mass taking this speed variation into account shows that the kinetic energy per unit mass needed is about  $0.12 \text{ J}\cdot\text{kg}^{-1}$  per step for

level walking and up to  $0.20 \text{ J}\cdot\text{kg}^{-1}$  per step for high negative gradients.

For potential energy, the vertical oscillation of the center of mass varies from 8 to 10 cm, depending on step length. This means a potential energy oscillation per unit mass from  $0.78 \text{ J}\cdot\text{kg}^{-1}$  per step up to  $0.98 \text{ J}\cdot\text{kg}^{-1}$  per step. It is clear that kinetic energy plays a lesser role in walking at low speeds, being from 5 to almost 10 times smaller than potential energy depending on a number of variables. Another factor to take into account is that the transfer of energy from one walking phase to another usually transforms the excess potential energy, achieved during the single support phase, to kinetic energy for the body. The kinetic energy of the center of mass is almost constant and the main loss of kinetic energy is due to the contact between the still feet on the ground and braking work to avoid acceleration. In the next step phase, the muscles perform positive work to raise the center of mass, thus gaining potential energy again. This is another reason for focusing the analysis on potential energy: the energy transfer involves transforming potential energy into kinetic energy in such a way that the calculation done above for kinetic energy could be overestimated. The significant effect of gravity on walking has been evaluated in previous studies [5, 13] and the incomplete energetic transfer between potential and kinetic energy during walking has been widely discussed [14–17]. As shown by Heglund and Schepens [18], this energy transfer also varies depending on age, with less recovery in children than in adults.

For the reasons stated above, this work focuses on the variation in potential energy during the walking process, as a simple and first approximation analysis. Further corrections such as kinetic energy components could be introduced if the model's predictions are not sufficiently accurate. The main objective of the model is to prove that the vertical oscillation of the center of mass is ultimately responsible for the minimum energy spent at low negative gradient and that only with potential energy analysis will the model fit previous experimental results.

## 2. Model

In human walking there are basically two stages. In the first stage, the feet are simultaneously on the ground (double support) and the center of mass is at its lowest point, at a distance  $y_{\min}$  from the ground. In the second stage, one foot is on the ground (single support), with the corresponding leg straight. The center of mass is at its highest position, at a maximum distance from the ground ( $y_{\max}$ ).

Consider now a human with leg length  $l$ . Usually the step length tends to be smaller than the leg length. Thus it can be modeled as  $l/k$ , with the variable  $k$  being an arbitrary parameter that differs for each individual, within a range.

As shown in Figure 1, the maximum height of the center of mass occurs during the single support phase and can be defined as follows:

$$y_{\max} = y_0 + l, \quad (1)$$

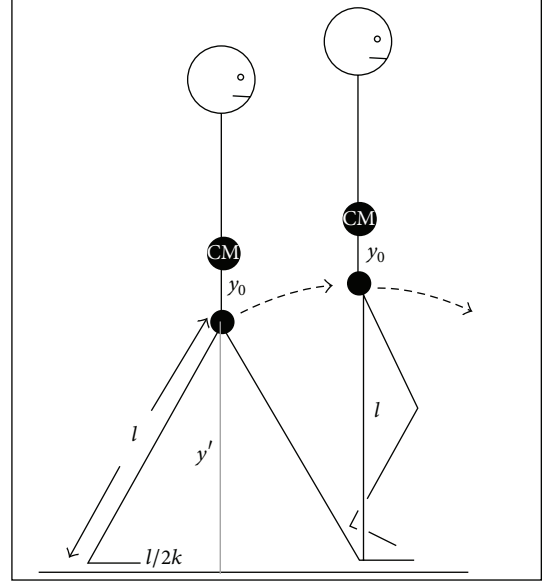


FIGURE 1: Height variation of the human center of mass during successive step phases. Double support phase (left) and single support phase (right) are shown. Extracted and modified from Alexander [19].

where  $y_0$  is the vertical distance from the center of mass to the acetabular joint and  $l$  is the distance from the acetabular joint to the ground. That means  $l$  is the leg length.

On the other hand, the minimum height of the center of mass occurs during the double support phase and can be defined as

$$y_{\min} = y_0 + y', \quad (2)$$

where  $y'$  is the distance from the acetabular joint to the ground and  $y_0$  is, again, the distance from this joint to the center of mass. Hence the distance between the acetabular joint and the ground can be defined as a cathetus of a right-angled triangle, the half-step ground distance ( $l/2k$ ) as the other cathetus, and the leg length ( $l$ ) as the hypotenuse.

From Figure 1, the right triangle is defined using the Pythagorean theorem:

$$l^2 = y'^2 + \frac{l^2}{4k^2}. \quad (3)$$

$y'$  can be found from (3):

$$y' = \sqrt{l^2 - \frac{l^2}{4k^2}} = l\sqrt{1 - \frac{1}{4k^2}}. \quad (4)$$

Replacing the  $y'$  in (2) we find

$$y_{\min} = y_0 + l\sqrt{1 - \frac{1}{4k^2}}. \quad (5)$$

The total oscillation of the center of mass  $\Delta y$  can be defined as

$$\Delta y = y_{\max} - y_{\min}. \quad (6)$$

Using the values found in (1) and (5),

$$\Delta y = y_0 + l - y_0 - l\sqrt{1 - \frac{1}{4k^2}} \quad (7)$$

and subsequently

$$\Delta y = l\left(1 - \sqrt{1 - \frac{1}{4k^2}}\right). \quad (8)$$

By definition, the variation in potential energy  $\Delta U$  of a body that suffers a change in height is

$$\Delta U = mg\Delta y. \quad (9)$$

Replacing the value found in (8) in (9),

$$\Delta U_{\text{osc}} = mgl\left(1 - \sqrt{1 - \frac{1}{4k^2}}\right). \quad (10)$$

Equation (10) is the total variation in potential energy of the center of mass during the oscillation that occurs at each step. It is termed  $\Delta U_{\text{osc}}$ , to differentiate it from any other potential energy variation.

Let us consider now the variation in potential energy due to a gradient. Conditions differ depending upon the sign of the gradient, but for mathematical simplicity a positive gradient will be considered. It should be noted that during gradient walking there is an adaptation of the step phases and they may not necessarily occur at the same point as in level walking. For instance, in downhill walking the rising of the center of mass is done faster than in level walking, and the later decline is done slower. In any case the height variation of the center of mass is not different than in level walking. So in terms of energy it is indifferent whether the elevation of the center of mass happens sooner or later, as at each step very similar variations of height occur. For simplicity of this first approximation model we suppose that the different timing of the walking phases between gradient and level walking does not affect significantly the energetic calculation.

Take the height attained ( $dy$ ) in a gradient with the step length ( $l/k$ ). These two distances and the horizontal projection of the step length ( $dx$ ) define a right triangle (Figure 2).

By definition, the gradient ( $i$ ) is the height variation per unit of displacement:

$$i = \frac{dy}{dx}. \quad (11)$$

Therefore, the height variation in terms of the gradient is

$$dy = idx. \quad (12)$$

The sides of the right triangle are defined using the Pythagorean theorem:

$$\frac{l^2}{k^2} = dy^2 + dx^2. \quad (13)$$

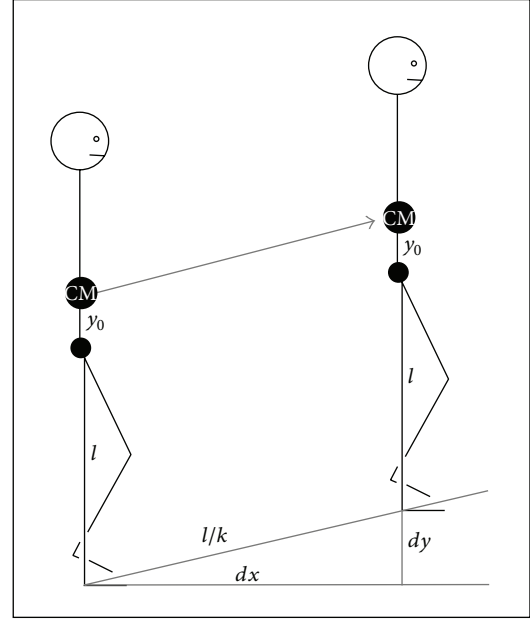


FIGURE 2: Gradient that a human overcomes in one step during uphill walking. Extracted and modified from Alexander [19].

Replacing  $dy$  by its value found in (12),

$$\frac{l^2}{k^2} = (idx)^2 + dx^2 = dx^2(1 + i^2). \quad (14)$$

Solving (14) for  $dx$  we find

$$dx^2 = \frac{l^2}{k^2(1 + i^2)} \quad (15)$$

and finally

$$dx = \frac{l}{k}\sqrt{\frac{1}{1 + i^2}}. \quad (16)$$

The variation in the potential energy is defined in (9). Using (12) again, the variation in potential energy due to a certain gradient for one step ( $\Delta U_{\text{grad}}$ ) is

$$\Delta U_{\text{grad}} = mgdy = mgidx \quad (17)$$

and using the value of  $dx$  found in (16),

$$\Delta U_{\text{grad}} = mgi\frac{l}{k}\sqrt{\frac{1}{1 + i^2}}. \quad (18)$$

Equation (18) defines the energy that must be supplied in one step to overcome gradient  $i$ . If the gradient is negative, that amount of energy would be supplied to the body instead, and, consequently, it would accelerate unless the subject brakes. According to previous results [1, 7], braking work requires four to five times less energy than positive work. In other words, to absorb and brake 100 J of potential energy, transformed to kinetic energy during downhill walking, the body does about 20 J of negative work. The negative work

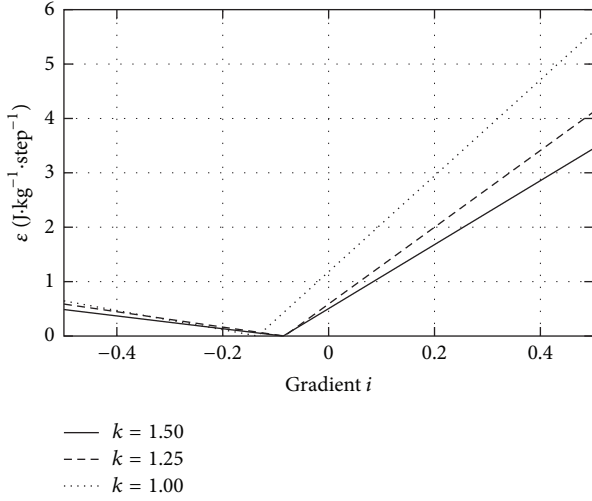


FIGURE 3: Total potential energy contribution to the energy expenditure as a function of gradient  $i$ . Multiple plots were constructed assuming  $k = 1$ ,  $k = 1.25$ , and  $k = 1.5$ . All lines were constructed assuming  $g = 9.81 \text{ m}\cdot\text{s}^{-2}$ .

required to brake is proportional to the energy previously transferred in the form of kinetic energy.

The total potential energy contribution to the whole energetic cost is the sum of two main factors: one for the oscillation of the center of mass due to the walking process and the other to overcome a given variable gradient, if any.

Thus, the total potential energy contribution ( $U_{\text{tot}}$ ) can be written as the sum of these two factors:

$$U_{\text{tot}} = \Delta U_{\text{grad}} + \Delta U_{\text{osc}}. \quad (19)$$

It must be taken into account that if the total energy is negative, that is, the body receives energy from a negative gradient, it must brake to avoid acceleration. As mentioned previously, the negative work is about five times more efficient than positive work. To reflect this, an auxiliary function  $\varepsilon$  is defined, which includes the cost of negative work, if necessary. If the total amount of energy is positive, the body must supply that energy, as it must overcome a certain gradient. If it is negative an excess of potential energy is received due to the loss of height. So braking work five times smaller than the excess of potential energy received must be performed [7]. As absolute work is positive, the factor introduced to reflect the difference in efficiency is  $-5$ , to ensure that  $\varepsilon$  is positive for negative gradients:

$$\begin{aligned} \varepsilon &= U_{\text{tot}} & \text{if } U_{\text{tot}} > 0, \\ \varepsilon &= \frac{U_{\text{tot}}}{-5} & \text{if } U_{\text{tot}} < 0. \end{aligned} \quad (20)$$

Plotting  $\varepsilon$  as a function of the gradient ( $i$ ) gives Figure 3, with very similar behavior to the experimental results found in Margaria [4] and Minetti et al. [5] for gradient walking and even Minetti's research [20] on gradient running.

Figure 3 faithfully reproduces experimental data found in previous oxygen consumption experiments. The fact that

we can reproduce this behavior with such a simple model confirms our hypothesis: as a first approximation kinetic energy variation is not relevant for low speed walking and the timing fluctuations between stages in gradient and level walking are insignificant in energetic terms. In addition to reproducing the pattern of oxygen consumption, our model predicts the optimal gradient and links it to step length, as this minimum varies with the value of the  $k$  parameter, which depends on step length. To find an analytic expression of the optimum gradient in terms of  $k$ , that is, in terms of step length,  $\Delta U_{\text{grad}}$  and  $\Delta U_{\text{osc}}$  must be the same since at the minimum energetic cost they are equal but with opposite sign. This means their sum is zero:

$$\Delta U_{\text{grad}} + \Delta U_{\text{tot}} = 0. \quad (21)$$

Taking the values found in (18) and (10) for  $\Delta U_{\text{grad}}$  and  $\Delta U_{\text{osc}}$ , respectively, each term is replaced:

$$mgl \frac{i}{k} \sqrt{\frac{1}{1+i^2}} + mgl \left( 1 - \sqrt{1 - \frac{1}{4k^2}} \right) = 0. \quad (22)$$

It should be noted that for low gradients ( $i \approx 0$ ) the first square root term is close to 1. For mathematical simplicity this root can be removed from the equation, without introducing any significant error, resulting in

$$mgl \frac{i}{k} + mgl \left( 1 - \sqrt{1 - \frac{1}{4k^2}} \right) = 0. \quad (23)$$

Developing and taking out the common factor  $mgl$ ,

$$\frac{i}{k} + 1 - \sqrt{1 - \frac{1}{4k^2}} = 0. \quad (24)$$

Solving the equation for  $i$  gives

$$\frac{i}{k} = \sqrt{1 - \frac{1}{4k^2}} - 1 \quad (25)$$

and finally

$$i = k \sqrt{1 - \frac{1}{4k^2}} - k. \quad (26)$$

Figure 4 shows the plot of  $i(k)$  function found in (26). As defined above, the  $k$  parameter is a function of step length, so it can be shown that there is an optimum gradient, around  $-10\%$ , for a given step length but that, depending on that step length, the optimum gradient can vary somewhat. For large step lengths ( $k \sim 1.10$ ), the optimum gradient tends to be around  $-12\%$ , and for short step lengths ( $k \sim 1.5$ ), the optimum gradient tends to be lower, around  $-8\%$ . Alexander [21] inferred that the range of comfortable variation in step length is  $k = 1.35 \pm 0.20$ . So the optimal gradient of a given subject can usually be expected to be around  $-10\%$ .

### 3. Conclusion

The model, which is based on analysis of the variation in potential energy during walking, fits the experimental

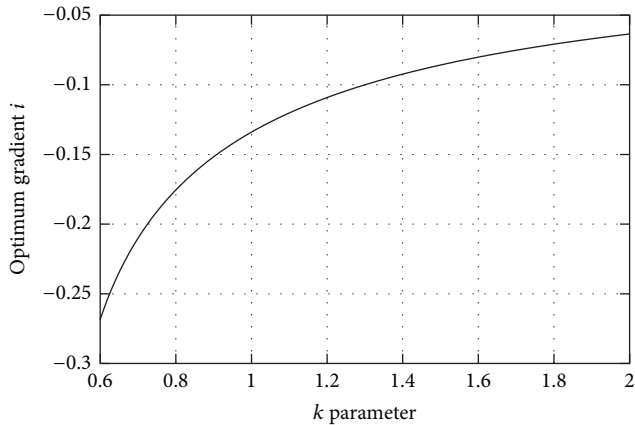


FIGURE 4: Optimum gradient as a function of the  $k$  parameter.

results on minimum energy expenditure obtained in previous studies and links this minimum to the step length of the subject. The hypothesis that kinetic energy plays a small role at low speeds and is not needed in a first approximation of the mechanical analysis of gradient walking appears to be correct.

The model proves mathematically that the minimum energy expenditure is due to potential energy exchange and is related to the subject's step length. The reason for this is that in every step the center of mass is raised and the body must supply some potential energy, but with a low negative gradient, this energy can be supplied instead by the loss of potential energy. In these circumstances the body saves energy and can move in a more efficient way, requiring less oxygen uptake.

Our work demonstrates that the negative gradient that minimizes energy expenditure depends on the  $k$  parameter. For long steps the potential energy involved is higher since the variation in height of the center of mass is bigger, and for short steps the variation in height of the center of mass is smaller. Therefore each step length has its own negative gradient of minimum energy expenditure. This suggests new strategies for minimizing energy expenditure during gradient walking. A solution for minimizing the energy spent in either downhill or uphill walking would be to adjust the step length for a given variable gradient to ensure that the subject remains on the optimal gradient range.

Common walking strategies for minimizing the energetic cost of movement usually involve either changing step length or stride frequency [22, 23]. Decreasing the stride frequency leads to variation in the walking velocity, similarly to step length decrease and therefore a decrease in kinetic energy and potential energy expenditure too, since the center of mass must be raised fewer times in a given period. Step length variation can be considered a valid strategy because people can slightly modify step length within a range in a comfortable fashion. In our model the possibility of step length modification is reflected in the range of variation of the  $k$  parameter ( $1.35 \pm 0.20$ ). This means that, assuming a leg length of 90 cm, people can comfortably use a step length range of 60–80 cm. Longer or shorter steps outside this range are possible, but it would be uncomfortable to

maintain this strategy over long periods. Given the range of variation mentioned above, it can be seen from Figure 4 that the optimum gradient range can easily extend from  $-8\%$  to  $-12\%$  by adjusting the step length to keep  $k$  between 1.10 and 1.50. From Figure 4 it can be seen that for gradients beyond  $-13\%$  the optimal step length ( $k = 1$ ) is too wide to be considered as a valid strategy. In such circumstances other strategies could be used, such as lowering the stride frequency and step length, but with the drawback of reducing the walking velocity. Leroux et al. [22] suggested that step length is slightly reduced as negative gradients increase beyond the comfortable range. This fits with the stated strategy of reducing the walking velocity, or keeping the same velocity by adjusting the stride frequency while reducing step length, as the body needs to absorb more energy from the negative gradient to avoid acceleration, and the more negative the gradient is, the more braking work needs to be done.

In conclusion, this work presents a parametric model based on an analysis of the variation in potential energy during gradient walking, which explains the energetic mechanism behind the minimum energy spent experimentally in many previous studies, and links this optimum gradient with step length.

## Conflict of Interests

All authors declare that there is no conflict of interests regarding the publication of this paper.

## Authors' Contribution

Gerard Saborit and Adrià Casinos contributed equally to the work.

## Acknowledgments

This work was funded by the Spanish Ministry of Economy and Competitiveness (CGL2011-23919) and the Generalitat de Catalunya, program AGAUR (2009SGR884). The authors thank Dr. Rémi Hackert (Muséum, Paris) for technical advice and suggestions.

## References

- [1] G. A. Cavagna, N. C. Heglund, and C. R. Taylor, "Mechanical work in terrestrial locomotion: two basic mechanisms for minimizing energy expenditure," *The American Journal of Physiology*, vol. 233, no. 5, pp. R243–R261, 1977.
- [2] G. A. Cavagna and M. Kaneko, "Mechanical work and efficiency in level walking and running," *Journal of Physiology*, vol. 268, no. 2, pp. 467–481, 1977.
- [3] G. A. Cavagna, *Muscolo e locomozione*, Raffaello Cortina, Milan, Italy, 1988.
- [4] R. Margaria, *Biomechanics and Energetics of Muscular Exercise*, Clarendon Press, Oxford, UK, 1976.
- [5] A. E. Minetti, L. P. Ardigo, and F. Saibene, "Mechanical determinants of gradient walking energetics in man," *Journal of Physiology*, vol. 472, pp. 725–735, 1993.

- [6] A. E. Minetti, "Optimum gradient of mountain paths," *Journal of Applied Physiology*, vol. 79, no. 5, pp. 1698–1703, 1995.
- [7] E. Kamon, "Negative and positive work in climbing a ladder-mill," *Journal of applied physiology*, vol. 29, no. 1, pp. 1–5, 1970.
- [8] B. C. Abbot, B. Bigland, and J. M. Ritchie, "The physiological cost of negative work.," *The Journal of physiology*, vol. 117, no. 3, pp. 380–390, 1952.
- [9] J. M. Donelan, R. Kram, and A. D. Kuo, "Mechanical work for step-to-step transitions is a major determinant of the metabolic cost of human walking," *Journal of Experimental Biology*, vol. 205, no. 23, pp. 3717–3727, 2002.
- [10] J. M. Donelan, R. Kram, and A. D. Kuo, "Simultaneous positive and negative external mechanical work in human walking," *Journal of Biomechanics*, vol. 35, no. 1, pp. 117–124, 2002.
- [11] A. D. Kuo, "Energetics of actively powered locomotion using the simplest walking model," *Journal of Biomechanical Engineering*, vol. 124, no. 1, pp. 113–120, 2002.
- [12] J. S. Gottschall and R. Kram, "Mechanical energy fluctuations during hill walking: the effects of slope on inverted pendulum exchange," *Journal of Experimental Biology*, vol. 209, no. 24, pp. 4895–4900, 2006.
- [13] G. A. Cavagna, P. A. Willems, and N. C. Heglund, "The role of gravity in human walking: pendular energy exchange, external work and optimal speed," *Journal of Physiology*, vol. 528, no. 3, pp. 657–668, 2000.
- [14] R. R. Neptune, F. E. Zajac, and S. A. Kautz, "Muscle mechanical work requirements during normal walking: the energetic cost of raising the body's center-of-mass is significant," *Journal of Biomechanics*, vol. 37, no. 6, pp. 817–825, 2004.
- [15] M. Duff-Raffaele, D. C. Kerrigan, P. J. Corcoran, and M. Saini, "The proportional work of lifting the center of mass during walking," *The American Journal of Physical Medicine and Rehabilitation*, vol. 75, no. 5, pp. 375–379, 1996.
- [16] J. B. Saunders, V. T. Inman, and H. D. Eberhardt, "The major determinants in normal and pathological gait," *The Journal of Bone and Joint Surgery. American Volume*, vol. 35, no. 3, pp. 543–558, 1953.
- [17] N. C. Heglund, G. A. Cavagna, and C. R. Taylor, "Energetics and mechanics of terrestrial locomotion. III. Energy changes of the body centre of mass as a function of the speed and body size in birds and mammals," *Journal of Experimental Biology*, vol. 79, pp. 41–56, 1982.
- [18] N. C. Heglund and B. Schepens, "Ontogeny recapitulates phylogeny? Locomotion in children and other primitive hominids," in *Vertebrate Biomechanics and Evolution*, V. L. Bels, J. P. Gasc, and A. Casinos, Eds., pp. 283–295, Bios, Oxford, UK, 2003.
- [19] R. M. Alexander, "Walking and running," *The Mathematical Gazette*, vol. 80, no. 488, pp. 262–266, 1996.
- [20] A. E. Minetti, L. P. Ardigò, and F. Saibene, "Mechanical determinants of the minimum energy cost of gradient running in humans," *Journal of Experimental Biology*, vol. 195, pp. 211–225, 1994.
- [21] R. M. Alexander, "Stride length and speed for adults, children, and fossil hominids," *The American Journal of Physical Anthropology*, vol. 63, no. 1, pp. 23–27, 1984.
- [22] A. Leroux, J. Fung, and H. Barbeau, "Postural adaptation to walking on inclined surfaces: I. Normal strategies," *Gait & Posture*, vol. 15, no. 1, pp. 64–74, 2002.
- [23] K. G. Holt, R. Ratcliffe, and J. Hamill, "Energetic cost and stability during human walking at the preferred stride frequency," *Journal of Motor Behavior*, vol. 27, no. 2, pp. 164–178, 1995.

## Research Article

# Kinematic, Dynamic, and Energy Characteristics of Diastolic Flow in the Left Ventricle

Seyed Saeid Khalafvand,<sup>1</sup> Tin-Kan Hung,<sup>2</sup> Eddie Yin-Kwee Ng,<sup>1</sup> and Liang Zhong<sup>3,4</sup>

<sup>1</sup>*School of Mechanical and Aerospace Engineering, Nanyang Technological University, Singapore 639798*

<sup>2</sup>*Department of Bioengineering, University of Pittsburgh, Pittsburgh, PA 15261, USA*

<sup>3</sup>*National Heart Research Institute of Singapore, National Heart Centre Singapore, 5 Hospital Drive, Singapore 169609*

<sup>4</sup>*Duke-NUS Graduate Medical School Singapore, 8 College Road, Singapore 169857*

Correspondence should be addressed to Tin-Kan Hung; [tkhung@pitt.edu](mailto:tkhung@pitt.edu)

Received 17 December 2014; Revised 10 April 2015; Accepted 15 April 2015

Academic Editor: Chung-Min Liao

Copyright © 2015 Seyed Saeid Khalafvand et al. This is an open access article distributed under the Creative Commons Attribution License, which permits unrestricted use, distribution, and reproduction in any medium, provided the original work is properly cited.

Blood flow characteristics in the normal left ventricle are studied by using the magnetic resonance imaging, the Navier-Stokes equations, and the work-energy equation. Vortices produced during the mitral valve opening and closing are modeled in a two-dimensional analysis and correlated with temporal variations of the Reynolds number and pressure drop. Low shear stress and net pressures on the mitral valve are obtained for flow acceleration and deceleration. Bernoulli energy flux delivered to blood from ventricular dilation is practically balanced by the energy influx and the rate change of kinetic energy in the ventricle. The rates of work done by shear and energy dissipation are small. The dynamic and energy characteristics of the 2D results are comparable to those of a 3D model.

## 1. Introduction

Analysis of blood flow in the left ventricle is of fundamental interest in studying cardiac function and dysfunction. Using magnetic resonance velocity mapping, Kim et al. [1] reported a large counterclockwise vortex in the ventricle during diastole. Kilner et al. [2] indicated flow patterns in the normal LV avoiding excessive dissipation of energy to facilitate an efficient ejection of blood. Asymmetric vortices appearing with anterior and posterior mitral leaflets were discussed by Ebbers et al. [3]. Other significant two-dimensional (2D) and three-dimensional (3D) mathematical models for inflow to the ventricle were reported by several groups [4–9]. Using a prolate spheroid model, Domenichini et al. [10] stated that flow patterns in normal heart were optimal in terms of minimal energy dissipation.

Numerical modeling of flow in LV was classified into three types [11]: geometry-prescribed CFD methods [12–16], immerse boundary (IB) methods [17–19], and fluid structure

interaction (FSI) methods [11, 20, 21]. A geometry-prescribed method employs the moving wall as a boundary condition, while the FSI methods couple the equations of motion for fluid and myocardium. The latter is a very challenging task because of the geometry and material properties of valve leaflets. Saber et al. [12, 13] used combination of MRI and CFD for flow simulation and obtained a counter clockwise vortex for diastolic flow in the ventricle. Long et al. [14, 15] investigated the influence of boundary motion to flow patterns and reported a main counter clockwise vortex in normal hearts. Schenkel et al. [16] modeled time-dependent mitral and aortic orifices without including valve leaflet movements and reported asymmetry vortices, isosurfaces, and schematic flow structure for mitral flow. All these studies were made for different ventricles and could not be considered as an alternative to one another [16, 22].

Using 2D velocities obtained from phase-contrast MR imaging, Thompson and McVeigh [23] calculated pressure drops in LV. The results were validated in a dog model

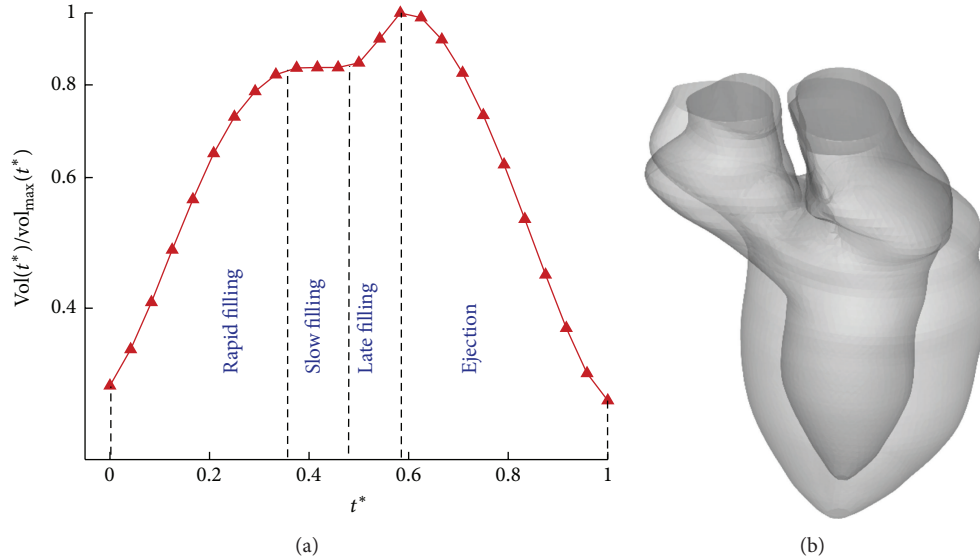


FIGURE 1: (a) Temporal variation of the left ventricle volume,  $\text{vol}(t^*)$ ;  $t^* = 0$  for the onset diastole and  $t^* = 1$  for the end systole. (b) The change of geometry from end systole to end diastole.

and in a pulsatile flow phantom with high-fidelity pressure transducers. Yotti et al. [24] obtained pressure difference between the ventricle apex and the outflow tract from postprocessing color Doppler M-mode images. Garcia et al. [25] showed 2D velocity measurement from Doppler-echocardiography with assumption that the large scales of the flow are approximately 2D in an LV plane of interest. The velocity component normal to ultrasound beams was estimated from the continuity equation. Uejima et al. [26] reported an echocardiographic method to show vortex flow pattern in the ventricle. Faludi et al. [27] discussed vortex formations in healthy ventricles, the effect of prosthetic valves on flow patterns, and low resolutions of echocardiographic 3D imaging technology. The onset mitral flow patterns were obtained by Eriksson et al. [28] using path lines traced for 25 msec. Charonko et al. [29] employed 2D phase-contrast MRI to calculate the temporal variation of pressure drop with the mitral flow velocity and discuss normal LV filling with vortices. The kinetic energy of inflow was calculated for 12 subjects. Using Doppler-echocardiography data to obtain 2D velocity field, Hendabadi et al. [30] reported a trajectory-based computation of blood transport patterns for assessments of stasis in the ventricle. Quantification of ventricular contraction was studied by Hung et al. [31] using kinetic energy flux calculated from velocity vectors of normal and dyssynchrony echocardiograms.

The present study is to relate kinematic, dynamic, and energy characteristics of inflow to a normal left ventricle. Because of rapid flow acceleration and deceleration with mitral valve motion, the 3D effect is relatively small in comparison with the longitudinal flow. The main feature of inflow can be captured and learned by using 2D finite volumes and MRI data of cardiac contraction and dilation.

The effect of mitral valve motion on pressure drop is studied by comparing cases with and without modeling mitral leaflet motions. The detailed flow patterns indicate momentum transfer in the rapid curvilinear flow produced by ventricular dilation and reveal alteration in boundary layer, vortices, shear stress, pressure variations, and net pressure on valve leaflets. The flow process is continued by the ventricular contraction and the results are reported by Hung et al. [32]. The work-energy equation is employed to study energy transfer from wall motion to blood flow during diastole. For the normal case, the rate of work done by shear and the energy dissipation are small. The results are in agreement with the optimal flow in the ventricle reported by Kilner et al. [2] and Domenichini et al. [10].

## 2. Computational and MRI Approach

MRI scanning was performed for a healthy adult on a 1.5T Siemens scanner (Avanto, Siemens Medical Solutions, Erlangen) using the steady-state-free precession cine gradient echo sequences. The data were acquired from 2-chamber, 4-chamber, and short-axis planes of the left ventricle using 12–14 equidistant slices. They were utilized for 3D reconstruction of movements of the left ventricle and atrium. The end-systolic and end-diastolic volumes are, respectively, 48.8 and 162.5 mL, producing a stroke volume of 113.7 mL and an ejection fraction of 70%. To simulate blood flow, 25 frames of LV endocardial walls were obtained from the MRI during one cardiac cycle. The temporal variation of ventricle volume,  $\text{vol}(t^*)$ , is shown in Figure 1(a) in which the cardiac period,  $T = 0.88$  seconds, is used to define the dimensionless time,

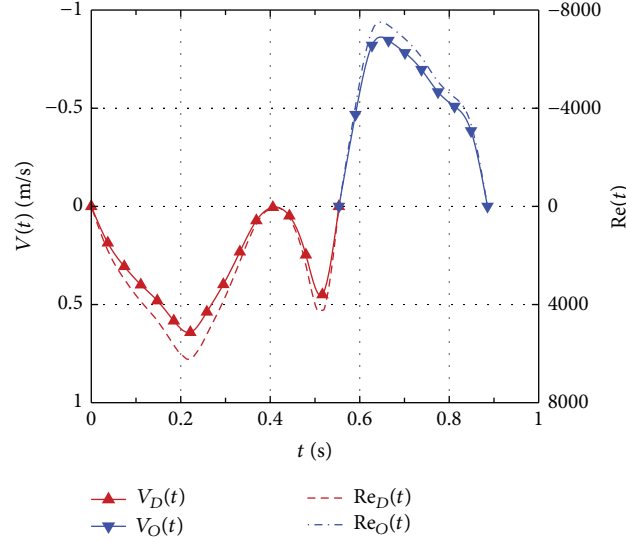


FIGURE 2: Time variations of inlet velocity  $V_D(t)$  and the associated Reynolds numbers  $Re_D(t)$  for diastolic flow.  $V_O(t)$  and  $Re_O(t)$  for systolic flow.

$t^* = t/T$ , and  $vol_{\max}$  is equal to the end-diastolic volume. The change of geometry from end systole to end diastole is shown in Figure 1(b).

Blood flow in large arteries can be treated as homogeneous Newtonian fluid of density  $1050 \text{ kg/m}^3$  and dynamic viscosity of  $0.00316 \text{ Pa}\cdot\text{sec}$ . An arbitrary Lagrangian-Eulerian (ALE) formulation of the Navier-Stokes equations can be expressed as [33]

$$\begin{aligned} \frac{\partial}{\partial t} \int_A \rho \vec{v} dA + \int_s \rho \vec{v} (\vec{v} - \vec{v}_b) \cdot \vec{n} ds \\ = - \int_s p \mathbf{I} \cdot \vec{n} ds + \int_s \boldsymbol{\tau} \cdot \vec{n} ds, \end{aligned} \quad (1)$$

where  $\vec{v}$  is the velocity vector,  $\vec{v}_b$  is the local velocity along the boundary  $s$ ,  $p$  is the pressure,  $\mathbf{I}$  is the unit tensor,  $\vec{n}$  is the unit normal vector, and  $\boldsymbol{\tau}$  is the viscous stress tensor. The integral form of two-dimensional continuity equation is

$$\frac{\partial}{\partial t} \int_A \rho dx dy + \int_s \rho (\vec{v} - \vec{v}_b) \cdot \vec{n} ds = 0. \quad (2)$$

The moving boundaries are determined from MRI data, providing velocities on the wall and mitral leaflets for computation. The Navier-Stokes equations for flow with moving meshes were solved using a finite volume CFD solver: ANSYS Fluent 14 (ANSYS, Inc.). A time-dependent uniform velocity profile is prescribed at the atrium inlet for modeling inflow to the mitral valve with the aortic valve closed. At each time step, the ventricle motion and mitral valve movements were implemented with the user defined functions (UDFs). For the 2D case, long axis images were used for the analysis and the mitral valve movements are derived from MRI data. Before the periodic flow was obtained, a grid dependency study was conducted for five cases with number of triangular

cells increasing from 6000 to 9000, 13500, 20250, and 30375. The test results showed that the flow patterns became the same when the number reached 20250. This number was used and the grid was monitored, and remeshing method in ANSYS Fluent was applied when the grid quality was poor. The criterion for grid quality required the maximum value of face skew angle below 40 degrees. The grid convergence index (GCI) was used for assessing grid invariant solution [34]. The pressure implicit method with splitting of operators (PISO) algorithm [35] and a second-order upwind scheme were employed. Also, the Courant number criterion was satisfied; it resulted in 1800 time steps for one cardiac period (0.88 second) flow simulation. The results of diastolic flow in the left ventricle are presented in this paper.

### 3. Results and Discussions

The computation was initiated at the onset diastole and periodic solutions were obtained after 4 cycles of diastolic and systolic flow simulation. Figure 2 shows the temporal variations of velocity  $V_D(t)$  at the atrium inlet for diastolic flow and  $V_O(t)$  at the outlet of the sinus of Valsalva for systole; they are plotted as negative for inflow and positive for outflow, respectively. The nonlinear pulsating flow processes cannot be effectively characterized by the mean Reynolds number with several frequency parameters but by the time-dependent Reynolds numbers (see Figure 2) for the diastole and systole [36]:

$$Re_D(t) = \frac{\rho V_D(t) D_1(t)}{\mu}, \quad (3a)$$

$$Re_O(t) = \frac{\rho V_O(t) D_2(t)}{\mu} \quad (3b)$$

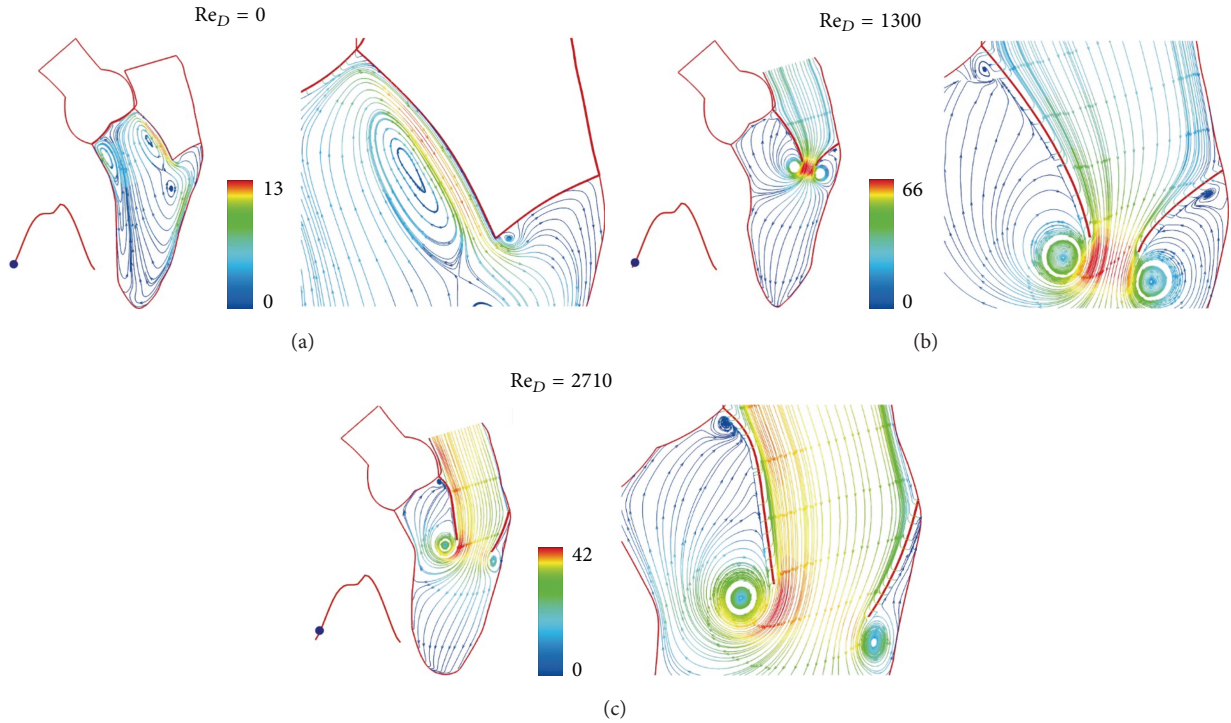


FIGURE 3: Streamlines at (a)  $t = 0$  sec, (b)  $t = 0.0185$  sec, and (c)  $t = 0.0738$  sec. Streamlines colored by velocity (cm/sec).

in which  $D_1(t)$  and  $D_2(t)$  are the inlet and outlet diameters. Notice that using the time-dependent diameters leads to expressing the instantaneous flow rate by  $Re^2 \mu^2 \pi / 4 \rho^2 V$ . Correlation of  $Re_D(t)$  with pressure drop is an effective way to present nonlinear pulsating flow processes. Figure 3(a) shows ventricular vortices at the end systole with the aortic and mitral valves closed and the ventricle momentarily stationary. An early phase of flow acceleration is shown in Figure 3(b) for the Reynolds number ( $Re_D$ ) rising from zero to 1300 in 0.0185 seconds. The suction and momentum produced by wall dilation disperse immediately end-systolic vortices in Figure 3(a) and produce a pair of asymmetric vortices with mitral leaflets being opened by the inflow. Due to curvature effect, high momentum appears near the anterior leaflet. The streamlines near the leaflet tip contribute momentum to its vortex, while the other streamlines from the leaflet are pushed backward by momentum from outer region of the vortex, producing a small counter rotating vortex at the leaflet root. On the atrial side, the leaflet momentum interrupts the transient boundary layer, resulting in a sharp turn of streamlines towards the moving boundary. Due to mesh size effect on contour plots, streamlines near the leaflet appear parallel instead of slightly tapered.

The color scale 66 in Figure 3(b) is for velocity scale of 66 cm/sec. Figures 3(c) and 4 show the continued flow acceleration when  $Re_D$  reaches 2710, 4256, 5166, and 5684. Because the ventricle dilation includes an upward movement of the closed aortic valve, the streamlines in this region move with the valve. Similar to laminar flow in a conduit

expansion reported by Macagno and Hung [37], the zone of vortices provides a smooth pathway for blood flowing to the ventricle. As the rate of ventricular dilation decreases with elastic recoil of cardiac contraction, the flow begins to decelerate. A rapid growth of vortices appears in Figure 5(a) as  $Re_D$  reduces from 5684 to 3524 in 0.0738 seconds; it indicates momentum transfer from the main flow to vortices during deceleration [36]. More vortices are generated for momentum balance when  $Re_D$  drops to 2050, 640, and 416 (Figures 5 and 6(a)). Although the Reynolds number decreases drastically, velocities in the ventricle do not, reflecting small viscous effect in this rapid flow deceleration. This phenomenon correlates well with small energy loss shown in Figure 11. The momentum transfer produces a strong vortex near the apex when  $Re_D = 416$ . Before the complete closure of mitral leaflets, the ventricle dilation and inflow are assisted by atrial contraction. Increase in vortex momentum and reopening of the mitral valve are demonstrated for  $Re_D$  increasing to 2188 and 3984 in Figures 6(b) and 6(c). Figure 7 portrays the final flow deceleration for the mitral valve closure. On the ventricular side the vortex momentum moves with valve closure which also pushes inflow to the ventricle. They are indicated by the streamlines moving with the leaflets for  $Re_D = 1994$  and 796. These detailed flow characteristics reflect the capability of combining CFD with MRI data for blood flow with moving boundary. When the inflow vanishes at the end diastole ( $Re_D = 0$ ), the ventricle is occupied by vortices. The formation of these vortices is simply for momentum balance at the end diastole. In

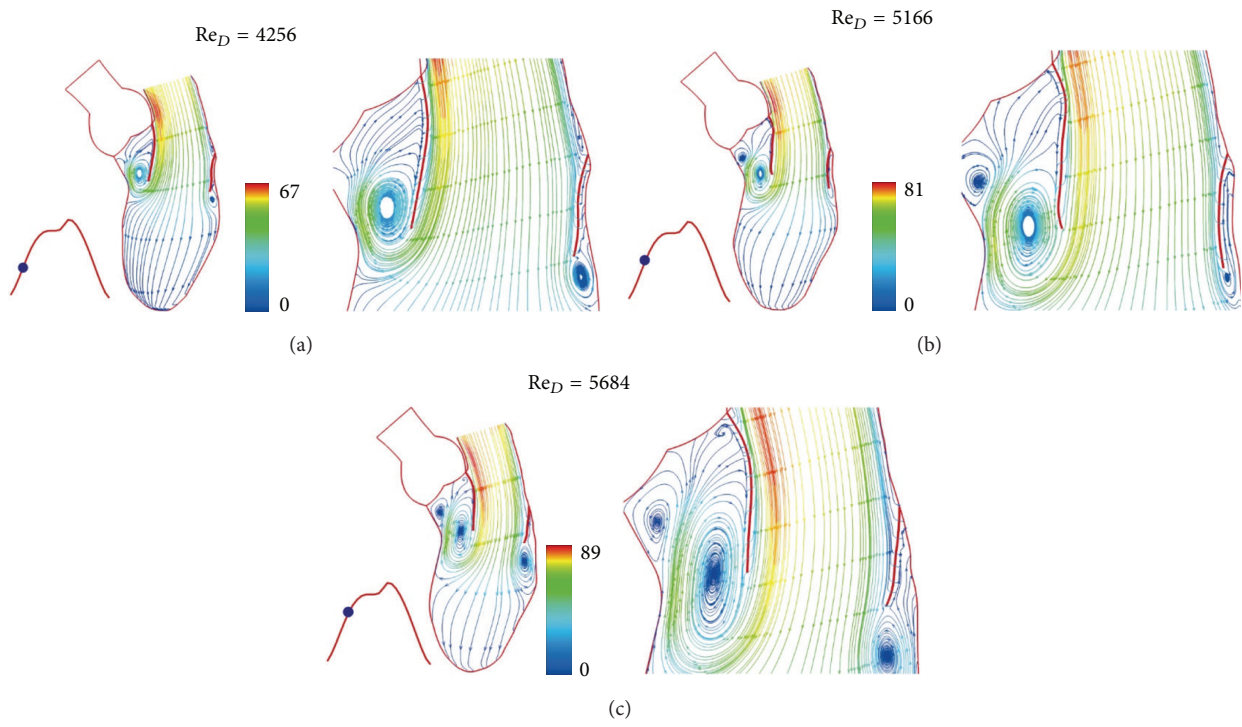


FIGURE 4: Streamlines at (a)  $t = 0.1476$  sec, (b)  $t = 0.1845$  sec, and (c)  $t = 0.2214$  sec. Streamlines colored by velocity (cm/sec).

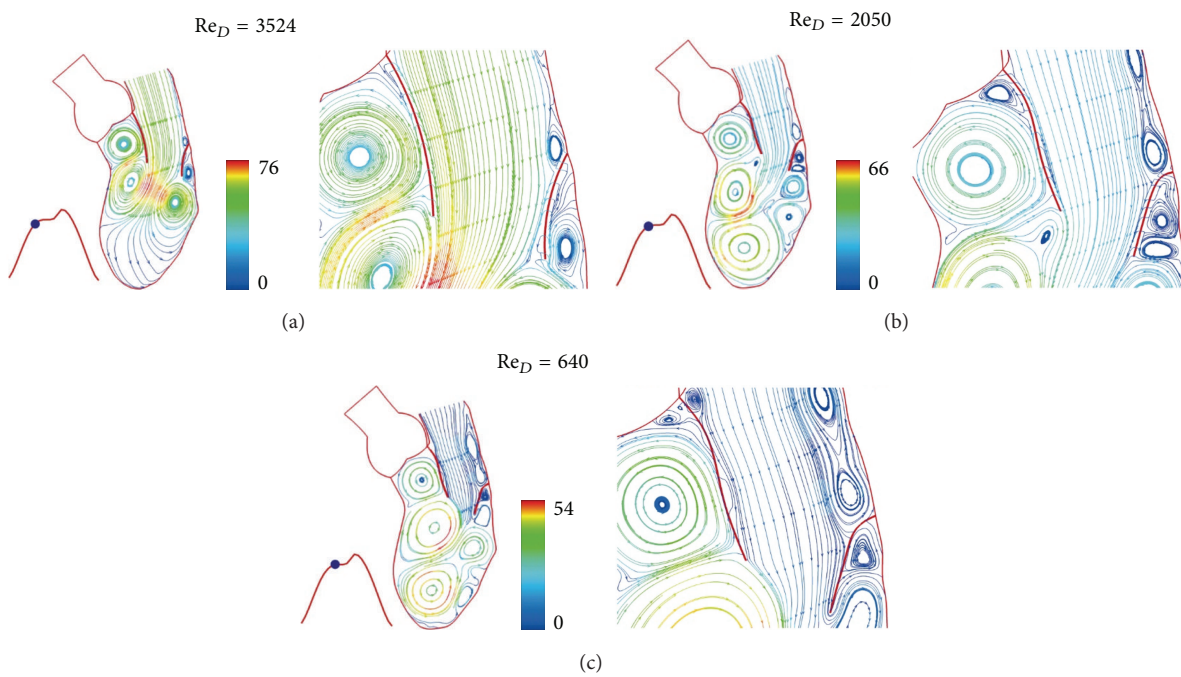


FIGURE 5: Streamlines at (a)  $t = 0.2952$  sec, (b)  $t = 0.3321$  sec, and (c)  $t = 0.369$  sec. Streamlines colored by velocity (cm/sec).

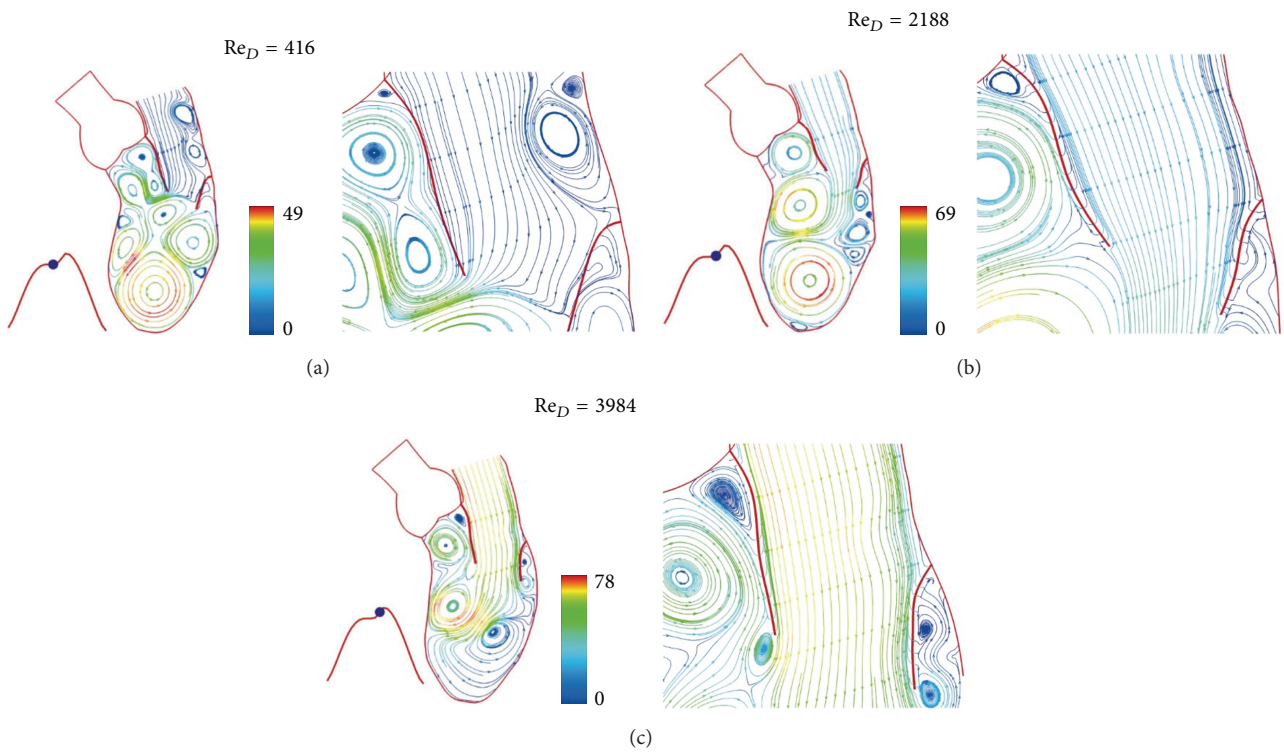


FIGURE 6: Streamlines at (a)  $t = 0.4428$  sec, (b)  $t = 0.4797$  sec, and (c)  $t = 0.5166$  sec. Streamlines colored by velocity (cm/sec).

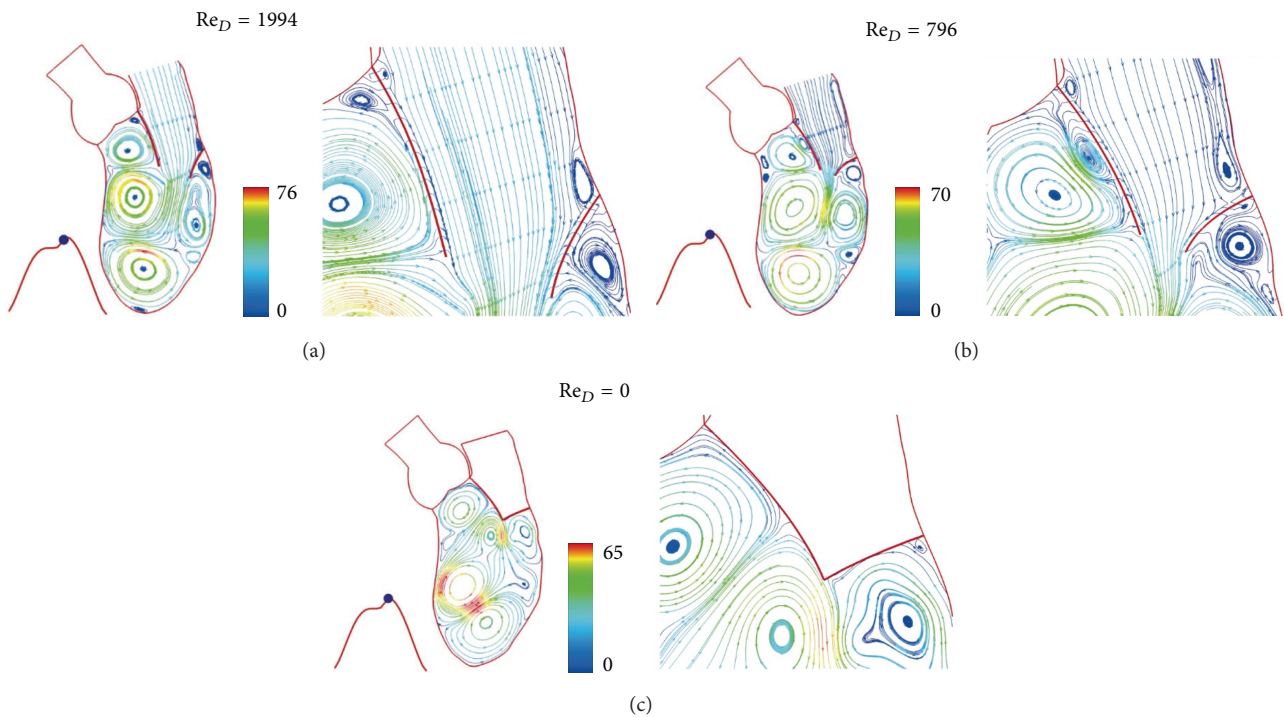


FIGURE 7: Streamlines at (a)  $t = 0.5289$  sec, (b)  $t = 0.5412$  sec, and (c)  $t = 0.5535$  sec. Streamlines colored by velocity (cm/sec).

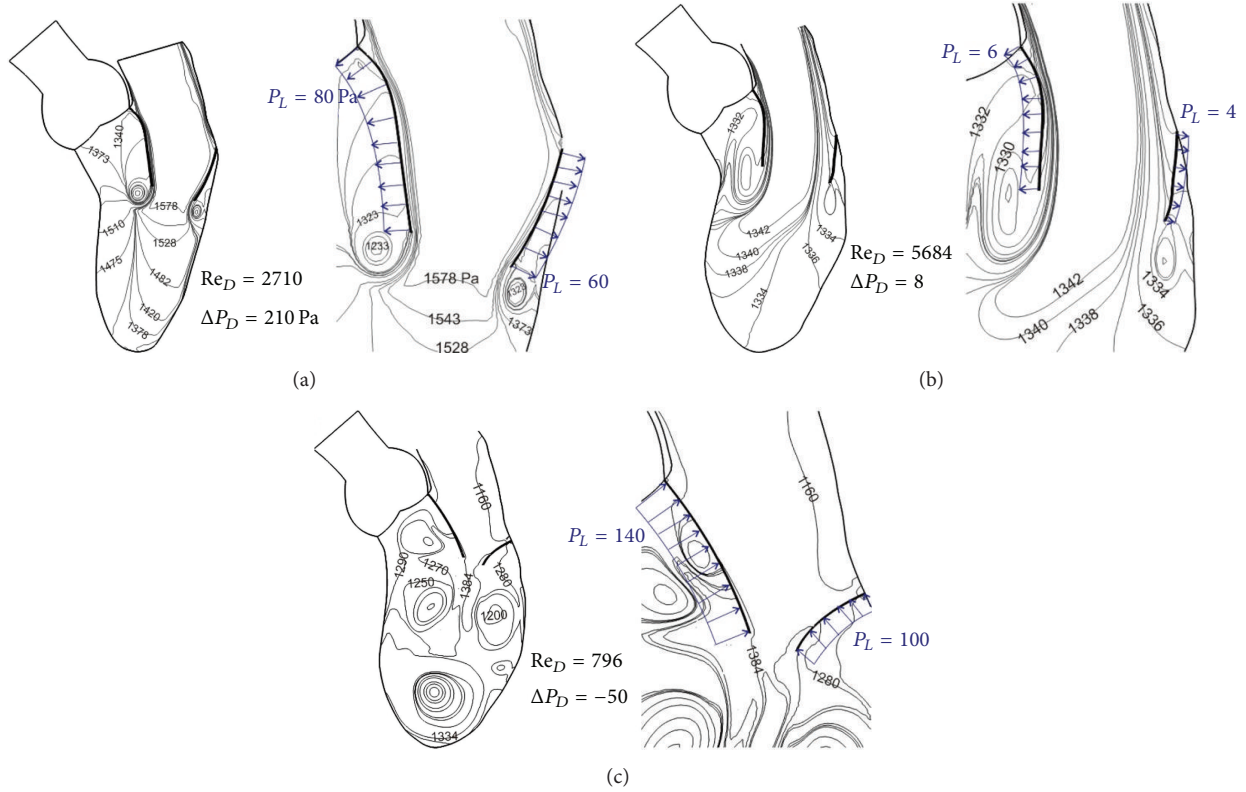


FIGURE 8: Pressure contours and net pressure on the mitral valve leaflets for (a) rapid filling, (b) for peak of inlet velocity, and (c) during closing of mitral valve.

the absence of end-diastolic atrial contraction, the stroke volume is likely to reduce unless the ventricular dilation is stronger.

Dynamic characteristics are demonstrated by pressure contours in Figure 8(a) for  $Re_D = 2710$  during valve opening. The pressure drop between the center of the mitral annulus and the apex is indicated in the figure by  $\Delta P_D = 210$  Pa (1.6 mm Hg). The tip of tongue-shaped contours (e.g., marked by 1420 and 1378 Pa) correlates with streamlines (for similar velocities) in the region. The contour plot is based on a reference pressure of 1333 Pa (10 mm Hg) at the apex. The centrifugal force effect is reflected by low pressure at the center of strong vortex. Also shown in the figure are net pressures,  $P_L = 60$  and  $80$  Pa, on mitral leaflets; they are related to the valve motion. The tongue-shaped pressure contours for  $Re_D = 5684$  shown in Figure 8(b) are due to high momentum near the anterior leaflet. The small pressure drop ( $\Delta P_D = 8$  Pa) at this instant is related to diminishing flow acceleration. The net pressures ( $P_L = 4$  and  $6$  Pa) on mitral leaflets correspond to valve in a fully open position; it is about 7% of that during the rapid opening phase (see Figure 8(a)). Adverse net pressures on leaflets appear in Figure 8(c) for  $Re_D = 796$  with  $\Delta P_D = -50$  Pa. They are associated with the rapid flow deceleration and valve closure. Further dynamic characteristics can be seen from shear distributions on both

sides of mitral leaflets (Figure 9). During the mitral valve opening phase shear stresses on the atrial side of leaflets are higher than those on the ventricular side. Because of leaflet motion, shear stresses are rather small and relate with vorticity ( $\omega$ ). The maximum vorticity ( $\omega_{max}$ ) listed in the figure can be compared with wall vorticity ( $=620 \text{ sec}^{-1}$ ) of the Poiseuille flow for the median Reynolds number of 2842.

Figure 10(a) shows the time variation of the Reynolds number ( $Re_D$ ) with pressure difference  $\Delta P_D$  between the mitral annulus and the apex. They are due to ventricular dilatation produced by elastic energy stored in myocardium during contraction. Because of inertial effect, the peak flow is lag behind the maximum pressure drop which is in phase with the flow acceleration. Decreasing  $Re_D$  correlates well with adverse pressure drop. Also shown in this figure is the pressure drop for a case without modeling leaflets. Small differences in pressure drop between cases with and without mitral leaflets indicate that a normal valve motion would not induce much of flow resistance. Justification of using 2D models can be made by similar pressure-flow curves of a 3D model shown in Figure 10(b) with the same inflow velocity  $V_D(t^*)$  of the 2D model. The pressure drops for the 2D and 3D models are comparable though the latter does not include the mitral valve motion.

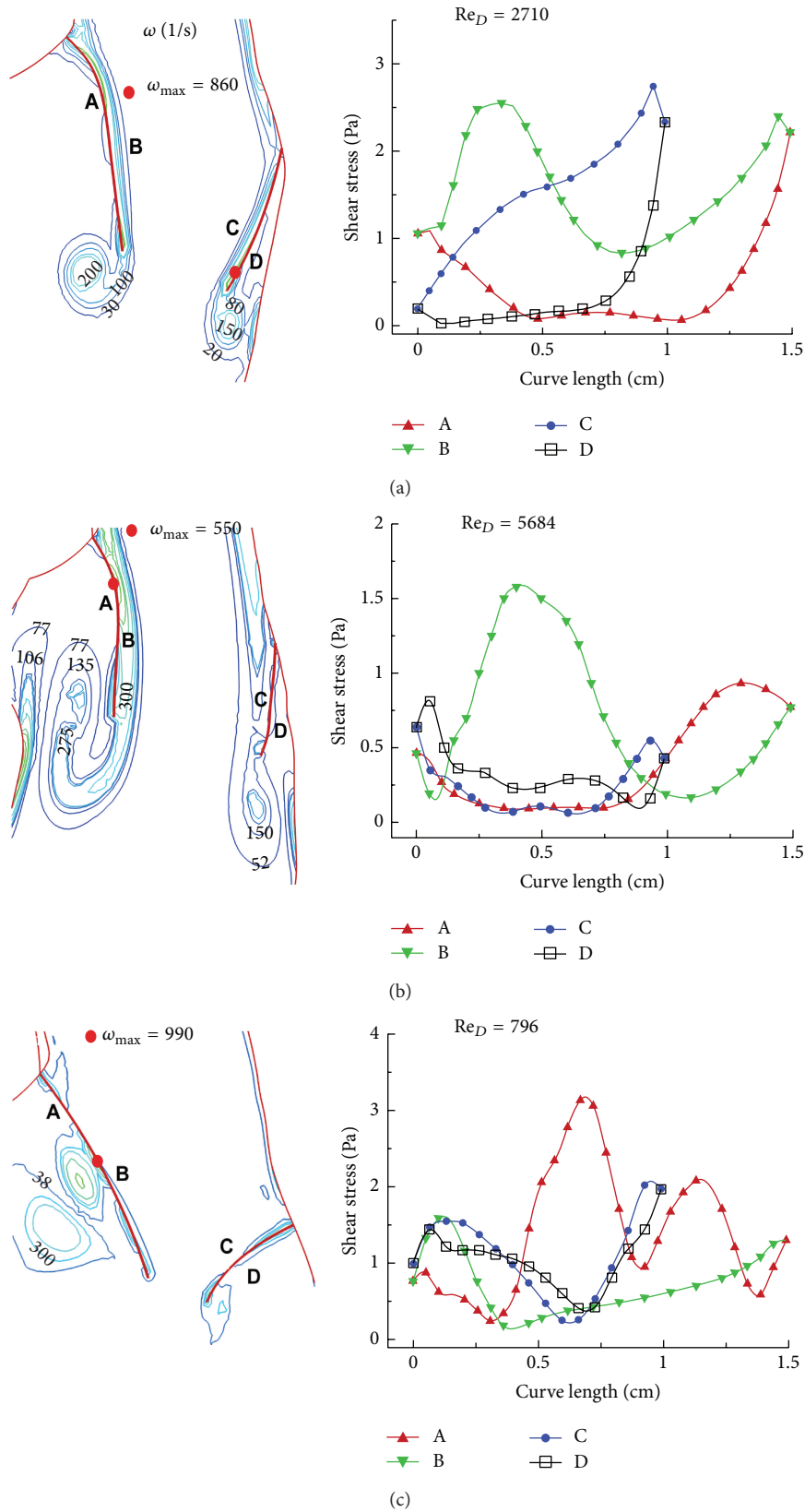


FIGURE 9: Vorticity and shear stress distribution of the flow past the mitral valve for (a) rapid filling, (b) for peak of inlet velocity, and (c) during closing of mitral valve.

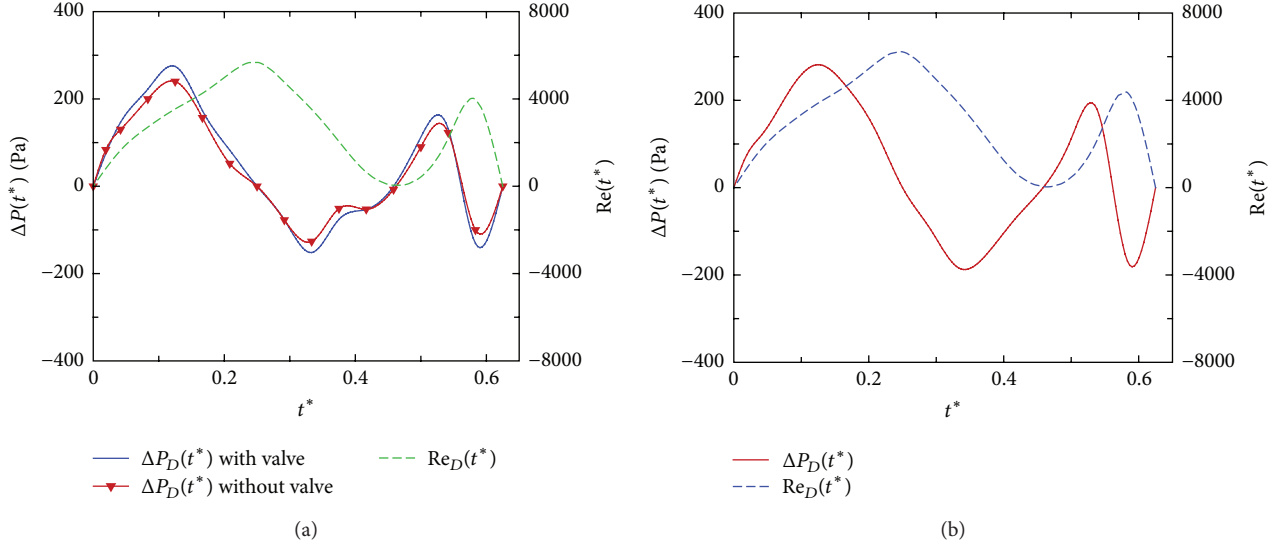


FIGURE 10: Time variation of inflow Reynolds number  $Re_D(t^*)$  and the pressure drop  $\Delta P_D(t^*)$  for (a) 2D modelling of LV with and without mitral valve leaflets. (b) 3D modelling of LV.

The fluid dynamics of cardiac pumping can be further studied by using an integral form of the work-energy equation [37, 38]:

$$\begin{aligned}
 & \int_W \left( \frac{\rho V^2}{2} \right) V_N d\ell + \int_W (p) V_N d\ell + \iint \left( \frac{\rho}{2} \frac{\partial V^2}{\partial t} \right) dx dy \\
 & - \int_m (p_m) V_m d\ell - \int_m \left( \frac{\rho V_m^2}{2} \right) V_m d\ell \\
 & - \int_{W+m} \vec{V} \cdot \vec{\tau} d\ell \\
 & + \mu \iint \left( 2 \left( \frac{\partial u}{\partial x} \right)^2 + 2 \left( \frac{\partial v}{\partial y} \right)^2 + \left( \frac{\partial u}{\partial y} + \frac{\partial v}{\partial x} \right)^2 \right) dx dy \\
 & = 0
 \end{aligned} \tag{4}$$

in which  $(u, v, w)$  are the velocity components in the Cartesian coordinates,  $V_m$  and  $p_m$  are the velocity and pressure across the mitral annulus,  $V_N$  is the normal velocity on the ventricle, and  $d\ell$  is the incremental line integral. The first five integrals are, respectively, the kinetic energy flux delivered to blood from the ventricle, the rate of work done by pressure on the wall, the rate of change of kinetic energy in the ventricle, the rate of work done by pressure across the mitral annulus, and the associated kinetic energy flux. The last two integrals are the rate of work done by shear and the rate of dissipation of energy, respectively. Notice that all the energy terms are positive; the sign for each term of (4) is related to the out flux and influx of energy. Curve A in Figure 11(a) is the kinetic energy flux delivered to blood from the ventricle during dilatation. It is amplified by about 100 times in Figure 11(b) for comparison with viscous terms in (4). The distance between curves B and A is the rate of work done by pressure on the wall. The gap between curves C and

B represents the rate change of kinetic energy in the ventricle. It is positive when curve C is higher than curve B, otherwise, negative. The distance between curves C and D is the rate of work done by pressure across the mitral annulus. Since time variations of pressure are not known, calculation of the work done by pressure is based on an estimated reference pressure (1333 Pa or 10 mmHg) at the apex. The work done by pressure can be corrected by adding  $\Delta p_1(t) V_D(t) A_D(t)$  if  $\Delta p_1(t) = p_A(t) - 1333$  Pa,  $p_A(t)$  is the actual pressure at the apex, and  $A_D(t)$  is the cross-sectional area of the mitral section.

The kinetic energy influx at the mitral section is indicated by the difference between curves D and E. It is about 13 times higher than that of kinetic energy flux from the ventricular wall (see curve A in Figure 11(b)). Notice that curve E is the sum of Bernoulli energy flux on the ventricle wall, the influx across the mitral annulus, and the rate change of kinetic energy in the ventricle. The value of E is very small, reflecting that the Bernoulli energy produced by ventricular dilation is practically conservative during the normal filling phase of blood to the ventricle. The gap between curves E and F is the rate of work done by shear stress on the wall. This small amount of energy is approximately equal to the rate of energy dissipation indicated by the spacing between curves G and F. All the aforementioned terms and curves are arranged so that curve G represents the sum of the left hand side of (4); it should be zero. The small values shown by curve G indicate the insignificant numerical residues of energy balance. The balance also reflects that the velocity and pressure fields obtained from CFD are quite accurate. In other words, the momentum balance achieved by the Navier-Stokes equations is well checked by energy balance of (4). Similar results are obtained for the 3D model; they will be reported separately. Figure 12 compares the dissipation of energy between the 2D

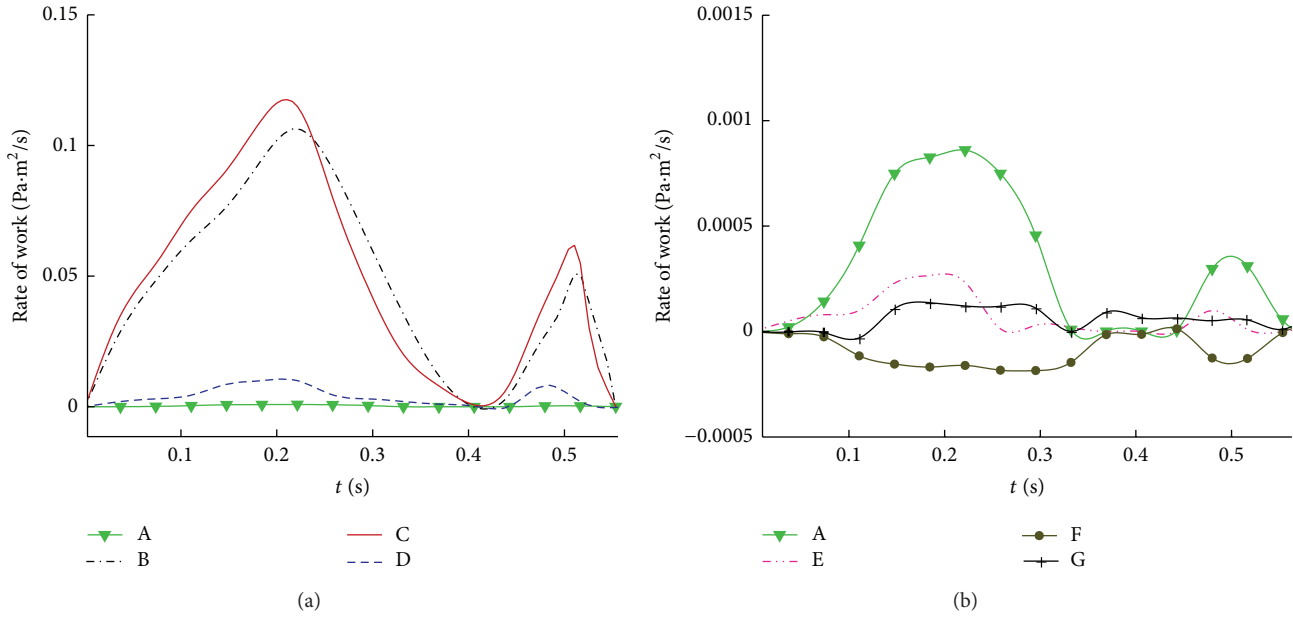


FIGURE 11: Rate of energy transfer of 2D model of diastolic flow in the left ventricle: curve A: kinetic energy flux on the wall, B – A: rate of work done by pressure on the wall, C – B: rate change of kinetic energy, C – D: rate of work by pressure at the outlet, D – E: kinetic energy influx, E – F: rate of work done by shear on the wall, and G – F: rate of energy dissipation.

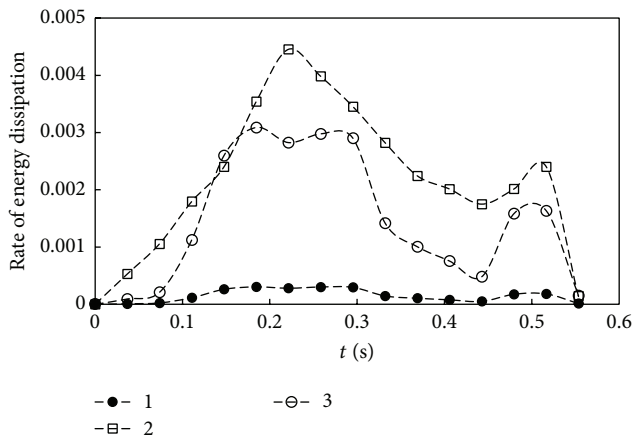


FIGURE 12: Comparison of the rate of energy dissipation between the 2D model (curve 1) and the 3D model (curve 2); curve 3 is the 2D results multiplied by the ratio between 3D and 2D flow rates.

(curve 1) and 3D (curve 2) models. Curve 3 represents the results of the 2D case multiplied by the ratio of flow rates between 3D and 2D cases. It is lower than curve 2, indicating the effect of spiral flow on energy loss for the 3D case. Notice that the rate of kinetic energy flux on the wall can be directly calculated from the velocity of wall motion. This quantity was demonstrated as a useful index for quantification of echocardiograms with or without dyssynchrony [31]. The velocity vectors of echocardiogram are much easier to obtain than to reconstruct the LV motion from MRI data and conduct a CFD analysis. However the goal of this study is towards a comprehensive analysis of the dynamic and energy characteristics of blood flow produced by the left ventricle.

Further quantification of energy parameters can be indicated by time integral of each energy term in (4). For example, the work done by pressure on the ventricle during dilation is the time integration of the area between curves B and A in Figure 11. Clearly, a physiological quantification of energy flux delivered from the ventricular chamber dilation requires 3D computational results.

## 4. Conclusions

Fluid dynamic characteristics of blood flow in the left ventricle are obtained by using 2D CFD with MRI data of a normal adult. The flow patterns are dominated by ventricular dilation and flow induced mitral valve movements. Generation and growth of vortices correlate well with flow acceleration and deceleration and mitral valve motion. They are solely for momentum balance and energy transfer from ventricle dilation to the curvilinear inflow of blood. Boundary layer and high shear stress do not develop on moving leaflets and ventricle. The work done by viscous stresses and dissipation of energy are small for normal diastolic flow. The energy loss is about 2% of the kinetic energy influx to the ventricle and is almost balanced with work done by viscous stresses. The Bernoulli energy flux from the ventricle dilation to blood flow is practically balanced by the energy flux across the mitral annulus and the rate change of kinetic energy in the ventricle. In other words, the Bernoulli energy is conservative, indicating an optimal transport of blood from the left atrium to the ventricle. The dynamic and energy transfer characteristics obtained in the 2D model are in agreement with those of the 3D model. Similar dynamic and energy transfer characteristics were identified for the ejection phase of cardiac pumping of the left ventricle [32].

## Conflict of Interests

The authors declare that there is no conflict of interests regarding the publication of this paper.

## Acknowledgments

The study was supported by the Nanyang Technological University, the University of Pittsburgh, the Singapore International Graduate Award to Seyed Saeid Khalafvand, and the research grant from Singapore Ministry of Health National Medical Research Council (NMRC/EDG/1037/2011) to Liang Zhong.

## References

- [1] W. Y. Kim, P. G. Walker, E. M. Pedersen et al., "Left ventricular blood flow patterns in normal subjects: a quantitative analysis by three-dimensional magnetic resonance velocity mapping," *Journal of the American College of Cardiology*, vol. 26, no. 1, pp. 224–238, 1995.
- [2] P. J. Kilner, G.-Z. Yang, A. J. Wilkest, R. H. Mohladdlin, D. N. Firmin, and M. H. Yacoub, "Asymmetric redirection of flow through the heart," *Nature*, vol. 404, no. 6779, pp. 759–761, 2000.
- [3] T. Ebbers, L. Wigström, A. F. Bolger, B. Wranne, and M. Karlsson, "Noninvasive measurement of time-varying three-dimensional relative pressure fields within the human heart," *Journal of Biomechanical Engineering*, vol. 124, no. 3, pp. 288–293, 2002.
- [4] J. A. Vierendeels, K. Riemsdagh, E. Dick, and P. R. Verdonck, "Computer simulation of intraventricular flow and pressure gradients during diastole," *Journal of Biomechanical Engineering*, vol. 122, no. 6, pp. 667–674, 2000.
- [5] G. Bolzon, L. Zovatto, and G. Pedrizzetti, "Birth of three-dimensionality in a pulsed jet through a circular orifice," *Journal of Fluid Mechanics*, vol. 493, no. 1, pp. 209–218, 2003.
- [6] B. Baccani, F. Domenichini, and G. Pedrizzetti, "Vortex dynamics in a model left ventricle during filling," *European Journal of Mechanics. B. Fluids*, vol. 21, no. 5, pp. 527–543, 2002.
- [7] B. Baccani, F. Domenichini, G. Pedrizzetti, and G. Tonti, "Fluid dynamics of the left ventricular filling in dilated cardiomyopathy," *Journal of Biomechanics*, vol. 35, no. 5, pp. 665–671, 2002.
- [8] B. Baccani, F. Domenichini, and G. Pedrizzetti, "Model and influence of mitral valve opening during the left ventricular filling," *Journal of Biomechanics*, vol. 36, no. 3, pp. 355–361, 2003.
- [9] S. S. Khalafvand, E. Y. K. Ng, L. Zhong, and T. K. Hung, "Fluid-dynamics modelling of the human left ventricle with dynamic mesh for normal and myocardial infarction: preliminary study," *Computers in Biology and Medicine*, vol. 42, no. 8, pp. 863–870, 2012.
- [10] F. Domenichini, G. Pedrizzetti, and B. Baccani, "Three-dimensional filling flow into a model left ventricle," *Journal of Fluid Mechanics*, vol. 539, pp. 179–198, 2005.
- [11] Y. Cheng, H. Oertel, and T. Schenkel, "Fluid-structure coupled CFD simulation of the left ventricular flow during filling phase," *Annals of Biomedical Engineering*, vol. 33, no. 5, pp. 567–576, 2005.
- [12] N. R. Saber, A. D. Gosman, N. B. Wood, P. J. Kilner, C. L. Charrier, and D. N. Firmin, "Computational flow modeling of the left ventricle based on in vivo MRI data: initial experience," *Annals of Biomedical Engineering*, vol. 29, no. 4, pp. 275–283, 2001.
- [13] N. R. Saber, N. B. Wood, A. D. Gosman et al., "Progress towards patient-specific computational flow modeling of the left heart via combination of magnetic resonance imaging with computational fluid dynamics," *Annals of Biomedical Engineering*, vol. 31, no. 1, pp. 42–52, 2003.
- [14] Q. Long, R. Merrifield, G. Z. Yang, X. Y. Xu, P. J. Kilner, and D. N. Firmin, "The influence of inflow boundary conditions on intra left ventricle flow predictions," *Journal of Biomechanical Engineering*, vol. 125, no. 6, pp. 922–927, 2003.
- [15] Q. Long, R. Merrifield, X. Y. Xu, P. Kilner, D. N. Firmin, and G.-Z. Yang, "Subject-specific computational simulation of left ventricular flow based on magnetic resonance imaging," *Proceedings of the Institution of Mechanical Engineers, Part H: Journal of Engineering in Medicine*, vol. 222, no. 4, pp. 475–485, 2008.
- [16] T. Schenkel, M. Malve, M. Reik, M. Markl, B. Jung, and H. Oertel, "MRI-Based CFD analysis of flow in a human left ventricle: methodology and application to a healthy heart," *Annals of Biomedical Engineering*, vol. 37, no. 3, pp. 503–515, 2009.
- [17] D. M. McQueen and C. S. Peskin, "A three-dimensional computational method for blood flow in the heart. II. contractile fibers," *Journal of Computational Physics*, vol. 82, no. 2, pp. 289–297, 1989.
- [18] D. M. McQueen and C. S. Peskin, "Shared-memory parallel vector implementation of the immersed boundary method for the computation of blood flow in the beating Mammalian heart," *The Journal of Supercomputing*, vol. 11, no. 3, pp. 213–236, 1997.
- [19] D. M. McQueen and C. S. Peskin, "A three-dimensional computer model of the human heart for studying cardiac fluid dynamics," *Computer Graphics*, vol. 34, no. 1, pp. 56–60, 2000.
- [20] H. Watanabe, S. Sugiura, H. Kafuku, and T. Hisada, "Multi-physics simulation of left ventricular filling dynamics using fluid–structure interaction finite element method," *Biophysical Journal*, vol. 87, no. 3, pp. 2074–2085, 2004.
- [21] S. Krittian, U. Janoske, H. Oertel, and T. Böhlke, "Partitioned fluid-solid coupling for cardiovascular blood flow," *Annals of Biomedical Engineering*, vol. 38, no. 4, pp. 1426–1441, 2010.
- [22] S. S. Khalafvand, E. Y. K. Ng, and L. Zhong, "CFD simulation of flow through heart: a perspective review," *Computer Methods in Biomechanics and Biomedical Engineering*, vol. 14, no. 1, pp. 113–132, 2011.
- [23] R. B. Thompson and E. R. McVeigh, "Fast measurement of intracardiac pressure differences with 2D breath-hold phase-contrast MRI," *Magnetic Resonance in Medicine*, vol. 49, no. 6, pp. 1056–1066, 2003.
- [24] R. Yotti, J. Bermejo, M. M. Desco et al., "Doppler-derived ejection intraventricular pressure gradients provide a reliable assessment of left ventricular systolic chamber function," *Circulation*, vol. 112, no. 12, pp. 1771–1779, 2005.
- [25] D. Garcia, J. C. Del Alamo, D. Tanne et al., "Two-dimensional intraventricular flow mapping by digital processing conventional color-doppler echocardiography images," *IEEE Transactions on Medical Imaging*, vol. 29, no. 10, pp. 1701–1713, 2010.
- [26] T. Uejima, A. Koike, H. Sawada et al., "A new echocardiographic method for identifying vortex flow in the left ventricle: numerical validation," *Ultrasound in Medicine and Biology*, vol. 36, no. 5, pp. 772–788, 2010.
- [27] R. Faludi, M. Szulik, J. D'hooge et al., "Left ventricular flow patterns in healthy subjects and patients with prosthetic mitral valves: an in vivo study using echocardiographic particle image

- velocimetry,” *Journal of Thoracic and Cardiovascular Surgery*, vol. 139, no. 6, pp. 1501–1510, 2010.
- [28] J. Eriksson, P. Dyverfeldt, J. Engvall, A. F. Bolger, T. Ebberts, and C. J. Carlhäll, “Quantification of presystolic blood flow organization and energetics in the human left ventricle,” *The American Journal of Physiology—Heart and Circulatory Physiology*, vol. 300, no. 6, pp. H2135–H2141, 2011.
- [29] J. J. Charonko, R. Kumar, K. Stewart, W. C. Little, and P. P. Vlachos, “Vortices formed on the mitral valve tips aid normal left ventricular filling,” *Annals of Biomedical Engineering*, vol. 41, no. 5, pp. 1049–1061, 2013.
- [30] S. Hendabadi, J. Bermejo, Y. Benito et al., “Topology of blood transport in the human left ventricle by novel processing of doppler echocardiography,” *Annals of Biomedical Engineering*, vol. 41, no. 12, pp. 2603–2616, 2013.
- [31] T. K. Hung, S. R. Balasubramanian, M. A. Simon, M. S. Suffoletto, H. S. Borovetz, and J. Gorcsan, “Hemodynamic information and analysis of cardiac pumping,” *Journal of Mechanics in Medicine and Biology*, vol. 8, no. 1, pp. 87–95, 2008.
- [32] T. K. Hung, S. S. Khalafvand, and E. Y. K. Ng, “Fluid dynamic characteristics of systolic blood flow of the left ventricle,” *Journal of Mechanics in Medicine and Biology*, vol. 15, no. 1, pp. 1–20, 2015.
- [33] C. W. Hirt, A. A. Amsden, and J. L. Cook, “An arbitrary Lagrangian-Eulerian computing method for all flow speeds,” *Journal of Computational Physics*, vol. 14, no. 3, pp. 227–253, 1974.
- [34] P. J. Roache, *Verification and Validation in Computational Science and Engineering*, Hermosa Publishers, Albuquerque, NM, USA, 1998.
- [35] R. I. Issa, “Solution of the implicitly discretised fluid flow equations by operator-splitting,” *Journal of Computational Physics*, vol. 62, no. 1, pp. 40–65, 1986.
- [36] T.-K. Hung and T. M.-C. Tsai, “Kinematic and dynamic characteristics of pulsatile flows in stenotic vessels,” *Journal of Engineering Mechanics*, vol. 123, no. 3, pp. 247–259, 1997.
- [37] E. O. Macagno and T.-K. Hung, “Computational and experimental study of a captive annular eddy,” *Journal of Fluid Mechanics*, vol. 28, no. 1, pp. 43–64, 1967.
- [38] T. D. Brown and T.-K. Hung, “Computational and experimental investigations of two-dimensional nonlinear peristaltic flows,” *Journal of Fluid Mechanics*, vol. 83, no. 2, pp. 249–272, 1977.

## Research Article

# Comparative Sensitivity Analysis of Muscle Activation Dynamics

Robert Rockenfeller,<sup>1</sup> Michael Günther,<sup>2,3</sup> Syn Schmitt,<sup>2,4</sup> and Thomas Götz<sup>1</sup>

<sup>1</sup>*Institut für Mathematik, Universität Koblenz, 56070 Koblenz, Germany*

<sup>2</sup>*Institut für Sport- und Bewegungswissenschaft, Universität Stuttgart, Allmandring 28, 70569 Stuttgart, Germany*

<sup>3</sup>*Institut für Sportwissenschaft, Lehrstuhl für Bewegungswissenschaft, Friedrich-Schiller-Universität, Seidelstraße 20, 07749 Jena, Germany*

<sup>4</sup>*Stuttgart Research Centre for Simulation Technology, Pfaffenwaldring 7a, 70569 Stuttgart, Germany*

Correspondence should be addressed to Michael Günther; [s7gumi@uni-jena.de](mailto:s7gumi@uni-jena.de)

Received 15 December 2014; Accepted 5 February 2015

Academic Editor: Eduardo Soudah

Copyright © 2015 Robert Rockenfeller et al. This is an open access article distributed under the Creative Commons Attribution License, which permits unrestricted use, distribution, and reproduction in any medium, provided the original work is properly cited.

We mathematically compared two models of mammalian striated muscle activation dynamics proposed by Hatze and Zajac. Both models are representative for a broad variety of biomechanical models formulated as ordinary differential equations (ODEs). These models incorporate parameters that directly represent known physiological properties. Other parameters have been introduced to reproduce empirical observations. We used sensitivity analysis to investigate the influence of model parameters on the ODE solutions. In addition, we expanded an existing approach to treating initial conditions as parameters and to calculating second-order sensitivities. Furthermore, we used a global sensitivity analysis approach to include finite ranges of parameter values. Hence, a theoretician striving for model reduction could use the method for identifying particularly low sensitivities to detect superfluous parameters. An experimenter could use it for identifying particularly high sensitivities to improve parameter estimation. Hatze's nonlinear model incorporates some parameters to which activation dynamics is clearly more sensitive than to any parameter in Zajac's linear model. Other than Zajac's model, Hatze's model can, however, reproduce measured shifts in optimal muscle length with varied muscle activity. Accordingly we extracted a specific parameter set for Hatze's model that combines best with a particular muscle force-length relation.

## 1. Introduction

Scientific knowledge is gained by an interplay between quantitative real world measurements of physical, chemical, or biological phenomena and the development of mathematical models for understanding the dynamical processes behind. In general, such phenomena are determined as spatiotemporal patterns of physical measures (state variables). Modelling consists of distinguishing the surrounding world from the system that yields the phenomena and formulating a mathematical description of the system, a model, that can predict values of the state variables. The calculations depend on model parameters and often on giving measured input variables. By changing parameter values and analysing the resulting changes in the values of the state variables, the model may then be used as a predictive tool. This way, the

model's validity can be verified. If the mathematical model description is moreover derived from first principles, the model has the potential to explain the phenomena in a causal sense.

Calculating the sensitivities of a model's predicted output, that is, the system's state variables, with respect to model parameters is a means of eliminating redundancy and indeterminacy from models and thus helps to identify valid models. Sensitivity analyses can be helpful both in model-based experimental approaches and in purely theoretical work. A modelling theoretician could be looking for parameters to which all state variables are nonsensitive. Such parameters might be superfluous. An experimenter may inspect the model that represents his working hypothesis and analyse which of the model's state variables are specifically sensitive to a selected parameter. Hence, the experimenter would have

to measure exactly this state variable to identify the value of the selected parameter.

In a biomechanical study Scovil and Ronsky [1] applied sensitivity analysis to examine the dynamics of a mechanical multibody system: a runner's skeleton coupled to muscle activation-contraction dynamics. They calculated specific sensitivity coefficients in three slightly different ways. A sensitivity coefficient is the difference quotient calculated from dividing the change in a state variable by the change in a model parameter value, evaluated in a selected system state [2]. The corresponding partial derivative may be simply called "sensitivity." Therefore, a sensitivity function is the time evolution of a sensitivity [2]. Accordingly, Lehman and Stark [2] had proposed a more general and unified approach than Scovil and Ronsky [1], which allows systematically calculating the sensitivities of any dynamical system described in terms of ordinary differential equations. As an example for sensitivity functions, Lehman and Stark [2] had applied their proposed method to a muscle-driven model of saccadic eye movement. By calculating a percentage change in a state variable value per percentage change in a parameter value, all sensitivities can be made comprehensively comparable, even across models.

A sensitivity as defined so far is of first order. Methodically, we aim at introducing a step beyond, namely, at calculating second order sensitivities. These measures are suited to quantify how much the sensitivity of a state variable with respect to one model parameter depends on changing another parameter. By analysing second order sensitivities, the strength of their interdependent influence on model dynamics can be determined. In addition to this so-called local sensitivity analysis, we will take the whole parameter variability into account by calculating global sensitivities according to Chan et al. [3] and Saltelli and Chan [4]. This approach allows translating the impact of one parameter on a state variable into a parameter's importance, by completely comprising its interdependent influence in combination with all other parameters' sensitivities.

In this study, we will apply the sensitivity analysis to models that predict how the activity of a muscle (its chemical state) changes when the muscle is stimulated by neural signals (electrical excitation). Such models are used for simulations of muscles' contractions coupled to their activation dynamics. Models for coupled muscular dynamics are often part of neuromusculoskeletal models of biological movement systems. In particular, we want to try and rate two specific model variants of activation dynamics formulated by Zajac [5] and by Hatze [6]. As a first result, we present an example of a simplified version of the Zajac [5] model, in which sensitivity functions can in fact be calculated in closed form. Subsequently we calculate the sensitivities numerically with respect to all model parameters in both models, aiming at an increased understanding of the influence of changes in model parameters on the solutions of the underlying ordinary differential equations (ODEs). Additionally, we discuss which of both models may be physiologically more accurate. The arguments come from a mixture of three different aspects: sensitivity analysis, others' experimental findings, and an

additional attempt to best fit different combinations of activation dynamics and force-length relations of the contractile element (CE) in a muscle to known data on shifts in optimal CE length with muscle activity [7].

## 2. Two Models for Muscle Activation Dynamics

Macroscopically, a muscle fibre or an assembly thereof, a muscle belly, is often mapped mathematically by a one-dimensional massless thread called "contractile component" or "contractile element" (CE) [8–12]. Its absolute length is  $\ell_{CE}$  which may be normalised to the optimal fibre length  $\ell_{CE,opt}$  by  $\ell_{CE,rel} = \ell_{CE}/\ell_{CE,opt}$ . In macroscopic muscle models, the CE muscle force is usually modelled as a function of a force-(CE-)length relation, a force-(CE-)velocity relation, and (CE-)activity  $q$ . Commonly the muscle activity  $q$  represents the number of attached cross-bridges within the muscle, normalised to the maximum number available ( $q_0 \leq q \leq 1$ ). It can also be considered as the concentration of bound  $Ca^{2+}$ -ions in the muscle sarcoplasm relative to its physiological maximum. The parameter  $q_0$  represents the minimum activity that is assumed to occur without any stimulation [6].

We analyse two different formulations of muscle activation dynamics, that is, the time (its symbol:  $t$ ) evolution of muscle activity  $q(t)$ . One formulation of muscle activation dynamics was suggested by Zajac [5], which we modified slightly to take  $q_0$  into account:

$$\dot{q}_Z = \frac{1}{\tau \cdot (1 - q_0)} \cdot [\sigma \cdot (1 - q_0) - \sigma \cdot (1 - \beta) \cdot (q_Z - q_0) - \beta \cdot (q_Z - q_0)], \quad (1)$$

with the initial condition  $q_Z(0) = q_{Z,0}$ . In this context,  $\sigma$  is supposed to represent the (electrical) stimulation of the muscle, being a parameter for controlling muscle dynamics. It represents the output of the nervous system's dynamics applied to the muscle which in turn interacts with the skeleton, the body mass distribution, the external environment, and therefore the nervous system in a feedback loop. Electromyographic (EMG) signals can be seen as a compound of such neural stimulations collected in a finite volume (being the input to a number of muscle fibres) over a frequency range and coming from a number of (moto-)neurons. The parameter  $\tau$  denotes the activation time constant, and  $\beta = \tau/\tau_{deact}$  is the ratio of activation to deactivation time constants (deactivation boost).

An alternative formulation of muscle activation dynamics was introduced by Hatze [6]:

$$\dot{\gamma} = m \cdot (\sigma - \gamma). \quad (2)$$

We divided the original equation from Hatze [6] by the parameter  $c = 1.37 \cdot 10^{-4}$  mol/L which represents the maximum concentration of free  $Ca^{2+}$ -ions in the muscle sarcoplasm. Thus, the values of the corresponding normalised

concentration are  $0 \leq \gamma \leq 1$ . The activity is finally calculated by the function

$$q_H(\gamma, \ell_{\text{CERel}}) = \frac{q_0 + [\rho(\ell_{\text{CERel}}) \cdot \gamma]^\nu}{1 + [\rho(\ell_{\text{CERel}}) \cdot \gamma]^\nu}, \quad (3)$$

and the parameter  $c$  is shifted to the accordingly renormalised function

$$\rho(\ell_{\text{CERel}}) = \rho_c \cdot \frac{\ell_\rho - 1}{\ell_\rho / \ell_{\text{CERel}} - 1}, \quad (4)$$

with  $\rho_c = c \cdot \rho_0$  and  $\ell_\rho = 2.9$ . Two cases have been suggested by Hatze [13]:  $\rho_0 = 6.62 \cdot 10^4$  L/mol (i.e.,  $\rho_c = 9.10$ ) for  $\nu = 2$  and  $\rho_0 = 5.27 \cdot 10^4$  L/mol (i.e.,  $\rho_c = 7.24$ ) for  $\nu = 3$ , which have been applied in the literature [7, 8, 14, 15]. By substituting (2) and (3) into  $\dot{q}_H = dq_H(\gamma, \ell_{\text{CERel}})/d\gamma \cdot \dot{\gamma}$  and resubstituting the inverse of (3) afterwards, Hatze's formulation of an activation dynamics can be transformed into a nonlinear differential equation directly in terms of the activity:

$$\begin{aligned} \dot{q}_H = \frac{\nu \cdot m}{1 - q_0} \cdot \left[ \sigma \cdot \rho(\ell_{\text{CERel}}) \cdot (1 - q_H)^{1+1/\nu} \cdot (q_H - q_0)^{1-1/\nu} \right. \\ \left. - (1 - q_H) \cdot (q_H - q_0) \right], \end{aligned} \quad (5)$$

with the initial condition  $q_H(0) = q_{H,0}$ .

The solutions  $q_Z(t)$  and  $q_H(t)$  of both formulations of activation dynamics (1) and (5) can now be directly compared by integrating them with the same initial condition  $q_{Z,0} = q_{H,0}$  using the same stimulation  $\sigma$ .

### 3. Local First and Second Order Sensitivity of ODE Systems regarding Their Parameters

Let  $\Omega \subseteq \mathbb{R} \times \mathbb{R}^M \times \mathbb{R}^N$  and  $f: \Omega \rightarrow \mathbb{R}^M$ . We then consider a system of ordinary, first order initial value problems (IVP):

$$\dot{Y} = f(t, Y(t, \Lambda), \Lambda), \quad Y(0) = Y_0, \quad (6)$$

where  $Y(t) = (y_1(t), y_2(t), \dots, y_M(t))$  denotes the vector of state variables,  $f = (f_1, f_2, \dots, f_M)$  the vector of right hand sides of the ODE, and  $\Lambda = \{\lambda_1, \lambda_2, \dots, \lambda_N\}$  the set of parameters which the ODE depends on. The vector of initial conditions is abbreviated by

$$\begin{aligned} Y(0) &= (y_1(0), y_2(0), \dots, y_M(0)) \\ &= (y_{1,0}, y_{2,0}, \dots, y_{M,0}) = Y_0. \end{aligned} \quad (7)$$

The first order sensitivity of the solution  $Y(t, \Lambda)$  with respect to the parameter set  $\Lambda$  is defined as the matrix

$$\begin{aligned} S(t, \Lambda) &= (S_{ik}(t, \Lambda))_{i=1, \dots, N, k=1, \dots, M}, \\ \text{with } S_{ik}(t, \Lambda) &= \frac{d}{d\lambda_i} y_k(t, \Lambda). \end{aligned} \quad (8)$$

Simplifying, we denote  $Y = Y(t, \Lambda)$ ,  $f = f(t, Y, \Lambda)$ , and  $S_{ik} = S_{ik}(t, \Lambda)$  but keep the dependencies in mind. Because

the solution  $Y(t)$  might only be gained numerically rather than in a closed-form expression, we have to apply the well-known theory of sensitivity analysis as stated in Vukobratovic [16], Dickinson and Gelinias [17], Lehman and Stark [2], and ZivariPiran [18]. Differentiating (8) with respect to  $t$  and applying the chain rule yield

$$\begin{aligned} \frac{d}{dt} S_{ik} &= \frac{d^2}{dt d\lambda_i} y_k = \frac{d^2}{d\lambda_i dt} y_k = \frac{d}{d\lambda_i} f_k \\ &= \frac{d}{d\lambda_i} Y \cdot \frac{\partial}{\partial Y} f_k + \frac{\partial}{\partial \lambda_i} f_k, \end{aligned} \quad (9)$$

with  $\partial/\partial Y$  being the gradient of state variables. Hence we obtain the following ODE for the first order solution sensitivity:

$$\dot{S}_{ik} = \sum_{l=1}^M S_{il} \cdot \frac{\partial}{\partial y_l} f_k + \frac{\partial}{\partial \lambda_i} f_k, \quad S_{ik}(0) = \frac{\partial}{\partial \lambda_i} y_{k,0} = 0, \quad (10)$$

or in short terms

$$\dot{S} = S \cdot J + B, \quad S(0) = \mathbf{0}_{N \times M}, \quad (11)$$

where  $S = S(t)$  is the  $N \times M$  sensitivity matrix and  $J = J(t)$  is the  $M \times M$  Jacobian matrix with  $J_{kl} = (\partial/\partial y_l) f_k$ ; furthermore,  $B = B(t)$  denotes the  $N \times M$ -matrix containing the partial derivatives  $B_{ik} = (\partial/\partial \lambda_i) f_k$  and  $\mathbf{0}_{N \times M}$  denotes the  $N \times M$ -matrix consisting of zeros only.

By analogy, the second order sensitivity of  $Y(t)$  with respect to  $\Lambda$  is defined as the following  $N \times N \times M$ -tensor:

$$R(t, \Lambda) = (R_{ijk}(t, \Lambda))_{i,j=1, \dots, N, k=1, \dots, M}, \quad (12)$$

with

$$R_{ijk}(t, \Lambda) = \frac{d}{d\lambda_i} S_{jk} = \frac{d}{d\lambda_j} S_{ik} = \frac{d^2}{d\lambda_i d\lambda_j} y_k = R_{jik}(t, \Lambda), \quad (13)$$

assuming  $R_{ijk} = R_{jik}$  for all  $k = 1, \dots, M$ , therefore assuming that the prerequisites of Schwarz theorem (symmetry of the second derivatives) are fulfilled throughout. Differentiating with respect to  $t$  and applying the chain rule lead to the ODE

$$\begin{aligned} \dot{R}_{ijk} &= \sum_{l=1}^M \left( R_{ijl} \frac{\partial}{\partial y_l} f_k + S_{il} \frac{\partial}{\partial \lambda_j} f_k + S_{jl} \frac{\partial}{\partial \lambda_i} f_k \right) \\ &+ \sum_{l_1=1}^M \sum_{l_2=1}^M S_{il_1} S_{jl_2} \frac{\partial^2}{\partial y_{l_1} \partial y_{l_2}} f_k + \frac{\partial^2}{\partial \lambda_i \partial \lambda_j} f_k, \end{aligned} \quad (14)$$

with  $R_{ijk}(0) = 0$ . For purposes beyond the aim of this paper, a condensed notation introducing the concept of tensor (or Kronecker) products as in ZivariPiran [18] may be helpful. For a practical implementation in MATLAB see Bader and Kolda [19].

Furthermore, if an initial condition  $y_{k,0}$  (see (7)) is considered as another parameter, we can derive a separate

sensitivity differential equation by rewriting (6) in its integral form

$$Y(t) = Y_0 + \int_0^t f(s, Y(s)) ds. \quad (15)$$

Differentiating this equation with respect to  $Y_0$  yields

$$S_{Y_0}(t) = \frac{\partial}{\partial Y_0} Y(t) = 1 + \int_0^t \frac{\partial}{\partial Y} f \cdot \frac{\partial}{\partial Y_0} Y(s) ds \quad (16)$$

and differentiating again with respect to  $t$  results in a homogeneous ODE for each component  $S_{y_{k,0}}(t)$ ; namely,

$$\dot{S}_{y_{k,0}}(t) = \sum_{l=1}^M \frac{\partial}{\partial y_l} f_k \cdot S_{y_{l,0}}, \quad \text{with } S_{y_{k,0}}(0) = \frac{\partial}{\partial y_{k,0}} y_{k,0} = 1. \quad (17)$$

The parameters of our analysed models are supposed to represent physiological processes and bear physical dimensions therefore. For example,  $m$  and  $1/\tau$  are frequencies measured in (Hz), whereas  $c$  is measured in (mol/L). Accordingly,  $S_\tau = (d/d\tau)q_Z$  would be measured in (Hz) and  $S_m$  in (s) (note that our model only consists of *one* ODE and therefore we do not need a second index). Normalisation provides a comprehensive comparison between all sensitivities, even across models. For any parameter, the value  $\lambda_i$  fixed for a specific simulation is a natural choice. For any state variable, we chose its current value  $y_k(t)$  at each point in time of the corresponding ODE solution. Hence, we normalise each sensitivity  $S_{ik} = dy_k/d\lambda_i$  by multiplying it with the ratio  $\lambda_i/y_k(t)$  to get the relative sensitivity

$$\tilde{S}_{ik} = S_{ik} \cdot \frac{\lambda_i}{y_k}. \quad (18)$$

A relative sensitivity  $\tilde{S}_{ik}$  thus quantifies the percentage change in the  $k$ th state variable value per percentage change in the  $i$ th parameter value. This applies accordingly to the second order sensitivity

$$\tilde{R}_{ijk} = R_{ijk} \cdot \frac{\lambda_i \cdot \lambda_j}{y_k}. \quad (19)$$

It can be shown that this method is valid and mathematically equivalent to another common method in which the whole model is nondimensionalised a priori [20]. A nonnormalised model formulation has the additional advantage of usually allowing a more immediate appreciation of and transparent access for experimenters. In the remainder of this paper, we are always going to present and discuss relative sensitivity values normalised that way.

In our model the specific case  $M = 1$  applies, so (10) and (14) simplify to the case  $k = 1$  (no summation).

#### 4. Variance-Based Global Sensitivity Analysis

The differential sensitivity analysis above is called a local method because it does not take the physiological range

of parameter values into account. Additionally factoring in such ranges characterises the so-called global methods. The main idea behind most global methods is to include a statistical component to scan the whole parameter space  $\mathcal{C}$  and combine the percentage change in a state variable value per percentage change in a parameter value with the variability of all of the parameters. The parameter space  $\mathcal{C}$  can be seen as a  $N$ -dimensional cuboid  $\mathcal{C} = [\lambda_1^-; \lambda_1^+] \times \dots \times [\lambda_N^-; \lambda_N^+]$ , where  $\lambda_i^-$  and  $\lambda_i^+$  are the minimal and maximal parameter values and  $N$  is the number of parameters. We can now fix a certain point  $\hat{\Lambda} = (\hat{\lambda}_1, \dots, \hat{\lambda}_N) \in \mathcal{C}$  and calculate the local gradient of the solution with respect to  $\hat{\Lambda}$ . The volume of the star-shaped area, investigated by changing only one parameter at once and lying within a ball around  $\hat{\Lambda}$ , vanishes in comparison to  $\mathcal{C}$  for an increasing number of parameters [21]. For an overview of the numerous methods like ANOVA, FAST, Regression, or Sobol's Indexing, the reader is referred to Saltelli and Chan [4] and Frey et al. [22].

In this section we want to sketch just the main idea of the variance-based sensitivity analysis approach as presented in Chan et al. [3], which is based on Sobol's Indexing. We chose this method because of its transparency and low computational cost. This method aims at calculating two measurands of sensitivity of a state variable with respect to parameter  $\lambda_i$ : the variance-based sensitivity function denoted by  $VBS_i(t)$  and the total sensitivity index function denoted by  $TSI_i(t)$ . The VBS functions give a normalised first order sensitivity quite similar to  $\tilde{S}$  from the previous section but include the parameter range. The TSI functions, however, additionally include higher order sensitivities and give a measurand for interdependencies of parameter influences.

A receipt for calculating VBS and TSI is as follows. First of all, set boundaries for all model parameters, either by model assumptions or by literature reference, thus fixing  $\mathcal{C}$ . Secondly, generate two sets of  $n$  sample points  $\hat{\Lambda}_{1,j}, \hat{\Lambda}_{2,j} \in \mathcal{C}$ ,  $j = 1, \dots, n$ , suited to represent the underlying probability distribution of each parameter, in our case the uniform distribution. Thirdly, with  $i$  indicating a parameter, generate  $2nN$  sets of new sample points  $\hat{\Lambda}_{1,j}^i, \hat{\Lambda}_{2,j}^i$ ,  $j = 1, \dots, n$ ,  $i = 1, \dots, N$ , where  $\hat{\Lambda}_{1,j}^i$  consists of all sample points in  $\hat{\Lambda}_{1,j}$  except for its  $i$ th component (parameter value) replaced by the  $i$ th component of  $\hat{\Lambda}_{2,j}$ . Consequently,  $\hat{\Lambda}_{2,j}^i$  consists of the  $i$ th component of  $\hat{\Lambda}_{1,j}$  and every other component taken from  $\hat{\Lambda}_{2,j}$ . Fourthly, evaluate the model from (6) at all of the  $2n(N + 1)$  sample points  $\hat{\Lambda}_{1,j}, \hat{\Lambda}_{2,j}, \hat{\Lambda}_{1,j}^i, \hat{\Lambda}_{2,j}^i$  resulting in a family of solutions.

For this family perform the following calculations.

- (1) Compute the variance of the family of all  $2n(N + 1)$  solutions as a function of time, namely,  $V(t)$ . This variance function indicates the general model output variety throughout the whole parameter range.
- (2) Compute the variances  $V_i$  of the family of  $n(N + 1)$  solutions resulting from an evaluation of the model at all  $\hat{\Lambda}_{1,j}$  and  $\hat{\Lambda}_{2,j}^i$ , that is, for every  $j$  and  $i$ . Each  $V_i(t)$  is a function of time and indicates the model output variety if solely the value  $\lambda_i$  of parameter  $i$  is changed.

- (3) Compute the variances  $V_{\sim i}$  of the family of  $n(N + 1)$  solutions resulting from an evaluation of the model at all  $\widehat{\Lambda}_{1,j}$  and  $\widehat{\Lambda}_{1,j}^i$ , that is, for every  $j$  and  $i$ . Each  $V_{\sim i}(t)$  is a function of time and indicates the model output variety if the value of  $\lambda_i$  is fixed, whereas all other parameter values are changed.

Note that the computations in Chan et al. [3] are done using Monte-Carlo integrals as an approximation. The VBS and TSI can be finally calculated as

$$\text{VBS}_i(t) = \frac{V_i(t)}{V(t)}, \quad \text{TSI}_i(t) = 1 - \frac{V_{\sim i}(t)}{V(t)}. \quad (20)$$

The normalisation entails additional properties of VBS and TSI (see [3, Figure 1]):

$$\sum_{i=1}^N \text{VBS}_i(t) \leq 1, \quad \sum_{i=1}^N \text{TSI}_i(t) \geq 1. \quad (21)$$

In other words,  $\text{VBS}_i(t)$  gives the normalised global first order sensitivity function of the solution with respect to  $\lambda_i$  in relation to the model output range. Accordingly,  $\text{TSI}_i(t)$  quantifies a relative impact of the variability in parameter  $\lambda_i$  on the model output, factoring in the interdependent influence in combination with all other parameters' sensitivities. Chan et al. [3] suggested to denote the  $\text{TSI}_i(t)$  value as the ‘‘importance’’ of  $\lambda_i$ .

## 5. An Analytical Example for Local Sensitivity Analysis including a Link between Zajac’s and Hatze’s Formulations

By further simplifying Zajac’s formulation of an activation dynamics (1) through assuming a deactivation boost  $\beta = 1$  (activation and deactivation time constants are equal) and a basic activity  $q_0 = 0$ , we obtain a linear ODE for this specific case  $q_Z^{\text{sp}}$ , which is equivalent to Hatze’s equation (2) modelling the time evolution of the free  $\text{Ca}^{2+}$ -ion concentration:

$$\dot{q}_Z^{\text{sp}} = \frac{1}{\tau} (\sigma - q_Z^{\text{sp}}), \quad q_Z^{\text{sp}}(0) = q_{Z,0}. \quad (22)$$

By analysing this specific case, we aim at making the above described sensitivity analysis method more transparent for the reader. Solving (22) yields

$$q_Z^{\text{sp}}(t) = \sigma \cdot (1 - e^{-t/\tau}) + q_{Z,0} \cdot e^{-t/\tau} \quad (23)$$

depending on just two parameters  $\sigma$  (stimulation: control parameter) and  $\tau$  (time constant of activation: internal parameter) in addition to the initial value  $y_0 = q_{Z,0}$ . The solution  $q_Z(t)$  equals the  $\sigma$  value after about  $\tau$ .

We apply the more generally applicable, implicit methods (10) and (17) to determine the derivatives of the solution with respect to the parameters (the sensitivities), although we already know solution (23) in a closed form. Hence, for the

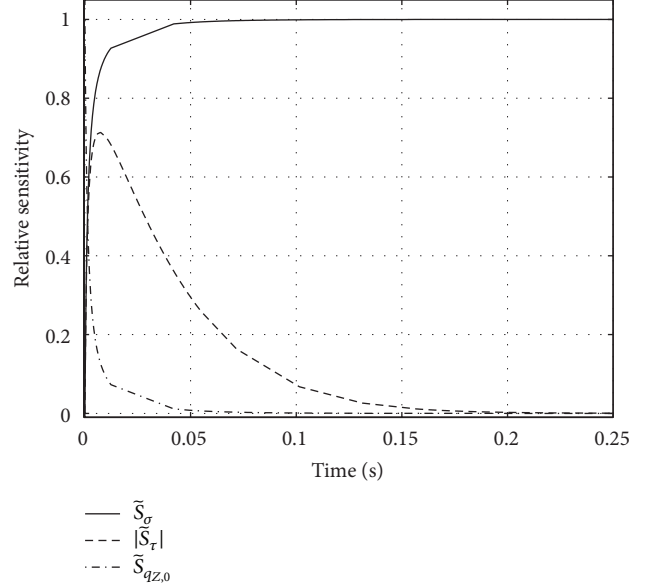


FIGURE 1: Relative sensitivities  $\widetilde{S}_i$  with respect to the three parameters in the simplified formulation (22) of Zajac’s activation dynamics (1). Parameters: stimulation  $\sigma$  (see (25): solid line), activation time constant  $\tau$  (see (26): dashed line), and initial activation  $q_{Z,0}$  (see (27): dash-dotted line). Note that  $\widetilde{S}_\tau$  is negative, but for reasons of comparability we have plotted its absolute value. Parameter values are  $\sigma = 1$ ,  $\tau = 1/40 \text{ s} = 0.025 \text{ s}$ , and  $q_{Z,0} = 0.05$ . Because ODE (22) for  $q_Z^{\text{sp}}$  is equivalent to Hatze’s ODE (2) for the free  $\text{Ca}^{2+}$ -ion concentration,  $\gamma$ , we can identify the sensitivity of  $1/\tau$  with that of  $m$ .

transparency of our method, we calculate the gradient of the right hand side  $f(q_Z^{\text{sp}}, \sigma, \tau)$  of ODE (22)

$$\frac{\partial}{\partial q_Z^{\text{sp}}} f = -\frac{1}{\tau}, \quad \frac{\partial}{\partial \sigma} f = \frac{1}{\tau}, \quad (24)$$

$$\frac{\partial}{\partial \tau} f = -\frac{\sigma - q_Z^{\text{sp}}}{\tau^2} = \frac{q_{Z,0} - \sigma}{\tau^2} e^{-t/\tau}$$

and insert these partial derivatives into (10) and (17). Solving the respective three ODEs for the three parameters ( $\sigma$ ,  $\tau$ , and  $q_{Z,0}$ ) and normalising them according to (18) give the relative sensitivities of  $q_Z^{\text{sp}}$  with respect to  $\sigma$ ,  $\tau$ , and  $q_{Z,0}$  as functions of time (see Figure 1):

$$\widetilde{S}_\sigma(t) = (1 - e^{-t/\tau}) \cdot \frac{\sigma}{q_Z^{\text{sp}}(t)} = \frac{\sigma \cdot (e^{t/\tau} - 1)}{\sigma \cdot (e^{t/\tau} - 1) + q_{Z,0}}, \quad (25)$$

$$\begin{aligned} \widetilde{S}_\tau(t) &= \left( \frac{(q_{Z,0} - \sigma) \cdot t}{\tau^2} e^{-t/\tau} \right) \cdot \frac{\tau}{q_Z^{\text{sp}}(t)} \\ &= \frac{t \cdot (q_{Z,0} - \sigma)}{\tau \cdot [\sigma \cdot (e^{t/\tau} - 1) + q_{Z,0}]}, \end{aligned} \quad (26)$$

$$\widetilde{S}_{q_{Z,0}}(t) = e^{-t/\tau} \cdot \frac{q_{Z,0}}{q_Z^{\text{sp}}(t)} = \frac{q_{Z,0}}{\sigma \cdot (e^{t/\tau} - 1) + q_{Z,0}}. \quad (27)$$

A straightforward result is that the time constant  $\tau$  has its maximum effect on the solution (Figure 1, see  $\tilde{S}_\tau(t)$ ) at time  $t = \tau$ . In case of a step in stimulation, the sensitivity  $\tilde{S}_\tau(t)$  vanishes in the initial situation and exponentially approaches zero again after a few further multiples of the typical period  $\tau$ . Note that  $\tilde{S}_\tau(t)$  is negative, which means that an increase in  $\tau$  decelerates activation. Thus, for a fixed initial value  $q_{Z,0}$ , the solution value  $q_Z(t)$  decreases at a given point in time if  $\tau$  is increased. After a step in stimulation  $\sigma$ , the time in which the solution  $q_Z(t)$  bears some memory of its initial value  $q_{Z,0}$  is equal to the period of being nonsensitive to any further step in  $\sigma$  (compare  $\tilde{S}_{q_{Z,0}}(t)$  to  $\tilde{S}_\sigma(t)$  and (25) to (27)). After about  $\tau/2$ , the sensitivity  $\tilde{S}_{q_{Z,0}}(t)$  has already fallen to about 0.1 and  $\tilde{S}_\sigma(t)$  to about 0.9 accordingly.

## 6. The Numerical Approach and Results

Typically, biological dynamics are represented by nonlinear ODEs. Therefore, the linear ODE used for describing activation dynamics in the Zajac [5] case (1) is more of an exception. For example, a closed-form solution can be given. Equation (23) is an example as shown in the previous section for the reduced case of nonboosted deactivation (22).

In general, however, nonlinear ODEs used in biomechanical modelling, as the Hatze [6] case (5) for describing activation dynamics, can only be solved numerically. It is understood that any explicit formulation of a model in terms of ODEs allows providing the partial derivatives of their right hand sides  $f$  with respect to the model parameters in a closed form. Fortunately, this is exactly what is required as part of the sensitivity analysis approach presented in Section 3, in particular in (10).

As an application for applying this approach, we will now present a comparison of both formulations of activation dynamics. The example indicates that the approach may be of general value because it is common practice in biomechanical modelling to (i) formulate the ODEs in closed form and (ii) integrate the ODEs numerically. Adding further sensitivity ODEs for model parameters then becomes an inexpensive enhancement of the procedure used to solve the problem anyway.

For the two different activation dynamics [5, 6], the parameter sets  $\Lambda_Z$  and  $\Lambda_H$ , respectively, consist of

$$\Lambda_Z = \{q_{Z,0}, \sigma, q_0, \tau, \beta\}, \quad (28)$$

$$\Lambda_H = \{q_{H,0}, \sigma, q_0, m, \rho_c, \nu, \ell_\rho, \ell_{Crel}\}, \quad (29)$$

including the initial conditions. The numerical solutions for these ODEs were computed within the MATLAB environment (The MathWorks, Natick, USA; version R2013b), using the preimplemented numerical solver *ode45* which is a Runge-Kutta algorithm of order 5 (for details see [23]).

**6.1. Results for Zajac's Activation Dynamics: Sensitivity Functions.** We simulated activation dynamics for the parameter set  $\Lambda_Z$  (28) leaving two of the values constant ( $q_0 = 0.005$ ,  $\tau = 1/40$  s) and varying the other three (initial condition  $q_{Z,0}$ ,

stimulation  $\sigma$ , and deactivation boost  $\beta$ ). The time courses of the relative sensitivities  $\tilde{S}_i(t)$  with respect to all parameters  $\lambda_i \in \Lambda_Z$  are plotted in Figure 2. In the left column of Figure 2 we used  $\beta = 1$ , in the right column  $\beta = 1/3$ . Pairs of the parameter values  $q_0 = 0.005 \leq q_{Z,0} \leq 0.5$  and  $0.01 \leq \sigma \leq 1$  are specified in the legend of Figure 2, with increasing values of both parameters from top to bottom.

**6.1.1. Relative Sensitivity  $\tilde{S}_{q_0}$ .** Solutions are nonsensitive to the  $q_0$  choice except if both initial activity and stimulation (also approximating the final activity if  $\beta = 1$  and  $\sigma \gg q_0$ ) are very low near  $q_0$  itself.

**6.1.2. Relative Sensitivity  $\tilde{S}_{q_{Z,0}}$ .** The memory (influence on solution) of the initial value is lost after about  $2\tau$ , almost independently of all other parameters. This loss in memory is obviously slower than in that case  $q_{Z,0} = 0$  (initial value) and  $\sigma = 1$  (for  $\beta = 1$  and  $q_0 = 0$  exactly the final value; see Section 5 and Figure 1). In that extreme case, the influence (relative sensitivity) of the lowest possible initial value ( $q_{Z,0} = 0$ ) on the most rapidly increasing solution (maximum possible final value:  $\sigma = 1$ ) is lost earlier.

**6.1.3. Relative Sensitivity  $\tilde{S}_\tau$ .** The influence of the time constant  $\tau$  on the solution is reduced with decreasing difference between initial and final activity values (compare maximum  $\tilde{S}_\tau$  values in Figures 1 and 2) and, no matter the  $\beta$  value, with jointly raised levels of initial activity  $q_{Z,0}$  and  $\sigma$ , the latter determining the final activity value if  $\beta = 1$ . When deactivation is slower than activation ( $\beta < 1$ : right column in Figure 2),  $\tilde{S}_\tau$  is higher than in the case  $\beta = 1$ , both in its maximum amplitude and for longer times after the step in stimulation, especially at low activity levels (upper rows in Figure 2).

**6.1.4. Relative Sensitivity  $\tilde{S}_\sigma$ .** Across all parameters, the solution in general is most sensitive to  $\sigma$ . However, the influence of the deactivation boost parameter  $\beta$  is usually comparable. In some situations, this also applies to the activation time constant  $\tau$  (see below). For  $\beta = 1$  (Figure 2, left), the solution becomes a little less sensitive to  $\sigma$  with decreasing activity level ( $\tilde{S}_\sigma < 1$ ), which reflects that the final solution value is not determined by  $\sigma$  alone but by  $q_0 > 0$  and  $\beta \neq 1$  as much. If deactivation is much slower than activation ( $\beta = 1/3 < 1$ : Figure 2, right), we find the opposite to the  $\beta = 1$  case: the more the activity level rises, the lesser  $\sigma$  determines the solution. Additionally, stimulation  $\sigma$  somehow competes with both deactivation boost  $\beta$  and time constant  $\tau$  (see further below). Using the term ‘‘compete’’ illustrates the idea that any single parameter should have an individual interest in influencing the dynamics as much as possible in order not to be considered superfluous.

**6.1.5. Relative Sensitivity  $\tilde{S}_\beta$ .** Sensitivity with respect to  $\beta$  generally decreases with increasing activity  $q_{Z,0}$  and stimulation  $\sigma$  levels. It vanishes at maximum stimulation  $\sigma = 1$ .

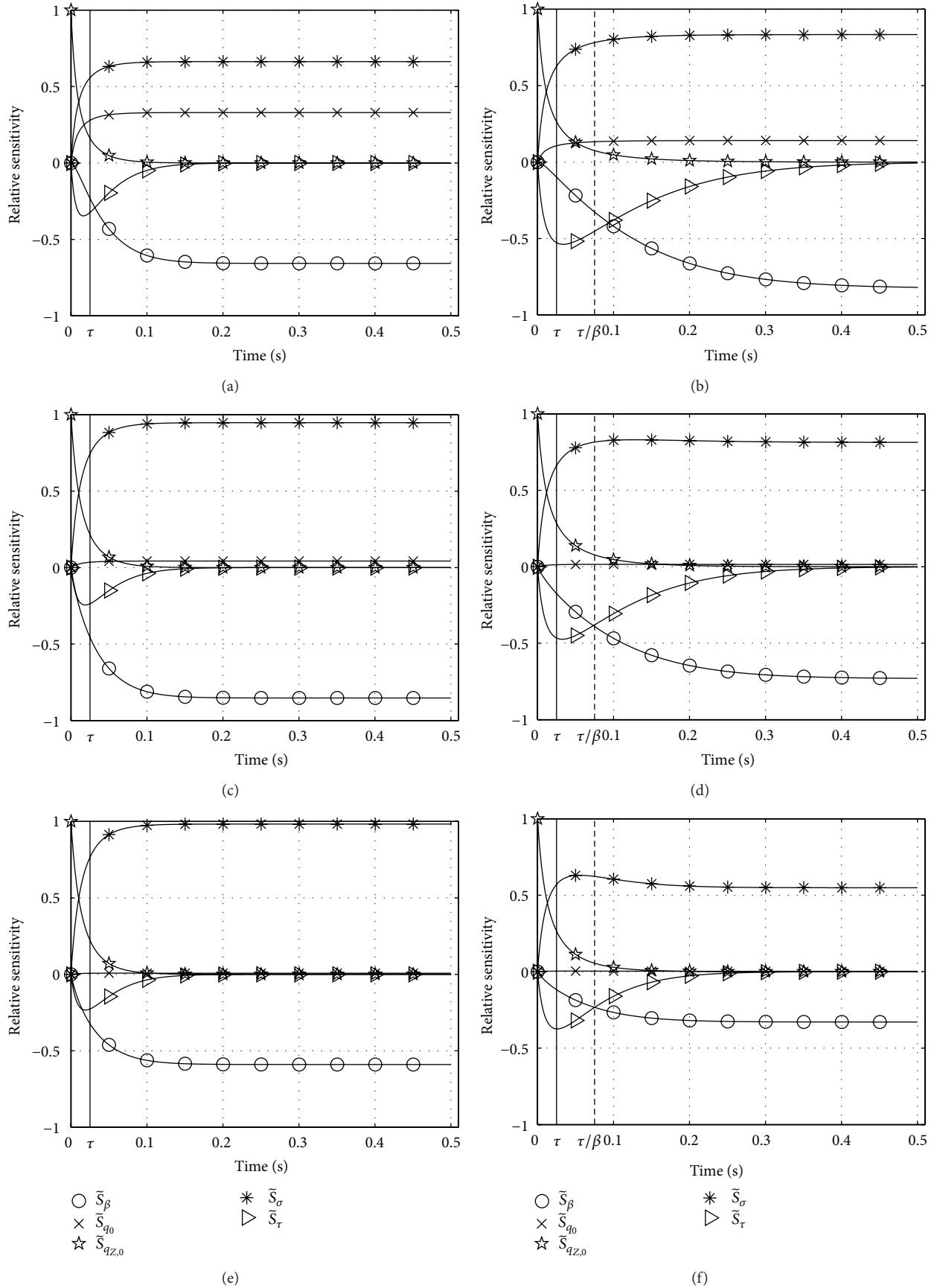


FIGURE 2: Continued.

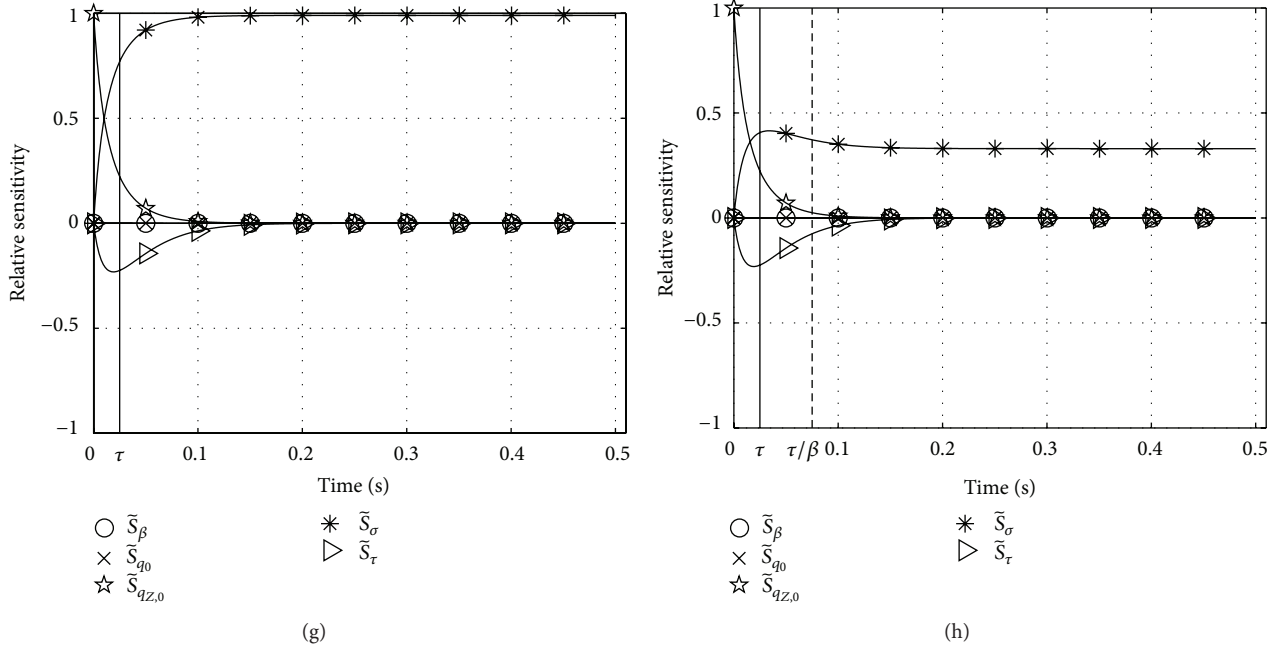


FIGURE 2: Relative sensitivities  $\tilde{S}_i$  with respect to all parameters  $\lambda_i$  (set  $\Lambda_Z$  (28)) in Zajac's activation dynamics (1). Parameter values varied from top (i) to bottom (iv) row: (i)  $q_{Z,0} = q_0 = 0.005$ ,  $\sigma = 0.01$ , (ii)  $q_{Z,0} = 0.05$ ,  $\sigma = 0.1$ , (iii)  $q_{Z,0} = 0.2$ ,  $\sigma = 0.4$ , and (iv)  $q_{Z,0} = 0.5$ ,  $\sigma = 1$ ; left column:  $\beta = 1$ , right column:  $\beta = 1/3$ .

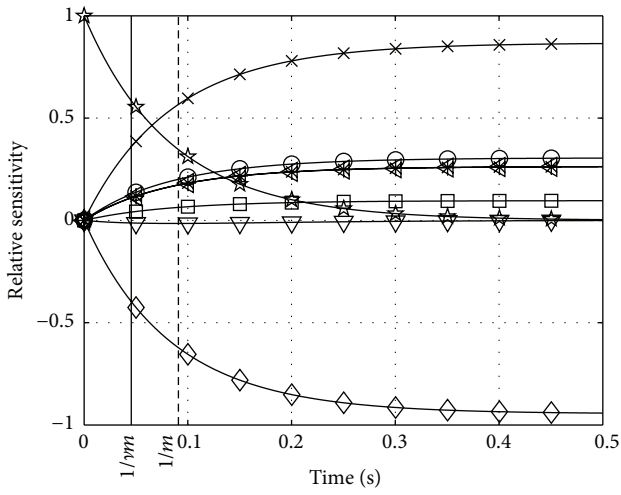
6.1.6. *Relative Sensitivities  $\tilde{S}_\sigma$ ,  $\tilde{S}_\beta$ ,  $\tilde{S}_\tau$ .* At submaximal stimulation levels  $\sigma < 1$ , the final solution value is determined to almost the same degree by stimulation  $\sigma$  and deactivation boost  $\beta$ , yet with opposite tendencies ( $\tilde{S}_\sigma > 0$ ,  $\tilde{S}_\beta < 0$ ). As explained, both parameters compete for their impact on the final solution value. Only at maximum stimulation  $\sigma = 1$  (lowest row in Figure 2), this parameter competition is resolved in favour of  $\sigma$ . In this specific case,  $\beta$  does not influence the solution at all. For  $\beta = 1$  the competition about influencing the solution is intermittently but only slightly biased by  $\tau$ : sensitivity  $\tilde{S}_\tau$  peaks at comparably low magnitude around  $t = \tau$ . This  $\tau$  influence comes likewise intermittently at the cost of  $\beta$  influence: the absolute value of  $\tilde{S}_\beta$  rises a little slower than  $\tilde{S}_\sigma$ . In the case  $\beta < 1$ , this competition becomes more differentiated and spread out in time. Again at submaximal stimulation and activity levels, the absolute value of  $\tilde{S}_\tau$  is lower than that of  $\tilde{S}_\sigma$  but higher than that of  $\tilde{S}_\beta$ , making all three parameters  $\sigma$ ,  $\beta$ , and  $\tau$  compete to comparable degrees for an impact on the solution until about  $t = 4\tau$ . Also,  $\tilde{S}_\tau$  does not vanish before about  $t = 10\tau$ .

6.2. *Results for Hatze's Activation Dynamics: Sensitivity Functions.* We also simulated activation dynamics for the parameter set  $\Lambda_H$  (29), leaving now four of the values constant ( $q_0 = 0.005$ ,  $m = 10$  1/s,  $\ell_\rho = 2.9$ ,  $\ell_{C\text{Erel}} = 1$ ) and again varying three others (initial condition  $q_{Z,0}$ , stimulation  $\sigma$ , and nonlinearity  $\nu$ ), keeping in mind that the eighth parameter ( $\rho_c$ ) is assumed to depend on  $\nu$ . Time courses of the relative sensitivities  $\tilde{S}_i(t)$  with respect to all parameters  $\lambda_i \in \Lambda_H$  are plotted (see Figure 3). In the left column of Figure 3,  $\nu = 2$ ,

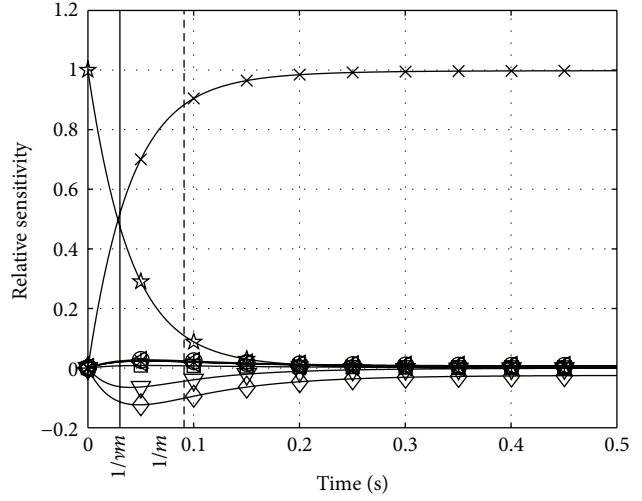
$\rho_c = 9.10$  is used, in the right column  $\nu = 3$ ,  $\rho_c = 7.24$ . Here, the same pairs of the parameter values ( $q_0 = 0.005 \leq q_{Z,0} \leq 0.5$  and  $0.01 \leq \sigma \leq 1$ , increasing from top to bottom; see legend of Figure 3) are used as in Section 6.1 (Figure 2).

Hatze's activation dynamics (5) are nonlinear unlike Zajac's activation dynamics (1). This nonlinearity manifests particularly in a changeful influence of the parameter  $\nu$ . Additionally, the parameter  $m$  is just roughly comparable to the inverse of the exponential time constant  $\tau$  in Zajac's linear activation dynamics.

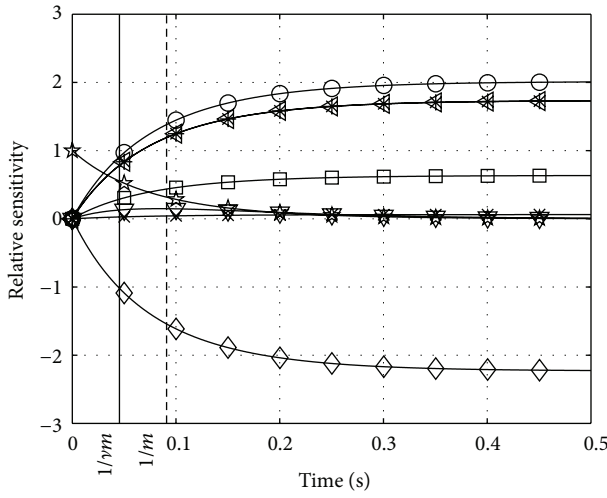
6.2.1. *Relative Sensitivity  $\tilde{S}_m$ .* In Zajac's linear differential equation (1),  $\tau$  establishes a distinct time scale independent of all other parameters. The parameter  $m$  in Hatze's activation dynamics (5) is just formally equivalent to the reciprocal of  $\tau$ : the sensitivity  $\tilde{S}_m$  does not peak stringently at  $t = 1/m = 0.1$  s but rather diffusely between about 0.05 s and 0.1 s in both of the cases  $\nu = 2$  and  $\nu = 3$ . At first this is not surprising because the scaling factor in Hatze's dynamics is  $\nu \cdot m$  rather than just  $m$ . However,  $\nu \cdot m$  does not fix an invariant time scale for Hatze's nonlinear differential equation. This fact becomes particularly prominent at extremely low activity levels for  $\nu = 2$  (Figure 3, left, top row) and up to moderately submaximal activity levels for  $\nu = 3$  (Figure 3, right, top two rows). Here,  $\tilde{S}_m$  is negative, which means that increasing the parameter  $m$  results in less steeply increasing activity. This observation is counterintuitive to identifying  $m$  with a reciprocal of a time constant like  $\tau$ . Rather than being expected from the product  $\nu \cdot m$ , the exponent  $\nu$  does not linearly scale the time behaviour because  $\tilde{S}_m$  peaks do not occur systematically earlier in the  $\nu = 3$  case as compared to  $\nu = 2$ .



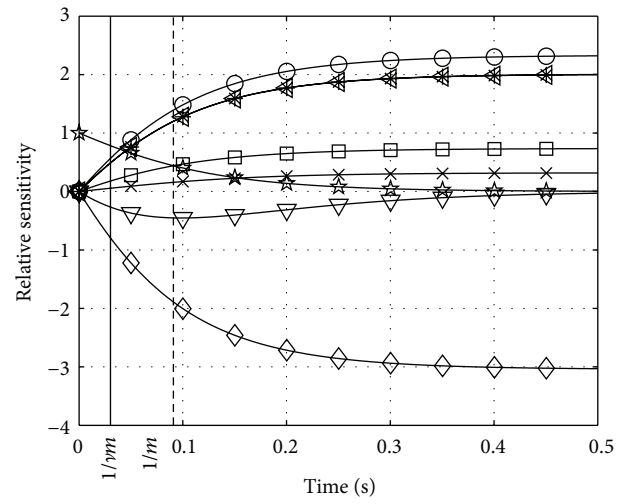
(a)



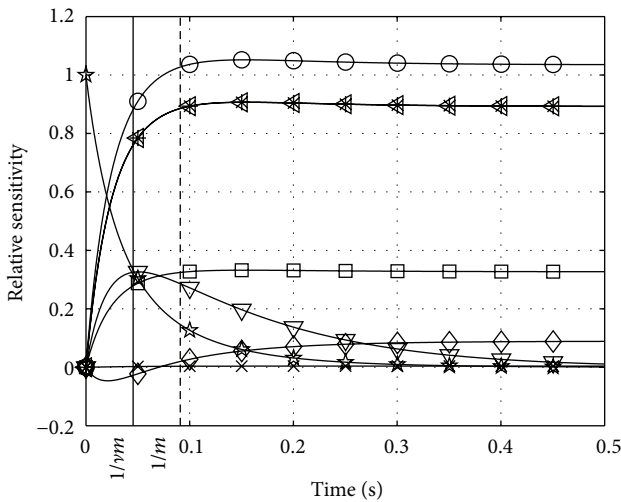
(b)



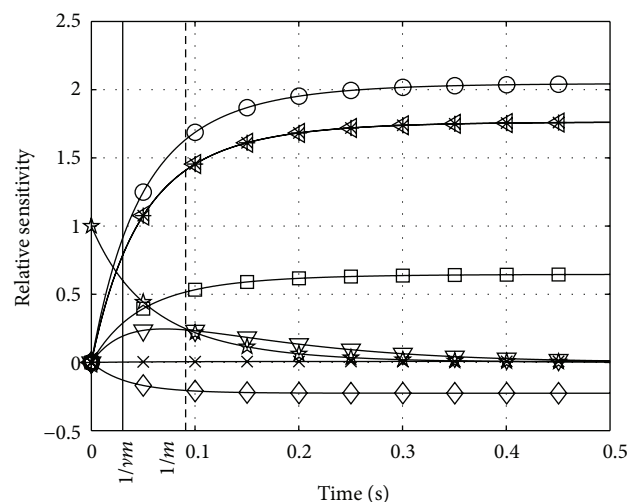
(c)



(d)



(e)



(f)

- |                            |                            |
|----------------------------|----------------------------|
| $\circ$ $S_{l_{CE}}^i$     | $\times$ $S_{q_0}^i$       |
| $\square$ $S_{l_{\rho}}^i$ | $\star$ $S_{q_{H,0}}^i$    |
| $\nabla$ $S_m^i$           | $\triangle$ $S_{\rho_c}^i$ |
| $\diamond$ $S_{\sigma}^i$  | $*$ $S_{\sigma}^i$         |

FIGURE 3: Continued.

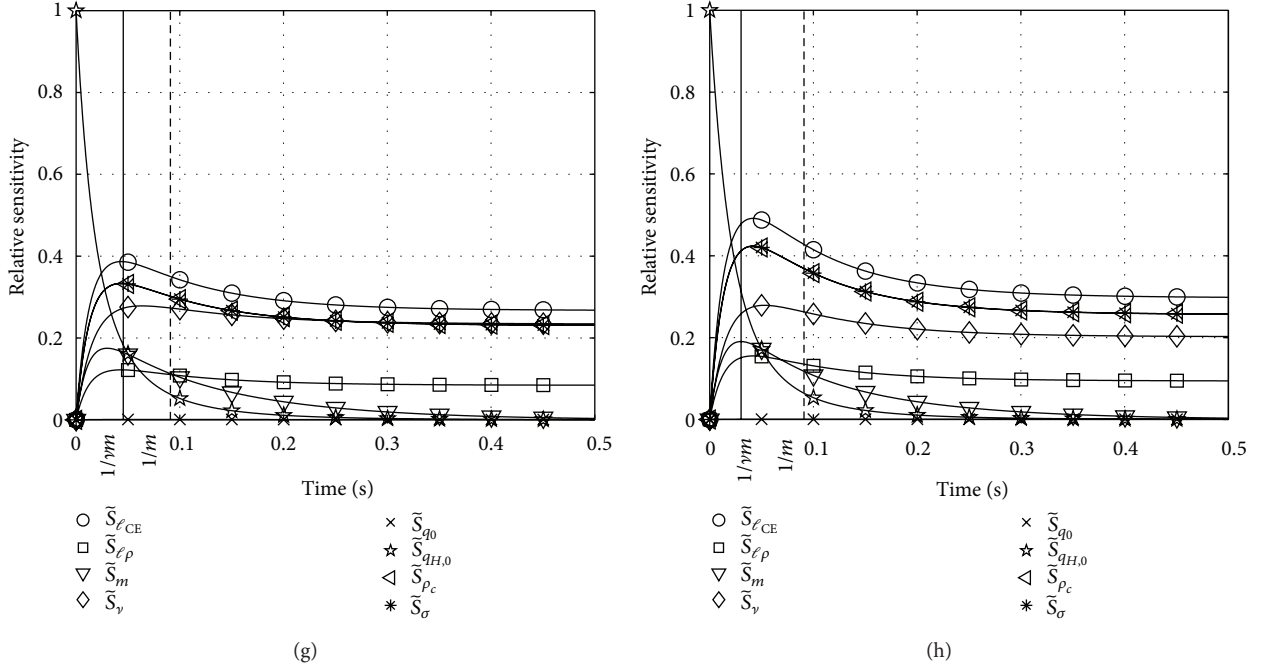


FIGURE 3: Relative sensitivities  $\tilde{S}_i$  with respect to all parameters  $\lambda_i$  (set  $\Lambda_H$  (29)) in Hatze's activation dynamics (5). Parameter values varied from top (i) to bottom (iv) row: (i)  $q_{H,0} = q_0 = 0.005$ ,  $\sigma = 0.01$ , (ii)  $q_{H,0} = 0.05$ ,  $\sigma = 0.1$ , (iii)  $q_{H,0} = 0.2$ ,  $\sigma = 0.4$ , and (iv)  $q_{H,0} = 0.5$ ,  $\sigma = 1$ ; left column:  $\nu = 2$ ,  $\rho_c = 9.10$ , right column:  $\nu = 3$ ,  $\rho_c = 7.24$ .

6.2.2. *Relative Sensitivity  $\tilde{S}_{q_{H,0}}$ .* Losing the memory of the initial condition confirms the analysis of time behaviour based on  $\tilde{S}_m$ . At high activity levels (Figure 3, bottom row), Hatze's activation dynamics loses memory at identical time horizons (no matter the  $\nu$  value) seemingly slower for higher  $\nu$  at intermediate levels (Figure 3, two middle rows) and clearly faster at very low levels (Figure 3, top row). The parameter  $m$  still does roughly determine the time horizon in which the memory of the initial condition  $q_{H,0}$  is lost and the influence of all other parameters is continuously switched on from zero influence at  $t = 0$ .

6.2.3. *Relative Sensitivity  $\tilde{S}_{q_0}$ .* As in Zajac's dynamics the solution is generally only sensitive to  $q_0$  at very low stimulation levels  $\sigma \approx q_0$  (Figure 3, top row). At such levels, the  $\nu = 3$  case shows the peculiarity that the solution becomes strikingly insensitive to any other parameter than  $q_0$  itself (and  $q_{H,0}$ ). The time evolution of the solution is more or less determined by just this minimum ( $q_0$ ) and initial ( $q_{H,0}$ ) activities, and  $m$  determining the approximate switching time horizon between both. The  $\ell_{CE}$  dependency, constituting a crucial property of Hatze's activation dynamics, is practically suppressed for  $\nu = 3$  at very low activities and stimulations. In contrast,  $\tilde{S}_{\ell_{CErel}}$  remains for  $\nu = 2$  on a low but still significant level of about a fourth of the three dominating quantities  $\tilde{S}_{q_0}$ ,  $\tilde{S}_{q_{H,0}}$ , and  $\tilde{S}_\nu$ .

6.2.4. *Relative Sensitivity  $\tilde{S}_\nu$ .* The sensitivity with respect to  $\nu$  is extraordinarily high at low activities and stimulations around 0.1, both for  $\nu = 2$  and for  $\nu = 3$  (Figure 3, second

row from top), additionally at extremely low levels for  $\nu = 2$  (Figure 3, left, top row). At moderately submaximal levels (Figure 3, third row from top), the solution is influenced with an already inverted tendency ( $\tilde{S}_\nu$  changes sign to positive) after around a  $1/m$  time horizon for  $\nu = 2$ . However, at these levels the solution is practically insensitive to  $\nu$  for any  $\nu$ . At high levels (Figure 3, bottom row) we find that there is no change in the character of time evolution of the solution, despite the specific value of  $\nu$ . The degree of nonlinearity  $\nu$  is unimportant because the time evolution and the ranking of all other sensitivities are hardly influenced by  $\nu$ . In both cases, the rise in activity is quickened by increasing  $\nu$  ( $\tilde{S}_\nu > 0$ ), as opposed to low activity and stimulation levels where rises in activity are slowed down ( $\tilde{S}_\nu < 0$ ; see also above).

6.2.5. *Relative Sensitivities  $\tilde{S}_\sigma$ ,  $\tilde{S}_{\rho_c}$ ,  $\tilde{S}_{\ell_{CErel}}$ , and  $\tilde{S}_{\ell_\rho}$ .* Of all the remaining parameters, stimulation  $\sigma$ , scaled maximum free  $Ca^{2+}$ -ion concentration  $\rho_c$ , relative CE length  $\ell_{CErel}$ , and the pole  $\ell_\rho$  of the length dependency in Hatze's activation dynamics, the latter has the lowest influence on the solution. The influence characters of all four parameters are yet completely identical. Their sensitivities are always positive and coupled by fixed scaling ratios due to all of them occurring within just one product on the right side of (5).  $\tilde{S}_\sigma$  and  $\tilde{S}_{\rho_c}$  are identical, while the sensitivity with respect to  $\ell_{CErel}$  is the highest, with ratios  $\tilde{S}_{\ell_{CErel}}/\tilde{S}_{\ell_\rho} \approx 3$  and  $\tilde{S}_{\ell_{CErel}}/\tilde{S}_\sigma \approx 1.2$ . Except at very low activity (where  $q_0$  plays a dominating role) and except for the generally changeable  $\nu$  influence, these are the four parameters that dominate the solution after an initial phase in which the initial activity  $q_{H,0}$  determines its evolution. The parameter

TABLE 1: Lower and upper bounds for the parameter choices in both Zajac's and Hatze's models of activation dynamics.

Parameter	$\beta$	$\ell_{\text{CErel}}$	$\ell_p$	$m$	$\nu$	$q_0$	$q_{Z,0}, q_{H,0}$	$\rho_c$	$\sigma$	$\tau$
Lower bound	0.1	0.4	2.2	3	1.5	0.001	0.01	4	0	0.01
Upper bound	1	1.6	3.6	11	4	0.05	1	11	1	0.05

$m$  does not have a strong direct influence on the solution. As stated above, it defines the approximate time horizon in which the  $q_{H,0}$  influence gets lost and all other parameters' influence is switched on from zero at  $t = 0$ .

**6.3. Variance-Based Sensitivity (VBS) and Total Sensitivity Indices (TSI) for Zajac's and Hatze's Activation Dynamics.** Table 1 pools the lower and upper boundaries for every parameter in  $\Lambda_Z$  and  $\Lambda_H$  used in our calculations. We refer to Hatze [24], Zajac [5], or Günther et al. [11] for traceability of our choices. The left hand side of Figure 4 shows the VBS functions of every parameter in  $\Lambda_Z$  of Zajac's model. The plotted functions can be compared to our previously computed relative first order sensitivity functions from Figure 2: at first sight,  $\tilde{S}_{q_{Z,0}}$  and  $\text{VBS}_{q_{Z,0}}$  look equal, but the VBS function indicates a slightly increased duration of influence of  $q_{Z,0}$ . Regarding  $\tau$ , the VBS function peaks at the same time as  $\tilde{S}_\tau$ , but with a smaller amplitude. Likewise, the courses of  $\text{VBS}_\sigma$  and  $\text{VBS}_\beta$  are comparable to  $\tilde{S}_\sigma$  and  $\tilde{S}_\beta$  from the second and third row of Figure 2. The calculated VBS functions in the Zajac case show what would be expected intuitively: a VBS represents a parameter's mean influence averaged over its range of values. Additionally, we plotted the sum of all first order sensitivities. This sum indicates which amount of the total variance is covered by first order sensitivities. The closer the sum to 1 the smaller the impact of the second and higher order sensitivities.

The right hand side of Figure 4 shows the TSI functions of every parameter in  $\Lambda_Z$  of Zajac's model. Generally, there are only minor deviations of the  $\text{TSI}_i$  functions from their counterparts  $\text{VBS}_i$ . That is, the influence of none of the parameters is significantly enhanced by an interdependent effect in combination with other parameters. According to both analyses, there are just four globally important parameters that govern the system's state throughout the whole examined solution space: the initial condition  $q_{Z,0}$  within a typical time horizon  $\tau$  after a step in  $\sigma$ , the new stimulation level  $\sigma$  determining activity after about  $\tau$ , the deactivation boost  $\beta$  with smaller impact than  $\sigma$ , and  $\tau$  determining the time horizon itself.

The left hand side of Figure 5 shows the VBS functions of every parameter in  $\Lambda_H$  of Hatze's model. Very similar to the Zajac case, the calculated VBS seemingly represent to a high degree a parameter's mean influence averaged over its range of values (compare Figure 3). As in the Zajac case, there are four globally important parameters, according to both VBS and TSI analyses. Compared to Zajac's model, the interdependent effect in combination with other parameters (TSI: right hand side of Figure 5) is more pronounced for two parameters: both the stimulation  $\sigma$  and the CE length  $\ell_{\text{CE}}$  importance are distinctly higher than their first order

effects as expressed by VBS functions. Furthermore, the time horizon within the initial condition  $q_{H,0}$  has an aftereffect in response to a step in  $\sigma$  globally a little higher in VBS as compared to local sensitivity analysis (Figure 3). In addition, the time horizon of  $q_{H,0}$  is clearly enhanced by interdependencies with other parameters (TSI: right hand side of Figure 5).

Altogether, VBS versus TSI analysis substantiate local first and second order sensitivity analyses: for one thing, Hatze's model is more inert against steps in stimulation than Zajac's model. For another thing, the dynamics described by Hatze's model incorporates stronger nonlinear coupling effects from combinations of parameters than Zajac's model. These latter effects are better seen in detail when looking at local sensitivities, that is, analysing just small and selected volumes of the parameter space  $\mathcal{C}$ . In turn, VBS and TSI provide a broad but coarse overview about first and higher order sensitivities of all parameters.

## 7. Consequences, Discussion, and Conclusions

**7.1. A Bottom Line for Comparing Zajac's and Hatze's Activation Dynamics: Second Order Sensitivities.** At first sight, Zajac's activation dynamics [5] is more transparent because it is descriptive in a sense that it captures the physiological behaviour of activity rise and fall in an apparently simple way. It thereto utilises a linear differential equation with well-known properties, allowing for a closed-form solution. It needs only four parameters to describe the  $\text{Ca}^{2+}$ -ion influx to the muscle as a response to electrical stimulation: the stimulation  $\sigma$  itself as a control parameter, the time constant  $\tau$  for an exponential response to a step increase in stimulation, a third parameter  $\beta$  (deactivation boost) biasing both the rise and fall times, and the saturation value  $q_{Z,0}^{\infty}$  of activity which in turn depends on  $\sigma$  and the basic activity  $q_0$  being the fourth parameter. The smaller the  $\beta < 1$  is (deactivation slower than activation), the faster the very activity level  $q_{Z,0}^{\infty} = q_0 + \sigma \cdot (1 - q_0)$  is reached, at which saturation would occur for  $\beta = 1$ . Saturation for  $\beta < 1$  occurs at a level  $q_{Z,0}^{\infty} = q_0 + (1 - q_0) / (1 - \beta + \beta/\sigma)$  that is higher than  $q_{Z,0}^{\infty}|_{\beta=1}$ . Altogether, in Zajac's as compared to Hatze's activation dynamics, the outcome of setting a control parameter value  $\sigma$ , with regard to how fast and at which level the activity saturates, seems easier to be handled by a controller.

A worse controllability of Hatze's activation dynamics [6] may be expected from its nonlinearity, a higher number of parameters, and their interdependent influence on model dynamics. Additionally, Hatze's formulation depends on the CE length  $\ell_{\text{CE}}$ , which makes the mutual coupling of activation with contraction dynamics more interwoven. So, at first sight, Hatze's dynamics seems a less manageable construct for a

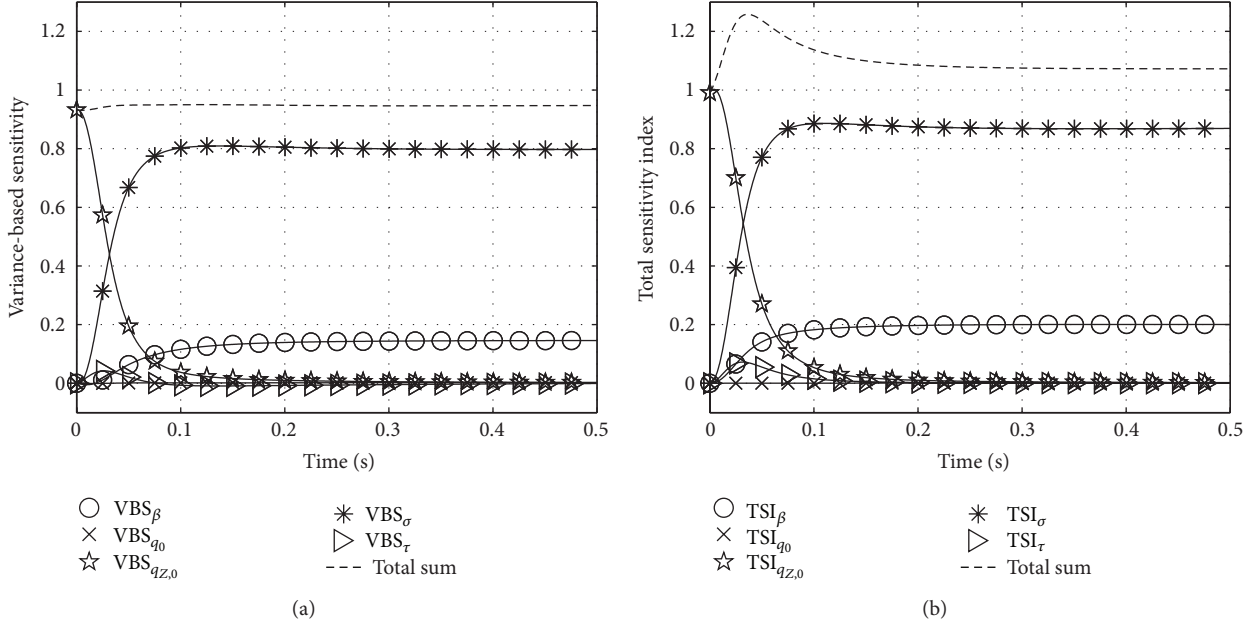


FIGURE 4: Variance-based sensitivity (a) and total sensitivity index (b) of every parameter of Zajac's activation dynamics equation.

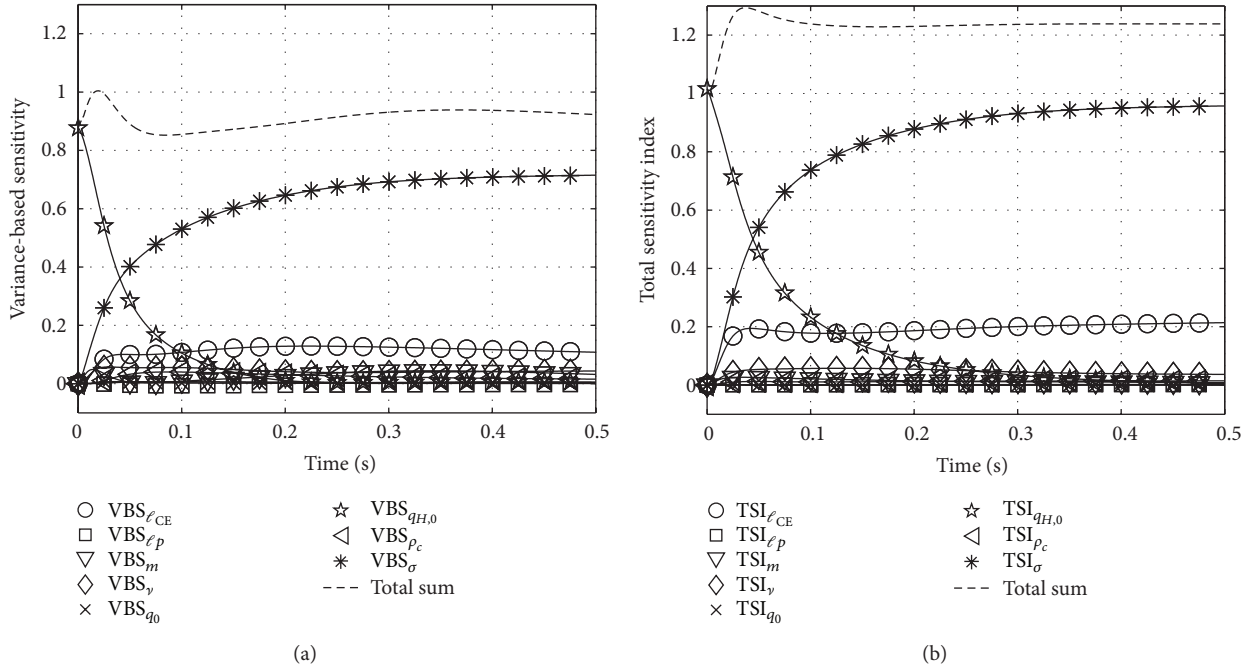


FIGURE 5: Variance-based sensitivity (a) and total sensitivity index (b) of every parameter of Hatze's activation dynamics equation.

controller to deal with a muscle as the biological actuator. Regarding the nonlinearity exponent  $\nu$ , solution sensitivity further depends nonmonotonously on activity level, partly even with the strongest influence, partly without any influence. We also found that the solution is more sensitive to its parameters  $\sigma$ ,  $\ell_{CErel}$ , and  $\ell_P$  than is Zajac's activation dynamics to any of its parameters.

This higher complexity of Hatze's dynamics becomes even more evident by analysing the second order sensitivities (see (13) or (19) for their relative values). They express how a first order sensitivity changes upon variation of any other model parameter. In other words, they are a measure of model entanglement and complexity. Here, we found that the highest values amongst all relative second order sensitivities

in Zajac's activation dynamics are about  $-0.8$  ( $\tilde{R}_{\beta\sigma}$ ) and  $1.6$  ( $\tilde{R}_{\beta\beta}$ ). In Hatze's activation dynamics, the highest relative second order sensitivities are those with respect to  $\nu$  or  $\ell_{\text{CErel}}$  (in particular for  $\sigma$ ,  $\rho_c$ , and  $\nu$ ,  $\ell_{\text{CErel}}$  themselves) with maximum values between about  $-8.0$  ( $\tilde{R}_{\ell_{\text{CErel}}\nu}$ ,  $\tilde{R}_{\nu\rho_c}$ ) and  $13.4$  ( $\tilde{R}_{\ell_{\text{CErel}}\ell_{\text{CErel}}}$ ,  $\tilde{R}_{\ell_{\text{CErel}}\rho_c}$ ,  $\tilde{R}_{\ell_{\text{CErel}}\sigma}$ ,  $\tilde{R}_{\nu\nu}$  at submaximal activity). That is, they are an order of magnitude higher than in Zajac's activation dynamics.

Yet, we have to acknowledge that Hatze's activation dynamics contains crucial physiological features that go beyond Zajac's description.

**7.2. A Plus for Hatze's Approach: Length Dependency.** It has been established that the length dependency of activation dynamics is both physiological [7] and functionally vital [15] because it largely contributes to low-frequency muscle stiffness. It has also been verified that Hatze's model approach provides a good approximation for experimental data [7]. In that study,  $\nu = 3$  was used without comparing to the  $\nu = 2$  case. There seem to be arguments in favour of  $\nu = 2$  from a mathematical point of view. In particular, the less changeable scaling of the activation dynamics' characteristics down to very low activity and stimulation levels, at which some CE length sensitivity remains, seem to be an advantage when compared to the  $\nu = 3$  case. Up to this point, we have argued solely mathematically. It is, however, physiological reality that is eventually aimed at. We therefore repeated the model fit done by Kistemaker et al. [7] while now allowing a variation in  $\nu$  and in force-length relations.

**7.3. An Optimal Parameter Set for Hatze's Activation Dynamics Plus CE Force-Length Relation.** Sensitivity analysis allows rating Hatze's approach as an entangled construct. Additionally, Kistemaker et al. [7] decided to choose  $\nu = 3$  without giving a reason for discarding  $\nu = 2$ . It further seemed that they did not perform an algorithmic optimisation across various submaximal stimulation levels to find a muscle parameter set, which best fits known shifts  $\Delta\ell_{\text{CE, opt, submax}} = \ell_{\text{CE, opt}} - \ell_{\text{CE, opt, submax}}$  in optimal, submaximal CE length  $\ell_{\text{CE, opt, submax}}$  at which isometric force  $F_{\text{isom}} = F_{\text{isom}}(q, \ell_{\text{CE}})$  peaks. Accordingly, it seemed worth performing such an optimisation because  $F_{\text{isom}}$  generally depends on length  $\ell_{\text{CE}}$  and activity  $q$ , and the latter may be additionally biased by an  $\ell_{\text{CE}}$ -dependent capability for building up cross-bridges at a given level  $\gamma$  of free  $\text{Ca}^{2+}$ -ions in the sarcoplasm, as formulated in Hatze's approach:  $F_{\text{isom}}(q, \ell_{\text{CE}}) = F_{\text{max}} \cdot q(\gamma, \ell_{\text{CE}}) \cdot F_{\ell}(\ell_{\text{CE}})$ . Thus, a shift in optimal CE length  $\Delta\ell_{\text{CE, opt, submax}}$  with changing  $\gamma$  can occur depending on the specific choices of both the length dependency of activation  $q(\gamma, \ell_{\text{CE}})$  (see (3) and (4)) and the CE's force-length relation  $F_{\ell}(\ell_{\text{CE}})$ .

Consequently, we searched for optimal parameter sets of Hatze's activation dynamics in combination with two different force-length relations  $F_{\ell}(\ell_{\text{CE}})$ : either a parabola [7] or bell-shaped curves [11, 25]. For a given optimal CE length  $\ell_{\text{CE, opt}} = 14.8$  mm [26] representing a rat gastrocnemius muscle and three fixed exponent values  $\nu = 2, 3, 4$  in Hatze's activation dynamics (all other parameters as given in Section 2), we thus determined Hatze's constant  $\rho_0$  and the

width parameters of the two different force-length relations  $F_{\ell}(\ell_{\text{CE}})$  (WIDTH in Kistemaker et al. [7] and van Soest and Bobbert [9] and  $\Delta W_{\text{asc}} = \Delta W_{\text{des}} = \Delta W$  in Mörl et al. [25], resp.) by an optimisation approach. The objective function to be minimised was the sum of squared differences between the  $\Delta\ell_{\text{CE, opt, submax}}$  values as predicted by the model and as derived from experiments (see Table 2 in Kistemaker et al. [7]) over five stimulation levels  $\sigma = 0.55, 0.28, 0.22, 0.17, 0.08$ . Note that  $\gamma = \sigma$  applies in the isometric situation (see (2) and compare (3)). Further note that experimental data for muscle contractions at very low stimulation levels are missing in the literature so far: the lowest analysed level available for Kistemaker et al. [7] was  $\sigma = 0.08$ , that is, comparable to the second rows from top in Figures 2 and 3.

The optimisation results are summarised in Table 2. The higher the  $\nu$  value, the smaller the optimisation error. The predicted width values WIDTH or  $\Delta W$ , respectively, decrease along with the error. We would yet tend to exclude the case  $\nu = 4$  because the predicted width values seem unrealistically low when compared to published values from other sources (e.g., WIDTH = 0.56 [9],  $\Delta W = 0.35$  [25]). Furthermore,  $\rho_0$  decreases with  $\nu$  using the parabola model for  $F_{\ell}(\ell_{\text{CE}})$  whereas it saturates between  $\nu = 3$  and  $\nu = 4$  for the bell-shaped model. The bell-shaped model shows the most realistic  $\Delta W$  in the case  $\nu = 3$  ( $\Delta W = 0.32$ ). Fitting the same model to other contraction modes of the muscle [25], a value of  $\Delta W = 0.32$  had been found. In contrast, when using the parabola model, realistic WIDTH values between 0.5 and 0.6 are predicted by our optimisation for  $\nu = 2$ .

When comparing the optimised parameter values across all start values of the  $F_{\ell}(\ell_{\text{CE}})$  widths, across all  $\nu$  values, and across both  $F_{\ell}(\ell_{\text{CE}})$  model functions, we find that the resulting optimal parameter sets are more consistent for bell-shaped  $F_{\ell}(\ell_{\text{CE}})$  than for the parabola function. The bell-shaped force-length relation gives generally a better fit. For each single  $\nu$  value, the corresponding optimisation error is smaller when comparing realistic, published WIDTH and  $\Delta W$  values that may correspond to each other (WIDTH = 0.56 [9] and  $\Delta W = 0.35$  [25]). Additionally, the error values from our optimisation are generally smaller than the corresponding value calculated from Table 2 in Kistemaker et al. [7] (0.23 mm).

In a nutshell, we would say that the most realistic model for the isometric force  $F_{\text{isom}}$  at submaximal activity levels is the combination of Hatze's approach for activation dynamics with  $\nu = 3$  and a bell-shaped curve for the force-length relation  $F_{\ell}(\ell_{\text{CE}})$  with  $\nu_{\text{asc}} = 3$ . As a side effect, we predict that the parameter value  $\rho_0$ , being a weighting factor of the first addend in the compact formulation of Hatze's activation dynamics (5), should be reduced by about 40% ( $\rho_0 = 3.25 \cdot 10^4$  L/mol) as compared to the value originally published in Hatze [13] ( $\rho_0 = 5.27 \cdot 10^4$  L/mol).

**7.4. A Generalised Method for Calculating Parameter Sensitivities.** The findings in the last section were initiated by thoroughly comparing two different biomechanical models of muscular activation using a systematic sensitivity analysis as introduced in Dickinson and Gelinas [17] and Lehman and

TABLE 2: Parameters minimising the sum over five submaximal stimulation levels  $\gamma = \sigma = 0.55, 0.28, 0.22, 0.17, 0.08$  of squared differences between shifts in optimal CE length  $\Delta \ell_{\text{CE,opt,submax}}(\gamma)$  ( $\Delta l_{\text{MA,opt}}$  by Roszek et al. (1994) [27] in the third column of Table 2 in Kistemaker et al. [7]) at these levels predicted by the model with the isometric force  $F_{\text{isom}}(q, \ell_{\text{CE}}) = F_{\text{max}} \cdot q(\gamma = \sigma, \ell_{\text{CE}}) \cdot F_{\ell}(\ell_{\text{CE}})$  and by experiments; simulated data represent a rat gastrocnemius muscle with an optimal CE length  $\ell_{\text{CE,opt}} = 14.8$  mm [26]; start value of  $\rho_0$  was  $6.0 \cdot 10^4$  L/mol; the exponents of the bell-shaped force-length relations  $F_{\ell}(\ell_{\text{CE}})$  were fixed according to Mörl et al. [25] ( $\gamma_{\text{asc}} = 3, \gamma_{\text{des}} = 1.5$ ); the corresponding width values in the ascending and descending branch were assumed to be equal:  $\Delta W_{\text{asc}} = \Delta W_{\text{des}} = \Delta W$ ; van Soest and Bobbert [9] and Kistemaker et al. [7] used a parabola for  $F_{\ell}(\ell_{\text{CE}})$ ; for all other model parameters see Sections 7.3 and 2; optimisation was done by *fminsearch* (Nelder-Mead algorithm) in MATLAB with error tolerances of  $10^{-8}$ ; *error* is the square root of the above-mentioned sum divided by five; corresponding error value given in Table 2 in Kistemaker et al. [7] was 0.23 mm.

$\gamma$	Bell-shaped [11, 25]			Parabola [7, 9]		
	$\Delta W$ []	$\rho_0$ [ $10^4$ L/mol]	<i>error</i> [mm]	WIDTH []	$\rho_0$ [ $10^4$ L/mol]	<i>error</i> [mm]
	$\Delta W_{\text{start}} = 0.25$			WIDTH <sub>start</sub> = 0.46		
2	0.46	3.80	0.08	0.63	8.78	0.10
3	0.32	3.25	0.05	0.41	5.45	0.07
4	0.26	3.20	0.02	0.34	4.60	0.05
	$\Delta W_{\text{start}} = 0.35$			WIDTH <sub>start</sub> = 0.56		
2	0.45	3.80	0.07	0.53	6.92	0.11
3	0.32	3.30	0.05	0.41	5.67	0.07
4	0.26	3.20	0.02	0.34	4.55	0.05
	$\Delta W_{\text{start}} = 0.45$			WIDTH <sub>start</sub> = 0.66		
2	0.45	3.78	0.07	0.55	7.35	0.11
3	0.32	3.25	0.05	0.41	5.35	0.07
4	0.26	3.20	0.02	0.34	4.56	0.05

Stark [2], respectively. Starting with the latter formulation, Scovil and Ronsky [1] calculated specific parameter sensitivities for muscular contractions. They applied three variants of this method.

Method 1 applies to state variables that are explicitly known to the modeller as in, for example, an eye model [2], a musculoskeletal model for running that includes a Hill-type muscle model [1], or the activation models analysed in our study. Scovil and Ronsky [1] calculated the change in the value of a state variable averaged over time per a finite change in a parameter value, both normalised to each of their unperturbed values. They thus calculated just one (mean) sensitivity value for a finite time interval (e.g., a running cycle) rather than time-continuous sensitivity functions.

Method 2: whereas Dickinson and Gelinas [17] and Lehman and Stark [2] had introduced the full approach for calculating such sensitivity functions, Scovil and Ronsky [1] distorted this approach by suggesting that the partial derivative of the right hand side of an ODE, that is, of the *rate of change* of a state variable, with respect to a model parameter would be a “model sensitivity.” The distortion becomes explicitly obvious from our formulation: this partial derivative is just one of the two addends that contribute to the rate of change of the sensitivity function (10), rather than defining the sensitivity of the state variable itself (i.e., the solution of the ODE) with respect to a model parameter (8).

Method 3: Scovil and Ronsky [1] had also asked for calculating the influence of, for example, a parameter of the activation dynamics (like the time constant) on an arbitrary joint angle, that is, a variable that quantifies the overall output

of a coupled dynamical system. Of course, the time constant does not explicitly appear in the mechanical differential equation for the acceleration of this very joint angle, which renders applicability of method 2 impossible. The conclusion in Scovil and Ronsky [1] was to apply method 1. Here, the potential of our formulation comes particularly to the fore. It enables calculating the time-continuous sensitivity of all components of the coupled solution, that is, any state variable  $y_k(t)$ . This is because all effects of a parameter change are in principle reflected within *any* single state variable, and the time evolution of a sensitivity according to (10) takes this into account.

In this paper, we have further worked out the sensitivity function approach by Lehman and Stark [2], presenting the differential equations for sensitivity functions in more detail to those modellers who want to apply the method. Furthermore, we enhanced the approach by Lehman and Stark [2] to also calculating the sensitivities of the state variables with respect to their initial conditions (17). This should be helpful not only in biomechanics but also, for example, in meteorology when predicting the behaviour of storms [28]. Since initial conditions are often just known approximately but start with the relative sensitivity values of 1, their influence should be traced to verify how their uncertainty propagates during a simulation. In the case of muscle activation dynamics, the sensitivities  $\tilde{S}_{q_{z,0}}$  and  $\tilde{S}_{q_{H,0}}$ , respectively, decreased rapidly to zero: initial activity has no effect on the solution very early before steady state is reached.

Furthermore, we included a second order sensitivity analysis which is not only helpful for an enhanced understanding

of the parameter influence but also part of mathematical optimisation techniques [29]. The values of  $\bar{R}_{ijk}$  could be interpreted either as the relative sensitivity of the sensitivity  $\bar{S}_{ik}$  with respect to another parameter  $\lambda_j$  (and vice versa:  $\bar{S}_{jk}$  with respect to  $\lambda_i$ ) or as the curvature of the graph of the solution  $y_k(t)$  in the  $N + M$ -dimensional solution-parameter space. The latter may help to connect the results to the field of mathematical optimisation in which the second derivative (Hessian) of a function is often included in objective functions to find optimal parameter sets.

**7.5. Insights into Global Methods.** Some additional conclusions can be drawn from global sensitivity analysis, in particular from comparing results in Section 6.3 to those based on local sensitivity analysis (Sections 6.1, 6.2, and 7.1).

For Zajac's activation dynamics, global analysis confirms local analysis in stating that there are no significant second or higher order sensitivities, with the slight exception of the phase of rapid change in activity after a step in stimulation. An experimenter who wants to measure the activation time constant  $\tau$  can exclude influence from potentially slower deactivation processes ( $\beta < 1$ ) by starting from high activity levels (Figure 2, bottom). It should yet be kept in mind that build-up of activity to the new level is not solely determined by  $\tau$  but might be biased by other parameters than  $\tau$  because  $\text{TSI}_\tau$  peaks during the build-up phase (Figure 4, right).

In Hatze's activation dynamics, the higher order sensitivities play a clearly more significant role, even in the near-steady-state case (Figure 5: stronger deviation from 1 of both VBS and TSI). When arguing in terms of controllability of the models in Section 7.1, we speculated that Zajac's dynamics might be easier to control than Hatze's dynamics. Notwithstanding, Figure 5 shows that the stimulation is the most important control factor with even a higher importance than in Zajac's formulation.

At first sight unapparent, another result is the importance of  $\rho_c$ . From a strictly local point of view we concluded that this parameter should have the same sensitivity as  $\sigma$  since they both are formally equivalent multipliers in Hatze's ODE (see relative sensitivities in Figure 3). However, the importance of  $\rho_c$  is significantly smaller than that of  $\sigma$ , in fact almost negligible. Their different global variabilities of values can give an explanation. The parameter  $\rho_c$  in the product  $\rho_c \cdot \sigma \in [4; 11] \times [0; 1]$  has a clearly lower relative variability than  $\sigma$ , measured in maximum percentage deviation from the respective mean value. The parameter  $\rho_c$  thus acts as an amplifier for  $\sigma$ . Similarly, the parameter  $\nu$  has a relatively small variability throughout the literature. So, although its differential sensitivity is quite large,  $\nu$  is found to have a low importance for the model output. For the latter fact there is yet another reason. In Section 6.2, we have emphasised that  $\nu$  has a very changeful influence on solutions, depending on activity level. Additionally, its influence is highly dependent on other parameters like length  $\ell_{\text{CE}}$  and  $\rho_c$  (see end of Section 7.1). Its strong influence in some situations and configurations is thus hidden by global averaging.

This demonstrates that the findings of global sensitivity analysis must be treated with caution because the whole

dynamics of a system is condensed to a single average function per whole parameter range. Without local analyses of the solution space as exemplified in Sections 6.1 and 6.2 crucial features of its topology might be lost when solely relying on global analysis.

## Symbols

$\ell_{\text{CE}}$ :	Contractile element (CE) length; value: time-dependent
$\dot{\ell}_{\text{CE}}$ :	Contraction velocity; value: first time derivative of $\ell_{\text{CE}}$
$\ell_{\text{CE,opt}}$ :	Optimal CE length; value: muscle-specific
$\ell_{\text{CErel}}$ :	Relative CE length; value: $\ell_{\text{CErel}} = \ell_{\text{CE}}/\ell_{\text{CE,opt}}$ (dimensionless)
$F_{\text{max}}$ :	Maximum isometric force of the CE; value: muscle-specific
$\sigma$ :	Neural muscle stimulation; value: time-dependent; here: a fixed parameter
$q$ :	Muscle activity (bound $\text{Ca}^{2+}$ -concentration); value: time-dependent
$q_0$ :	Basic activity according to Hatze [13]; value: 0.005
$q_H$ :	Activity according to Hatze [6]; value: time-length-dependent
$q_{H,0}$ :	Initial condition for Hatze's activation ODE; value: mutable
$q_Z$ :	Activity according to Zajac [5]; value: time-dependent
$q_{Z,0}$ :	Initial condition for Zajac's activation ODE; value: mutable
$\tau$ :	Activation time constant in Zajac [5]; value: here: 1/40 s
$\tau_{\text{deact}}$ :	Deactivation time constant in Zajac [5]; value: here: 1/40 s or 3/40 s
$\beta$ :	Corresponding deactivation boost [5]; value: $\beta = \tau/\tau_{\text{deact}}$
$\nu$ :	Exponent in Hatze's formulation; value: 2 or 3
$m$ :	Activation frequency constant in Hatze [6]; value: range: 3.67, ..., 11.25 (1/s); here: 10 (1/s)
$c$ :	Maximal $\text{Ca}^{2+}$ -concentration in Hatze [24]; value: $1.37 \cdot 10^{-4}$ mol/L
$\gamma$ :	Representation of free $\text{Ca}^{2+}$ -concentration [6, 13]; value: time-dependent
$\rho$ :	Length dependency of Hatze [24] activation dynamics; value: $\rho(\ell_{\text{CErel}}) = \rho_c \cdot ((\ell_\rho - 1)/(\ell_\rho/\ell_{\text{CErel}} - 1))$
$\ell_\rho$ :	Pole in Hatze's length dependency function; value: 2.9
$\rho_0$ :	Factor in van Soest [8], Hatze [6]; value: $6.62 \cdot 10^4$ L/mol ( $\nu = 2$ ) or $5.27 \cdot 10^4$ L/mol ( $\nu = 3$ )
$\rho_c$ :	Merging of $\rho_0$ and $c$ ; value: $\rho_c = \rho_0 \cdot c$ ; here: 9.10 ( $\nu = 2$ ) or 7.24 ( $\nu = 3$ )
$\Lambda$ :	Model parameter set; value: $\Lambda = \{\lambda_1, \dots, \lambda_n\}$ .

## Conflict of Interests

The authors declare that there is no conflict of interests regarding the publication of this paper.

## Acknowledgments

Michael Günther was supported by “Berufsgenossenschaft Nahrungsmittel und Gastgewerbe, Geschäftsbereich Prävention, Mannheim” (BGN) and Deutsche Forschungsgemeinschaft (DFG: SCHM2392/5-1), both granted to Syn Schmitt.

## References

- [1] C. Y. Scovil and J. L. Ronsky, “Sensitivity of a Hill-based muscle model to perturbations in model parameters,” *Journal of Biomechanics*, vol. 39, no. 11, pp. 2055–2063, 2006.
- [2] S. L. Lehman and L. W. Stark, “Three algorithms for interpreting models consisting of ordinary differential equations: sensitivity coefficients, sensitivity functions, global optimization,” *Mathematical Biosciences*, vol. 62, no. 1, pp. 107–122, 1982.
- [3] K. Chan, A. Saltelli, and S. Tarantola, “Sensitivity analysis of model output: variance-based methods make the difference,” in *Proceedings of the 29th Conference on Winter Simulation (WSC ’97)*, S. Andradóttir, K. Healy, D. Withers, and B. Nelson, Eds., pp. 261–268, IEEE Computer Society, Washington, DC, USA, 1997.
- [4] A. Saltelli and K. S. E. Chan, *Sensitivity Analysis*, John Wiley & Sons, New York, NY, USA, 1st edition, 2000.
- [5] F. E. Zajac, “Muscle and tendon: properties, models, scaling, and application to biomechanics and motor control,” *Critical Reviews in Biomedical Engineering*, vol. 17, no. 4, pp. 359–411, 1989.
- [6] H. Hatze, “A myocybernetic control model of skeletal muscle,” *Biological Cybernetics*, vol. 25, no. 2, pp. 103–119, 1977.
- [7] D. A. Kistemaker, A. J. van Soest, and M. F. Bobbert, “Length-dependent  $[Ca^{2+}]$  sensitivity adds stiffness to muscle,” *Journal of Biomechanics*, vol. 38, no. 9, pp. 1816–1821, 2005.
- [8] A. van Soest, *Jumping from structure to control: a simulation study of explosive movements [Ph.D. thesis]*, Vrije Universiteit, Amsterdam, The Netherlands, 1992.
- [9] A. J. van Soest and M. F. Bobbert, “The contribution of muscle properties in the control of explosive movements,” *Biological Cybernetics*, vol. 69, no. 3, pp. 195–204, 1993.
- [10] G. Cole, A. van den Bogert, A. W. Herzog, and K. Gerritsen, “Modelling of force production in skeletal muscle undergoing stretch,” *Journal of Biomechanics*, vol. 29, pp. 1091–1104, 1996.
- [11] M. Günther, S. Schmitt, and V. Wank, “High-frequency oscillations as a consequence of neglected serial damping in Hill-type muscle models,” *Biological Cybernetics*, vol. 97, no. 1, pp. 63–79, 2007.
- [12] D. F. B. Haeufle, M. Günther, A. Bayer, and S. Schmitt, “Hill-type muscle model with serial damping and eccentric force-velocity relation,” *Journal of Biomechanics*, vol. 47, no. 6, pp. 1531–1536, 2014.
- [13] H. Hatze, *Myocybernetic Control Models of Skeletal Muscle*, University of South Africa, 1981.
- [14] D. A. Kistemaker, A. J. van Soest, and M. F. Bobbert, “Is equilibrium point control feasible for fast goal-directed single-joint movements?” *Journal of Neurophysiology*, vol. 95, no. 5, pp. 2898–2912, 2006.
- [15] D. A. Kistemaker, A. J. van Soest, and M. F. Bobbert, “A model of open-loop control of equilibrium position and stiffness of the human elbow joint,” *Biological Cybernetics*, vol. 96, no. 3, pp. 341–350, 2007.
- [16] R. T. M. Vukobratovic, *General Sensitivity Theory*, Elsevier, New York, NY, USA, 1962.
- [17] R. P. Dickinson and R. J. Gelinas, “Sensitivity analysis of ordinary differential equation systems—a direct method,” *Journal of Computational Physics*, vol. 21, no. 2, pp. 123–143, 1976.
- [18] H. ZivariPiran, *Efficient simulation, accurate sensitivity analysis and reliable parameter estimation for delay differential equations [Ph.D. thesis]*, University of Toronto, Toronto, Canada, 2009.
- [19] B. W. Bader and T. G. Kolda, “Algorithm 862: matlab tensor classes for fast algorithm prototyping,” *ACM Transactions on Mathematical Software*, vol. 32, no. 4, pp. 635–653, 2006.
- [20] O. Scherzer, *Mathematische Modellierung—Vorlesungsskript*, Universität Wien, 2009.
- [21] A. Saltelli and P. Annoni, “How to avoid a perfunctory sensitivity analysis,” *Environmental Modelling and Software*, vol. 25, no. 12, pp. 1508–1517, 2010.
- [22] H. C. Frey, A. Mokhtari, and T. Danish, “Evaluation of selected sensitivity analysis methods based upon application to two food safety process risk models,” Tech. Rep., Computational Laboratory for Energy, North Carolina State University, 2003.
- [23] H. Benker, *Differentialgleichungen mit MATHCAD und MATLAB*, vol. 1, Springer, Berlin, Germany, 2005.
- [24] H. Hatze, “A general myocybernetic control model of skeletal muscle,” *Biological Cybernetics*, vol. 28, no. 3, pp. 143–157, 1978.
- [25] F. Mörl, T. Siebert, S. Schmitt, R. Blickhan, and M. Günther, “Electro-mechanical delay in hill-type muscle models,” *Journal of Mechanics in Medicine and Biology*, vol. 12, no. 5, Article ID 1250085, 2012.
- [26] T. Siebert, O. Till, and R. Blickhan, “Work partitioning of transversally loaded muscle: experimentation and simulation,” *Computer Methods in Biomechanics and Biomedical Engineering*, vol. 17, no. 3, pp. 217–229, 2014.
- [27] B. Roszek, G. C. Baan, and P. A. Huijing, “Decreasing stimulation frequency-dependent length-force characteristics of rat muscle,” *Journal of Applied Physiology*, vol. 77, no. 5, pp. 2115–2124, 1994.
- [28] R. H. Langland, M. A. Shapiro, and R. Gelaro, “Initial condition sensitivity and error growth in forecasts of the 25 January 2000 east coast snowstorm,” *Monthly Weather Review*, vol. 130, no. 4, pp. 957–974, 2002.
- [29] M. Sunar and A. D. Belegundu, “Trust region methods for structural optimization using exact second order sensitivity,” *International Journal for Numerical Methods in Engineering*, vol. 32, no. 2, pp. 275–293, 1991.

## Research Article

# Bone Mineral Density and Fracture Risk Assessment to Optimize Prosthesis Selection in Total Hip Replacement

Pröstur Pétursson,<sup>1</sup> Kyle Joseph Edmunds,<sup>1</sup> Magnús Kjartan Gíslason,<sup>1</sup>  
Benedikt Magnússon,<sup>1</sup> Gígja Magnúsdóttir,<sup>2</sup> Grétar Halldórsson,<sup>2</sup>  
Halldór Jónsson Jr.,<sup>1,3,4</sup> and Paolo Gargiulo<sup>1,5</sup>

<sup>1</sup>*Institute for Biomedical and Neural Engineering, Háskólinn í Reykjavík, Menntavegur 1, 101 Reykjavík, Iceland*

<sup>2</sup>*Department of Rehabilitation, Landspítali, Norðurmýri, 101 Reykjavík, Iceland*

<sup>3</sup>*Orthopaedic Clinic, Landspítali Hospital, Norðurmýri, 101 Reykjavík, Iceland*

<sup>4</sup>*Medical Faculty, Háskóli Íslands, Sæmundargötu 2, 101 Reykjavík, Iceland*

<sup>5</sup>*Department of Science, Landspítali University Hospital, Norðurmýri, 101 Reykjavík, Iceland*

Correspondence should be addressed to Paolo Gargiulo; [paologar@landspitali.is](mailto:paologar@landspitali.is)

Received 17 December 2014; Revised 3 March 2015; Accepted 5 March 2015

Academic Editor: Zhonghua Sun

Copyright © 2015 Pröstur Pétursson et al. This is an open access article distributed under the Creative Commons Attribution License, which permits unrestricted use, distribution, and reproduction in any medium, provided the original work is properly cited.

The variability in patient outcome and propensity for surgical complications in total hip replacement (THR) necessitates the development of a comprehensive, quantitative methodology for prescribing the optimal type of prosthetic stem: cemented or cementless. The objective of the research presented herein was to describe a novel approach to this problem as a first step towards creating a patient-specific, presurgical application for determining the optimal prosthesis procedure. Finite element analysis (FEA) and bone mineral density (BMD) calculations were performed with ten voluntary primary THR patients to estimate the status of their operative femurs before surgery. A compilation model of the press-fitting procedure was generated to define a fracture risk index (FRI) from incurred forces on the periprosthetic femoral head. Comparing these values to patient age, sex, and gender elicited a high degree of variability between patients grouped by implant procedure, reinforcing the notion that age and gender alone are poor indicators for prescribing prosthesis type. Additionally, correlating FRI and BMD measurements indicated that at least two of the ten patients may have received nonideal implants. This investigation highlights the utility of our model as a foundation for presurgical software applications to assist orthopedic surgeons with selecting THR prostheses.

## 1. Introduction

Total hip replacement (THR) is one of the most globally-utilized and successful orthopaedic procedures. THR aims to restore hip function and relieve patients of pain by replacing damaged hip joints with artificial ones. THR prostheses fixation is typically classified by two general methods: with and without using acrylic bone cement. In cemented THR, the stem is fixed with bone cement, but the cementless procedure relies on extant tensile properties of the femoral head as the method of securing prosthesis stability. The use of cementless fixation is the preferable procedure for two main reasons: firstly, eventually all THR prostheses will fail and require revision or replacement surgery, a phenomenon

that usually occurs more than 10 years after operation. Although loosening of the stem is the typical cause for this periprosthetic failure, cementless stems mechanotransductively induce bone ingrowth and perform better in the long term, compared to cemented prostheses that typically fail earlier due to cement degradation [1–4]. Secondly, when revision surgery does eventually occur, cementless stems are more easily removed and result in fewer surgical complications, which mainly arise from residual cemented bone being removed by cement extraction from the femoral canal [5–8]. Furthermore, when the cemented stem starts to show signs of loosening, migration of the stem within the canal leads to smoothening of the endosteal surface which can make subsequent fixation very difficult [9]. Despite the preferred

avoidance of cementation, orthopedic surgeons must often prescribe cemented THR to patients whose femurs may not be capable of withstanding the tensile forces in press-fitting insertion of a cementless stem; if the periprosthetic bone is not strong enough, in-surgery femoral fracture can occur, introducing a very serious complication.

The hip is a load bearing joint, constantly subjected to high loads which lead to the gradual degradation of articular surfaces. Over time, this degradation (arthrosis) can cause functional impairment and pain. With increasing life expectancies in many populations worldwide, THR rates have increased considerably over the last few decades and are projected to continue to increase in the future [10].

Currently, there is no reliable method for quantitatively choosing between the cemented and cementless implant procedures in THR, despite the prevalence of periprosthetic fracture and unloading events in many THR patients. In most cases, it is still the respective opinion of the physicians involved that dictates this decision, an opinion typically founded upon both the surgeon's own experiences and qualitative generalizations based on possible indicators of bone quality (gender, age, and qualitative assessment of CT images). In general, there is a great need for a robust, quantitative method to securely choose the appropriate implant on an individual patient basis.

Many finite element studies on total hip replacement focus on the boundaries between the femoral bone, the cement, and the stem as well as the remodeling procedures of the bone due to changes in localized stresses within the tissue. The focus of this study was to evaluate the preoperative status of the bone by introducing a novel method for fracture risk index (FRI) computation and comparing this assessment to CT-based measurements of patient bone mineral density (BMD). The reported model relies on computer tomography (CT) images to build 3D models of the femur and perform localized finite element analyses (FEA). Likewise, femoral BMD is calculated on the proximal femur as an additional metric for quantitative assessment. This method provides a patient-specific estimation of the risk of preoperative fracture, which may be utilized by an orthopedic surgeon as a tool for THR surgical planning. The work flow for this study can be seen in Figure 1. Optimizing the preoperative planning can increase the overall success of THR surgeries and have a profoundly beneficial impact on both patient mobility and lessening the economic burden of revision surgeries within many healthcare systems.

## 2. Material and Methods

**2.1. Patient Recruitment.** Ten patients were voluntarily enrolled in the study (eight females and two males). Of these patients, five patients received cementless implants, while five received cemented implants. The implant type was decided according to the evaluation of the surgeons, qualitatively based on age, sex, and general physical condition, as typically assessed before surgery. The average age at the time of operation was  $61.4 \pm 10.1$  years for all patients. Ages averaged  $63.5 \pm 17.7$  years for males and  $54.5 \pm 18.9$  years for females,

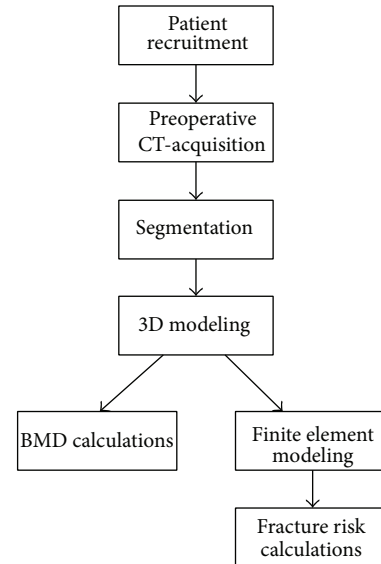


FIGURE 1: Study workflow.



FIGURE 2: CT scanning protocol range on the femoral head.

and when grouped according to implant procedure, average ages were  $55.0 \pm 9.5$  years for cementless and  $67.8 \pm 5.8$  years for cemented. Patients with total knee implants, previous hip implants, or those who received implants during this research period were excluded from the study.

**2.2. CT Acquisition.** All participants in the project were scanned with a 64 Philips Brilliance spiral-CT machine. Scanning occurred at three time points: immediately before surgery and 24 hours and 52 weeks after surgery. For the purpose of this study, only preoperative and 24-hour postoperative data were used. The scanning region extended from the iliac crest to the middle of the femur (Figure 2). The image protocol included slice thicknesses of 1 mm, with slice increments of 0.5 mm and the tube intensity set to 120 keV.

Prior to the study, the CT scanner was calibrated using a Quasar phantom to acquire the relationship between HU and BMD, resulting in the relationship given by

$$\text{BMD} \left[ \frac{\text{g}}{\text{cm}^3} \right] = (0.00036) \text{HU} + 0.56736. \quad (1)$$

Linear regression analysis of this calibration resulted in a correlation coefficient  $R^2 \sim 0.99$ .

**2.3. Segmentation and Finite Element Modeling.** In order to assemble the 3D models of each patient's femur for FEA analysis, each patient's preoperative CT scan was imported into MIMICS Software (Materialise, Belgium) where femoral contour segmentation was carried out. A solid 3D model was calculated based on these contours. Next, the femoral head was virtually cut, similarly to a typical THR surgical procedure, using Boolean operators on the 3D model. Additionally, a virtual distal cut was performed orthogonal to the femur's long axis. The final model can be seen in Figure 2.

Using the finite element module of MIMICS, known as 3-Matic, the model was divided into quadnode tetrahedral elements. Each model consisted of 130,000 to 170,000 of these elements, with overall element densities of around two elements per  $\text{mm}^3$ . Young's modulus and Poisson's ratio were then assigned to each element. Fifty different values of Young's modulus were assigned to the elements of each model, while the Poisson's ratio was considered a constant value of 0.33. Furthermore, these elements were considered to be isotropic. The aforementioned calibration equation was used to convert HU to BMD and (2) was used to convert BMD to Young's modulus [11]:

$$E = 10500 \cdot \rho_{\text{ash}}^{2.29}, \quad (2)$$

where  $\rho_{\text{ash}}$  is the bone mineral density obtained from (1). This formula was used to represent both trabecular and cortical bones. In Figure 3, a FE model of a respective femur can be seen, following the addition of material properties.

**2.4. Fracture Risk Index Computation.** In order to compute the FRI of each femur, each FEA model, complete with requisite material properties, was imported into Ansys Mechanical APDL v.14.0 (©ANSYS, Inc.). There, a static structural simulation and analysis were performed on the model. The objective of this simulation was to simulate the forces introduced on the femur during the press-fitting surgery in cementless THR. In this procedure, when the stem is pushed into the medullary canal, the highest tensile stresses can be expected to arise at the medial and lateral sides of the periprosthetic end of the femur. This is due to the fact that the flare of the stem is the steepest at the top. Therefore, as boundary conditions, two equal but opposite forces were applied in these areas. In a study by Sakai et al. the average measured hammering force for uncemented prosthesis was estimated to be 9.25 kN [12]. Since the forces in cemented prosthesis are considerably lower, our model utilized this force value as a worst-case-scenario to discern whether any of the ten patients could have withstood the cementless method (Figure 4).

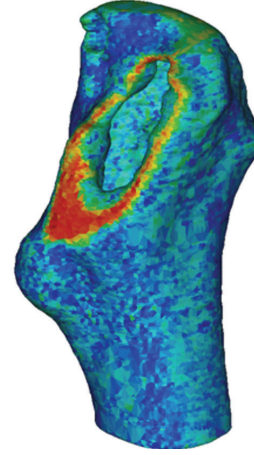


FIGURE 3: A finite element model of the femur consisting of more than 100,000 elements. The elements are given material properties, namely, Poisson's ratio and Young's modulus. Red colours indicate higher density bone.

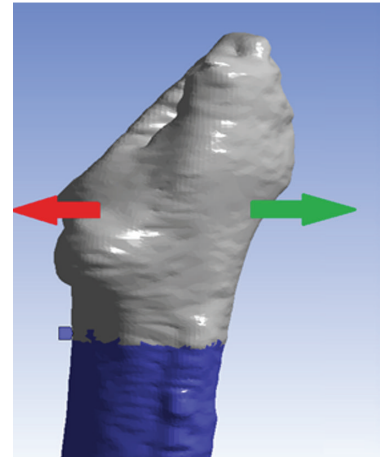


FIGURE 4: The 9.25 kN cementless prosthesis forces applied on the model where the highest stress can be expected during the press-fitting of the tapered stem.

To determine the FRI for each model, the stress value of every element was compared to its calculated ultimate tensile strength (UTS). The ultimate tensile strength was calculated with a relationship given by Bessho et al. ((3) and (4)) [13]:

$$\text{UTS} = 137 \cdot \text{BMD}^{1.88} \quad \text{for BMD} < 0.317, \quad (3)$$

$$\text{UTS} = 114 \cdot \text{BMD}^{1.72} \quad \text{for BMD} \geq 0.317. \quad (4)$$

The average stress experienced by each element was calculated by averaging the stress values at each node point. The fracture risk was calculated based on the preoperative scan, simulating for all the patients the uncemented fixation (press-fitting procedure) independent from surgeon's decision on

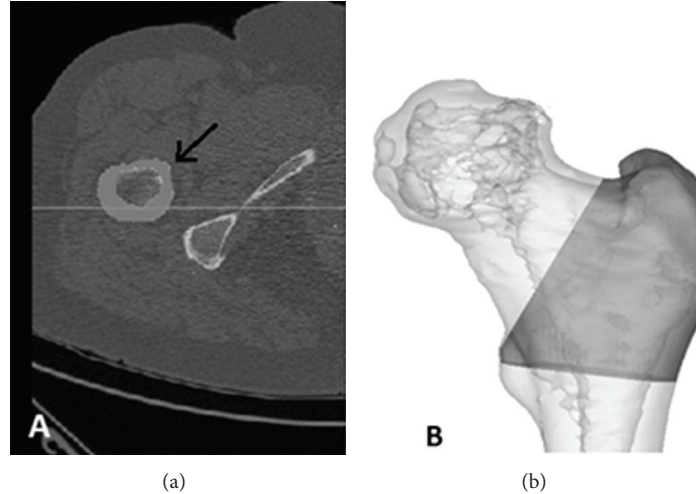


FIGURE 5: (a) Axial view of one slice of the CT-data from a patient. The arrow points to the area belonging to the mask. (b) The 3D view of the region of interest for BMD calculations.

the implant type. The fracture risk index was calculated for each element using [14]

$$\text{FRI} (\%) = \frac{\text{stress}}{\text{UTS}} \cdot 100\%. \quad (5)$$

**2.5. Bone Mineral Density Computation.** A model of the BMD region of interest was created in MIMICS, ranging from the periprosthetic femur, without the femoral head, to the greater trochanter, with a distal axial cut through the lesser trochanter (Figure 5). The study focused on the structural aspects of the cortical bone, since the structural integrity of the cancellous bone is compromised after operation. The horizontal line in Figure 5 demonstrates the cuts made above and below the area of interest. From this region, the HU values were extracted and converted to BMD using (1).

### 3. Results

Firstly, the FRI was calculated for ten patients, applying the uncemented loading condition for all subjects independent of the surgeon's decision. From the cohort five patients received a cemented implant and five an uncemented implant. The highest stresses on the models were usually experienced in the calcar femoral on the medial side of the femur and at a similar location on the lateral side.

In Figure 6, the von Mises stress in every element of each model is plotted against BMD. The black-crossed line represents the ultimate stress as a function of BMD, as stated in (3). Should the calculated stress values exceed the UTS, then the element would be considered fractured, which can be seen as a dark color in the figure.

Figure 6 depicts the position-independent von Mises stresses of all elements against their respective BMD values. To better visualize where the highest risk of fracture was experienced, these elements were also plotted in 3D. A typical result from the 3D plotted fracture risk index can be seen in

Figure 7. The red-colored elements are those that exceeded their fracture threshold.

In Table 1, the average fracture risk is calculated for the ten patients (five with cemented THR and five with cementless), as well as the ratio of those elements that exceeded 80% of their ultimate stress value.

For the five cementless patients, the average age was  $55 \pm 9.5$  years, the average percent of fractured elements was  $7.16 \pm 6.13\%$ , and the average BMD was  $1.10 \pm 0.03 \text{ g/cm}^2$ . For the five cemented patients, the average age was  $67.80 \pm 5.85$  years, the average percent of fractured elements was  $4.54 \pm 2.29\%$ , and the average BMD was  $1.122 \pm 0.06 \text{ g/cm}^2$ . These values in relation to patient age and sex can be seen in Figure 8.

## 4. Discussion and Conclusions

The most important criterion when choosing the type of implant for patients undergoing THR is bone quality. If the bone is of good quality, the cementless implantation method generally results in fewer patient complications and generally more delayed revision surgeries, compared to cemented THR. Since bone quality tends to decline with age and is usually lower in women than men, younger and/or male patients usually receive cementless implants, while older and/or female patients receive cemented ones. Although age and gender are somewhat reliable indicators of femoral bone quality, individual differences can be vast. The reported results highlight these differences and suggest the importance of developing a novel, quantitative approach to assessing patients' femoral heads before THR surgery [15, 16].

**4.1. Bone Mineral Density as a Potential Computational Tool in THR.** The notion that patient variation in bone quality as a function of age and sex is especially evident from the BMD measurements presented herein, where several patients received cemented prostheses despite having relatively higher BMD than patients who were given the cementless type. This

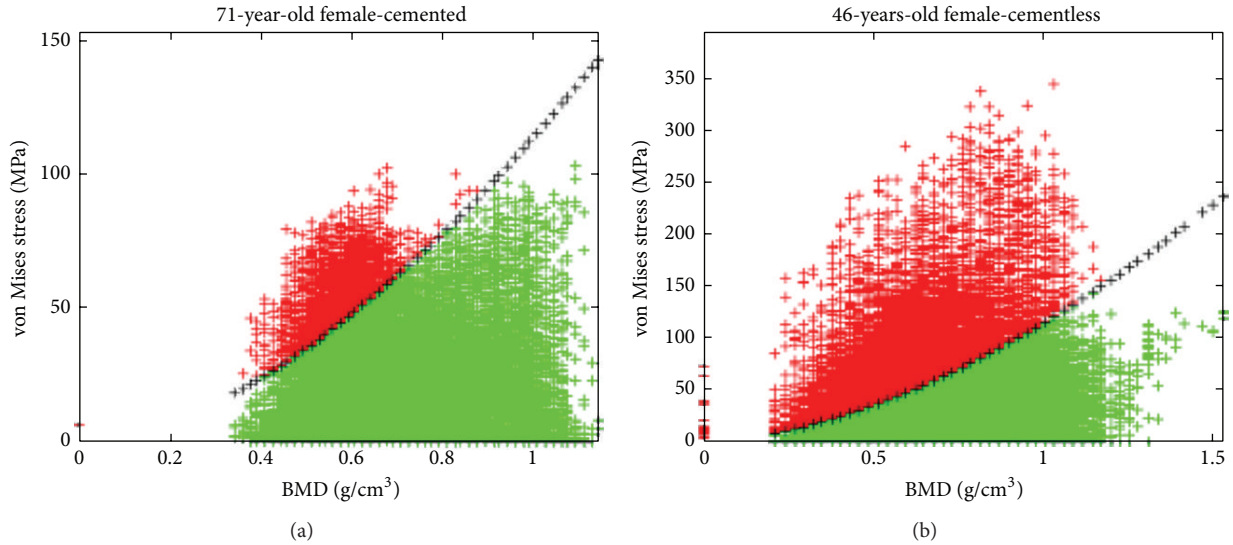


FIGURE 6: Examples of calculated FRI from (a) a 71-year-old female patient and (b) a 46-year-old female. Note that every element of the model has been plotted with von Mises stress as a function of bone mineral density. The black crossed line indicates element strength given by (3), and elements are considered failed if they surpass this line in stress. Subject B actually experienced femoral fracture due to the periprosthetic implant some days after the surgery.

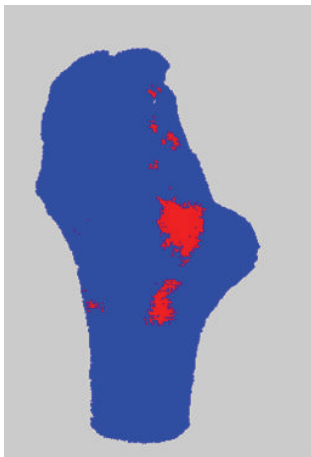


FIGURE 7: Elements plotted in their three-dimensional coordinates. Note that red elements were those that exceeded the acceptable limit for von Mises stress, indicating regions of most probable periprosthetic fracture.

decision was clearly based primarily on the patients' age, as the average age of cemented patients was much higher than those of cementless patients ( $67.8 \pm 5.8$  compared to  $55.0 \pm 9.5$ , resp.). Indeed, the patient with the highest BMD measurements was not only female but also the second oldest within the assessed population. This most likely justified her receiving a cemented implant, although our model suggests that she certainly may have withstood a press-fitting with a low risk of periprosthetic fracture. Additionally, our results indicate that BMD measurements may correlate inversely, to some degree, with the percentage of fractured elements computed by our FEA simulation. This is evident, as higher BMD

values indicate better bone quality and thereby a reduced chance of each element exceeding its fracture threshold. However, to determine if this relationship is indeed true, more patients would need to be assessed in a larger study. In general, the use of BMD as a metric in this investigation serves as an important first step in developing a quantitative method for computing bone quality at the moment of surgery, which may serve as a future tool for orthopedic surgeons to predict the ability for patient's femurs to handle the stresses in press-fitting a cementless THR prosthesis.

#### 4.2. Fracture Risk as a Potential Computational Tool in THR.

The calculated FRI for the 10 subjects additionally showed high degrees of variation between patients according to both their sex and age. Most importantly, our model shows that two of the five cementless patients had higher fracture risks than all of the five cemented patients, despite them being younger than four of the cemented patients. It is additionally critical to note that the 46-year-old female, cementless patient experienced a periprosthetic femoral fracture immediately after the surgery, which correlated with both the considerably higher fracture risk and lower BMD discerned from our computational model (Figures 8(a) and 8(b), resp.). However, with a larger population size for the reported assessment, it may be reasonably expected that a majority of younger patients, who typically receive cementless implants, would have lower risks of fracture and higher BMD than those of older patients. However, the reported results show again that patient age is not necessarily an adequate indicator of either fracture risk or bone quality; thus, implementing the computational technique that this paper introduces might serve as a better preoperative tool for orthopedic surgeons to dictate the optimal THR procedure.

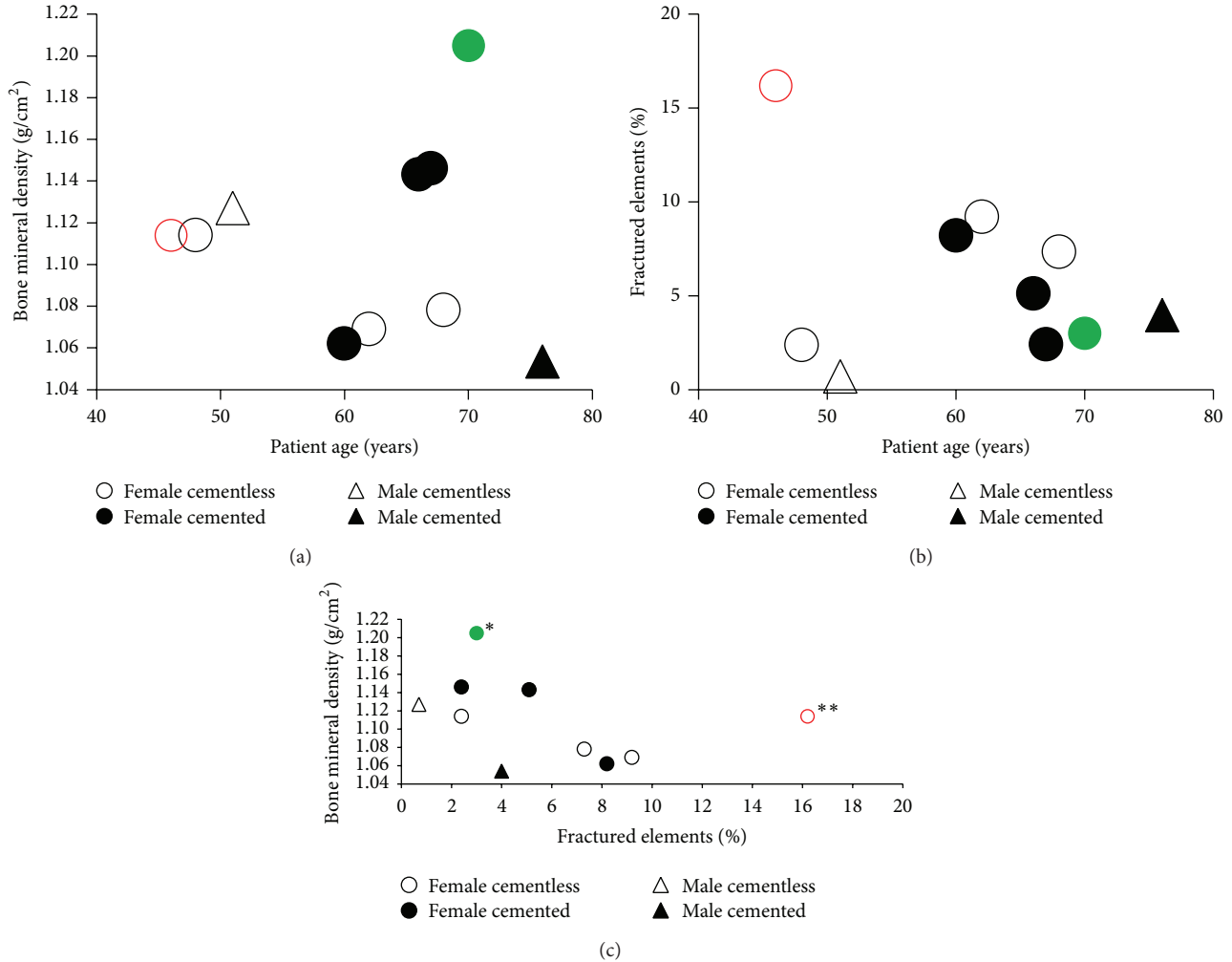


FIGURE 8: Results from FRI and BMD assessment for each patient grouped by sex and prosthesis type. (a) BMD versus patient age, (b) percent fractured elements versus patient age, and (c) BMD versus percent of fractured elements. Note that the female patients in green (\*) and red (\*\*) received nonoptimal cemented and cementless prostheses, respectively, according to our computational assessment. Furthermore, it should be noted that the red patient suffered a periprosthetic fracture during surgery, an event that could possibly have been predicted by the above results.

TABLE 1: FRI and BMD results from the ten cemented and cementless THR subjects.

Age	Sex	Cementless THR procedure		Age	Sex	Cemented THR procedure	
		% of elements >fracture threshold	BMD [g/cm <sup>2</sup> ]			% of elements >fracture threshold	BMD [g/cm <sup>2</sup> ]
51	M	0.7%	1.127	76	M	4.0%	1.054
48	F	2.4%	1.114	70	F	3.0%	1.205
46	F	16.2%	1.114	66	F	5.1%	1.143
68	F	7.3%	1.078	60	F	8.2%	1.062
62	F	9.2%	1.069	67	F	2.4%	1.146

**4.3. Limitations and Future Directions.** As previously mentioned, the purpose of this study was to investigate whether a novel FEA simulation of press-fitting could generate a potentially useful tool for assessing patient fracture risk indices, in combination with CT-based BMD measurement. Our results do indeed highlight the potential of this methodology and furthermore suggest the inadequacy of patient age and sex

in dictating the risk of periprosthetic fracture. However, a larger patient population is requisite to rigorously show the statistical dependency of FRI on measured BMR and to define limits that correlate to additional, real cases of patient periprosthetic fracture. In addition, there are some limitations of the reported FEA and FRI computations. The greatest of these is that the simulations carried out were

steady-state and did not take into consideration applied loads that are time-dependent or the prosthetic design and surface finish. The real forces induced by a surgical hammer during the surgery are high-impact and punctate forces or forces acting on the bone over a short period of time. This can instigate the development of microfissures in the periprosthetic region of the femur, leading to fractures in more extreme cases.

Overall, this study proposes a novel approach to the predictive simulation and computation of BMD and FRI during insertion of a cementless THR prosthesis. A large part of the novelty of this work lies in the fact that the bone quality was discerned at the time of surgery rather than long after surgery, incorporating both bone mineral density averages and fracture risk indices in the periprosthetic region of the femur. This real-time surgical evaluation could serve as the basis for the development of software applications that orthopedic surgeons may use to discern which prosthesis fitting procedure may be optimal for each patient on an individual basis. Such a tool could have a profound impact on THR surgical planning and serve as a model for future surgical planning software. However, the development of a patient database with which such tools may operate would require more patient data than what was acquired for the purpose of the reported work. Additionally, a more robust model would include variations in stem designs, such as material roughness, tapering degree, cross-sectional area, and coating thickness. Incorporating materials data could provide additional details regarding shear forces applied to the bone as a result of prosthetic friction, in addition to the radial forces presented herein. Nevertheless, our results highlight the feasibility of the methodology used and can be utilized as a foundation to develop a clinical database for correlating BMD and FRI to THR patient outcomes. As an eventual software application for orthopedic surgeons, our combinatory approach of CT-based BMD measurement and FEA-based assessment of femoral fracture risk could serve as a pivotal tool in the decision making process before total hip replacement. Optimizing the preoperative planning can increase the overall success of THR surgeries and have a profoundly beneficial impact on both patient mobility and overall surgical outcome, which could significantly aid in lessening the economic burden from revision surgeries upon many healthcare systems worldwide.

### Conflict of Interests

The authors declare that there is no conflict of interests regarding the publication of this paper.

### Acknowledgments

This work has been supported by funds from the National University Hospital of Iceland. This work was supported by the Icelandic Research Fund “Rannis” and by the Landspítali University Hospital Research Fund.

### References

- [1] C. A. Engh, J. D. Bobyn, and A. H. Glassman, “Porous-coated hip replacement. The factors governing bone ingrowth, stress shielding, and clinical results,” *The Journal of Bone & Joint Surgery—British Volume*, vol. 69, no. 1, pp. 45–55, 1987.
- [2] L. A. Müller, N. Wenger, M. Schramm, D. Hohmann, R. Forst, and H.-D. Carl, “Seventeen-year survival of the cementless CLS Spotorno stem,” *Archives of Orthopaedic and Trauma Surgery*, vol. 130, no. 2, pp. 269–275, 2010.
- [3] J. R. McLaughlin and K. R. Lee, “Total hip arthroplasty with an uncemented tapered femoral component,” *The Journal of Bone & Joint Surgery—American Volume*, vol. 90, no. 6, pp. 1290–1296, 2008.
- [4] *European Instructional Lectures*, Springer, New York, NY, USA, 2013.
- [5] C. A. Engh, A. H. Glassman, W. L. Griffin, and J. G. Mayer, “Results of cementless revision for failed cemented total hip arthroplasty,” *Clinical Orthopaedics and Related Research*, no. 235, pp. 91–110, 1988.
- [6] D. J. Engelbrecht, F. A. Weber, M. B. E. Sweet, and I. Jakim, “Long term results of revision total hip arthroplasty,” *The Journal of Bone & Joint Surgery—British Volume*, vol. 72, no. 1, pp. 41–45, 1990.
- [7] J. M. Lawrence, C. A. Engh, G. E. Macalino, and G. R. Lauro, “Outcome of revision hip arthroplasty done without cement,” *Journal of Bone and Joint Surgery—Series A*, vol. 76, no. 7, pp. 965–973, 1994.
- [8] J. R. Moreland and M. L. Bernstein, “Femoral revision hip arthroplasty with uncemented, porous-coated stems,” *Clinical Orthopaedics and Related Research*, no. 319, pp. 141–150, 1995.
- [9] R. K. Sinha, “Revision of the femoral component,” in *Hip Replacement: Current Trends and Controversies*, R. K. Sinha, Ed., Marcel Dekker, New York, NY, USA, 2002.
- [10] J. A. Singh, “Epidemiology of knee and hip arthroplasty: a systematic review,” *The Open Orthopaedics Journal*, vol. 5, no. 1, pp. 80–85, 2011.
- [11] T. S. Keller, “Predicting the compressive mechanical behavior of bone,” *Journal of Biomechanics*, vol. 27, no. 9, pp. 1159–1168, 1994.
- [12] R. Sakai, A. Takahashi, N. Takahira et al., “Hammering force during cementless total hip arthroplasty and risk of microfracture,” *HIP International*, vol. 21, no. 3, pp. 330–335, 2011.
- [13] M. Bessho, I. Ohnishi, J. Matsuyama, T. Matsumoto, K. Imai, and K. Nakamura, “Prediction of strength and strain of the proximal femur by a CT-based finite element method,” *Journal of Biomechanics*, vol. 40, no. 8, pp. 1745–1753, 2007.
- [14] M. K. Gislason, S. Coupaud, K. Sasagawa et al., “Prediction of risk of fracture in the tibia due to altered bone mineral density distribution resulting from disuse: a finite element study,” *Proceedings of the Institution of Mechanical Engineers Part H: Journal of Engineering in Medicine*, vol. 228, no. 2, pp. 165–174, 2014.
- [15] P. Gargiulo, T. Pétursson, B. Magnússon et al., “Assessment of total hip arthroplasty by means of computed tomography 3D models and fracture risk evaluation,” *Artificial Organs*, vol. 37, no. 6, pp. 567–573, 2013.
- [16] B. Magnússon, Þ. Pétursson, K. Edmunds et al., “Improving planning and post-operative assessment for total hip arthroplasty,” *European Journal of Translational Myology—Basic Applied Myology*, vol. 25, no. 2, pp. 101–108, 2015.

## Research Article

# Assessment of Knee Cartilage Stress Distribution and Deformation Using Motion Capture System and Wearable Sensors for Force Ratio Detection

N. Mijailovic,<sup>1</sup> R. Vulovic,<sup>1,2</sup> I. Milankovic,<sup>1,2</sup> R. Radakovic,<sup>2</sup> N. Filipovic,<sup>1,2</sup> and A. Peulic<sup>1</sup>

<sup>1</sup>Faculty of Engineering, University of Kragujevac, Sestre Janjic 6, 34000 Kragujevac, Serbia

<sup>2</sup>Bioengineering Research and Development Center Kragujevac, Prvoslava Stojanovica 6, 34000 Kragujevac, Serbia

Correspondence should be addressed to A. Peulic; [aleksandar.peulic@kg.ac.rs](mailto:aleksandar.peulic@kg.ac.rs)

Received 19 September 2014; Revised 19 December 2014; Accepted 16 January 2015

Academic Editor: Eduardo Soudah

Copyright © 2015 N. Mijailovic et al. This is an open access article distributed under the Creative Commons Attribution License, which permits unrestricted use, distribution, and reproduction in any medium, provided the original work is properly cited.

Knowledge about the knee cartilage deformation ratio as well as the knee cartilage stress distribution is of particular importance in clinical studies due to the fact that these represent some of the basic indicators of cartilage state and that they also provide information about joint cartilage wear so medical doctors can predict when it is necessary to perform surgery on a patient. In this research, we apply various kinds of sensors such as a system of infrared cameras and reflective markers, three-axis accelerometer, and force plate. The fluorescent marker and accelerometers are placed on the patient's hip, knee, and ankle, respectively. During a normal walk we are recording the space position of markers, acceleration, and ground reaction force by force plate. Measured data are included in the biomechanical model of the knee joint. Geometry for this model is defined from CT images. This model includes the impact of ground reaction forces, contact force between femur and tibia, patient body weight, ligaments, and muscle forces. The boundary conditions are created for the finite element method in order to noninvasively determine the cartilage stress distribution.

## 1. Introduction

Sports activities and daily routines such as standing, walking, running, jumping, and other recreational activities impose relatively large loads and movements on the human knee joint. These tasks could cause injuries and degenerations in the joint ligaments, menisci, cartilage, and bones. Thus, knowledge of in vivo joint motion and loading during functional activities is needed to improve our understanding of possible knee joint degeneration and restoration. Internal loadings of knee anatomical structures significantly depend on a lot of factors such as external loads, body weight, ligaments, strengths, and muscles forces.

In the paper [1] the knee implants were used to directly measure loads of participants during daily activities. In vivo knee measurements are very invasive and practically impossible for the case described in our study. There are many techniques for measuring an external variable which can

be further used to create biomechanical and mathematical models.

Other studies [2] were based on the registration of fluoroscopic images and computer model of the knee. The most recent method utilized force plate data, CT or MRI skeletal structure data, and motion capture obtained from the infrared position sensor [3, 4]. In another research paper [5] the accelerometer was used to estimate the angle of lower extremities. This is a pretty cheap technique but requires additional processing of collected data and the error of estimated angle is up to six percent. The measure performance can be improved using a combination of accelerometer and gyroscope sensor such as goniometer [6–8].

In the study [9] stress on the knee cartilage during kneeling and standing using finite element models is compared. They used magnetic resonance (MR) images of the flexed knee to build a geometrical model. As a computational tool they used commercial software MIMICS. The results

of those studies showed some differences in high-stress regions between kneeling and standing. The conclusion was that the peak von Mises stress and contact pressure on the cartilage were higher in kneeling. The study [10] used computed tomography (CT) images of knee structures during static loading to determine cartilage strains and meniscal movement in a human knee at different time periods of standing and to compare them with the subject-specific 3D finite element (FE) model. The results of these experiments showed that 80% of the maximum strain in cartilage developed immediately and after that cartilage continued to deform slowly. In the study [11] magnetic resonance (MR) images of the right knee of a 27-year-old male subject were used to determine the subsequent alteration in the fluid pressurization in the human knee using a three-dimensional computer model. The results of these studies indicated a redistribution of stresses within the tissue and a relocation of the loading between the tissue matrix and fluid pressure.

The purpose of this study was to estimate stress distribution in the knee cartilage. For that purpose the appropriate system of cameras and force plate platform were used. The deformation of cartilage was measured using marker position data and the 3D model of the lower leg segment. The models were established from computed tomography (CT) images. Simultaneously the deformation is assessed only matching single infrared camera images and CT image using software for image registration technique. In the experimental part the accelerometer sensor was used which potentially can provide more information about the gait. In the computer simulation the FEM analysis was applied with an adaptive change of mechanical parameters of tissue variation in order to match the measured force and deformation.

## 2. Materials and Methods

**2.1. Mechanical Model of the Knee Joint.** Knee joint motion represents a complex combination of rotations and translations. The major parts involved in the knee kinematical behavior include femur, tibia and patella. Forces that act at a knee joint are given in Figure 1.

The dominant forces that act at a knee joint are body weight and ground reaction force which are opposite to each other. Muscle forces as well as contact forces between femur and tibia are also included in the model. Equilibrium equations of the knee joint are given below [5]:

$$\begin{aligned}
 F_r + F_b + F_{p1} \cdot N_1 + F_{p2} \cdot N_2 + \sum_{i=1}^7 F_i &= 0, \\
 M_r + F_r \times P_r + F_b \times P_b + F_{p1} \cdot N_1 \times P_1 + F_{p2} \cdot N_2 \times P_2 \\
 + \sum_{i=1}^7 F_i \times V_i &= 0,
 \end{aligned} \tag{1}$$

where  $F_r$  is the ground reaction force,  $F_b$  is the body weight,  $F_{p1}$  and  $F_{p2}$  are the two contact point forces,  $N_1$  and  $N_2$  are the two contact points normal,  $F$  ( $i = 1 \dots 7$ ) are the ligament and capsule forces,  $M_r$  is the knee joint driver

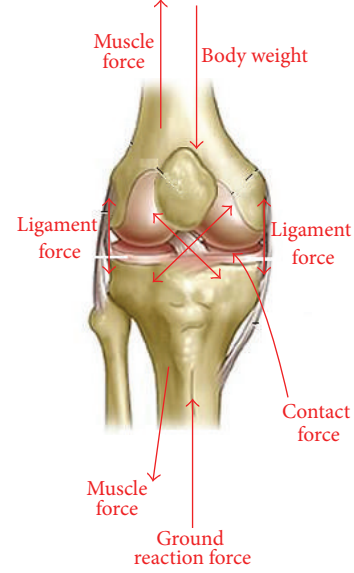


FIGURE 1: Forces on a knee joint.

moment along local  $z$  axis and  $P_r, P_b, P_1, P_2$  and  $V$  ( $i = 1 \dots 7$ ) are the position vectors where the corresponding forces are being applied [13]. We assumed that femur and tibia could be represented as rigid bodies and that their deformations were very small in contrast to relatively large deformations of cartilage and ligaments. Note that synovial fluid significantly reduces the friction between cartilage surfaces and menisci.

A simplified spring-damper-mass model which was used in this study is shown in Figure 2. It consists of four masses. The upper body was modeled using two masses, one representing its rigid mass,  $m_3$ , and the other representing its wobbling masses,  $m_4$ . The thigh, leg, and foot of the supporting leg were modeled using two masses, one representing its rigid mass,  $m_1$ , and the other representing its wobbling masses,  $m_2$ .

The total body mass was obtained from the participant. In the following system of equations (Equation (2)) a dynamics system is described [12] and was later used to calculate the resultant force and moment of the knee cartilage during the stance phase of the gait cycle:

$$\begin{aligned}
 m_1 \ddot{x}_1 + k_1 (x_1 - x_3) + k_2 (x_1 - x_2) + c_1 (\dot{x}_1 - \dot{x}_3) \\
 + c_2 (\dot{x}_1 - \dot{x}_2) &= m_1 g - F_g, \\
 m_2 \ddot{x}_2 - k_2 (x_1 - x_2) + k_3 (x_2 - x_3) \\
 + c_2 (\dot{x}_1 - \dot{x}_2) &= m_2 g, \\
 m_3 \ddot{x}_3 - k_1 (x_1 - x_3) - k_3 (x_2 - x_3) \\
 + (k_4 + k_5) (x_3 - x_4) - c_1 (\dot{x}_1 - \dot{x}_3) \\
 + c_4 (\dot{x}_3 - \dot{x}_4) &= m_3 g.
 \end{aligned} \tag{2}$$

In (2),  $m_1$  was the lower body rigid mass and  $m_2$  was the wobbling mass,  $m_3$  was the upper body rigid mass and  $m_4$  was the wobbling mass,  $k_1$  was the compressive spring and

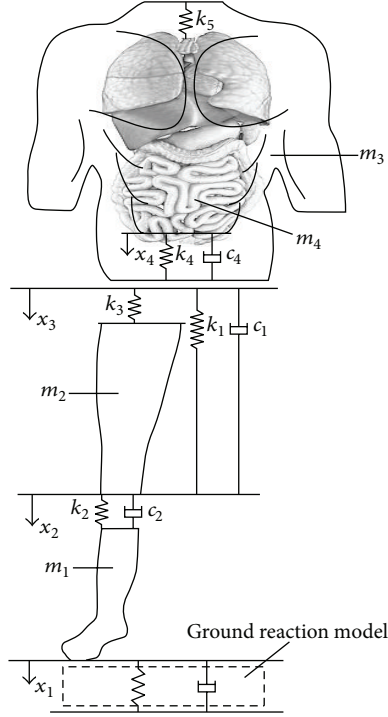


FIGURE 2: A simplified spring-damper-mass model used in the computer simulation. The components of the dynamics system presented are lower body rigid mass ( $m_1$ ) and wobbling mass ( $m_2$ ), upper body rigid mass ( $m_3$ ) and wobbling mass ( $m_4$ ), compressive spring ( $k_1$ ) and damper ( $c_1$ ) that connect the upper and lower rigid bodies, spring ( $k_2$ ) and spring/damper unit ( $k_2, c_2$ ) connecting the lower wobbling mass to the upper and lower rigid bodies, and spring ( $k_3$ ) and spring/damper unit ( $k_3, c_3$ ) connecting the lower wobbling mass to the upper and lower rigid bodies, and spring ( $k_4$ ) and spring/damper unit ( $k_4, c_4$ ) connecting the upper wobbling mass to the upper rigid mass (adopted from [12]).

$c_1$  was the damper that connected the upper and lower rigid bodies,  $k_3$  was the spring and  $k_2, c_2$  was the spring-damper unit which connected the lower wobbling mass to the upper and lower rigid bodies, and  $k_5$  was the spring and  $k_4, c_4$  was the spring damper unit which connected the upper wobbling mass to the upper rigid mass [12].  $F_g$  was the vertical contact force which was defined as

$$F_g = \begin{cases} A_c \cdot (ax_1^b + cx_1^d x_1^e) & x_1 > 0, \\ 0 & x_1 \leq 0. \end{cases} \quad (3)$$

$A_c$  is contact area and  $a, b, c, d$ , and  $e$  are the parameters of the ground reaction model which defined the deformation of the shoes during standing. Parameters for soft and hard shoes are shown in Table 1.

Cartilage was considered as a porous deformable body filled with fluid occupying the whole pore volume. The physical quantities for this analysis were the displacement of solid  $\mathbf{u}$ , relative fluid velocity with respect to the solid (Darcy's velocity)  $\mathbf{q}$ , fluid pressure  $\mathbf{p}$ , and electrical potential  $\phi$ . The governing equations for the coupled problem are described as follows. First, we considered the solid equilibrium equation:

$$(1-n)\mathbf{L}^T \boldsymbol{\sigma}_s + (1-n)\rho_s \mathbf{b} + \mathbf{k}^{-1} n \mathbf{q} - (1-n)\rho_s \ddot{\mathbf{u}} = 0, \quad (4)$$

TABLE 1: Parameter for ground reaction model.

	$a$	$b$	$c$	$d$	$e$
Soft shoe	$10^6$	1.56	$2 \times 10^4$	0.73	1.0
Hard shoe	$10^6$	1.38	$2 \times 10^4$	0.75	1.0

where  $\boldsymbol{\sigma}_s$  was the stress in the solid phase,  $n$  was porosity,  $\mathbf{k}$  was the permeability matrix,  $\rho_s$  was the density of the solid,  $\mathbf{b}$  was body force per unit mass,  $\mathbf{q}$  was relative velocity of the fluid, and  $\ddot{\mathbf{u}}$  was acceleration of the solid material. The operator  $\mathbf{L}^T$  was

$$\mathbf{L}^T = \begin{bmatrix} \frac{\partial}{\partial x_1} & 0 & 0 & \frac{\partial}{\partial x_2} & 0 & \frac{\partial}{\partial x_3} \\ 0 & \frac{\partial}{\partial x_2} & 0 & \frac{\partial}{\partial x_1} & \frac{\partial}{\partial x_3} & 0 \\ 0 & 0 & \frac{\partial}{\partial x_3} & 0 & \frac{\partial}{\partial x_2} & \frac{\partial}{\partial x_1} \end{bmatrix}. \quad (5)$$

The equilibrium equation of the fluid phase (no electrokinetic coupling) was

$$n \nabla \mathbf{p} + n \rho_f \mathbf{b} - \mathbf{k}^{-1} n \mathbf{q} - n \rho_f \dot{\mathbf{v}}_f = \mathbf{0}, \quad (6)$$

where  $\mathbf{p}$  was pore fluid pressure,  $\rho_f$  was fluid density, and was  $\dot{\mathbf{v}}_f$  fluid velocity. This equation is also known as the generalized Darcy's law. Both equilibrium equations were written per unit volume of the mixture. Combining (3) and (5) we obtain

$$\mathbf{L}^T \boldsymbol{\sigma} + \rho \mathbf{b} - \rho \ddot{\mathbf{u}} - \rho_f \dot{\mathbf{q}} = \mathbf{0}, \quad (7)$$

where  $\boldsymbol{\sigma}$  was the total stress which can be expressed in terms of  $\boldsymbol{\sigma}_s$  and  $\mathbf{p}$  as

$$\boldsymbol{\sigma} = (1-n)\boldsymbol{\sigma}_s - n \mathbf{m} \mathbf{p}, \quad (8)$$

and  $\rho = (1-n)\rho_s + n\rho_f$  was the mixture density.

Here  $\mathbf{m}$  was a constant vector defined as  $\mathbf{m}^T = \{1 \ 1 \ 1 \ 0 \ 0 \ 0\}$  to indicate that the pressure contributes to the normal stresses only. We also had to take into account the fact that the pressure has a positive sign in compression. Tensional stresses and strains were considered positive as well. In the following analysis we employed the effective stress,  $\boldsymbol{\sigma}'$ , defined as

$$\boldsymbol{\sigma}' = \boldsymbol{\sigma} + \mathbf{m} \mathbf{p}, \quad (9)$$

which was relevant for the constitutive relations of the solid. Using the definition of relative velocity  $\mathbf{q}$  as the volume of the fluid passing in a unit time through a unit area of the mixture (Darcy's velocity), we obtained

$$\mathbf{q} = n(\mathbf{v}_f - \dot{\mathbf{u}}) \quad (10)$$

and transformed (6) into

$$-\nabla \mathbf{p} + \rho_f \mathbf{b} - \mathbf{k}^{-1} \mathbf{q} - \rho_f \ddot{\mathbf{u}} - \frac{\rho_f}{n} \dot{\mathbf{q}} = \mathbf{0}. \quad (11)$$

The final continuity equation using the elastic constitutive law and fluid incompressibility was given in the form

$$\begin{aligned} \nabla^T \mathbf{q} + \left( \mathbf{m}^T - \frac{\mathbf{m}^T \mathbf{C}^E}{3K_s} \right) \dot{\mathbf{e}} \\ + \left( \frac{1-n}{K_s} + \frac{n}{K_f} - \frac{\mathbf{m}^T \mathbf{C}^E \mathbf{m}}{9K_s^2} \right) \dot{\mathbf{p}} = 0. \end{aligned} \quad (12)$$

The resulting FE system of equations was solved incrementally [14] with a time step  $\Delta t$ . We imposed the condition that the balance equations are satisfied at the end of each time step ( $t + \Delta t$ ). Hence, we derived the following system of equations:

$$\begin{aligned} \begin{bmatrix} \mathbf{m}_{uu} & 0 & 0 & 0 \\ 0 & 0 & 0 & 0 \\ \mathbf{m}_{qu} & 0 & 0 & 0 \\ 0 & 0 & 0 & 0 \end{bmatrix} \begin{Bmatrix} {}^{t+\Delta t} \underline{\dot{\mathbf{u}}} \\ {}^{t+\Delta t} \underline{\dot{\mathbf{p}}} \\ {}^{t+\Delta t} \underline{\dot{\mathbf{q}}} \\ {}^{t+\Delta t} \underline{\dot{\phi}} \end{Bmatrix} \\ + \begin{bmatrix} 0 & 0 & \mathbf{c}_{uq} & 0 \\ \mathbf{c}_{pu} & \mathbf{c}_{pp} & 0 & 0 \\ 0 & 0 & \mathbf{c}_{qq} & 0 \\ 0 & 0 & 0 & 0 \end{bmatrix} \begin{Bmatrix} {}^{t+\Delta t} \underline{\dot{\mathbf{u}}} \\ {}^{t+\Delta t} \underline{\dot{\mathbf{p}}} \\ {}^{t+\Delta t} \underline{\dot{\mathbf{q}}} \\ {}^{t+\Delta t} \underline{\dot{\phi}} \end{Bmatrix} \\ + \begin{bmatrix} \mathbf{k}_{uu} & \mathbf{k}_{up} & 0 & 0 \\ 0 & 0 & \mathbf{k}_{pq} & 0 \\ 0 & \mathbf{k}_{qp} & \mathbf{k}_{qq} & \mathbf{k}_{q\phi} \\ 0 & \mathbf{k}_{\phi p} & 0 & \mathbf{k}_{\phi\phi} \end{bmatrix} \begin{Bmatrix} \Delta \underline{\mathbf{u}} \\ \Delta \underline{\mathbf{p}} \\ \Delta \underline{\mathbf{q}} \\ \Delta \underline{\phi} \end{Bmatrix} = \begin{Bmatrix} {}^{t+\Delta t} F_u \\ {}^{t+\Delta t} F_p \\ {}^{t+\Delta t} F_q \\ {}^{t+\Delta t} F_\phi \end{Bmatrix}, \end{aligned} \quad (13)$$

where  $F_u, F_p, F_q$ , and  $F_\phi$  were forces in the balance equations for displacement, pressure, fluid velocity, and electrical potential, respectively, and  $\mathbf{m}_{uu}$  and  $\mathbf{m}_{qu}$  were mass terms in mass matrix [14].

**2.2. Experimental Parts.** In this study we used a commercial motion capture system OptiTrack. This system consists of six infrared cameras and four retroreflective markers. The markers are 1.5 cm in diameter and are attached at the precise anatomical locations of the participant's leg for unilateral gain analysis. These locations were great trochanter region, femoral lateral epicondyle, tuberosity of the tibia, and the center of the anterior region of ankle joint (see Figure 3).

The computerized camera system with accompanying software captures the exact motion of retroreflective markers and thus records their trajectory while the volunteer performs walking over the force plate. The cameras were connected to a computer that collects gait kinematical data. The result of motion tracking is a series of 3D coordinates for each numbered marker. To better understand kinematics and kinetics of gait we used a three-axial accelerometer.

We used Sun SPOT accelerometers (Sun Small Programmable Object Technology) to wirelessly detect the middle of the gait stance phase, that is, the moment when the ground reaction force reaches its maximum value. The Sun

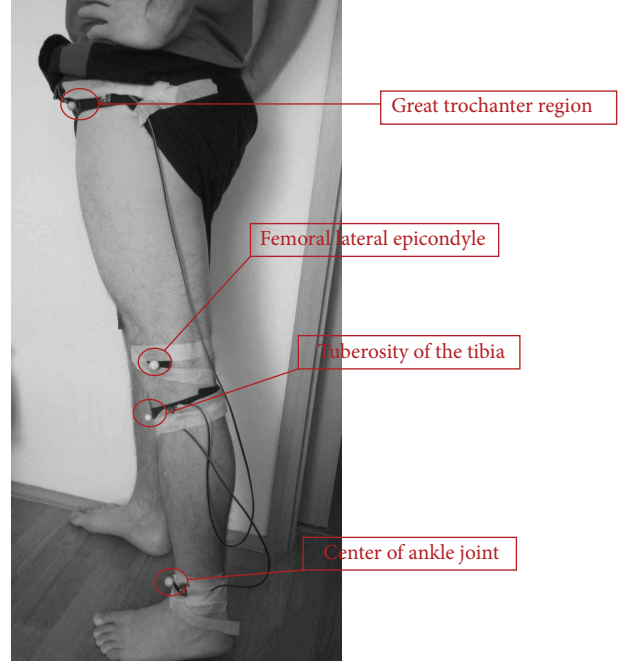


FIGURE 3: Reflective markers position on the examinee leg.

SPOT has a sensor board which consists of 2G/6G 3-axis accelerometer, temperature sensor, and light sensor. In the experimental part the Sun SPOT LIS3L02AQ accelerometer is used to measure the orientation or motion in three dimensions, X, Y, and Z with the sample rate of 100 Hz. Each of these components represents the sum of static accelerations defined by angle of inclination to the corresponding axis and dynamics component stemming from the movement during the walk. The ground reaction force was sampled from the multiaxis AMTI force plate at the rate of 100 Hz. Before the experiment, calibration was conducted to work out the space coordinate system for the camera system field of view. The calibration was performed fully in accordance with the proposed manufacturer's procedure.

The volunteer performs walking along 2.5 meter distance path away with his own ordinary velocity and attached infrared marker and accelerometers sensor on the left leg. Results for marker coordinates and corresponding accelerations, measured by the three-axial accelerometer, are presented in Figure 4.

According to [15–17] measured values for marker position are influenced by noise due to the wobbling of the participant's skin. The value of this uncertainty is in range  $\pm 2$  mm.

The force plate is positioned in the first half of the walking path. During the experiment, the participants were asked to walk along so the force plate records the value of the ground reaction force (Figure 5).

The force value is zero in the beginning of the walk and when the participant stands on the force plate, starting with the heel, the force gradually increases and reaches the maximum and then drops to zero again when the foot is detached by the force plate.

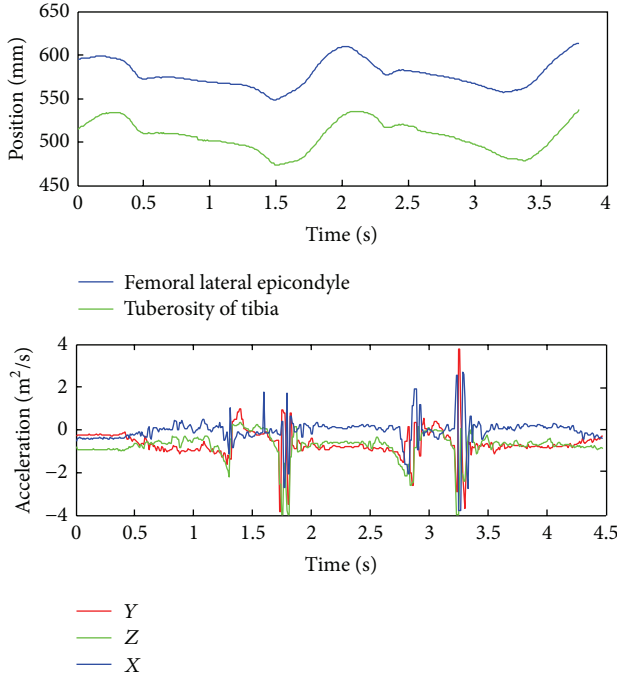


FIGURE 4: Position of reflective marker during walking and corresponding three-axial acceleration.

### 3. Results

One of the main tasks for preparing data for FEM simulation is matching the infrared reflective marker position obtained by infrared camera and landmark position on the CT images when cartilage is unreformed. This procedure is known as image registration and ANTs (Free software for image registration) is used [18].

Main goal of the registration process is obtained from the transformation parameter that maps the marker position in deformed and undeformed knee cartilage. In general this process is finding the optimal transformation that maps every pixel of image with the presence of deformation and another static image when cartilage is undeformed. As similarity measure of image the mutual information is used. The standard algorithm in registration process is elastic deformation procedure. The idea is to model the contours on one of the matching images as elastic object which deformed under the influence of some external forces [19]. In each step of the deformation the images are compared and value of external forces is now proportional to the difference between these cases on the basis of mutual information value. The process is repeated until the difference between the images is greater than some error of convergence. The result of registration between CT and infrared images is shown in Figure 6. The measured difference of the marker positions between deformed and undeformed cartilage is  $1.78 \pm 0.6$  mm. Images showing markers matching these cases are presented in Figures 6(a) and 6(c), respectively. The measured uncertainty of 0.06 mm corresponds to the dimension of a single pixel. The error in estimation of the deformation is significantly

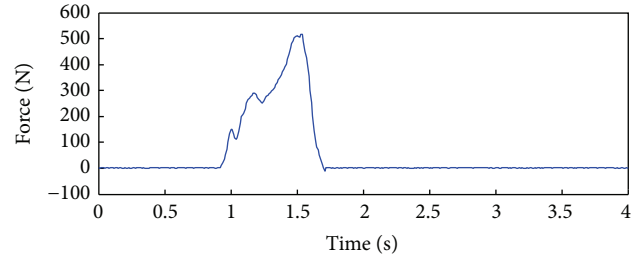


FIGURE 5: Ground reaction forces during standing on the force plate.

greater due to the influence of the distortion of the camera lens, skin movements, and insufficiently accurate registration result.

Simultaneously, we create a 3D model using CT slices. The CT slices are segmented using a threshold value and compared with gray value of the image pixel. The segmented images are submitted by the edge detection operator for boundary extraction. The merging of adjacent boundary is done in each slice and final 3D model is created (Figure 2). This model includes femur, tibia, cartilage, surrounding tissue, and skin.

The anatomical point (tuberosity of tibia and femoral lateral epicondyle) can be easily detected in the model and initial position of the marker can be obtained. Using the measured position of infrared marker (Figure 4) and anatomical position of the marked point on the created 3D model (Figure 7(c)) we can obtain a vertical deformation of cartilage as difference of these values. The observed measured value coincides with the point when the ground reaction force is in the maximum. According to Figure 5 this moment is 1.49 seconds after starting the recording of gait and the deformation is  $2.30 \pm 0.01$  mm. The measured uncertainty of 0.01 mm emerges as a consequence of the limited resolution of the motion capture camera system and resolution of the CT scanner. This methodology for obtained deformation is more precise than registration method but it requires more processor time and memory.

Using the same procedure for image segmentation, a full model of knee joint is created. The model consists of femur, tibia, and cartilage.

We used measured values for the displacement and ground reaction force in order to calculate corresponding matrix elements in the relation (13). Upon model creation we applied boundary conditions: (a) we clamped the distal end of tibia and (b) axially loaded the femur with the maximally measured ground reaction force  $F_{g-max} = 511$  N (Figure 8(a)).

For modeling the cartilage and meniscus we implemented a finite element formulation where the nodal variables are displacements of solid,  $\mathbf{u}$ ; fluid pressure,  $\mathbf{p}$ ; Darcy's velocity,  $\mathbf{q}$ ; and electrical potential,  $\phi$  with estimated matrix elements. A standard procedure of integration over the element volume was performed and the Gauss's theorem was employed. An implicit time integration scheme was implemented.

The tetrahedral mesh model had 20537 elements and 4693 nodes (Figure 8(b)). We used PAK solver [20] for the FEM



FIGURE 6: Registration infrared image and CT image. (a) Infrared camera image; (b) CT image; (c) registered image.

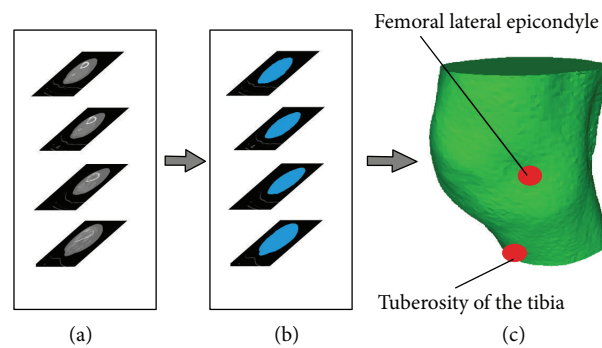


FIGURE 7: 3D model of knee. (a) Raw CT slices; (b) segmented CT images; (c) 3D model with marker position.

analysis. Total execution time of the analysis was around 30 minutes on the core I7 processor with 12 GB of RAM memory.

The initial mechanical characteristic, Young's modulus, and Poisson's ratio, for the femur and tibia, were amounted to  $E = 20$  GPa and  $\nu = 0.3$ , for the isotropic cartilage  $E = 10$  MPa and  $\nu = 0.45$ , and for the transversely isotropic menisci  $E = 20$  MPa and  $\nu = 0.3$ . All these values were taken from the literature [21].

These values were adaptively changed for the purpose of correspondence between the measured deformation and ground reaction force.

The final value of the Young's modulus of the cartilage is 5.62 MPa with error of estimation of 0.01 MPa. The Young's modulus for the femur and tibia is adapted to the 18 GPa while the Poisson's ratio is 0.45.

Resultant stress distribution of the FEM analysis for the elements of the knee joint is given in Figure 8(c).

The von Mises stress on the cartilage is presented in Figure 9. As it can be seen the maximal value of stress has MPa magnitude of order and is located on the boundary of the cartilage. This is in compliance with the fact that cartilage is the weakest part of the knee joint with a tendency to injury and fraying.

The procedure described in this study can offer very useful information for physicians in order to better understand injury formation and improve the process of rehabilitation

and, in some perspective, as a support in clinical decision making.

#### 4. Conclusion

The main goal of this study was to introduce a new approach towards a noninvasive effective stress calculation for a specific participant. Input data were provided from the experimental measurements during the participant's walking test whereupon finite element analysis was performed giving the distribution of the effective stress in the major anatomical elements of the knee joint: femur, tibia, and cartilage. This approach demonstrates a great possibility for preoperative and postoperative surgical planning and treatment of the knee injuries for specific patients.

This study contains some limitations. We neglected the skin movement artifact during the experiment and the influence of ligament presence. However, the current model allows us to investigate the effect of different biomechanical factors and loads on the stress distribution at the knee joint. In this study we used data obtained from infrared cameras and force plate sensors. Besides, in our future work we will try to replace a relatively expensive system of infrared cameras with a much cost effective system of accelerometers so that we will be able to calculate positional data of anatomical points of the lower extremities solely by using their accelerations. The very promising are techniques of the image registration that can be

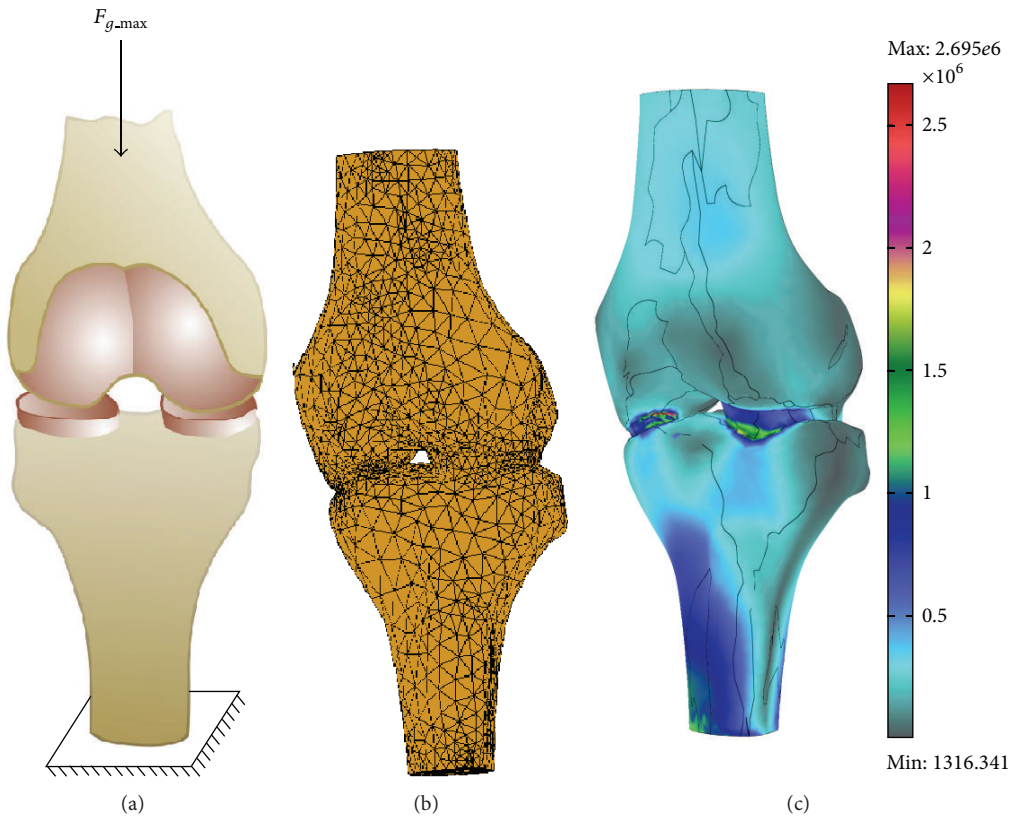


FIGURE 8: FEM analysis model. (a) Model filled with the tetrahedral mesh element; (b) knee von Mises stress distribution in [Pa].

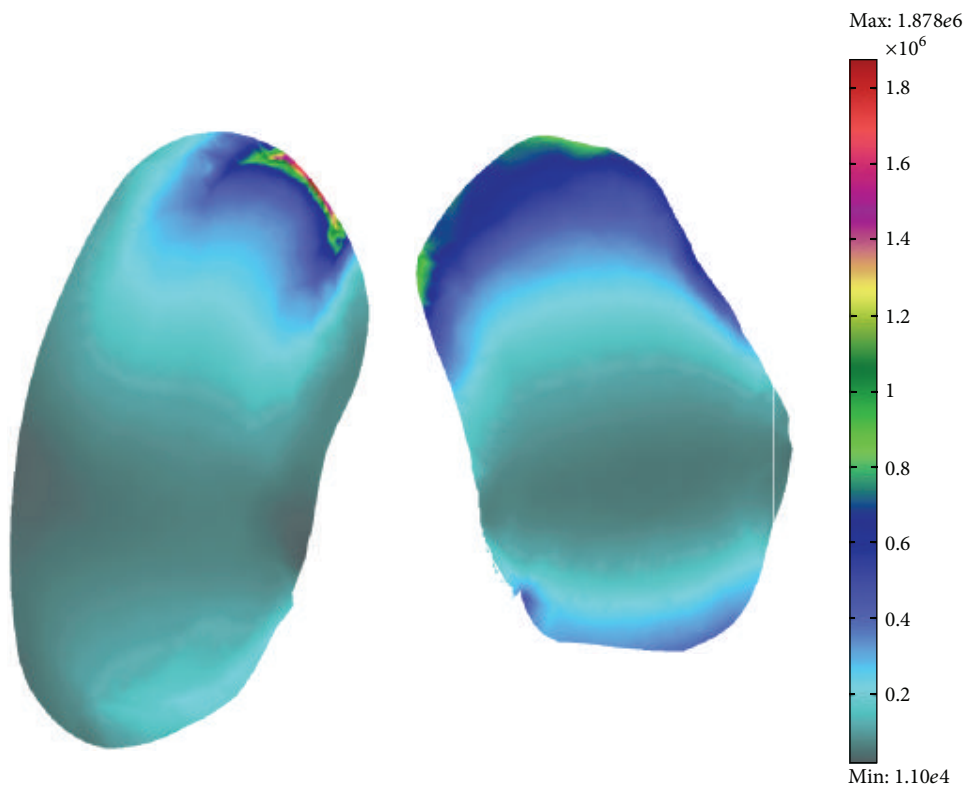


FIGURE 9: Knee cartilage von Mises stress distribution [Pa].

used for assessment of gait parameter using a cheaper mobile cell camera. This will be a consideration of the future work.

### Conflict of Interests

The authors declare that there is no conflict of interests regarding the publication of this paper.

### Acknowledgment

This paper is supported by the Ministry of Education, Science and Technological Development of the Republic of Serbia (Projects numbers III41007 and ON 174028).

### References

- [1] I. Kutzner, B. Heinlein, F. Graichen et al., "Loading of the knee joint during activities of daily living measured in vivo in five subjects," *Journal of Biomechanics*, vol. 43, no. 11, pp. 2164–2173, 2010.
- [2] G. Li, S. K. van de Velde, and J. T. Bingham, "Validation of a non-invasive fluoroscopic imaging technique for the measurement of dynamic knee joint motion," *Journal of Biomechanics*, vol. 41, no. 7, pp. 1616–1622, 2008.
- [3] C. Reinschmidt, A. J. van den Bogert, A. Lundberg et al., "Tibiofemoral and tibioacalcanal motion during walking: external vs. Skeletal markers," *Gait and Posture*, vol. 6, no. 2, pp. 98–109, 1997.
- [4] N. H. Yang, P. K. Canavan, H. Nayeb-Hashemi, B. Najafi, and A. Vaziri, "Protocol for constructing subject-specific biomechanical models of knee joint," *Computer Methods in Biomechanics and Biomedical Engineering*, vol. 13, no. 5, pp. 589–603, 2010.
- [5] M. D. Djurić-Jovičić, N. S. Jovičić, and D. B. Popović, "Kinematics of gait: new method for angle estimation based on accelerometers," *Sensors*, vol. 11, no. 11, pp. 10571–10585, 2011.
- [6] H. Dejnabadi, B. M. Jolles, and K. Aminian, "A new approach to accurate measurement of uniaxial joint angles based on a combination of accelerometers and gyroscopes," *IEEE Transactions on Biomedical Engineering*, vol. 52, no. 8, pp. 1478–1484, 2005.
- [7] K. Tong and M. H. Granat, "A practical gait analysis system using gyroscopes," *Medical Engineering and Physics*, vol. 21, no. 2, pp. 87–94, 1999.
- [8] W. Tao, T. Liu, R. Zheng, and H. Feng, "Gait analysis using wearable sensors," *Sensors*, vol. 12, no. 2, pp. 2255–2283, 2012.
- [9] Y. Wang, Y. Fan, and M. Zhang, "Comparison of stress on knee cartilage during kneeling and standing using finite element models," *Medical Engineering & Physics*, vol. 36, no. 4, pp. 439–447, 2014.
- [10] K. S. Halonen, M. E. Mononen, J. S. Jurvelin, J. Töyräs, J. Salo, and R. K. Korhonen, "Deformation of articular cartilage during static loading of a knee joint—experimental and finite element analysis," *Journal of Biomechanics*, vol. 47, no. 10, pp. 2467–2474, 2014.
- [11] Y. Dabiri and L. P. Li, "Altered knee joint mechanics in simple compression associated with early cartilage degeneration," *Computational & Mathematical Methods in Medicine*, vol. 2013, Article ID 862903, 11 pages, 2013.
- [12] N. Filipovic, R. Vulovic, A. Peulic, R. Radakovic, D. Kosanic, and B. Ristic, "Noninvasive determination of knee cartilage deformation during jumping," *Journal of Sports Science and Medicine*, vol. 8, no. 4, pp. 584–590, 2009.
- [13] J. Wismans, F. Veldpaus, J. Janssen, A. Huson, and P. Struben, "A three-dimensional mathematical model of the knee-joint," *Journal of Biomechanics*, vol. 13, no. 8, pp. 677–685, 1980.
- [14] M. Kojic, N. Filipovic, and S. Mijailovic, "A large strain finite element analysis of cartilage deformation with electrokinetic coupling," *Computer Methods in Applied Mechanics and Engineering*, vol. 190, no. 18-19, pp. 2447–2464, 2001.
- [15] E. H. Garling, B. L. Kaptein, B. Mertens et al., "Soft-tissue artefact assessment during step-up using fluoroscopy and skin-mounted markers," *Journal of Biomechanics*, vol. 40, supplement 1, pp. S18–S24, 2007.
- [16] C.-C. Chen, Y.-J. Chen, S.-C. Chen, H.-S. Lin, and T.-W. Lu, "Evaluation of soft-tissue artifacts when using anatomical and technical markers to measure mandibular motion," *Journal of Dental Sciences*, vol. 6, no. 2, pp. 95–101, 2011.
- [17] R. Dumas, V. Camomilla, T. Bonci, L. Cheze, and A. Cappozzo, "Generalized mathematical representation of the soft tissue artefact," *Journal of Biomechanics*, vol. 47, no. 2, pp. 476–481, 2014.
- [18] B. B. Avants, N. Tustison, and G. Song, "Advanced normalization tools (ANTS)," *The Insight Journal*, 2009, <http://hdl.handle.net/10380/3113>.
- [19] R. Bajcsy and S. Kovačić, "Multiresolution elastic matching," *Computer Vision, Graphics, and Image Processing*, vol. 46, no. 1, pp. 1–21, 1989.
- [20] N. Filipovic, M. Kojic, M. Živkovic, R. Slavkovic, and N. Grujovic, *PAK-FS Finite Element Program for Fluid-Structure Interaction*, Faculty of Mechanical Engineering, University of Kragujevac, Kragujevac, Serbia, 2010.
- [21] Z. Ming and F. Yubo, *Computational Biomechanics of the Musculoskeletal System*, CRC Press, 2014.

## Review Article

# Review of Modelling Techniques for *In Vivo* Muscle Force Estimation in the Lower Extremities during Strength Training

Florian Schellenberg, Katja Oberhofer, William R. Taylor, and Silvio Lorenzetti

*Institute for Biomechanics, ETH Zurich, HCI E 351, 8093 Zurich, Switzerland*

Correspondence should be addressed to Silvio Lorenzetti; [slorenzetti@ethz.ch](mailto:slorenzetti@ethz.ch)

Received 2 December 2014; Revised 11 February 2015; Accepted 12 February 2015

Academic Editor: Zhonghua Sun

Copyright © 2015 Florian Schellenberg et al. This is an open access article distributed under the Creative Commons Attribution License, which permits unrestricted use, distribution, and reproduction in any medium, provided the original work is properly cited.

**Background.** Knowledge of the musculoskeletal loading conditions during strength training is essential for performance monitoring, injury prevention, rehabilitation, and training design. However, measuring muscle forces during exercise performance as a primary determinant of training efficacy and safety has remained challenging. **Methods.** In this paper we review existing computational techniques to determine muscle forces in the lower limbs during strength exercises *in vivo* and discuss their potential for uptake into sports training and rehabilitation. **Results.** Muscle forces during exercise performance have almost exclusively been analysed using so-called forward dynamics simulations, inverse dynamics techniques, or alternative methods. Musculoskeletal models based on forward dynamics analyses have led to considerable new insights into muscular coordination, strength, and power during dynamic ballistic movement activities, resulting in, for example, improved techniques for optimal performance of the squat jump, while quasi-static inverse dynamics optimisation and EMG-driven modelling have helped to provide an understanding of low-speed exercises. **Conclusion.** The present review introduces the different computational techniques and outlines their advantages and disadvantages for the informed usage by nonexperts. With sufficient validation and widespread application, muscle force calculations during strength exercises *in vivo* are expected to provide biomechanically based evidence for clinicians and therapists to evaluate and improve training guidelines.

## 1. Introduction

The quantification of muscle forces during muscle strengthening exercises *in vivo* has tremendous potential for assisting with training design, performance monitoring, and injury prevention [1]. Due to the fact that 45.6% of all injuries during strength training in Switzerland occur due to overloading [2] and current exercise guidelines as well as training recommendations are based on the subjective experience of individual experts or coaches, knowledge about the effects of external loading on internal muscle forces during training or rehabilitation could help to improve exercise safety. In addition, the analysis of the internal loading conditions provides an evidence-based approach for defining specific targets and loading goals for effective training outcome while also reducing injury risk, since fewer loads can be used to achieve the same training effect. Furthermore, muscles are able to specifically adapt to their loading output to the

surrounding functional requirements and must therefore respond appropriately to allow the rehabilitation of unbalanced musculature in an effective and safe way. However, measuring muscle forces *in vivo* remains challenging due to the complexity of movement control, the nonlinear material properties of muscle tissue, the redundant number of muscle actuators, and the invasive nature of direct measurement techniques [3]. Existing guidelines on strength training (type of exercise, repetitions, number of sets, etc.) are often based on experience or simple measurements from dynamometry or surface electromyography (EMG) [4–7], but the actual stress levels in the muscle based on muscle force and cross-sectional area measures, which provide direct evidence for the efficacy and safety of specific muscle-strengthening exercises, have been difficult to obtain [8, 9].

It is not currently possible to measure muscle forces experimentally during exercise performance *in vivo*, and data from alternative measurement techniques have not been

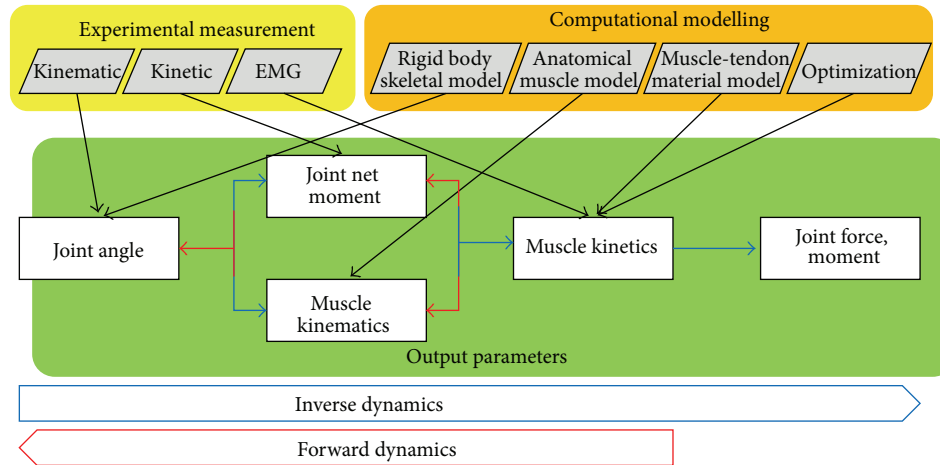


FIGURE 1: Muscle and joint forces are quantified *in vivo* by combining experimental measurements (yellow) with computational biomechanics (orange). Different measurement parameters (black arrows) or computational optimizations (black arrows) are required to achieve different output parameters (green) in inverse dynamics or forward dynamics processes. For forward dynamics simulations (red arrows), usually applied to dynamic ballistic movement exercises such as the squat jump, joint dynamics such as joint angles, joint net moment, or muscle kinematics are derived by finding an optimal set of muscle kinetics using computational modelling. For inverse dynamics analysis (blue arrows), usually applied to low-speed exercises such as the squat, joint moments, muscle forces, and finally joint contact forces are derived from joint angles and net joint moments.

sufficient for deducing internal forces and moments for complex dynamic systems, such as the lower limbs, in a straight forward manner [10]. Common measurement techniques in human motion analysis and sports science include surface EMG, optical motion capture, and force measures, for example, dynamometer or force platforms [8]. Dynamometry has frequently been used to determine strength and power during open chain leg extension or flexion exercises [6]. However, strength and power are scalar variables that provide only limited insights into actual muscle forces that occur internally, especially considering the complexity of inter- and intramuscular activity and coordination associated with free weights or multijoint dynamic training [6]. On the other hand, surface EMG provides a good insight into muscle activation levels during functional exercise performance compared to strength and power measures gained from dynamometry. However, while EMG offers more specific information on muscle function compared to dynamometry, it still provides insufficient data to deduce muscle force magnitudes [7], especially when analysing dynamic movements [11].

Computational models of the musculoskeletal system are therefore needed to provide a link between externally measured data and internal forces and moments (Figure 1). Musculoskeletal modelling techniques have been developed and extensively used in clinical and biomechanical gait analysis, in particular for studying lower limb dynamics. In order to predict muscle forces during movement, a computational model has to capture the anatomy of the musculoskeletal system, as well as the physiological force generating properties of muscle tissue, and then relate the target movement to the internal muscle forces through Newton's laws of motion [13]. Additional parameters, such as individual ratios of fast-twitch versus slow-twitch fibres within each muscle or muscle versus

fat volumes within the segments, could be taken into account in an optimization process and enhance the accuracy of a model but also its complexity (Figure 1).

Depending on model complexity, available experimental data, and study goal, the dynamic system of equations (originating from Newton's second law of motion) can be solved in different ways, including forward dynamics [12, 14–20], inverse dynamics [7, 13, 21–24], and EMG-driven analyses [4, 5, 25, 26]. Using forward dynamics, a set of muscle activation patterns are usually chosen as input into a physiological muscle model to derive muscle forces. Muscle forces are then applied to a rigid body skeletal model to estimate joint moments or joint angles (Figure 1). In contrast, inverse dynamics uses data from experimental measurements including skin marker positions and ground reaction forces as input into a rigid body skeletal model to calculate joint net moments. In addition, using optimization processes and musculoskeletal modelling, joint forces and moments can be computed from the results of the inverse dynamics analysis. An EMG-driven analysis uses normed muscle activation levels from EMG measurements in addition to skin marker positions and ground reaction forces to improve the estimation of muscle force magnitudes by means of musculoskeletal modelling. Unfortunately, the unknown muscle forces that cause a particular movement generally exceed the known parameters from experimental measurements, resulting in redundant systems of equations that require the use of various optimization techniques [4, 12, 20, 24, 26] (Figure 1).

Improved knowledge of the specific muscle forces that act during strength training could help coaches and athletes improve training protocols, as well as physiotherapists and patients to undertake rehabilitation exercises in an efficient and safe manner. Furthermore knowledge of the muscle forces can be used as boundary conditions within continuum

TABLE 1: Four concepts of search parameters were used to systematically search the literature and were combined using an “and” condition (horizontal). Each concept was created using “or” conditions (vertical) in order to ensure the inclusion of all papers using similar definition for the same case.

MeSH	Concept number 1	Concept number 2	Concept number 3	Concept number 4	
		<i>and</i>	<i>and</i>	<i>and</i>	
Subject [MeSH]	<i>or</i>	Resistance training	Musculoskeletal system Muscle, skeletal	Lower extremity Leg Ankle Knee Hip Foot	Computer simulation*
		Strength training	EMG	Lower limb	Muscle force
		Weight-lifting	Electromyogra*	Lower body	Muscle stress
		Weight-bearing		Lower extremities	Muscle control
		Strengthening			Musculoskeletal modeling Musculoskeletal modelling Optimization Optimisation Simulation Forward dynamic simulation Computer models
Text words [title/abstract]	<i>or</i>				

\*They were used as wildcards to replace part of a string.

organ models in order to estimate the biological change of the tissues such as muscle, bone, and tendon due to the mechanical stimuli of strength training. However, current approaches for deriving muscle forces are generally complex and require substantial expertise in computational modelling. In this review of the literature, we introduce nonexperts to current musculoskeletal modelling techniques for determining muscle forces (generally of the lower limbs) during strength training *in vivo* and discuss their potential as well as limitations for application to sports practice in order to assist with training recommendations and guidelines. In this manner, this review aims to result in an improved understanding of the existing computational techniques and thus provide a basis for future developments and more widespread and informed application of available biomechanical tools. Eventually, the results of in-depth biomechanical analyses are expected to help define objective, evidence-based guidelines for coaches and therapists to execute strength training exercises in an effective and safe manner.

## 2. Methods

A systematic electronic literature search of the US National Library of Medicine was conducted in August 2013. Four combined concepts including different search parameters were used to systematically search the literature (Table 1). A total of 77 papers were found complying with all four concepts and were further assessed for eligibility to be included in the review based on the following exclusion criteria: (1) no measurements were taken during a functional strength exercise of the lower extremities, or (2) results were limited

to EMG data, maximum voluntary isometric contraction, or net joint moments without adopting a computational model to determine muscle forces, or (3) *ex vivo* study. Out of these 77 papers, a total of 12 articles were eligible for the full review. Articles were mainly excluded because results were limited to measured data from EMG or dynamometry, without adopting musculoskeletal modelling techniques to determine muscle forces or other internal forces. Additional studies were excluded because muscle forces were analysed during activities other than strength training or were *ex vivo*, performed on cadaveric specimens. Strength training was defined as a physical exercise that induces muscular contraction to enhance strength, anaerobic endurance, or size of a skeletal muscle. References from the included papers were further searched for relevant work including the same criteria. An additional 9 papers were found within the references and included in the review process. Ultimately, the full text articles of 21 studies were included in the review.

## 3. Results

Musculoskeletal models with different levels of anatomical detail and computational complexity have been developed to determine muscle forces during strength exercises of the lower extremities *in vivo* (Table 2). The 21 included studies were divided into three categories, with 9 studies performing forward dynamics simulation, 2 studies adopting quasi-static inverse dynamics optimisation, and 10 studies outlining mixed inverse/forward dynamics (1 study) or mixed inverse dynamics/alternative methods including EMG-driven modelling (9 studies) (Table 2). Forward dynamics simulations

TABLE 2: Summary of studies reporting on computational techniques to determine muscle forces during strength training of the lower extremities *in vivo*. Dynamic squat jump was mainly analysed using forward dynamic (FD) simulation, while low-speed ankle, hip, and knee exercises were analysed using quasi-static inverse dynamics (ID) optimisation, electromyography-driven (EMG) modelling, or mixed inverse dynamics/forward dynamics analysis. Different approaches were adopted to distribute the net joint moments from ID across muscles, ranging from simple 1-muscle models to advanced optimization schemes taking muscle force-length-velocity ( $F-l-v$ ) into account. Data from EMG, optical motion capture (OMC), and ground reaction forces (GRF) were used as input or reference to assess the accuracy of modelling results.

Exercise	Modelling approach	Subjects	Experi. measure	Reported results	Reference
Foot plantar/dorsi flexion	ID (1-muscle model)	8 M, 8 F (22 y)	EMG, OMC, GRF	Muscle force	Henriksen et al. (2009) [7]
Deep knee bends	ID (1-muscle model)	3 M (26 y)	OMC, GRF	Muscle and joint forces	Reilly and Martens (1972) [27]
Squat, leg press, knee extension	ID (F-EMG)	10 M (30 y) experienced	EMG, OMC, GRF	Tibiofem joint kinetics, cruciate ligament force	Wilk et al. (1996) [23], Escamilla et al. (1998, 2001) [21, 22]
Squat, leg press	ID (optimized $F-l$ -EMG)	10 M (30 y) experienced	EMG, OMC, GRF	Tibiofem joint kinetics, cruciate ligament force	Zheng et al. (1998) [24]
Squat, leg press, knee extension	ID (optimized $F-l-v$ -EMG)	9 M (29 y), 9 F (25 y), low body fat	EMG, OMC, GRF	Patellofemoral force and stress	Escamilla et al. (2008) [4, 5]
Squat	EMG-driven/ID/FEM	8 M (29 y), 8 F (29 y)	EMG, OMC, GRF, MRI, open MRI	Knee cartilage stress	Besier et al. (2008) [25] based on Lloyd and Besier (2003) [26]
Hip extension/flexion	ID (min. stress)	Generic simul.	—	Hip joint forces	Lewis et al. (2009) [13]
Abdominal crunch	Mixed ID/FD equipment	Generic simul. (three anthropometric cases)	—	Intervertebral joint loading	Nolte et al. (2013) [28]
Dynamic ballistic	FD (activation $a$ _initial or $a = 1$ )	6 M (25 y) well-trained volleyball players	EMG, OMC, GRF	Gastro bioarticularity	van Soest et al. (1993) [20]
		6 M (25 y) well-trained volleyball players	EMG, OMC, GRF	Muscle strengthening	Bobbert and Van Soest (1994) [17]
		6 M (25 y) well-trained volleyball players	EMG, OMC, GRF	Triceps surae series elastic compliance	Bobbert (2001) [14]
		Generic simul.	—	Stimulation onset times	Bobbert and van Zandwijk (1999) [18]
		6 M (26 y)	EMG, OMC, GRF	Fatigue of plantarflexors	Bobbert et al. (2011) [16]
		8 M (20 y) well-trained volleyball and gymnastics	EMG, OMC, GRF	Bilateral deficit	Bobbert et al. (2006) [15]
		Generic simul.	—	Optimal controls	Pandy et al. (1990) [12]
		5 M (22 y)	EMG, OMC, GRF	Contribution of muscles to accelerate trunk	Pandy and Zajac (1991) [19]
		Generic simul.	—	Bilateral asymmetry	Yoshioka et al. (2011) [29]

have predominantly been used to study dynamic ballistic movement exercises such as the squat jump, while quasi-static inverse dynamics optimisation techniques or alternative methods have been adopted to analyse low-speed exercises such as the lunge or leg press under the assumption of “negligible acceleration in each segment.” Although Pearsall and Costigan [30] showed that accurate net moments may be achieved using quasi-static approaches in low-speed exercises, some studies have used a true inverse dynamics approach with inclusion of the accelerations of the segments and their moments of inertia [31–34]. All methodologies have in common that they draw on the physics principles of multibody dynamics (Newton’s laws of motion) and rely on accurate representations of musculoskeletal anatomy and physiology to accurately predict the muscle forces that cause the target motion (Figure 1).

**3.1. Anatomical and Physiological Model Parameters.** Musculoskeletal models with different numbers of muscles and joints, and different material property characteristics for active muscle and passive soft tissues, have been introduced depending on the research goal, available data, and expertise in computational modelling. Musculoskeletal models with a reduced number of muscles and/or a lower number of degrees of freedom at the joints have been adopted to simplify analyses. In particular, the knee joint has generally been represented as a planar hinge joint, neglecting translational and rotational degrees of freedom other than flexion-extension [7, 12, 13, 17, 20, 21, 24, 26, 28, 29]. In these models, individual muscles have often been grouped to reduce the unknown degrees of freedom of a musculoskeletal model, such as the hamstrings or quadriceps [17, 20, 21, 24, 25], or only key muscle players have been considered [7, 27]. Exceptions are the anatomical models adopted by different authors [13, 28, 29], which considered up to 43 muscle-tendon units per leg. These authors additionally subdivided large or complex muscles such as the gluteal muscles into multiple muscle units to more accurately represent their muscle paths and functions than would single muscle units [13]. The anatomical and physiological properties of these three models were based on experimental measurements of cadaveric specimens from the literature in an attempt to represent the modelled subject-specific properties [29]. Two of the models were generically implemented into commercially available or open-source software packages (LifeModeler, OpenSim) [13, 28].

The active and passive material properties of muscle-tendon structures have commonly been described by a Hill-type [35] active element, which comprises a so-called contractile element (CE) (force generation by actin and myosin cross-bridges) to capture the force-length-velocity dependency of muscle tissue. This active element is additionally coupled with two passive elements (represented by nonlinear spring elements); a series-elastic (SE) element to account for the tendon elasticity and a parallel-elastic element (PE) to account for the passive stiffness of the muscle connective tissue (Figure 2) [12, 14–20, 29]. The force-velocity dependency of a particular muscle can thus be derived directly from Hill’s equation  $(v + b)(F + a) = b(F_0 + a)$

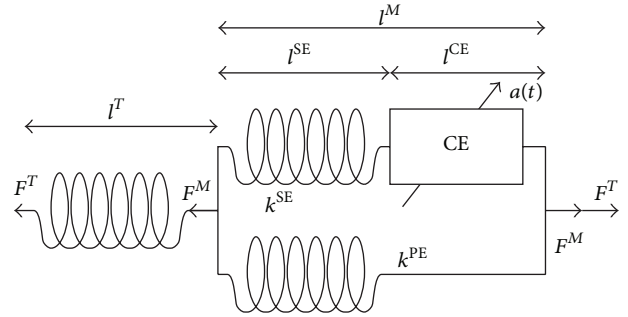


FIGURE 2: The Hill-type muscle-tendon model, showing muscle and tendon forces ( $F^M$ ,  $F^T$ ), as well as the series-elastic (SE), parallel-elastic (PE), and contractile (CE) elements of the muscle length ( $l$ ) and stiffness ( $k$ ) of the whole muscle-tendon actuator ( $M$ ,  $T$ ).  $a(t)$  represents the activation of the CE (adapted from Pandy and coworkers [12]).

[35], where larger forces can be produced by the CE during slow velocity contractions and vice versa. During eccentric movement, muscles are able to produce even higher forces, since passive structures additionally support the CE for force production. The force that can be produced by a muscle is further dependent on the actual length of a muscle, since the force generated actin myosin cross-bridges at the sarcomere level depend on their overlapping status. Furthermore passive structures (PE and SE) produce force when the muscle is stretched, even if the CE is not activated. The Hill-type muscle model has widely been accepted by the biomechanics community and has been implemented into musculoskeletal modelling software packages such as OpenSim [10, 36].

Material parameters (predetermined, constant values) for the Hill-type muscle model are generally derived from experimental measurements on cadaveric specimens reported in the literature, including maximum isometric force, muscle fibre pennation angle, tendon slack length, tendon and muscle passive stiffness, and physiological cross-sectional area (PCSA). Simplifications to the Hill-type model have been made by neglecting the force-velocity and/or force-length relationship as well as the passive material properties, especially to analyse quasi-static exercises using inverse dynamics techniques [13, 21–24, 28]. Adjustment of material parameters to individual subjects is generally achieved through simple scaling based on segmental lengths, calculated joint centers, EMG signals (normalized to the maximal voluntary isometric contraction (MVIC)), or subjects body weight [4, 5, 12, 18–24]. Alternatively, static or functional optimisation approaches can be used [26]. Other techniques to determine individual muscle parameters include ultrasound measurements, which allow the evaluation of muscle volume and thus PCSA [3], but no studies have been found that combine ultrasound measurements with musculoskeletal modelling to analyse muscle forces during strength training.

**3.2. Forward Dynamics Simulation.** In general, the problem to simulate a musculoskeletal model using a forward dynamics approach is to find a physiologically feasible set of controls regarding the muscle activity, for example, by

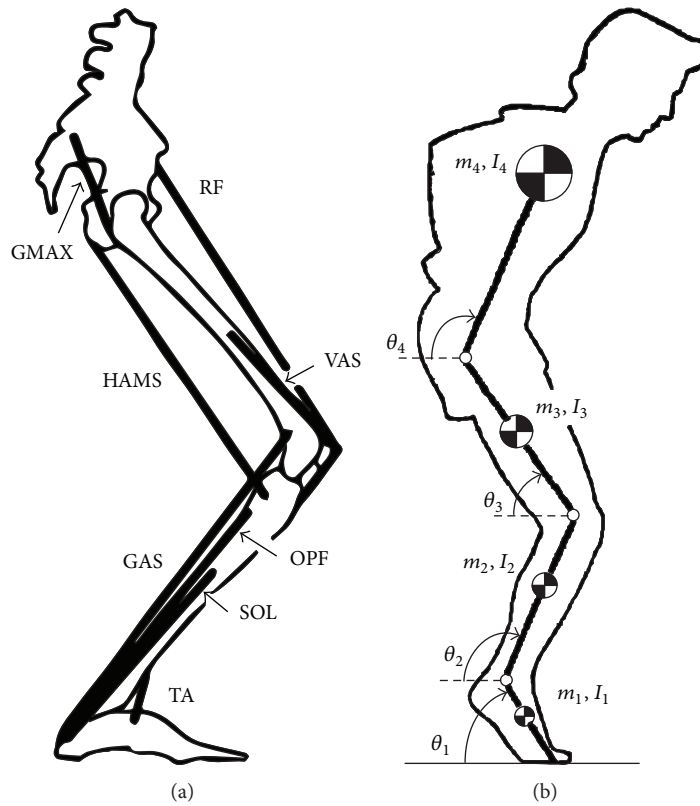


FIGURE 3: (a) Schematic representation of the musculoskeletal model for the vertical jump and (b) the four-segment multibody model with lumped masses and mass moments of inertia for the foot, shank, thigh, and head/arms/trunk (Pandy and coworkers [12]).

means of the minimized integral cost function. This usually includes a large set of boundary conditions and constraints to be defined. A set is related to different application area such as movement, loading conditions, physiology, and the time dependency of an optimization algorithm. Furthermore, forward dynamics simulations are usually associated to a control problem. Here, open loop solutions are often highly unstable and difficult to integrate while close loop solutions of the highly nonlinear musculoskeletal system remain still an unsolved problem. Significant attempts have been made to simulate the musculoskeletal system in motion based on forward dynamics, using muscle activation levels as input and the time-history of segmental positions and orientations as output, in particular to study dynamic ballistic movement exercises such as the squat jump. Here, different studies have introduced forward dynamics models of the musculoskeletal system to better understand, for example, how intermuscular control [12, 14, 18], bilateral-asymmetry [15, 29], or muscular fatigue [16] affect the maximum jump height. The dynamic equations of motion of the skeletal system are thereafter described by a set of differential equations, driven by muscle-tendon actuators which are controlled by neural signalling. Muscle-tendon actuators are commonly represented using the Hill-type muscle-tendon model, connected to a numerical model to capture the time lapse between the incoming neural signal and the onset of muscle activation. Forward dynamics simulations depend on optimisation algorithms to

find feasible sets of muscle activation patterns leading to the desired movement dynamics, with maximum jump height as a common performance criterion. For other movements such as squats or lunges, new criteria would need to be defined. Solutions to the optimisation problem are more likely found for unambiguous movement patterns with simplified musculoskeletal models that are with a limited number of muscle actuators and constrained conditions such as reduced degrees of freedom of the joints [12].

One of the first forward dynamics models for the planar squat jump was introduced by Pandy and coworkers [12], comprising all lower limb bones and eight major muscles (Figure 3). The constraints that defined the optimal control problem were the dynamic equations of motion, the terminal calculation point at takeoff, and the muscle activation levels being set to 0 or 1, with maximum jump height as the performance criterion. A more restricted form of dynamic optimisation was introduced by van Soest and coworkers [20], whereby muscles were only allowed to switch from the initial activation values once and then had to maintain maximum activation until takeoff. The problem was thus reduced to finding an optimal combination of the muscular switching times to result in maximum jump height. The resulting muscle activation patterns corresponded well with experimentally measured data from EMG, and the formulation has often been applied to biomechanical analyses of the squat jump [14–18].

In order to gain confidence in forward dynamics simulations, modelling results have often been compared with experimental data from optical motion capture, force platforms, and EMG [15–17, 19, 20], confirming the ability of forward dynamics models to accurately reproduce the major features of maximum-height squat jumps. Based on the present literature search, and in agreement with previous reviews on muscle force calculations in orthopaedics and clinical gait analysis [36], forward dynamic methods have not yet been applied to muscle strengthening exercises other than the squat jump. While the performance criterion for the squat jump is generally maximal jump height, the selection of performance criteria for other activities is considered more challenging [36]. Furthermore, forward dynamic models require multiple integration steps to reach optimal joint kinematics, resulting in a computational complexity that limits their implementation in user-friendly software packages and thus widespread use by nonexperts. However, using forward dynamics offers the possibility for coaches or therapists to simulate an optimal training or rehabilitation program for a specific athlete or patient without the need for elaborate experimental measurements such as EMG, optical motion capture, or ground reaction forces.

**3.3. Quasi-Static Inverse Dynamics Optimisation.** In contrast to forward dynamics simulation, the inverse dynamics formulation is comparably quick and computationally inexpensive. Inverse dynamics analysis refers to the calculation of segmental forces and moments based on data from optical motion capture and force sensors such as force platforms and has become a routine tool in clinical gait analysis [36] and strength training exercises [37–40]. It is important to note that joint contact forces and muscle forces cannot be calculated directly from inverse dynamics. Instead, the derivation of muscle forces necessitates distributing the net intersegmental forces from inverse dynamics across synergistic and antagonistic muscles, which leads to a problem of indeterminate nature that needs to be solved using numerical optimisation techniques. Joint contact forces can additionally be calculated as the sum of the net intersegmental forces and the synergistic and antagonistic muscle forces that cross the joint (Figure 1).

Quasi-static inverse dynamics optimisation techniques have generally been applied to low-speed movements, such as the leg press or lunge [7, 13, 21, 22, 24, 27]. For low-speed exercises, the quasi-static equilibrium condition holds true under the assumption that the angular acceleration of each segment is negligible. In an early study, Reilly and Martens [27] introduced a single-muscle model to quantify quadriceps muscle forces during deep knee bends based on inverse dynamics. The model worked under the assumption that only the quadriceps as a single muscle group is active during the exercise. Thus, the net knee joint moments from inverse dynamics were equal to the resulting muscle moments, and muscle forces could be determined geometrically by deriving the moment arms with respect to the knee joint centre. A similar modelling approach was adopted by Henriksen and coworkers [7], analysing the eccentric and concentric

forces in the Achilles tendon during ankle plantar- and dorsiflexion. Here, the advantage is that single-muscle models do not depend on computationally expensive optimisation techniques; however, the potential contribution of synergistic and antagonistic muscles to joint stability and movement control is neglected and the physiological differences in force generating capabilities between muscles cannot be accounted for.

More complex musculoskeletal models based on quasi-static inverse dynamics have been developed, accounting for the contribution of synergistic and antagonistic muscle groups to analyse open and closed chain knee extension [21–23] and hip flexion-extension [13]. Here, optimisation algorithms based on the least-squares method have generally been adopted to find weighting factors for each muscle force contribution to minimize the differences between the intersegmental torques from inverse dynamics and the resultant muscle torques from the biomechanical model. In early attempts, muscle forces were assumed to be proportional to physiological cross-sectional area (PCSA), maximum voluntary contraction force, and measured EMG activation levels, without taking the force-length [24], muscle fibre recruitment [7], and force-velocity [21, 23] relationships into account. To improve results, Zheng and coworkers [24] extended previous models by examining the role of muscle force-length properties and demonstrated that force-length dependent optimisation during squat and leg press exercises had a significant effect on muscle force magnitudes, which proved to be an important factor in determining tension in the cruciate ligaments.

A slightly different approach based on quasi-static inverse dynamics optimisation was adopted by Lewis and coworkers [13] to analyse the effect of position and alteration in synergist muscle forces on hip forces during hip strengthening exercises. Muscle-tendon paths and maximum isometric forces of 43 muscle units were adopted from a generic musculoskeletal model in the commercially available software SIMM (MusculoGraphics, Inc., Santa Rosa, CA, USA). Muscle material properties other than muscle-tendon paths and maximum isometric force were neglected, including force-length relationships and the passive response to stress. An optimisation algorithm was adopted that aimed to minimise muscle stress with the goal of maximizing muscle endurance. Such an approach has been widely accepted for biomechanical analyses of the lower limbs during gait [36]. However, quasi-static optimisation techniques based on minimizing muscle stresses have been shown to underestimate antagonistic muscle activity as well as muscle force contributions of low magnitudes [41]. Furthermore, subjects who are fatigued or in pain are unlikely to activate muscles according to a minimal effort principle but rather with the aim of avoiding mechanical stress on fatigued or painful tissue.

**3.4. Alternative Methods.** A group of alternative methods have been introduced to calculate muscle forces based on a mixed inverse-forward dynamics approach [28] or by using EMG data to drive a musculoskeletal model towards given joint kinematics (EMG-driven modelling) [4, 25, 26]. In

particular, Nolte and coworkers [28] outlined a combined inverse-forward dynamics simulation to quantify intervertebral loading during the abdominal crunch exercise based on a full-body musculoskeletal model using the LifeModeler software. The modelling output depended on the initial estimation of muscle-tendon lengths from inverse dynamics to provide reference values for the derivation of muscle activation levels and thus muscle forces. However, the model did not account for physiologically realistic material properties of muscle tissue. Instead, muscle forces were derived using a closed loop algorithm containing proportional-integral-differential controllers to reach the target length-time curve. Despite questions arising in terms of model validity, the study remains unique in that it included a Computer Aided Design (CAD) model of the training machine. By using musculoskeletal models of different sizes together with the CAD model, the authors were able to analyse the effectiveness and safety of the exercise machine to accommodate very small or large individuals based on the predicted muscle forces and intervertebral joint loading.

Other alternative methods to determine muscle forces during strength training include so-called EMG-driven musculoskeletal models, introduced by Lloyd and Besier [26] and Escamilla and coworkers [4, 5]. The basic concept behind EMG-driven models consists of collecting EMG data, which are filtered, rectified, and input into a calibrated musculoskeletal model to predict muscle forces. However, extensive calibration trials, including optical motion capture and ground reaction force measurements, are required to define subject-specific model parameters before accurate predictions of muscle forces for individual subjects across a number of different tasks are possible. Calibration trials allow the adjustment of model parameters by minimizing the differences between joint kinematics and/or joint torques from inverse dynamics analysis and corresponding results from the EMG-driven model. In contrast to quasi-static inverse dynamics optimisation techniques, EMG-driven models account for the dynamic force generating properties of muscles and, upon successful calibration, have been adopted to predict muscle forces during dynamic exercises such as sidestepping or dynamic lunge activities [4, 5]. Challenges remain in the placement of the electrodes and processing of the EMG signals as well as in the calibration of reference or generic musculoskeletal models to subject- and task-specific conditions [3]. Despite these challenges, high density EMG measurements have been shown to reduce errors in muscle force predictions, but these analyses often result in an instrumentation complexity that may not be achievable during sports practice [3].

#### 4. Discussion

The relevance of understanding the internal muscle forces during strength exercises becomes clear when examining the wide range of studies and research questions reported in the literature. Musculoskeletal modelling techniques have been applied to strength training to analyse the effect of altered muscle physiology on exercise performance (physiological

adaptations) [14, 17, 20], the impact of exercise execution on muscle and joint forces (best choice of exercise to avoid injury) [4, 5, 21–23], and the internal loading state of differently sized people using the same exercise machines (safety and efficacy of equipment) [28]. Muscular weaknesses, bilateral asymmetries, or changes in exercise performance have been shown to result in altered and potentially harmful internal tissue loading that cannot be investigated based on external observation or simple measurements.

Accurate assessment of the risks involved in strength exercises, and subsequent design of effective exercise schemes, is dependent on the accurate estimation of muscle forces and joint loading during the target exercise. Different numerical techniques have been introduced to determine muscle forces in the lower extremities during strength training *in vivo*, including (1) forward dynamics analysis to study dynamic ballistic movement exercises such as the squat jump, (2) quasi-static inverse dynamics optimisation to study low-speed exercises, such as the lunge or leg press, and (3) alternative methods such as EMG-driven modelling. All methodologies are challenged by the limitations of externally measurable data and the complexity of the musculoskeletal system, that is, the indeterminate nature of the simulation problem. Forward dynamics analyses depend on optimisation algorithms to find the most suitable set of muscle activation levels that lead to the desired movement patterns, while muscle force calculations from inverse dynamics analyses require optimisation algorithms to distribute the net joint moments across synergistic and antagonistic muscles in a physiological manner.

The findings by studies presented in this review have provided insights into the biomechanical principles underlying strength training that would not otherwise be possible. Using musculoskeletal modelling techniques, health care related factors could be detected. For example, co-contraction forces of the hamstrings and quadriceps during squats and leg presses have been shown to significantly affect tension in the cruciate ligaments [21–23], which in turn is a crucial factor for establishing safe and effective rehabilitation programs. Furthermore, the results from musculoskeletal modelling have provided sports performance related factors, such as the muscle activation delays between stimulation onset times of proximal muscles versus plantar flexors during the squat jump and their influence on jump height deficits [18]. Lastly, the knowledge gained from computational studies has helped to support and establish training and injury prevention recommendations. For example, the reduced quadriceps muscle forces during long step lunges compared to short step lunges have supported the belief of clinicians and trainers that anterior knee translation beyond the toes during the forward lunge may be harmful to the patellofemoral joint [4].

Essentially, the forward dynamics simulation is a method of systematic trial and error and could represent the process by which an athlete optimizes control of muscle recruitment and physiological strength for best performance of explosive movements such as the squat jump [12]. Predictive analyses based on forward dynamics provide a powerful tool to elucidate the impact of alterations in neurological activation, muscular physiology, or joint alignment on performance

output. As such, predictive analyses have considerable potential to improve strength training guidelines, without the need for extensive experimental measurements on individual subjects. Compared to forward dynamics simulation, quasi-static inverse dynamics optimisation techniques are computationally efficient and do not depend on EMG measurements. In particular, quasi-static optimisation techniques based on maximising muscle endurance (minimizing stress) have been widely accepted to estimate muscle forces in the lower extremities during walking and stair climbing [36, 42]. Application of the same techniques to strength training may be valid for quasi-static exercises when the training goal is maximising strength endurance. However, static optimisation techniques are generally not sufficient for predicting antagonistic muscle activity that does not occur with the goal of minimizing stress but rather to stabilize joints and maintain joint integrity [43]. EMG-driven models provide an alternative to static optimisation techniques, especially to determine muscle forces following injury or muscular fatigue where muscle recruitment patterns might be altered. However, EMG-driven models are challenged by extensive validation trials to formulate valid muscle model parameters, and difficulties remain in the placement of EMG electrodes, signal normalization, and filter choice.

Unfortunately, it remains challenging to confirm the validity of musculoskeletal models for accurately reproducing muscle forces due to the invasive nature of internal measurement techniques. Other than, for example, tendon-force measurements during surgery [36] or telemetric implants [42, 44], a gold standard for model validation remains lacking. To address this issue, an international consortium of biomechanics researchers has received funding from the National Institutes of Health to organise a series of five “Grand Challenge Competitions to Predict *In Vivo* Knee Loads” [45]. The goal is for competitors to predict the *in vivo* medial and lateral knee contact forces for specific movement trials collected from subjects implanted with a force-measuring tibial prosthesis. Muscle forces are the primary determinants of joint contact forces, and thus instrumented implant data provide a direct validation of joint contact forces and an indirect validation of muscle forces. The validation of musculoskeletal models by means of instrumented joint implants has proven invaluable in orthopaedic research, for example, as a basis for standardizing preclinical testing [42]; however, instrumented implants have exclusively been used in elderly subjects to analyse joint loading during daily activities such as walking or stair-climbing and have therefore not been applied to training and sports problems that involve dynamic ballistic movement loading conditions and/or impact.

It is important to note that the required degree of model complexity is dependent on the particular research question. Simplifications regarding motion, anatomy, and physiology are often required in order to reduce the computational costs. However, simplified musculoskeletal models with generic material properties may lead to invalid results for certain cases. For example, the knee abduction angle during jump landing tasks was shown to be a predictor of anterior cruciate

ligament injury risk in female athletes [46], whereby all rotational degrees of freedom should be involved in the knee joint during rehabilitation from anterior cruciate ligament injury; or the relationship between the measured EMG signal and the actual muscle force of the triceps surae was shown to be different for the eccentric versus the concentric contraction phase of one-legged full weight bearing ankle plantar and dorsiflexion exercises [7]. These studies suggest that all rotational degrees of freedom in the joints, or contraction-specific EMG-to-force relationships, may be required to improve modelling results in specific cases. Ideally, the influence of model complexity on the simulation results is assessed prior to making any conclusions.

Limitations of musculoskeletal simulations remain in the accurate capturing of subject-specific anatomy (e.g., segment lengths, degrees of freedom, and muscle paths) and physiology (e.g., Hill-type muscle, force-length, and force-velocity relationships). As a result, anatomical and physiological parameters such as the PCSA of muscles have mainly been adopted from cadaveric measurements on a few elderly human subjects (5 cadaver specimens, mean age 79.2 years in Herzog and Read [47], or 2 male cadaver specimens, mean age 82 years in Spoor and coworkers [48]) and scaled to subject-specific dimensions based on a few measurements. Lloyd and Besier [26] introduced more extensive techniques to calibrate an EMG-driven model to subject-specific conditions; however, the physiological basis of the calibration process was questioned and seemed rather tedious for application to sports practice. In the broader field of human motion analysis, increased efforts have been directed towards developing efficient computational techniques to create subject-specific anatomical models based on magnetic resonance images [49, 50]. The future application of such techniques to strength training could certainly provide a basis for analysing the influence of individual differences in muscle physiology and anatomy on exercise performance. Furthermore, subject-specific customisation of muscle model properties may be based on supplementary parameters from ultrasound or dynamometry. Such parameters could include the type of muscle fibre, maximal isometric or dynamic muscle force, or physiological performance parameters such as maximal power.

Substantial efforts have been directed towards translating musculoskeletal modelling techniques into user-friendly tools to facilitate their application in clinical and sports practice. In particular, the open source software OpenSim, developed and maintained on <https://simtk.org/> by the NIH National Center for Physics-Based Simulation of Biological Structures (Simbios, Stanford University, CA, USA), has significantly contributed to the uptake of computational biomechanics by the nonexpert [10]. OpenSim provides a user-friendly interface for coupling forward dynamics, quasi-static inverse dynamics, and EMG-driven modelling with subject-specific experimental data to calculate joint and muscle dynamics during human movement. The development of easy-to-use and freely available software such as OpenSim marks a significant step towards the more wide-spread application of advanced computational techniques for improving the efficacy and safety of strength training. Interestingly,

only a few studies have reported actual muscle force values, even though many have outlined computational techniques that entailed the calculation of muscle forces (Table 2). It appears that muscle forces are often used only as intermediate parameters to analyse, for example, maximal jump height through forward dynamics simulation or quantify joint forces and moments through inverse dynamics analyses. As a result, it seems that the potential of muscle force calculations to provide evidence for the efficacy and safety of strength training programmes has not yet been fully grasped, possibly due to the difficulties in validating the presented solutions, thus explaining the limited confidence for uptake.

Knowledge of the acting muscle forces during strength training based on musculoskeletal modelling offers a means to establish effective and safe training guidelines to achieve specific training aims such as improved intermuscular coordination, monitoring muscular changes, eliminating or preventing unbalanced muscular adaptation, pointing out injury predictors, and improving efficiency and safety of exercise equipment. In the future, it might be possible to model subject-specific loading conditions during exercising and further use the predicted muscle forces as boundary conditions for finite element continuum models in order to estimate the biological tissue adaptation due to training. The application of existing musculoskeletal modelling techniques to strength training of the lower limbs is particularly attractive because of standardised conditions and simple movement patterns that are often associated with strength exercises. A key factor in limiting the applicability and uptake of the musculoskeletal modelling techniques to clinical and sports practice seems to be the lack of experimental solutions for validating internal forces, stresses, and strains *in vivo*. Cross-institutional initiatives, like the grand challenge to determine *in vivo* knee loads, should be extended to include more subjects in different age groups and a range of different activities including strength exercises. Upon successful model validation, the quantification of muscle forces during strength training based on inverse and forward dynamic analyses is expected to help improve current training guidelines to the benefit of coaches, clinicians, athletes, and patients alike.

### Ethical Approval

All authors abide by the Ethics Committee of ETH Zurich, Switzerland ethical rules of disclosure.

### Conflict of Interests

The authors declare that there is no conflict of interests regarding the publication of this paper.

### Authors' Contribution

All authors contributed to conception and design, paper preparation, read, and approved the final paper.

### References

- [1] W. Blajer, A. Czaplicki, K. Dziewiecki, and Z. Mazur, "Influence of selected modeling and computational issues on muscle force estimates," *Multibody System Dynamics*, vol. 24, no. 4, pp. 473–492, 2010.
- [2] R. Mueller, *Fitness Centers: Injuries and Discomforts during Training*, BFU, Bern Switzerland Federal Institute for Injury Prevention, Bern, Switzerland, 1999.
- [3] L. L. Menegaldo and L. F. Oliveira, "The influence of modeling hypothesis and experimental methodologies in the accuracy of muscle force estimation using EMG-driven models," *Multibody System Dynamics*, vol. 28, no. 1-2, pp. 21–36, 2012.
- [4] R. F. Escamilla, N. Zheng, T. D. Macleod et al., "Patellofemoral joint force and stress between a short- and long-step forward lunge," *Journal of Orthopaedic & Sports Physical Therapy*, vol. 38, no. 11, pp. 681–690, 2008.
- [5] R. F. Escamilla, N. Zheng, T. MacLeod et al., "Patellofemoral compressive force and stress during the forward and side lunge with and without a stride," *Medicine & Science in Sports & Exercise*, vol. 40, no. 5, p. S79, 2008.
- [6] N. Harris, J. Cronin, and J. Keogh, "Contraction force specificity and its relationship to functional performance," *Journal of Sports Sciences*, vol. 25, no. 2, pp. 201–212, 2007.
- [7] M. Henriksen, J. Aaboe, H. Bliddal, and H. Langberg, "Biomechanical characteristics of the eccentric Achilles tendon exercise," *Journal of Biomechanics*, vol. 42, no. 16, pp. 2702–2707, 2009.
- [8] D. M. Frost, J. Cronin, and R. U. Newton, "A biomechanical evaluation of resistance: fundamental concepts for training and sports performance," *Sports Medicine*, vol. 40, no. 4, pp. 303–326, 2010.
- [9] R. T. Kell, G. Bell, and A. Quinney, "Musculoskeletal fitness, health outcomes and quality of life," *Sports Medicine*, vol. 31, no. 12, pp. 863–873, 2001.
- [10] S. L. Delp, F. C. Anderson, A. S. Arnold et al., "OpenSim: open-source software to create and analyze dynamic simulations of movement," *IEEE Transactions on Biomedical Engineering*, vol. 54, no. 11, pp. 1940–1950, 2007.
- [11] C. J. De Luca, "The use of surface electromyography in biomechanics," *Journal of Applied Biomechanics*, vol. 13, no. 2, pp. 135–163, 1997.
- [12] M. G. Pandy, F. E. Zajac, E. Sim, and W. S. Levine, "An optimal control model for maximum-height human jumping," *Journal of Biomechanics*, vol. 23, no. 12, pp. 1185–1198, 1990.
- [13] C. L. Lewis, S. A. Sahrman, and D. W. Moran, "Effect of position and alteration in synergist muscle force contribution on hip forces when performing hip strengthening exercises," *Clinical Biomechanics*, vol. 24, no. 1, pp. 35–42, 2009.
- [14] M. F. Bobbert, "Dependence of human squat jump performance on the series elastic compliance of the triceps surae: a simulation study," *Journal of Experimental Biology*, vol. 204, no. 3, pp. 533–542, 2001.
- [15] M. F. Bobbert, W. W. De Graaf, J. N. Jonk, and L. J. R. Casius, "Explanation of the bilateral deficit in human vertical squat jumping," *Journal of Applied Physiology*, vol. 100, no. 2, pp. 493–499, 2006.
- [16] M. F. Bobbert, M. M. van der Krogt, H. van Doorn, and C. J. de Ruyter, "Effects of fatigue of plantarflexors on control and performance in vertical jumping," *Medicine & Science in Sports & Exercise*, vol. 43, no. 4, pp. 673–684, 2011.

- [17] M. F. Bobbert and A. J. Van Soest, "Effects of muscle strengthening on vertical jump height: a simulation study," *Medicine and Science in Sports and Exercise*, vol. 26, no. 8, pp. 1012–1020, 1994.
- [18] M. F. Bobbert and J. P. van Zandwijk, "Sensitivity of vertical jumping performance to changes in muscle stimulation onset times: a simulation study," *Biological Cybernetics*, vol. 81, no. 2, pp. 101–108, 1999.
- [19] M. G. Pandy and F. E. Zajac, "Optimal muscular coordination strategies for jumping," *Journal of Biomechanics*, vol. 24, no. 1, pp. 1–10, 1991.
- [20] A. J. van Soest, A. L. Schwab, M. F. Bobbert, and G. J. van Ingen Schenau, "The influence of the biarticularity of the gastrocnemius muscle on vertical-jumping achievement," *Journal of Biomechanics*, vol. 26, no. 1, pp. 1–8, 1993.
- [21] R. F. Escamilla, G. S. Fleisig, N. Zheng, S. W. Barrentine, K. E. Wilk, and J. R. Andrews, "Biomechanics of the knee during closed kinetic chain and open kinetic chain exercises," *Medicine and Science in Sports and Exercise*, vol. 30, no. 4, pp. 556–569, 1998.
- [22] R. F. Escamilla, G. S. Fleisig, N. Zheng et al., "Effects of technique variations on knee biomechanics during the squat and leg press," *Medicine and Science in Sports and Exercise*, vol. 33, no. 9, pp. 1552–1566, 2001.
- [23] K. E. Wilk, R. F. Escamilla, G. S. Fleisig, S. W. Barrentine, J. R. Andrews, and M. L. Boyd, "A comparison of tibiofemoral joint forces and electromyographic activity during open and closed kinetic chain exercises," *The American Journal of Sports Medicine*, vol. 24, no. 4, pp. 518–527, 1996.
- [24] N. Zheng, G. S. Fleisig, R. F. Escamilla, and S. W. Barrentine, "An analytical model of the knee for estimation of internal forces during exercise," *Journal of Biomechanics*, vol. 31, no. 10, pp. 963–967, 1998.
- [25] T. F. Besier, G. E. Gold, S. L. Delp, M. Fredericson, and G. S. Beaupré, "The influence of femoral internal and external rotation on cartilage stresses within the patellofemoral joint," *Journal of Orthopaedic Research*, vol. 26, no. 12, pp. 1627–1635, 2008.
- [26] D. G. Lloyd and T. F. Besier, "An EMG-driven musculoskeletal model to estimate muscle forces and knee joint moments in vivo," *Journal of Biomechanics*, vol. 36, no. 6, pp. 765–776, 2003.
- [27] D. T. Reilly and M. Martens, "Experimental analysis of the quadriceps muscle force and patello-femoral joint reaction force for various activities," *Acta Orthopaedica Scandinavica*, vol. 43, no. 2, pp. 126–137, 1972.
- [28] K. Nolte, P. E. Krüger, P. S. Els, and H. Nolte, "Three dimensional musculoskeletal modelling of the abdominal crunch resistance training exercise," *Journal of Sports Sciences*, vol. 31, no. 3, pp. 264–275, 2013.
- [29] S. Yoshioka, A. Nagano, D. C. Hay, and S. Fukashiro, "The effect of bilateral asymmetry of muscle strength on the height of a squat jump: a computer simulation study," *Journal of Sports Sciences*, vol. 29, no. 8, pp. 867–877, 2011.
- [30] D. J. Pearsall and P. A. Costigan, "The effect of segment parameter error on gait analysis results," *Gait and Posture*, vol. 9, no. 3, pp. 173–183, 1999.
- [31] G. Rao, D. Amarantini, and E. Berton, "Influence of additional load on the moments of the agonist and antagonist muscle groups at the knee joint during closed chain exercise," *Journal of Electromyography and Kinesiology*, vol. 19, no. 3, pp. 459–466, 2009.
- [32] D. G. E. Robertson, J.-M. J. Wilson, and T. A. St. Pierre, "Lower extremity muscle functions during full squats," *Journal of Applied Biomechanics*, vol. 24, no. 4, pp. 333–339, 2008.
- [33] G. J. Salem and C. M. Powers, "Patellofemoral joint kinetics during squatting in collegiate women athletes," *Clinical Biomechanics*, vol. 16, no. 5, pp. 424–430, 2001.
- [34] D. A. Wallace, G. J. Salem, R. Salinas, and C. M. Powers, "Patellofemoral joint kinetics while squatting with and without an external load," *Journal of Orthopaedic & Sports Physical Therapy*, vol. 32, no. 4, pp. 141–148, 2002.
- [35] A. V. Hill, "The heat of shortening and the dynamic constants of muscle," *Proceedings of the Royal Society of London. Series B. Biological Sciences*, vol. 126, no. 843, pp. 136–195, 1938.
- [36] A. Erdemir, S. McLean, W. Herzog, and A. J. van den Bogert, "Model-based estimation of muscle forces exerted during movements," *Clinical Biomechanics*, vol. 22, no. 2, pp. 131–154, 2007.
- [37] S. Lorenzetti, T. Gülay, M. Stoop et al., "Comparison of the angles and corresponding moments in the knee and hip during restricted and unrestricted squats," *Journal of Strength and Conditioning Research*, vol. 26, no. 10, pp. 2829–2836, 2012.
- [38] F. Schellenberg, J. Lindorfer, R. List, W. R. Taylor, and S. Lorenzetti, "Kinetic and kinematic differences between deadlifts and goodmornings," *BMC Sports Science, Medicine and Rehabilitation*, vol. 5, no. 1, p. 27, 2013.
- [39] R. List, T. Gülay, M. Stoop, and S. Lorenzetti, "Kinematics of the trunk and the lower extremities during restricted and unrestricted squats," *Journal of Strength and Conditioning Research*, vol. 27, no. 6, pp. 1529–1538, 2013.
- [40] P. Schütz, R. List, R. Zemp, F. Schellenberg, W. R. Taylor, and S. Lorenzetti, "Joint angles of the ankle, knee, and hip and loading conditions during split squats," *Journal of Applied Biomechanics*, vol. 30, no. 3, pp. 373–380, 2014.
- [41] A. Stops, R. Wilcox, and Z. Jin, "Computational modelling of the natural hip: a review of finite element and multibody simulations," *Computer Methods in Biomechanics and Biomedical Engineering*, vol. 15, no. 9, pp. 963–979, 2012.
- [42] M. O. Heller, G. Bergmann, J.-P. Kassi, L. Claes, N. P. Haas, and G. N. Duda, "Determination of muscle loading at the hip joint for use in pre-clinical testing," *Journal of Biomechanics*, vol. 38, no. 5, pp. 1155–1163, 2005.
- [43] G. Bergmann, F. Graichen, and A. Rohlmann, "Hip joint contact forces during stumbling," *Langenbeck's Archives of Surgery*, vol. 389, no. 1, pp. 53–59, 2004.
- [44] A. Trepczynski, I. Kutzner, E. Kornaropoulos et al., "Patellofemoral joint contact forces during activities with high knee flexion," *Journal of Orthopaedic Research*, vol. 30, no. 3, pp. 408–415, 2012.
- [45] B. J. Fregly, T. F. Besier, D. G. Lloyd et al., "Grand challenge competition to predict in vivo knee loads," *Journal of Orthopaedic Research*, vol. 30, no. 4, pp. 503–513, 2012.
- [46] T. E. Hewett, G. D. Myer, K. R. Ford et al., "Biomechanical measures of neuromuscular control and valgus loading of the knee predict anterior cruciate ligament injury risk in female athletes: a prospective study," *The American Journal of Sports Medicine*, vol. 33, no. 4, pp. 492–501, 2005.
- [47] W. Herzog and L. J. Read, "Lines of action and moment arms of the major force-carrying structures crossing the human knee joint," *Journal of Anatomy*, vol. 182, part 2, pp. 213–230, 1993.
- [48] C. W. Spoor, J. L. van Leeuwen, C. G. M. Meskers, A. F. Titulaer, and A. Huson, "Estimation of instantaneous moment arms of

- lower-leg muscles,” *Journal of Biomechanics*, vol. 23, no. 12, pp. 1247–1259, 1990.
- [49] B. Gilles and N. Magnenat-Thalmann, “Musculoskeletal MRI segmentation using multi-resolution simplex meshes with medial representations,” *Medical Image Analysis*, vol. 14, no. 3, pp. 291–302, 2010.
- [50] K. Oberhofer, K. Mithraratne, N. S. Stott, and I. A. Anderson, “Anatomically-based musculoskeletal modeling: prediction and validation of muscle deformation during walking,” *Visual Computer*, vol. 25, no. 9, pp. 843–851, 2009.

## Research Article

# Vehicular Causation Factors and Conceptual Design Modifications to Reduce Aortic Strain in Numerically Reconstructed Real World Nearside Lateral Automotive Crashes

Aditya Belwadi<sup>1,2</sup> and King H. Yang<sup>2</sup>

<sup>1</sup>The Center for Injury Research and Prevention, The Children's Hospital of Philadelphia, 3535 Market Street, Suite 1150, PA 19104, USA

<sup>2</sup>Department of Biomedical Engineering, Wayne State University, 818 W. Hancock, Detroit, MI 48201, USA

Correspondence should be addressed to Aditya Belwadi; [adityabn@gmail.com](mailto:adityabn@gmail.com)

Received 8 September 2014; Accepted 26 March 2015

Academic Editor: Irini Doytchinova

Copyright © 2015 A. Belwadi and K. H. Yang. This is an open access article distributed under the Creative Commons Attribution License, which permits unrestricted use, distribution, and reproduction in any medium, provided the original work is properly cited.

Aortic injury (AI) leading to disruption of the aorta is an uncommon but highly lethal consequence of trauma in modern society. Most recent estimates range from 7,500 to 8,000 cases per year from a variety of causes. It is observed that more than 80% of occupants who suffer an aortic injury die at the scene due to exsanguination into the chest cavity. It is evident that effective means of substantially improving the outcome of motor vehicle crash-induced AIs is by preventing the injury in the first place. In the current study, 16 design of computer experiments (DOCE) were carried out with varying levels of principal direction of force (PDOF), impact velocity, impact height, and impact position of the bullet vehicle combined with occupant seating positions in the case vehicle to determine the effects of these factors on aortic injury. Further, a combination of real world crash data reported in the Crash Injury Research and Engineering Network (CIREN) database, Finite Element (FE) vehicle models, and the Wayne State Human Body Model-II (WSHBM-II) indicates that *occupant seating position, impact height, and PDOF*, in that order play, a primary role in aortic injury.

## 1. Introduction

TRA and blunt aortic injury (BAI) are leading causes of death in high-speed impact trauma. Smith and Chang [1] reported on 387 cases of blunt traumatic death in vehicular crashes and found that aortic injury was second only to head injury as the leading cause of death. They also reported that nearly 85% of the victims who sustained an aortic tear died at the scene. Further, most cases of aortic injuries are accompanied by head injury, rib fractures, and/or hepatic trauma (Burkhart et al. [2]).

The mechanism of injury and the threshold for injury in these cases may be related to the particular anatomy and physiology of the aorta and the surrounding tissue. However, data from literature has shown that in lateral impacts B-pillar intrusion combined with lateral sliding of the occupant into

the intruding B-pillar and associated structures are mainly responsible for aortic injury [3, 4]. Further, higher aortic strain which was seen as a primary factor for aortic tears is primarily regionalized in the peri-isthmic region, distal to the origin of the left subclavian artery [3–7].

The advent of sophisticated Finite Element (FE) computer models has in the recent years significantly aided determination of injury causation. In 2005, Shah et al. refined the first version of the human body model to develop the Wayne State Human Body Model-II (WSHBM-II) that has detailed thoracic organs including the heart, aorta, and lungs. Additional thoracic modeling, material models, and validation information can be found in Shah et al. [3]. The WSHBM has a total of 79,471 nodes and 94,484 elements with a mass of 75.6 kilograms.

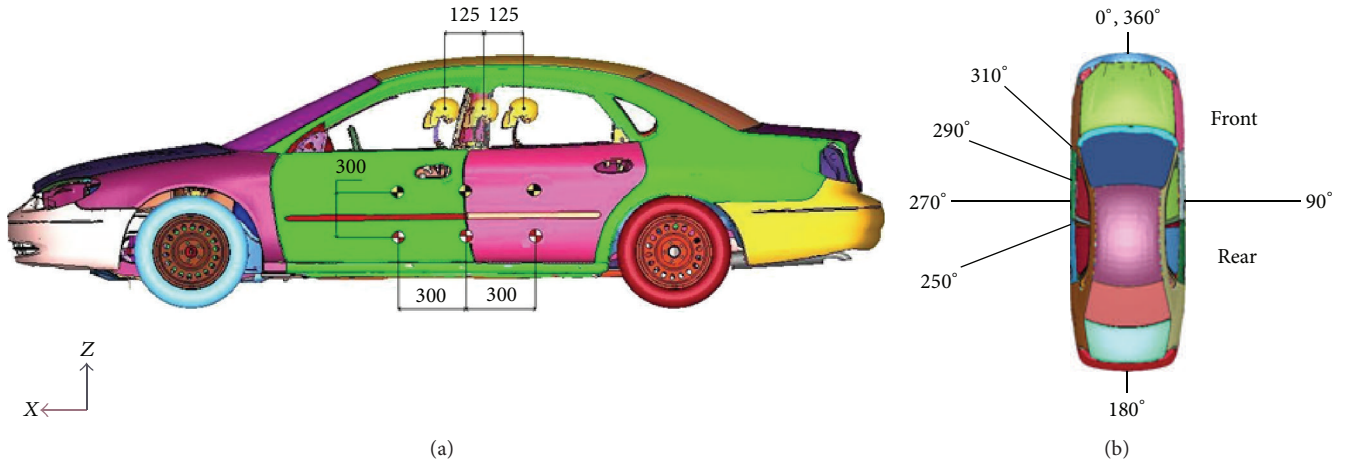


FIGURE 1: (a) Position of the impact vehicle, height of impact, and occupant seating position for Phase B simulations; (b) PDF for Phase B simulations.

TABLE 1: Range of values for the five design factors chosen for the DOCE study.

Number	Design factor	Range			
Striking vehicle					
1	Bumper profile	Low	High	—	—
2	Impact position (mm)*	-300	0	+300	—
3	PDOF (degrees)	250	270	290	310
4	Initial velocity (km/h)	30	38.3	46.6	54.9
5	Occupant position (mm)*	-125	0	+125	—

\*Note. Impact position and occupant position are determined from the center of the case vehicles' B-pillar.

## 2. Methods and Materials

To further understand the mechanism of aortic injury a cause and effect based DOCE study was performed on 16 different combinations of five design factors generated using a Latin Square method in modeFRONTIER 4.0 (ESTECO North America) [6, 8]. The reconstructions were carried out in two stages as outlined in Siegel et al. 2010. In Stage I, vehicle-to-vehicle kinematics and deformation were reconstructed from accident reports obtained from the Crash Injury Research and Engineering Network (CIREN) database (Case #7 from [4]). In Stage II, the occupant impact was considered for 16 cases. Appendices A and B describe the reconstruction process and details Case #7 for the sake of completeness.

Five design factors, impact height, impact position, PDOF, and initial velocity of the bullet vehicle combined with varying occupant seating positions in the case vehicle, each with two to four levels of variations chosen from the proximity of CIREN data presented in Siegel et al. 2010 were chosen. Table 1 lists the design factors and ranges simulated while Figures 1(a) and 1(b) graphically demonstrate these locations. Again, the vehicle kinematics time histories were used as input to the WSHBM to determine the FE model predicted risk of aorta injury.

The baseline case vehicle, a 2001 FE Ford Taurus model, similar to the struck vehicle model in the selected case was used as the target vehicle for the DOCE study. For the striking vehicle, FE models of a 2002 Dodge Caravan, which has a low bumper profile similar to a sedan, and a 2002 Ford Explorer, which has a higher bumper profile than a sedan, were used for the simulations. Impact position was chosen to be the center, 300 mm forward or 300 mm backward of the case vehicles' B-pillar. The PDOF and initial velocity were chosen to cover the range of values in previous CIREN cases. Finally, the occupant seating position selected covered the full range of for-aft range of the seat (250 mm) for a 2001 Ford Taurus with the angle of seat back at 110 degrees. That is, the occupant was positioned mid-track, 125 mm forward of mid-track, or 125 mm backward of mid-track. Table 2 lists the outputs of DOCE using the Latin square sampling method (modeFRONTIER 4.0).

The response variables were average maximum principal strain (AMPS) and maximum pressure in the aorta. For AMPS, four adjacent elements in the region with the highest maximum principal strain were selected and averaged, while for pressure, the maximum value in the aorta obtained during the entire simulation was tabulated.

## 3. Results and Discussion

Table 2 lists the DOCE test matrix derived using a Latin square sampling from modeFRONTIER and the output variables. Maximum simulation time for each case run has been tabulated to establish a standardized time scale for comparison. Some simulations terminated earlier than the other due to "negative volume" based on LS-DYNA terminology.

It was observed from the simulation that in all runs the maximum principal strain occurred near the isthmus of the aorta, distal to the orifice of the left subclavian artery. A maximum of 32.4% strain was seen in run #5 which was a sedan impacting the B-pillar (270 degrees) at 55 km/h with the occupant seated at the B-pillar. A low of 2.5% strain was observed in run #14 which was a sedan impacting 300 mm to

TABLE 2: Latin square sampling for DOCE and output response variables; average maximum principal strain (AMPS) and maximum pressure in the aorta.

Run #	Bumper profile height	Impact position (mm)	PDOF (degrees)	Velocity (km/h)	Occupant position (mm)	Maximum simulation time (ms)	AMPS*	Time at AMPS (ms)	Maximum pressure (kPa)	Time at maximum pressure (ms)
1	Low	-300	290	30	+125	56	0.1180	55	105.8	50
2	Low	-300	270	38.3	0	65	0.2240	44	113.5	46
3	High	-300	250	46.6	-125	54	0.1650	54	148.0	48
4	High	-300	310	54.9	0	33	0.0540	33	109.0	33
5	Low	0	270	54.9	0	52	0.3240	40	135.0	36
6	Low	0	290	46.6	+125	46	0.1580	44	119.6	36
7	High	0	310	30	0	78	0.0675	78	104.4	70
8	High	0	250	38.3	-125	64	0.1650	56	120.0	50
9	Low	0	310	46.6	-125	80	0.2100	60	127.6	50
10	Low	0	250	54.9	0	44	0.2580	43	117.7	42
11	High	0	290	38.3	0	44	0.0330	43	104.3	42
12	High	0	270	30	+125	70	0.1520	54	110.8	54
13	Low	+300	250	38.3	0	72	0.2300	44	113.2	48
14	Low	+300	310	30	-125	80	0.0250	78	103.0	78
15	High	+300	270	54.9	+125	36	0.2350	34	149.0	34
16	High	+300	290	46.6	0	76	0.1600	54	123.7	52

\* Average maximum principal strain (%) = lower surface average maximum tensile principal strain in the longitudinal axis of the aorta.

\* AMPS and maximum strain curves for each run are presented in Figure 5.

the left of B-pillar at an angle of 310 degrees and a velocity of 30 km/h with the occupant seated 125 mm in front of the B-pillar.

In order to determine the critical factors, a “main effects” analysis was performed in Minitab 16.1 (Minitab Inc., PA) based on FE model predicted results listed in Table 2. Figures 2 and 3, respectively, summarize the relationship between selected design factors, AMPS in the isthmus, and peak pressure in the aorta, respectively, predicted by the WSHBM.

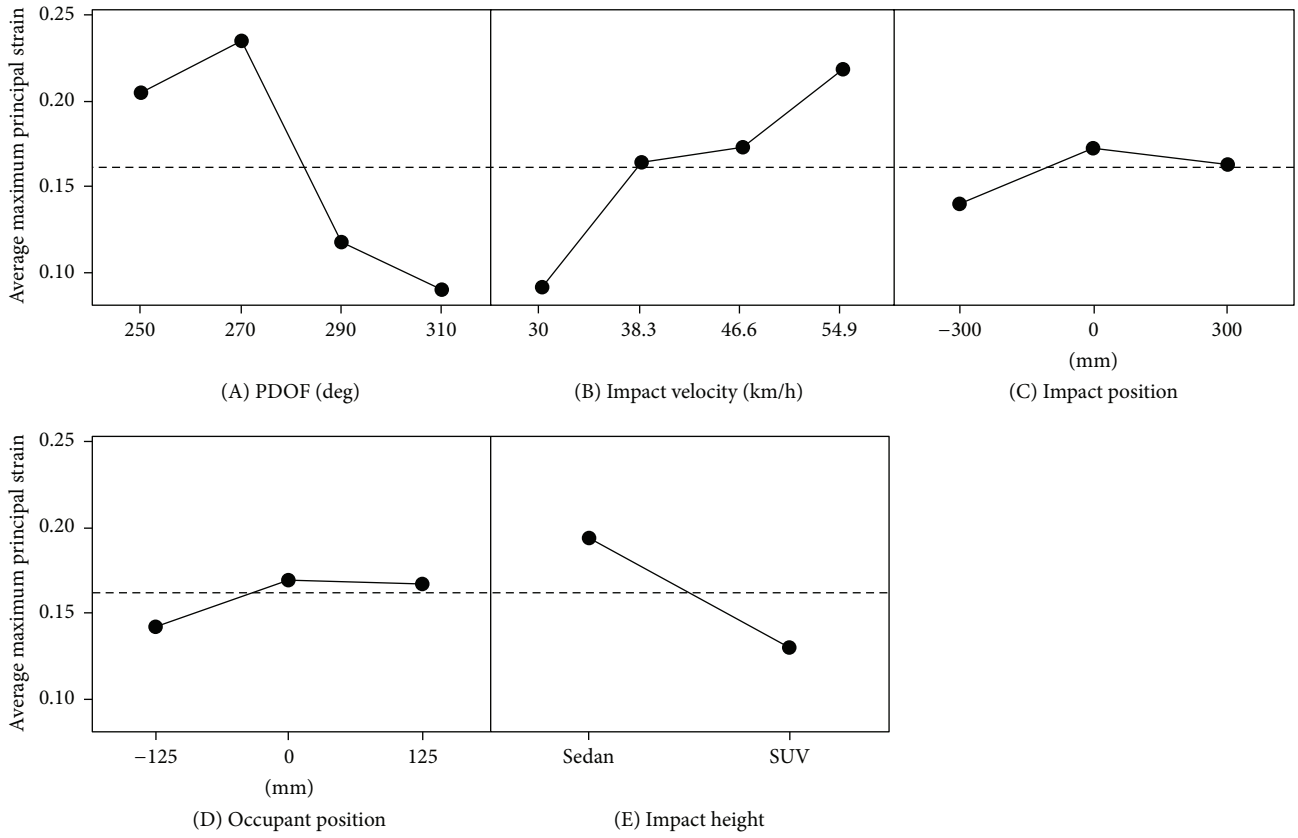
It is noted that a PDOF of 270 degrees resulted in the highest average AMPS (Figure 2(a)(A)) among all factors and levels studied. An increase in impact velocity had a direct correlation with the increase in maximum principal strain (Figure 2(a)(B)) while an occupant seated at the B-pillar and an impact directed to the B-pillar seemed to generate higher strain in the isthmus region (Figures 2(a)(C) and 2(a)(D)). In contrast to intuitive thinking, impacts from a Dodge caravan with a low profile bumper generated a higher isthmus strain compared to a high profile SUV represented here by a Ford Explorer model (Figure 2(a)(E)). From the Pareto effects chart we observe that a combination of PDOF and occupant seating position followed by bumper profile height with occupant position has a significant impact on the strain generated (Figure 2(b)).

From Figure 3(a)(A), a PDOF of 270 degrees resulted in the highest aortic pressure among all four PDOFs simulated. As the impact velocity increased, the aortic pressure also increased and seemed to vary negligibly after a velocity of 46.6 km/h (Figure 3(a)(B)). In contrast to the findings for maximum principal strain, an impact position centered on

the B-pillar (Figure 3(a)(C)), occupant seated at the B-pillar (Figure 3(a)(D)) generated the lowest aortic pressure, and a higher bumper profile generated a higher aortic pressure (Figure 3(a)(E)). Similar to earlier findings, the Pareto effects chart revealed a combination of PDOF and occupant seating position followed by bumper profile height with occupant position had a significant impact on the maximum pressure generated in the aorta in the 16 simulations (Figure 3(b)).

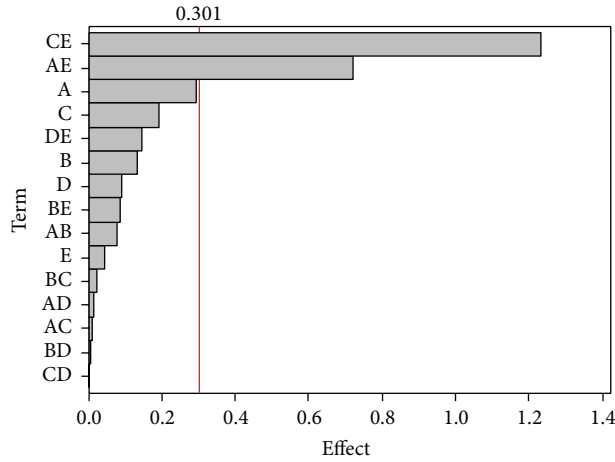
Student’s *t*-test was performed to determine the level of significance for each design factor using modeFRONTIER 4.0. It was found that PDOF ( $p = 0.001$ ) had a significant negative effect, impact velocity ( $p = 0.055$ ) had a marginally significant positive effect, and impact height ( $p = 0.068$ ) had a marginally significant negative effect on FE model predicted maximum principal strain. The impact position ( $p = 0.295$ ) and occupant position ( $p = 0.304$ ) did not significantly affect the FE model predicted maximum principal strain. In terms of FE model predicted peak aortic pressure, impact velocity ( $p = 0.002$ ) had a significant positive effect while PDOF ( $p = 0.028$ ) had a significant negative effect. Other factors, occupant position ( $p = 0.185$ ), impact height ( $p = 0.283$ ), and impact position ( $p = 0.475$ ), did not significantly affect the FE model predicted aortic pressure.

Bass et al. [9] reported a 50% risk of tear to the aorta at 120 kPa for occupants 68 years of age. Further, Shah et al. in 2006 [10] tested eight cruciate shaped cadaveric aortas until failure utilizing a biaxial fixture and reported an average longitudinal failure strain of 22.1%. They defined failure to be a complete tear of all three layers of the aorta (tunica intima, tunica media, and tunica adventitia). Utilizing strain



(a)

Pareto chart of the effects  
(response is AMPS\*,  $\alpha = 0.05$ )

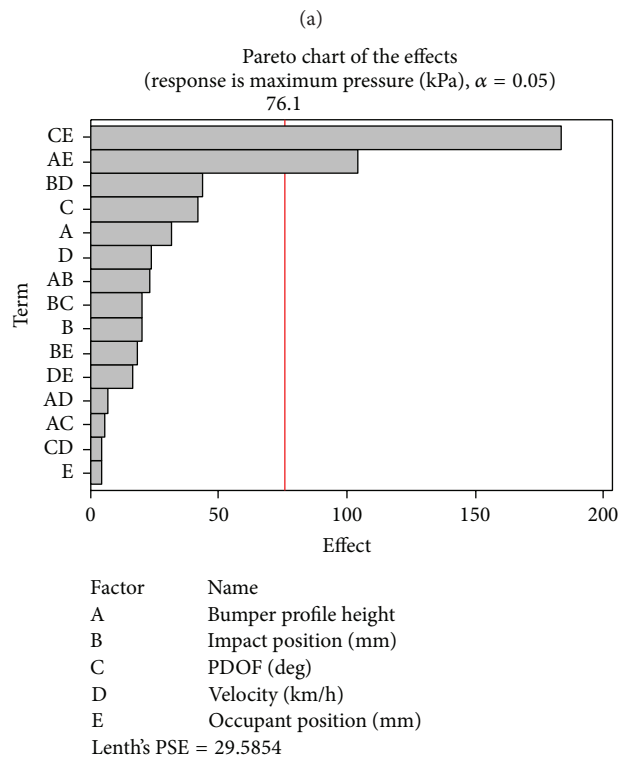
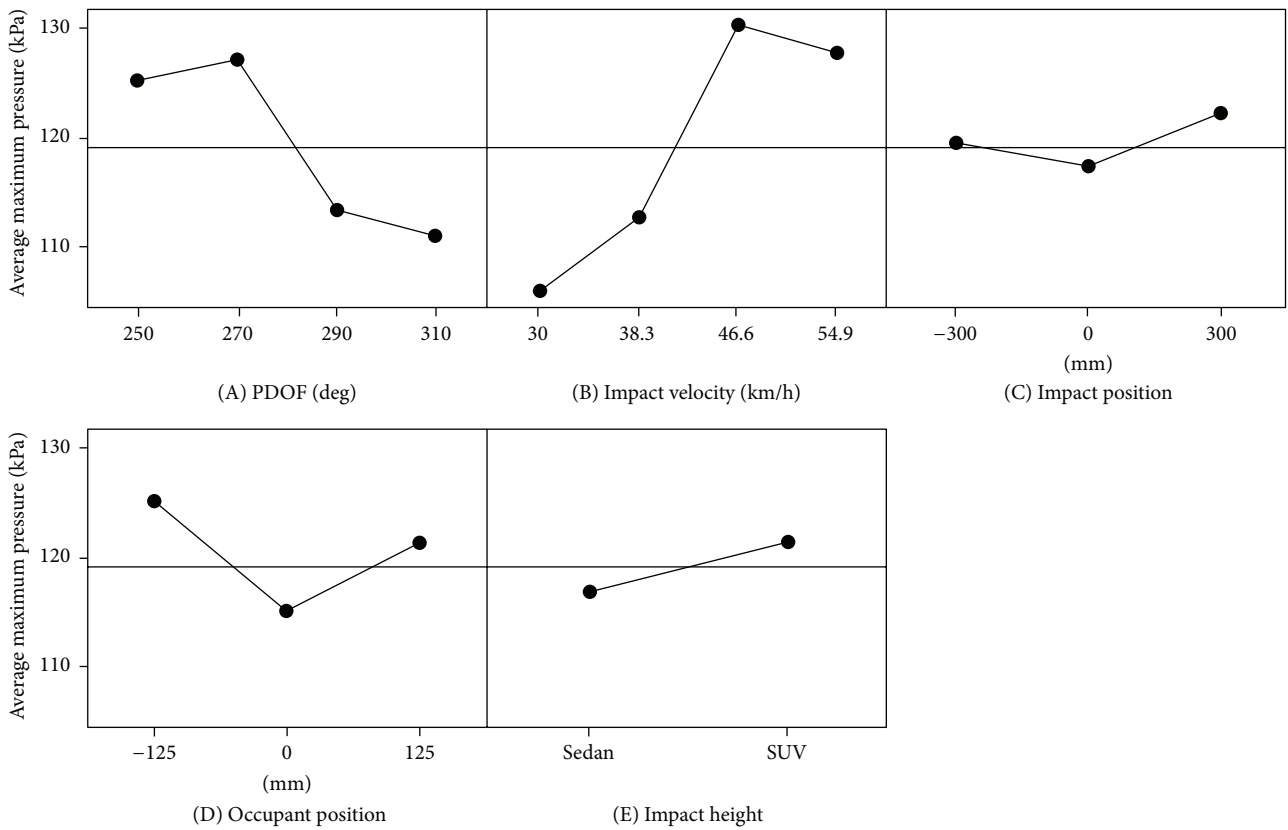


Factor	Name
A	Bumper profile height
B	Impact position (mm)
C	PDOF (deg)
D	Velocity (km/h)
E	Occupant position (mm)

Lenth's PSE = 0.116900

(b)

FIGURE 2: AMPS: (a) main effects chart; (b) Pareto chart of combination effects.



(b)

FIGURE 3: (a) Main effects chart: maximum pressure (kPa); (b) Pareto chart of combined effects.

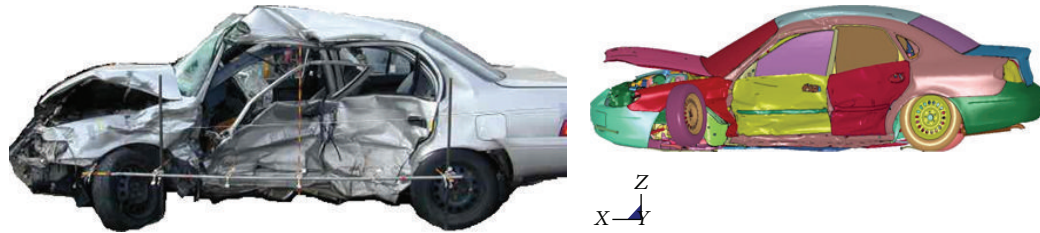


FIGURE 4: Vehicle deformation comparison of simulated FE vehicle against actual vehicle, CASE 7.

(0.221) and pressure (120 kPa) as thresholds for aortic failure, Table 3 reports the average AMPS and average maximum pressure along with their significance for each factor analyzed separately for failure based on strain and pressure criterion.

It is seen from Table 3 that for a strain based criterion the number of runs with failure was significant for AMPS while for a pressure based criterion, the number of failure runs was significant for maximum pressure. There was no correlation found between aortic failure with strain and pressure combined. This was also supported by data from Table 2 where no correlation was found between times of occurrence of maximum AMPS and maximum pressure in the aorta for a particular run.

Although there was no significant difference in impact velocity, PDOF, or maximum pressure it is interesting to note that the runs with aortic failure had a bullet vehicle with a low bumper profile (sedan). It was observed that in runs with lower bumper profile the armrest gets pushed into the thorax while it is completely missed with a higher bumper profile. Further, it was also seen that there was a mass difference of 488.5 kilograms between the Dodge Caravan (2028.1 kgs) and the Ford Explorer (1539.6 kgs) FE models. The difference in momentum between the two impacts might have had an effect on the intrusion pattern. A one-way ANOVA performed between the two FE models for average maximum principal strain ( $p = 0.136$ ) and maximum pressure in the aorta ( $p = 0.58$ ) was not significant.

Several limitations of the current study are noted. Even though the vehicle models were accurately scaled to match the size and weight of the case vehicle, the stiffness and interior compartment details were not compensated. It is also important to observe that measured external deformation may not correspond to similar occupant compartment intrusion and contact force due to differences in elastic modulus of various interior components. This problem is exacerbated by the fact that deformation profiles are measured at individual points on the external surface leading to variations in actual and simulated profiles.

## 4. Conclusions

Sixteen DOCE runs were carried out using FE vehicle models and the second version of the Wayne State Human Body Model. In simulated nearside left lateral crashes, peak average maximum principal strain primarily occurred in the isthmus of the aorta, distal to the orifice of the left subclavian artery. Results of design of computer experiments concluded that

*occupant seating position, bumper profile height, and PDOF of impact*, in that order, play a crucial role in the generation of strain and pressure in the aorta, a potential injury mechanism responsible for traumatic rupture of the aorta in automobile crashes.

## Appendices

### A. FE Reconstruction Methodology

For the case and bullet vehicles, a 2001 Ford Taurus and 2002 Dodge Caravan FE models, respectively, downloaded from the National Crash Analysis Center (NCAC) website were scaled to match with the overall dimensions such as wheelbase, width, and height. In addition, the vehicle mass was adjusted by removing a few components, such as the rear bumper, which would typically not be involved in left lateral or frontal crashes. The driver's weight was compensated for by adding a lumped mass (from the case data) to the center of gravity of the driver's seat. Care was taken to ensure that the overall center of gravity and total mass were not altered. Similarly, the striking vehicle was modeled, and the two vehicles were positioned as suggested by the crash investigation data. Initial velocity was applied to the striking vehicle as a vector component defined by the PDOF. The total simulation time was assigned to ensure maximum deformations were reached (elastic-plastic). All simulations were modeled using Hypermesh 9.0 (Altair Corporation, Troy, MI) as the preprocessor, a Massively Parallel Platform (MPP) version of LS-DYNA 970 on a four-node cluster (two processors per node) as the solver and LS-PrePost 2.4 (LSTC Corporation, Livermore, CA) as the postprocessor. Structural deformation depths obtained in the simulations were compared with the deformation profile C1 to C6 reported as per SAEJ2433 in the CIREN data (Figure 4).

A local coordinate system was established on the struck case vehicle to obtain deformation in the local axis. For the case vehicles, the driver side structures (including the front and rear doorframe, door armrest, and left B-pillar nodes) were grouped and their motions were recorded in separate binary interface files. These interface files were used as inputs for Stage II simulations.

In Stage II, the interface files which consist of nodal kinematic histories and the submodel (left door structures) of the case vehicles' structures that might interact with the occupant were used as inputs to the WSHBM occupant model. The WSHBM was positioned as per the range of values

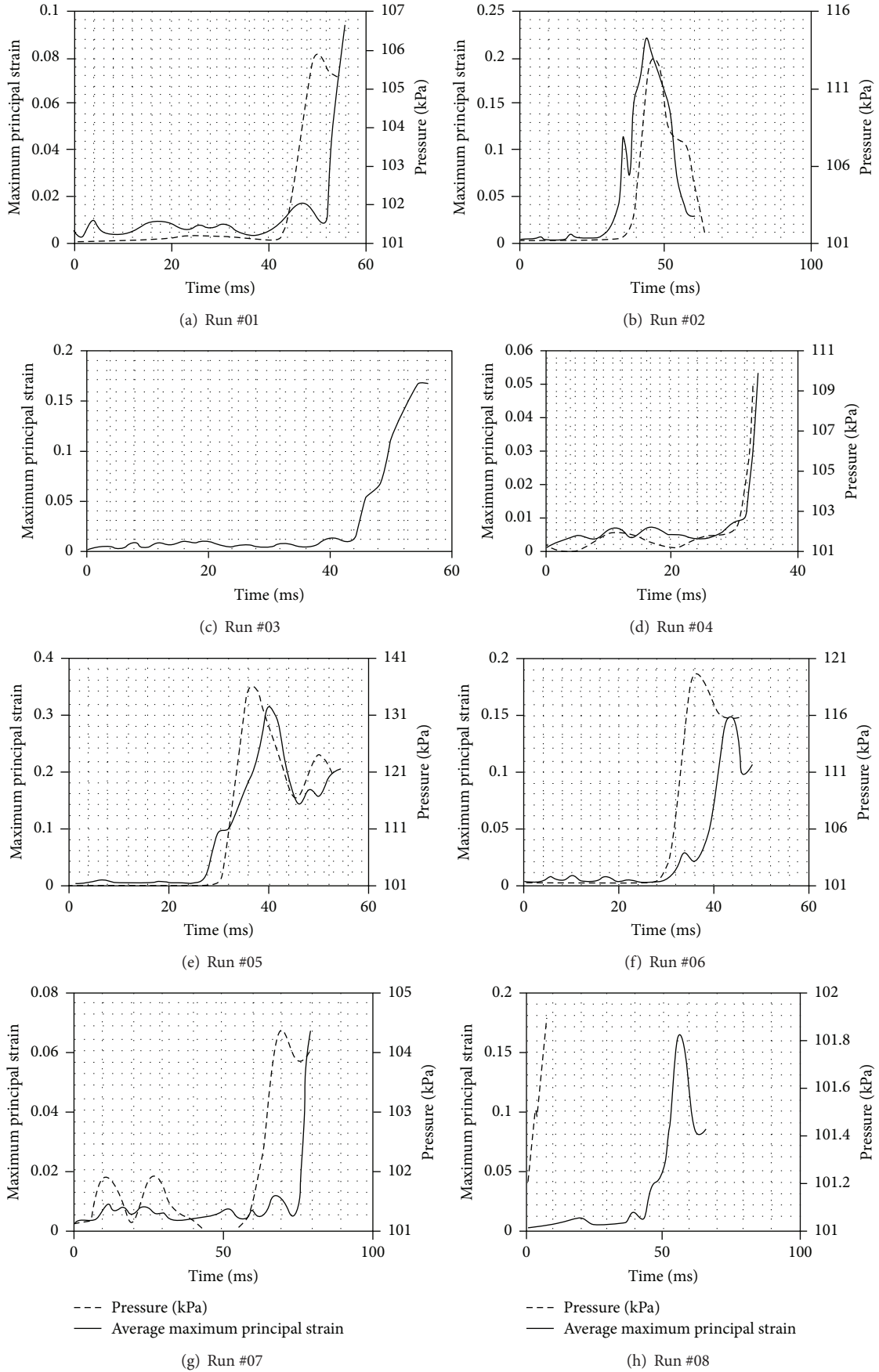


FIGURE 5: Continued.

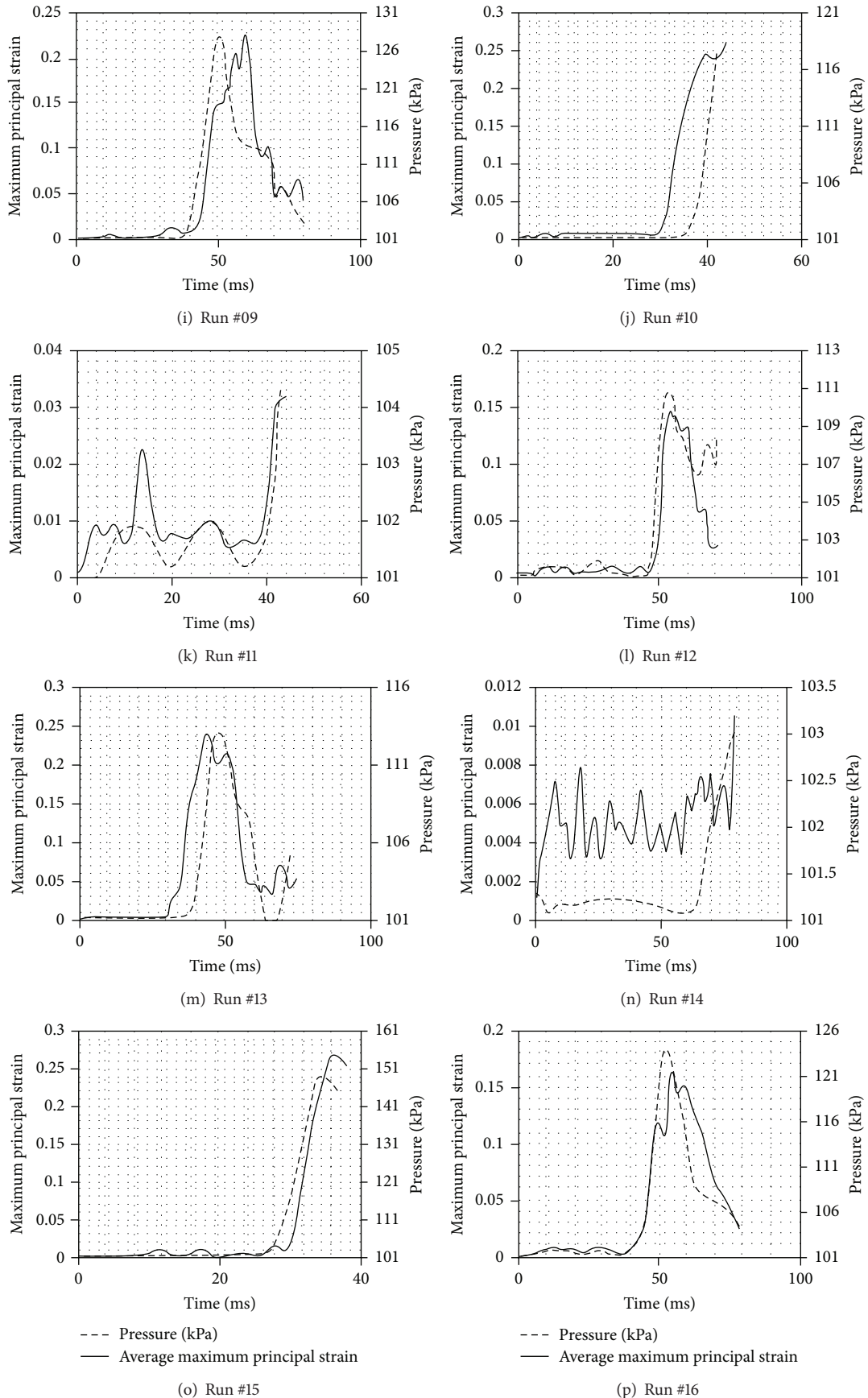


FIGURE 5: Average maximum principal strain in the isthmus and pressure: runs #01 through #08. Average maximum principal strain in the isthmus and pressure: runs #09 through #16.

TABLE 3: Failure versus nonfailure values of AMPS and maximum pressure in the aorta assessed based on failure criterion.

	Failure runs	Nonfailure runs	Significance ( $p$ )
Failure criterion = 22.1% strain [3]			
Average AMPS	0.247 $\pm$ 0.041	0.109 $\pm$ 0.058	0.001
Maximum pressure (kPa)	126.00 $\pm$ 14.15	114.86 $\pm$ 13.82	0.155
Failure criterion = 120 kPa pressure [9]			
Average AMPS	0.203 $\pm$ 0.061	0.129 $\pm$ 0.091	0.076
Maximum pressure (kPa)	131.85 $\pm$ 12.51	109.08 $\pm$ 5.017	0.003

for the DOCE setup defined in Table 1. A contact interface was created between the interior structures of the vehicle interior submodel and the occupant model. Simulation output provided the overall occupant kinematics at the time of the peak vehicle deformation and the average maximum principal strain (AMPS) and maximum pressure in the aorta predicted by the occupant model.

## B. Case #7 Description

This case involved a 34-year-old African-American male driver (weight = 83 kgs and height = 1630 mm) of a 1993 Toyota Corolla (weight = 1085 kgs) struck broadside by a 1996 Dodge Caravan (weight = 1085 kgs). The subject was utilizing the three-point belt system and the frontal air bag deployed at the time of impact. The patient sustained fatal injuries including a 30 mm transverse laceration of the aortic isthmus on the posterior right side of the isthmus, located 35 mm distal to the left subclavian artery orifice. There was an associated aortic dissection and mediastinal hemorrhage. There was a second fatal injury involving a basilar skull fracture of the “hinge” type with atlantooccipital dislocation. The driver was dead at the scene. The Delta-V on impact for the case vehicle calculated by WinSmash was 59 kph with an impact at a PDOF of 280 degrees.

## Conflict of Interests

This is to certify that neither Aditya Belwadi nor King H. Yang has/had any financial interests or support or assistance from any organization or trademark for this paper.

## Acknowledgments

The Southern Consortium of Injury Biomechanics (SCIB) has funded the current study. The authors are extremely grateful to Dr. John Siegel (New Jersey Medical School, NJ) for providing the CIREN data. The primary author was also supported by the 2009 Anthony and Kales Scholarship Award.

## References

- [1] R. S. Smith and F. C. Chang, “Traumatic rupture of the aorta: still a lethal injury,” *The American Journal of Surgery*, vol. 152, no. 6, pp. 660–663, 1986.
- [2] H. M. Burkhart, G. A. Gomez, L. E. Jacobson, J. E. Pless, and T. A. Broadie, “Fatal blunt aortic injuries: a review of 242 autopsy cases,” *Journal of Trauma—Injury, Infection and Critical Care*, vol. 50, no. 1, pp. 113–115, 2001.
- [3] C. S. Shah, W. N. Hardy, K. H. Yang, C. A. Van Ee, R. M. Morgan, and K. H. Digges, “Investigation of the traumatic rupture of the aorta (TRA) by simulating real-world accidents,” in *Proceedings of the International IRCOBI Conference on the Biomechanics of Injury*, pp. 349–359, Maastricht, The Netherlands, September 2007.
- [4] J. H. Siegel, A. Belwadi, J. A. Smith, C. Shah, and K. Yang, “Analysis of the mechanism of lateral impact aortic isthmus disruption in real-life motor vehicle crashes using a computer-based finite element numeric model: with simulation of prevention strategies,” *Journal of Trauma—Injury, Infection and Critical Care*, vol. 68, no. 6, pp. 1375–1394, 2010.
- [5] C. S. Shah, M. Maddali, S. A. Mungikar et al., “Analysis of a real-world crash using finite element modeling to examine traumatic rupture of the aorta,” in *Proceedings of the SAE World Congress on Occupant Safety, Safety-Critical Systems, and Crashworthiness*, Detroit, Mich, USA, April 2005.
- [6] A. Belwadi, J. H. Siegel, A. Singh, J. A. Smith, K. H. Yang, and A. I. King, “Finite element aortic injury reconstruction of near side lateral impacts using real world crash data,” *Journal of Biomechanical Engineering*, vol. 134, no. 1, Article ID 011006, 2012.
- [7] W. N. Hardy, C. S. Shah, M. J. Mason et al., “Mechanisms of traumatic rupture of the aorta and associated peri-isthmus motion and deformation,” *Stapp Car Crash Journal*, vol. 52, pp. 233–265, 2008.
- [8] S. E. Bammel and J. Rothstein, “The number of  $9 \times 9$  latin squares,” *Discrete Mathematics*, vol. 11, pp. 93–95, 1975.
- [9] C. R. Bass, K. Darvish, B. Bush et al., “Material properties for modeling traumatic aortic rupture,” *Stapp Car Crash Journal*, vol. 45, pp. 143–160, 2001.
- [10] C. S. Shah, W. N. Hardy, M. J. Mason et al., “Dynamic biaxial tissue properties of the human cadaver aorta,” *Stapp Car Crash Journal*, vol. 50, pp. 217–246, 2006.

## Research Article

# Numerical Study of Turbulent Pulsatile Blood Flow through Stenosed Artery Using Fluid-Solid Interaction

Mehdi Jahangiri,<sup>1</sup> Mohsen Saghafian,<sup>1</sup> and Mahmood Reza Sadeghi<sup>2</sup>

<sup>1</sup>Department of Mechanical Engineering, Isfahan University of Technology, Isfahan 8415683111, Iran

<sup>2</sup>Department of Biomedical Engineering, University of Isfahan, Isfahan 8174673441, Iran

Correspondence should be addressed to Mehdi Jahangiri; [m.jahangiri@me.iut.ac.ir](mailto:m.jahangiri@me.iut.ac.ir)

Received 4 November 2014; Accepted 24 March 2015

Academic Editor: Eduardo Soudah

Copyright © 2015 Mehdi Jahangiri et al. This is an open access article distributed under the Creative Commons Attribution License, which permits unrestricted use, distribution, and reproduction in any medium, provided the original work is properly cited.

The turbulent pulsatile blood flow through stenosed arteries considering the elastic property of the wall is investigated numerically. During the numerical model validation both standard  $k-\epsilon$  model and RNG  $K-\epsilon$  model are used. Compared with the RNG  $K-\epsilon$  model, the standard  $K-\epsilon$  model shows better agreement with previous experimental results and is better able to show the reverse flow region. Also, compared with experimental data, the results show that, up to 70% stenosis, the flow is laminar and for 80% stenosis the flow becomes turbulent. Assuming laminar or turbulent flow and also rigid or elastic walls, the results are compared with each other. The investigation of time-averaged shear stress and the oscillatory shear index for 80% stenosis show that assuming laminar flow will cause more error than assuming a rigid wall. The results also show that, in turbulent flow compared with laminar flow, the importance of assuming a flexible artery wall is more than assuming a rigid artery wall.

## 1. Introduction

Atherosclerosis is a disease that is characterized by the formation of plaques that narrow the arterial lumen. The narrowing of the coronary arteries can stop the perfusion of blood to the lower parts of the myocardium and possibly lead to myocardial ischemia, myocardial infarction, and sudden cardiac death [1].

In the study of the causes and progression of this disease, in addition to conventional methods in the medicine for forecasting and evaluating the disease progress, computational fluid dynamics are used to examine the role of hemodynamics on the localization, development, and progression of atherosclerosis disease. Simultaneous with hemodynamic studies, some researchers have focused on modeling the arterial wall and have examined the relationship between arterial wall stress and vessel wall diseases [2–4].

Recently, researchers have paid great attention to the effect of fluid-solid interaction in biological systems, especially cardiovascular ones. They believe that the simultaneous

solution of fluid-solid will greatly help in better understanding the pattern of arterial disease [5, 6].

For example, Bathe and Kamm [7] simulated the laminar pulsatile flow passing through a flexible artery with stenosis using ADINA Software. They considered stenoses of 51% and 96% area reduction and evaluated and compared the pressure drop and circumferential stress across the artery at different times. They also studied the effect of Reynolds number on the pressure drop.

Tang et al. [8] numerically examined laminar flow in flexible carotid artery with symmetric stenosis using ADINA software. Their results showed that severe stenosis causes critical flow conditions such as negative pressure and high and low shear stress which may lead to artery compression, plaque rupture, platelet activation, and arterial thrombosis.

Although in such studies the flexibility of the artery wall has been considered, they have ignored the turbulence caused by stenosis. In fact, blood flow in arteries is usually laminar. However, a moderate or severe stenosis can cause turbulent flow in the vasculature [9]. A better understanding of the flow

and flow turbulence in the poststenotic region can lead to more accurate diagnostic methods [10]. Turbulent blood flow due to arterial stenosis has long been investigated [11].

Many experimental studies have been conducted for studying a steady turbulent flow [12–14]. Deshpande and Giddens [13] studied the steady turbulent flow through a 75% stenosed tube at Reynolds numbers ranging from 5000 to 15000 by laser Doppler anemometer (LDA). Ahmed and Giddens [14] measured the steady velocity field in the presence of a symmetric stenosis with a rigid wall by the LDA. The range of the Reynolds number was 500–2000 in the upstream of the stenosis and stenoses of 25, 50, and 75% area reduction were studied.

Due to difficulties in performing experimental tests, there are only a few experimental studies for unsteady turbulent flow in the presence of stenosis.

Ahmed and Giddens [15] measured pulsating flow field in the presence of a symmetric stenosis by the LDA. They considered sinusoidal velocity profile, a Womersley number of 7.5, stenoses of 25, 50, and 75% area reduction, and the average Reynolds number of 600 for testing.

These experimental studies showed that, even with a low percentage of stenosis, transient or turbulent flow may occur. The above experimental data were used for assessment of numerical methods for modeling of turbulent flow in internal flows. On the other hand since the turbulent flow calculations are difficult and time-consuming, there are very few computational studies on the turbulent pulsatile flow in the artery with a stenosis. For example, using the finite element software FIDAP, Ghalichi et al. [16] investigated transient and turbulent flow through 50%, 75%, and 85% stenosed models over a Reynolds number range of 500 to 2000. Their results showed that the laminar flow model overestimates the vortex length when the flow becomes transitional or turbulent.

Banks and Bressloff [17] modeled pulsatile turbulent flow in the carotid bifurcation with a stenosis by a three-dimensional model. FLUENT software was used for solving the set of governing equations. Three types of stenosis (mild, moderate, and severe) were considered, and the effect of turbulence intensity and turbulent viscosity on velocity profiles was studied.

Since wall elastic property and physiological pulses are not considered as boundary conditions in these studies, in the present study the turbulent blood flow through a stenotic artery model is numerically simulated considering fluid-structure interaction (FSI) using ADINA 8.8. At first the effect of turbulent blood flow on the variations of time-averaged shear stress and the oscillatory shear index for 80% stenosis is investigated. Then the obtained results are compared with the results of assuming laminar flow and rigid wall of coronary artery.

## 2. Governing Equations

*2.1. Reynolds-Averaged Navier–Stokes Equations (RANS) [18].* In unsteady turbulent flows, if we consider each parameter as the sum of an average component and an oscillating

component in the Navier–Stokes equation, then the RANS equations are obtained as follows:

$$\begin{aligned} \frac{\partial \bar{u}_i}{\partial x_i} &= 0, \\ \frac{D\bar{u}_i}{Dt} &= -\frac{1}{\rho} \frac{\partial \bar{P}}{\partial x_i} + \frac{\partial}{\partial x_j} \left( \frac{\mu + \mu_T}{\rho} \left( \frac{\partial \bar{u}_i}{\partial x_j} + \frac{\partial \bar{u}_j}{\partial x_i} \right) \right). \end{aligned} \quad (1)$$

*2.2. Turbulence Models [18].* To calculate  $\mu_T$ , this paper uses the two-equation turbulence  $K$ - $\varepsilon$  standard and  $K$ - $\varepsilon$  RNG models. In the turbulence flow, viscosity is defined as follows, where  $\mu_0$  is laminar viscosity and  $\mu_T$  is turbulence viscosity:

$$\mu = \mu_T + \mu_0. \quad (2)$$

In  $K$ - $\varepsilon$  standard turbulence model,  $\mu_T$  is calculated as follows:

$$\mu_T = \rho c_\mu \frac{k^2}{\varepsilon}, \quad (3)$$

where  $k$  is turbulence kinetic energy and  $\varepsilon$  is turbulence dissipation rate.

## 3. Numerical Validation

To check the accuracy of our numerical solution, the numerical results of the present work are compared with the experimental results presented by Ahmed and Giddens [15] and the numerical results provided by the Banks and Bressloff [17] and Varghese and Frankel [19].

If we consider the origin of coordinates at the center of stenosis, the numerical results of the present work were compared with the experimental results presented by Ahmed and Giddens [15] and the numerical results provided by Banks and Bressloff [17] and Varghese and Frankel [19] at two different distances of stenosis downstream and in the time of maximum speed. The results of Figures 1 and 2 indicate a better agreement of numerical data of the present work with the results of Ahmed and Giddens [15] than the numerical results of Banks and Bressloff [17] and the numerical work of Varghese and Frankel [19].

The results indicate a higher consistency between the  $K$ - $\varepsilon$  standard model and experimental results. As a result, the  $K$ - $\varepsilon$  standard model was used in this study.

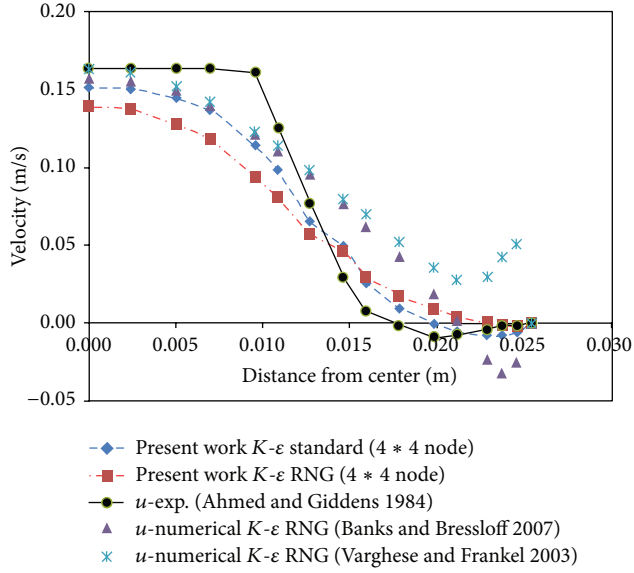
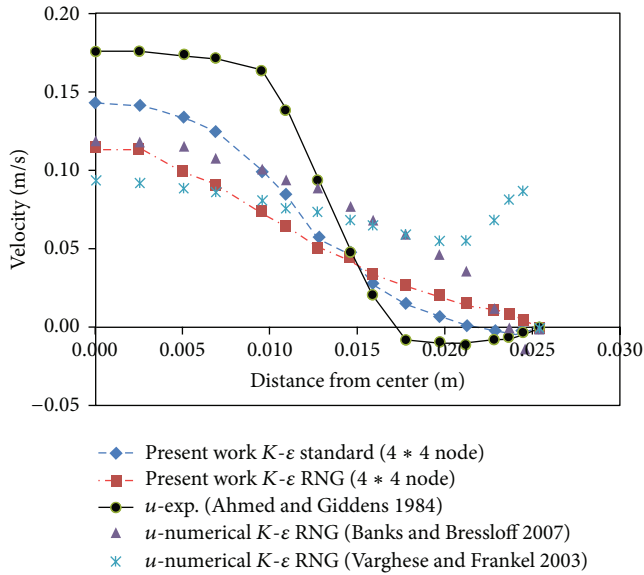
## 4. Present Work and Numerical Methods Used

In this study a model of coronary artery with a simple, symmetrical stenosis with flexible wall is considered. The computational domain and its dimensions are shown in Figure 3.

The geometry of stenosis is defined as follows [21]:

$$\frac{R(z)}{R_0} = 1 - \left( \frac{R_0 - R_{0,t}}{2R_0} \right) \left( 1 + \cos \frac{2\pi(z - z_m)}{L_{st}} \right), \quad (4)$$

where  $R_0$  is the radius of the healthy artery,  $R(z)$  is the artery radius in the stenosis region,  $R_{0,t}$  is artery radius at the stenosis throat,  $z_m$  is the location of the center of the stenosis,


 FIGURE 1: Velocity profile at distance  $z = D$  from throat of stenosis.

 FIGURE 2: Velocity profile at distance  $z = 1.5D$  from throat of stenosis.

and  $L_{st}$  is the length of stenosis. The characteristics of blood as a Newtonian, incompressible fluid and the characteristics of artery wall are given in Table 1 [21].

The pulsatile velocity profile of the right coronary artery was used as the inlet boundary condition [20]. Figure 4 shows the pulsatile velocity profile which is dimensionless by the period of pulsatile cycle,  $t_p$ , which is 0.8 s.

The fluid-structure interaction (FSI) conditions were used in the common boundary of fluid and solid. The

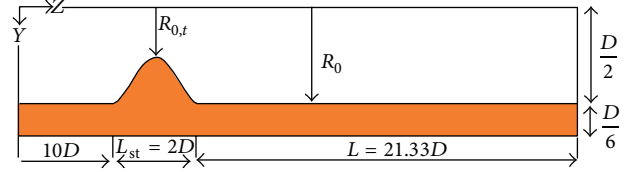


FIGURE 3: Computational domain.

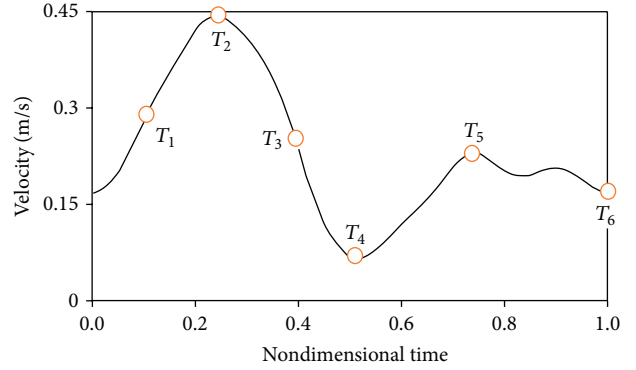


FIGURE 4: Inlet pulsatile velocity profile [20].

TABLE 1: Properties of fluid and artery wall.

Thickness of artery wall (m)	0.0005
Elasticity modulus of the artery wall (kPa)	910
Density of artery wall ( $\text{Kg/m}^3$ )	1300
Poisson ratio of artery wall	0.49
Blood density ( $\text{Kg/m}^3$ )	1050
Blood viscosity ( $\text{Pa}\cdot\text{s}$ )	0.0033

governing equations for the solid-fluid coupled problem are as follows [21]:

$$d_f = d_s; \text{ Displacement,}$$

$$n \cdot \sigma_f = n \cdot \sigma_s; \text{ Traction,} \quad (5)$$

$$\dot{d}_f = \dot{d}_s; \text{ No slip,}$$

where  $d$ ,  $\sigma$ , and  $n$  are displacement, stress tensor, and normal vectors. The governing equations of the solid domain are as follows [21]:

$$\rho_s \ddot{d}_s = \nabla \cdot \sigma_s + \rho_s f_s, \quad (6)$$

where  $\rho_s$  is the wall density,  $\sigma_s$  is the Cauchy stress tensor,  $f_s$  is the body force vector, and  $d_s$  is the wall displacement vector.

When studying the solid-fluid coupled problem, we should apply blood pressure pulse to the problem as the output condition. These pulses are obtained from experimental conditions and were shown in Figure 5 [21].

The axial velocity profiles at a distance of  $1D$  from the stenosis throat in three types of meshing are shown in Figure 6. The results indicated that the results of 10200 computational cells and 15300 computational cells are consistent with each other. Thus, for reducing the computational time, 10200 computational cells will be used for calculations.

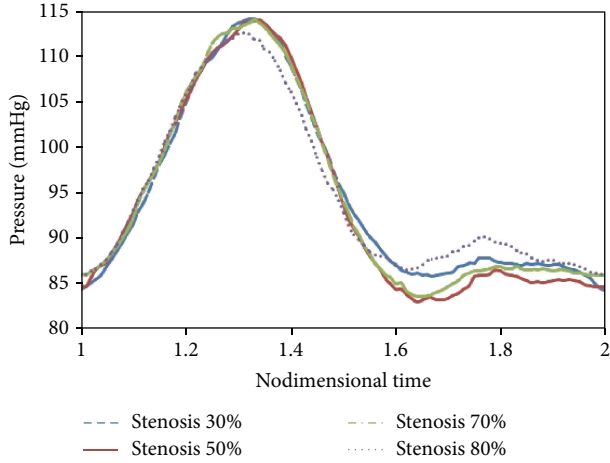


FIGURE 5: Outlet pressure pulse.

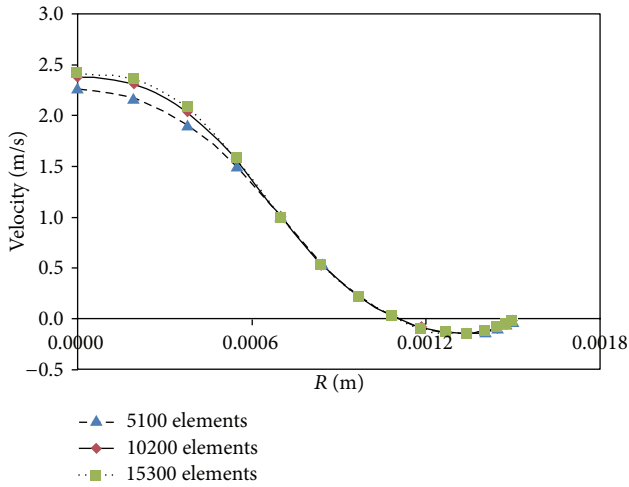


FIGURE 6: Results independency from grid of solution domain.

## 5. Results

Comparisons between the mean inlet pressure ( $P_1$ ) for stenosis percentages of 30%, 50%, 70%, and 80% are given in Figure 7. As can be seen, up to 70% stenosis, there is a very good consistency between experimental results [21] and the laminar flow assumption which suggests that, up to 70% stenosis, the flow is laminar. Shifting from 70% to 80%, the difference between experimental results and the laminar flow assumption increases, and there is a much higher consistency between experimental results and the turbulence flow assumption which suggests that, for 80% stenosis and higher, the flow is turbulent and the laminar flow assumption is not appropriate anymore. Mean inlet pressure for 80% stenosis in the case of laminar flow assumption is 102.4 mmHg, in the turbulent flow case is 105 mmHg, and in the experimental case is 104.8 mmHg. Given above, we select 80% stenosis and perform next calculations on it.

Figures 8 to 15 show the timed-averaged changes of shear stress and the oscillatory shear index in the axial

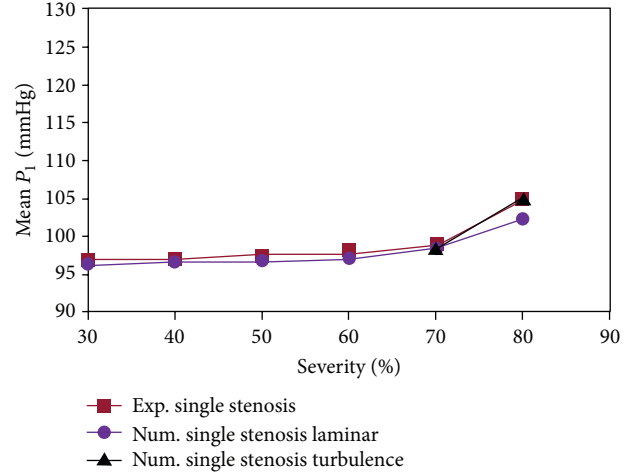


FIGURE 7: Comparisons between the inlet pressure.

direction for 80% stenosis for the laminar or turbulent flow assumption and the rigid or flexible wall assumption. The time-averaged shear stress and the oscillatory shear index are among hemodynamic parameters used for identifying areas prone to arteriosclerosis.

The oscillatory shear index (OSI) is a mechanical parameter for flow oscillation showing the deviation of the wall shear stress from the dominant direction of blood flow during the cardiac cycle. The OSI value ranges from zero (for no change in the direction of wall shear stress) to 0.5 (for a 180-degree change in the direction of wall shear stress) [22]. To determine the OSI value, the following equation is used:

$$\text{OSI} = 0.5 \times \left( 1 - \frac{\left| \int_0^T \tau_w dt \right|}{\int_0^T |\tau_w| dt} \right). \quad (7)$$

Time-averaged shear rate is defined as follows:

$$\text{Mean WSS} = \frac{1}{T} \int_0^T \tau_w dt. \quad (8)$$

In the above equations,  $T$  is the periodicity of the cardiac cycle and  $\tau_w$  is the shear stress vector.

As is clear from Figures 8 to 11, by changing from the flexible-wall mode to the rigid-wall mode as well as from the laminar flow assumption to the turbulent flow assumption, the time-averaged shear stress slightly increases in the prestenotic area. At the proximal shoulder region, the time-averaged shear stress significantly increases and, at the distal shoulder and poststenotic region, the time-averaged shear stress decreases further. This decrease in shear stress increases the production of reactive oxygen species and essentially increases the oxidation of LDLs in the intima. Oxidized LDLs stimulate endothelial cells to express leukocyte adhesion molecules such as vascular cell adhesion molecule-1 (VCAM-1) and intercellular adhesion molecule-1 (ICAM-1). Consequently, platelet adhesion to the endothelium and activation is possible, in an area where shear stress is low. Activated platelets release growth factors

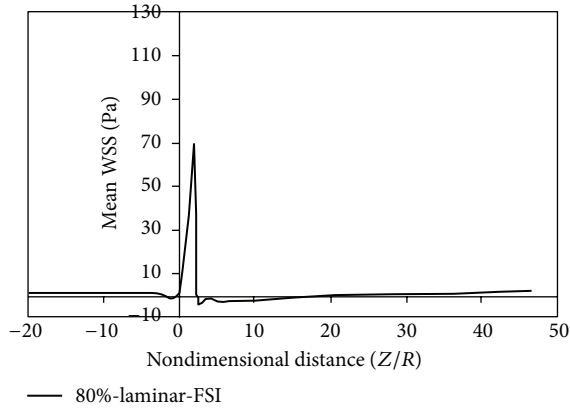


FIGURE 8: Mean WSS, laminar, flexible mode.

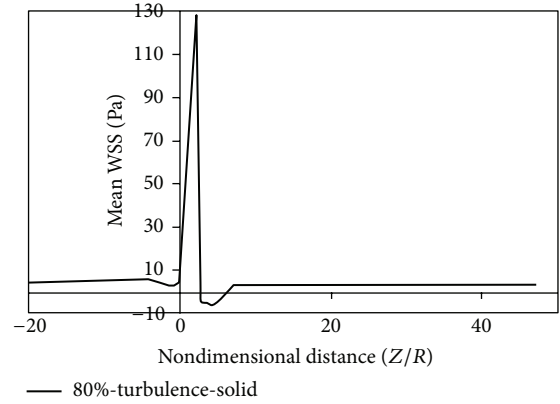


FIGURE 11: Mean WSS, turbulence, and solid mode.

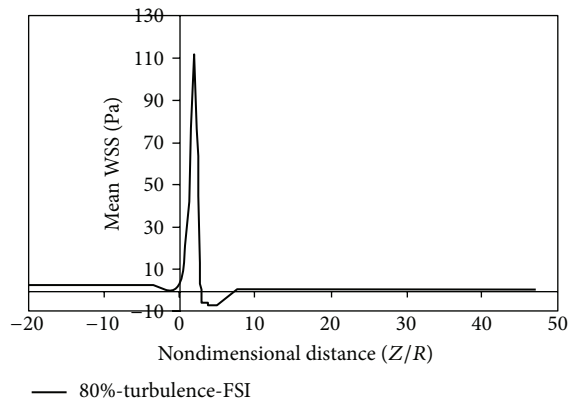


FIGURE 9: Mean WSS, turbulence, flexible mode.

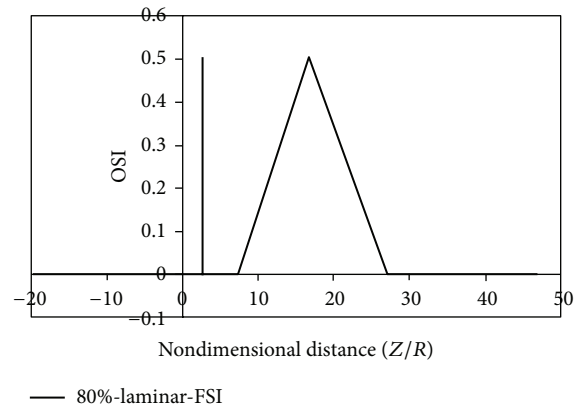


FIGURE 12: OSI, laminar, flexible mode.

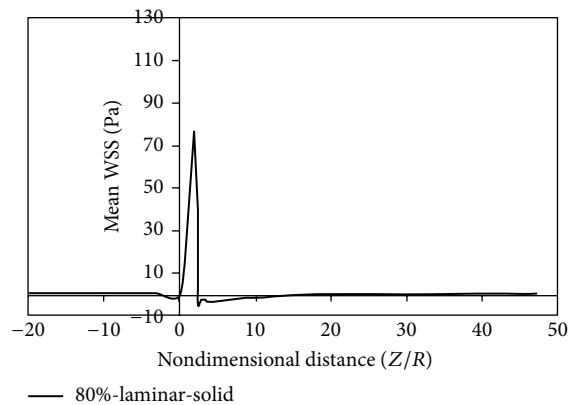


FIGURE 10: Mean WSS, laminar, and solid mode.

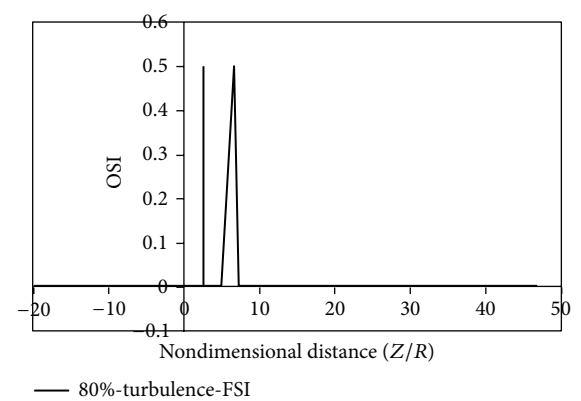


FIGURE 13: OSI, turbulence, flexible mode.

such as TGF- $\beta$ . TGF- $\beta$  significantly enhances proliferation of smooth muscle cells [23]. Studies have also shown that activated platelets release MMP-2, which mediates further platelet aggregation [24]. Thus poststenotic area not only is prone to develop plaque and new plaque formation, but also is more prone to the development of thrombosis. Angiographic studies have shown that plaque development occurs more in the poststenotic area [25] and the number of smooth muscle cells in the distal shoulder is far more than the proximal [26].

It can be seen from Figures 12 to 15 that there are two peaks for simple stenoses. In the simple stenosis, the first peak shows flow separation point and the second peak represents the reattachment point. Small values of time-averaged shear stress and high values of the oscillatory shear index both influence the cell secretion resulting in increased cell displacement and increased dissociation of intercellular junctions thereby increasing permeability of the LDL particles to the wall [27–29]. The experimental

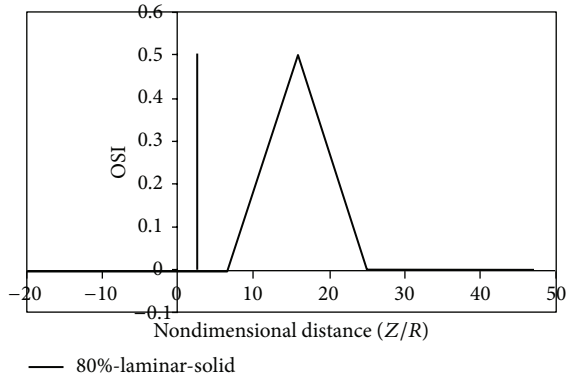


FIGURE 14: OSI, laminar, solid mode.

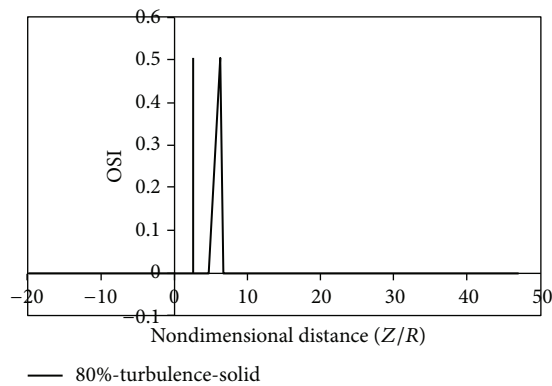


FIGURE 15: OSI, turbulence, solid mode.

results of Deng et al. [30] also show high absorption of cholesterol in the flow reattachment point. Another thing that can be seen in Figures 12 to 15 is that for both the rigid artery wall mode and the flexible artery wall mode, by changing the laminar flow assumption to the turbulent flow assumption, the length of oscillatory zone highly decreases. This shows that, in high percentages of stenosis when using any of hemodynamic parameters, average shear stress, and oscillatory shear index for describing how the disease is developed, failure to consider the turbulent flow behavior can cause a large numerical error.

Fry [31] stated that a shear stress over 40 Pa causes damage to endothelial cells. Ramstack et al. [32] stated that a shear stress greater than 100 Pa causes detachment of endothelial cells and clot formation. According to the contents of references [31, 32] and Figures 8–11 it can be seen that, in 80% stenosis with the laminar flow assumption, the endothelial cell operation is damaged. However, in 80% stenosis assuming turbulent flow, given that the maximum stress is greater than 100 Pa, the clot will form. Thus ignoring turbulence can make a different change in predicting damages. As can be seen in Figures 8 up to 15, the effect of turbulent flow on the maximum time-averaged shear stress of the wall on stenosis and the mean reverse flow area is more important than assuming flexible wall. The result that can be derived from Figure 16 is that the wall displacement with

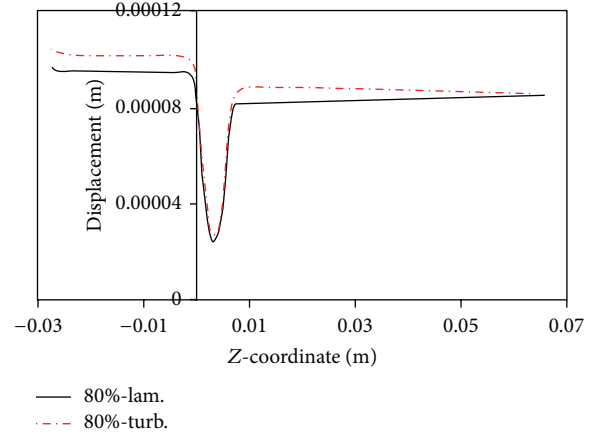
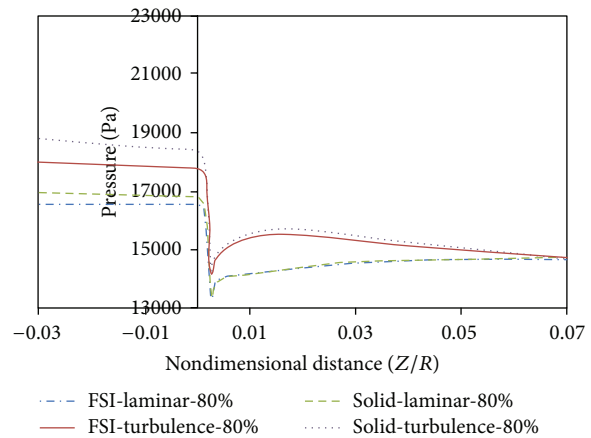


FIGURE 16: Radial displacement of wall at different mode.

FIGURE 17: Changes in arterial pressure in the axial direction,  $T_2$ .

the turbulent flow assumption is more than the laminar flow assumption. Moreover, due to hypotension, the artery wall displacement in front of stenosis is more than the artery wall displacement at the back of stenoses.

Figure 17 shows changes in arterial pressure in the axial direction for simple stenosis with 80% stenosis at the maximum flow rate time. As can be seen from Figure 17, changing from flexible to rigid wall will increase the pressure in the proximal of stenosis. Moreover, changing from laminar to turbulent flow will increase the pressure in the proximal of stenosis. The hypotension in the turbulent mode is higher than the laminar mode and in the rigid wall artery mode higher than the flexible wall artery because of higher shear stress along the artery and consequently increased hypotension across the artery. Another result from Figure 17 is that, in front of the stenosis, the pressure difference at rigid and flexible modes is lower than at the back of stenosis. The reason is that, with decreasing pressure, the displacement of artery wall decreases and the artery wall becomes closer to the rigid mode.

Figures 18 to 20 compare changes in circumferential stresses in time at different points for 80% stenosis. As can be seen, compared to the turbulent flow assumption,

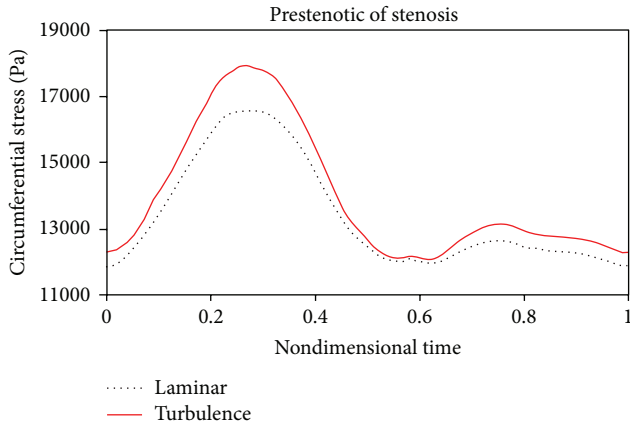


FIGURE 18: Circumferential stress, prestenotic.

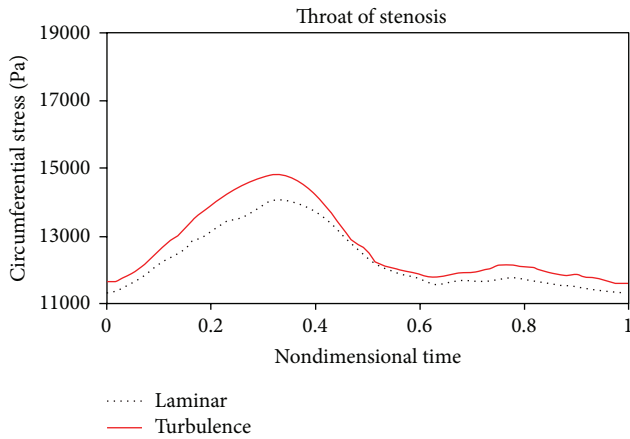


FIGURE 19: Circumferential stress, throat of stenosis.

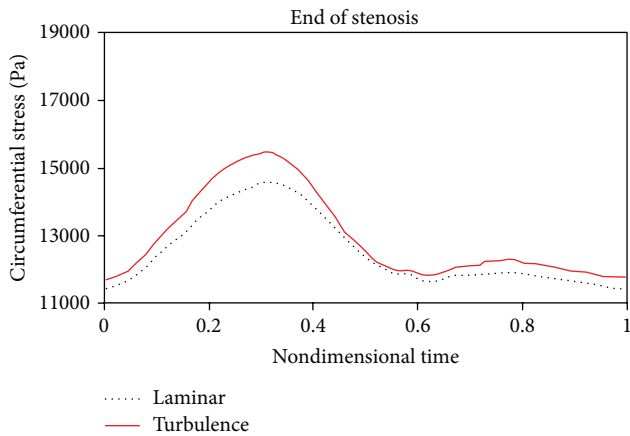


FIGURE 20: Circumferential stress, end of stenosis.

the laminar flow assumption shows lower circumferential stresses for the artery wall. The maximum circumferential stress is related to prestenotic zone because, according to Figure 17, the pressure exerted on the wall before the stenosis is higher. The minimum circumferential stresses are related to the stenosis peak because according to Figure 17, there is a

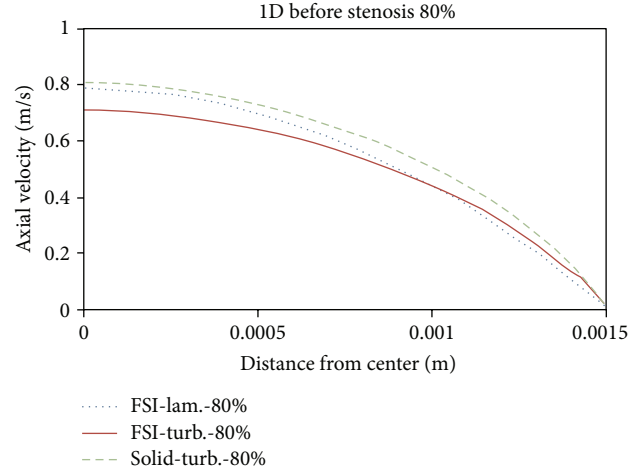


FIGURE 21: Axial velocity, 1D before stenosis.

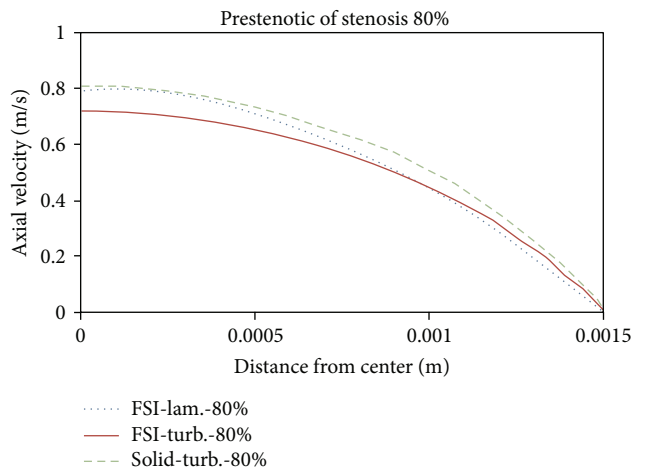


FIGURE 22: Axial velocity, prestenotic of stenosis.

sudden pressure drop due to serious tweaking. Another result from Figures 18 to 20 is that the laminar flow assumption at the stenosis peak shows circumferential stress lower than the turbulent flow assumption.

Figures 21 to 24 show axial velocity profiles at the time of maximum flow rate (0.24 s), at a distance equal to the diameter before the stenosis, at the beginning of the stenosis, the throat, and the poststenotic of a simple 80% stenosis. Due to axial velocity profiles and also as expected the profile of turbulent flow assumption was obtained flatter than the laminar flow assumption, and the rigid wall mode further demonstrates maximum axial velocity. Figure 23 shows velocity profiles at the throat of the simple stenosis. It shows that the maximum velocity reaches a value much higher than 1 m/s. This value is beyond a normal biological mode and may cause disturbances in the blood circulatory system. Also, as can be seen in Figure 24, at the end of stenosis compared with the throat of the stenoses, the maximum velocity is reduced and both the laminar flow assumption and the turbulent flow assumption at near of the wall predict the reverse flow.

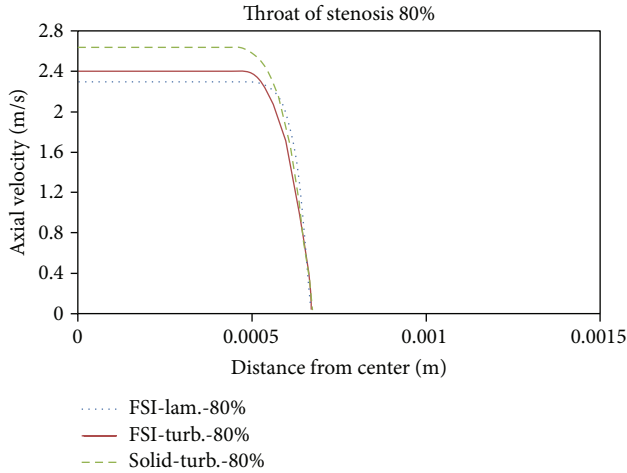


FIGURE 23: Axial velocity, throat of stenosis.

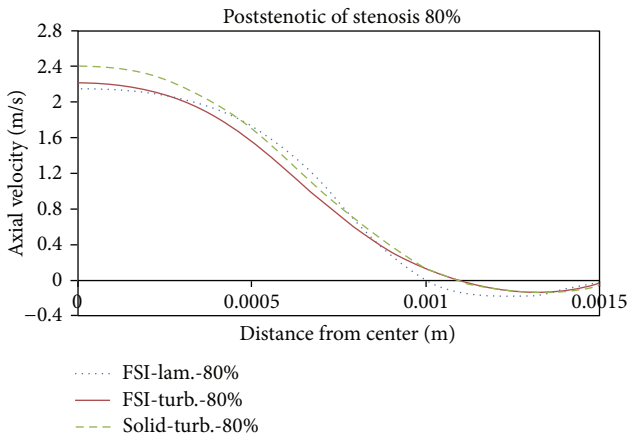


FIGURE 24: Axial velocity, poststenotic of stenosis.

However, the laminar flow overestimates the reverse flow and shows the reverse flow zone larger which is obvious because the fluid has a lower energy and is soon detached from the surface. In other words, using the laminar flow assumption a wider zone at the back of stenosis is exposed to the disease and using the turbulent flow assumption the growth speed of plaques is higher.

In Figures 25–28 distribution of pressure, shear stress at  $T_2$  and  $T_4$  and axial velocity along the artery are shown, respectively. As seen, minimum pressure and maximum axial velocity occurred in the throat of stenosis. In distal of stenosis by reducing the velocity, the pressure is increased and Figure 17 also showed this. By away from stenosis region and reducing the effects of narrowing and opening of the flow cross section, pressure is reduced linearly. Blood shear stresses that exerted from the artery wall are shown in Figures 26 and 27. Because of high similarity between turbulent and FSI case study contour by other case studies, contours of other cases have been ignored. At the narrowest of cross section it can be seen from Figure 26 that shear stress increased suddenly and immediately after stenosis throat reduced



FIGURE 25: Pressure distribution at maximum flow rate  $T_2$ , FSI-Turb.



FIGURE 26: Shear stress distribution at maximum flow rate  $T_2$ , FSI-Turb.



FIGURE 27: Shear stress distribution at minimum flow rate  $T_4$ , FSI-Turb.

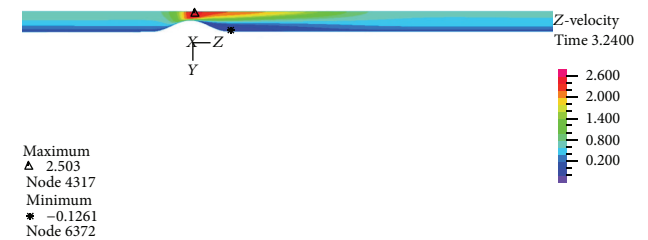


FIGURE 28: Velocity distribution at maximum flow rate  $T_2$ , FSI-Turb.

severely and even negative values are seen. Then shear stress in the reverse flow region increased by mild slope and again gives positive value and remains constant until the end of the artery. As can be seen from Figures 26 and 27 the difference between the shear stress on the artery wall at maximum and minimum flow rate is very high and almost 11.6 times and, at other times of the cardiac cycle, shear stress on the artery wall has continuous changes. These frequent changes on the inner surface of the artery can lead to plaque rupture that can cause severe cramping and formation and the development of blood clot in the arteries. According to Figure 28, minimum axial velocity is  $-0.1261$  m/s and occurred at the end of stenosis and maximum axial velocity is  $2.503$  m/s and occurred at the throat of stenosis.

## 6. Conclusion

Using ADINA software and taking into account the elastic wall and physiological pulses as a boundary condition, this paper assesses blood flow passing through the right coronary artery with a local stenosis. Compared with other numerical works, the  $K-\epsilon$  standard model had a better consistency with the experimental work and was better able to show the reverse flow region. We therefore used the  $K-\epsilon$  standard turbulence model to resolve the turbulent flow in the present numerical work. In the present work, the average inlet pressure for 80% stenosis in the laminar flow assumption was obtained 102.4 and at the turbulent flow assumption was obtained 105 compared with the other experimental works which was 104.8. This indicates that, for 80% stenosis, the flow is turbulent. As a result, 80% stenosis was selected as the sample stenosis. The effects of turbulent blood flow were examined on pressure drop and velocity profiles. The obtained results were compared with those of the laminar flow assumption and the rigid coronary artery wall. For both the rigid artery wall and the flexible artery wall, by changing from the laminar flow assumption to the turbulent flow assumption, the length of oscillatory region becomes much lower. This shows that in high percentages of stenosis when using any of the hemodynamic parameters of the average shear stress and the oscillatory shear index for describing how the disease is spread, failure to consider the turbulent flow behavior can cause a large numerical error. Another result of the present work is that, in 80% stenosis, the rigid artery wall assumption makes a smaller error compared to the laminar blood flow assumption.

## Conflict of Interests

The authors declare that there are no financial or personal relationships with people or organizations that have inappropriately influenced this work.

## References

- [1] V. Fuster, "Human lesion studies," *Annals of the New York Academy of Sciences*, vol. 811, no. 1, pp. 207–225, 1997.
- [2] M. Tafazzoli, *Analysis of mechanical stress in arteries with changes in wall structural properties [Ph.D. thesis]*, Graduate School of Biomedical Engineering, University of New South Wales, New South Wales, Australia, 1999.
- [3] M. A. Zulligera, P. Frideza, K. Hayashib, and N. Stegiopulosa, "A strain energy function for arteries accounting for wall composition and structure," *Journal of Biomechanics*, vol. 37, no. 7, pp. 989–1000, 2004.
- [4] T. Matsumoto, T. Goto, T. Furukawa, and M. Sato, "Residual stress and strain in the lamellar unit of the porcine aorta: experiment and analysis," *Journal of Biomechanics*, vol. 37, no. 6, pp. 807–815, 2004.
- [5] W. Shyy, M. Francois, H. S. Udaykumar, N. N'dri, and R. Tran-Son-Tay, "Moving boundaries in micro-scale biofluid dynamics," *Applied Mechanics Reviews*, vol. 54, no. 5, pp. 405–452, 2001.
- [6] X. Y. Xu, A. D. Augst, B. Ariff, and S. A. Thom, "Analysis of complex flow and its relationship with wall thickening in the carotid artery bifurcation," in *Proceedings of the 11th International Conference on Computational Bioengineering*, Lisbon, Portugal, September 2005.
- [7] M. Bathe and R. D. Kamm, "A fluid-structure interaction finite element analysis of pulsatile blood flow through a compliant stenotic artery," *Journal of Biomechanical Engineering*, vol. 121, no. 4, pp. 361–369, 1999.
- [8] D. Tang, C. Yang, and D. N. Ku, "A 3-D thin-wall model with fluid-structure interactions for blood flow in carotid arteries with symmetric and asymmetric stenoses," *Computers and Structures*, vol. 72, no. 1–3, pp. 357–377, 1999.
- [9] L. Wei, *Numerical study of steady and pulsatile flow through stenosed tubes [Ph.D. thesis]*, Department of Mechanical Engineering, National University of Singapore, Singapore, 2004.
- [10] R. Mittal, S. P. Simmons, and H. S. Udaykumar, "Application of large-eddy simulation to the study of pulsatile flow in a modeled arterial stenosis," *Journal of Biomechanical Engineering*, vol. 123, no. 4, pp. 325–332, 2001.
- [11] M. R. Roach, "Poststenotic dilatation in arteries," *Cardiovascular Fluid Dynamics*, vol. 2, pp. 111–139, 1972.
- [12] C. Clark, "Turbulent velocity measurements in a model of aortic stenosis," *Journal of Biomechanics*, vol. 9, no. 11, pp. 677–687, 1976.
- [13] M. D. Deshpande and D. P. Giddens, "Turbulence measurements in a constricted tube," *Journal of Fluid Mechanics*, vol. 97, no. 1, pp. 65–89, 1980.
- [14] S. A. Ahmed and D. P. Giddens, "Velocity measurements in steady flow through axisymmetric stenoses at moderate Reynolds numbers," *Journal of Biomechanics*, vol. 16, no. 7, pp. 505–516, 1983.
- [15] S. A. Ahmed and D. P. Giddens, "Pulsatile poststenotic flow studies with laser Doppler anemometry," *Journal of Biomechanics*, vol. 17, no. 9, pp. 695–705, 1984.
- [16] F. Ghalichi, X. Deng, A. De Champlain, Y. Douville, M. King, and R. Guidoin, "Low Reynolds number turbulence modeling of blood flow in arterial stenoses," *Biorheology*, vol. 35, no. 4–5, pp. 281–294, 1998.
- [17] J. Banks and N. W. Bressloff, "Turbulence modeling in three-dimensional stenosed arterial bifurcations," *Journal of Biomechanical Engineering*, vol. 129, no. 1, pp. 40–50, 2007.
- [18] ADINA R&D, *Theory and Modeling Guide, Volume III: ADINA CFD & FSI, Help of ADINA Software*, ADINA R&D, 2011.
- [19] S. S. Varghese and S. H. Frankel, "Numerical modeling of pulsatile turbulent flow in stenotic vessels," *Journal of Biomechanical Engineering*, vol. 125, no. 4, pp. 445–460, 2003.
- [20] D. Zeng, E. Boutsianis, M. Ammann, K. Boomsma, S. Wildermuth, and D. Poulidakos, "A study on the compliance of a right coronary artery and its impact on wall shear stress," *Journal of Biomechanical Engineering*, vol. 130, no. 4, Article ID 041014, 2008.
- [21] M. R. Sadeghi, E. Shirani, M. Tafazzoli-Shadpour, and M. Samaee, "The effects of stenosis severity on the hemodynamic parameters-assessment of the correlation between stress phase angle and wall shear stress," *Journal of Biomechanics*, vol. 44, no. 15, pp. 2614–2626, 2011.
- [22] J. V. Soulis, O. P. Lampri, D. K. Fytanidis, and G. D. Giannoglou, "Relative residence time and oscillatory shear index of non-newtonian flow models in aorta," in *Proceedings of the 10th International Workshop on Biomedical Engineering*, pp. 1–4, Kos, Greece, October 2011.

- [23] M. Gawaz, "Role of platelets in coronary thrombosis and reperfusion of ischemic myocardium," *Cardiovascular Research*, vol. 61, no. 3, pp. 498–511, 2004.
- [24] H. S. Bassiouny, R. H. Song, X. F. Hong, A. Singh, H. Kocharyan, and S. Glagov, "Flow regulation of 72-kD collagenase IV (MMP-2) after experimental arterial injury," *Circulation*, vol. 98, no. 2, pp. 157–163, 1998.
- [25] M. T. Dirksen, A. C. van der Wal, F. M. van den Berg, C. M. van der Loos, and A. E. Becker, "Distribution of inflammatory cells in atherosclerotic plaques relates to the direction of flow," *Circulation*, vol. 98, no. 19, pp. 2000–2003, 1998.
- [26] Ö. Smedby, "Do plaques grow upstream or downstream? An angiographic study in the femoral artery," *Arteriosclerosis, Thrombosis, and Vascular Biology*, vol. 17, no. 5, pp. 912–918, 1997.
- [27] D. N. Ku, D. P. Giddens, C. K. Zarins, and S. Glagov, "Pulsatile flow and atherosclerosis in the human carotid bifurcation. Positive correlation between plaque location and low oscillating shear stress," *Arteriosclerosis, Thrombosis, and Vascular Biology*, vol. 5, no. 3, pp. 293–302, 1985.
- [28] T. Kadohama, K. Nishimura, Y. Hoshino, T. Sasajima, and B. E. Sumpio, "Effects of different types of fluid shear stress on endothelial cell proliferation and survival," *Journal of Cellular Physiology*, vol. 212, no. 1, pp. 244–251, 2007.
- [29] U. Olgac, V. Kurtcuoglu, and D. Poulikakos, "Computational modeling of coupled blood-wall mass transport of LDL: effects of local wall shear stress," *The American Journal of Physiology—Heart and Circulatory Physiology*, vol. 294, no. 2, pp. H909–H919, 2008.
- [30] X. Deng, Y. Marois, M. W. King, and R. Guidoin, "Uptake of 3H-7-cholesterol along the arterial wall at an area of stenosis," *ASAIO Journal*, vol. 40, no. 2, pp. 186–191, 1994.
- [31] D. L. Fry, "Acute vascular endothelial changes associated with increased blood velocity gradients," *Circulation Research*, vol. 22, no. 2, pp. 165–197, 1968.
- [32] J. M. Ramstack, L. Zuckerman, and L. F. Mockros, "Shear-induced activation of platelets," *Journal of Biomechanics*, vol. 12, no. 2, pp. 113–125, 1979.

## Research Article

# Three-Dimensional Lower Extremity Joint Loading in a Carved Ski and Snowboard Turn: A Pilot Study

Miriam Klous,<sup>1,2</sup> Erich Müller,<sup>2</sup> and Hermann Schwameder<sup>2</sup>

<sup>1</sup> Department of Health and Human Performance, College of Charleston, Charleston, SC 29424, USA

<sup>2</sup> Department of Sport Science and Kinesiology, Christian Doppler Laboratory "Biomechanics in Skiing", University of Salzburg, 5400 Hallein, Salzburg, Austria

Correspondence should be addressed to Miriam Klous; [klousm@cofc.edu](mailto:klousm@cofc.edu)

Received 10 July 2014; Accepted 30 July 2014; Published 15 September 2014

Academic Editor: Eddie Y. K. Ng

Copyright © 2014 Miriam Klous et al. This is an open access article distributed under the Creative Commons Attribution License, which permits unrestricted use, distribution, and reproduction in any medium, provided the original work is properly cited.

A large number of injuries to the lower extremity occur in skiing and snowboarding. Due to the difficulty of collecting 3D kinematic and kinetic data with high accuracy, a possible relationship between injury statistic and joint loading has not been studied. Therefore, the purpose of the current study was to compare ankle and knee joint loading at the steering leg between carved ski and snowboard turns. Kinetic data were collected using mobile force plates mounted under the toe and heel part of the binding on skies or snowboard (KISTLER). Kinematic data were collected with five synchronized, panning, tilting, and zooming cameras. An extended version of the Yeadon model was applied to calculate inertial properties of the segments. Ankle and knee joint forces and moments were calculated using inverse dynamic analysis. Results showed higher forces along the longitudinal axis in skiing and similar forces for skiing and snowboarding in anterior-posterior and mediolateral direction. Joint moments were consistently greater during a snowboard turn, but more fluctuations were observed in skiing. Hence, when comparing joint loading between carved ski and snowboard turns, one should differentiate between forces and moments, including the direction of forces and moments and the turn phase.

## 1. Introduction

Skiing and snowboarding are the prominent winter sports and the general trend shows an increasing number of people participating in these sports [1–3]. With the increased number of practitioners, the number of injuries increased. Injury statistics have shown that skiing injuries mainly involve the lower extremities, predominantly the knee (18.1%–36.7%) [4–8] and the ankle joint (6%–12.2%) [6, 9–11]. In snowboarding, injuries occur when falling or during landings after a jump and mainly the upper extremities are injured [7, 8, 12]. However, still a considerable number of injuries occur in the lower extremities, with 6.4–17% in the knee joint and 4.9%–16% in the ankle joint [7, 13–16]. These values clearly show the vulnerability of the lower extremities in skiing and snowboarding. If we assume that higher joint loading is related to injuries, injury statistic would suggest greater knee joint loading in skiing and greater ankle joint loading in snowboarding.

It has been suggested that the introduction of the carved turning technique is contributing to the increase in the severity of lower extremity injuries in skiing. Based on biomechanical concepts described by Howe [17], external forces acting on skier/snowboarder include gravity and normal force, snow friction, air resistance, propulsion force, and, while turning, centripetal force. The characteristically higher velocity and smaller turn radius in carved turns increase the centripetal force and thereby increase the lower extremity joint loading. This concept applies to both skiing and snowboarding. However, the magnitude and direction of joint loading for each of the joints could vary between skiing and snowboarding due to technique, position, and equipment differences. With the use of soft boots in snowboarding, a minimal amount of movement in the ankle is expected, whereas in the stiff ski boots forces and moments are transferred to the knee joint. This would suggest higher joint loading in the ankle joint in snowboarding and higher joint loading in the knee joint in

skiing and would be in agreement with the injury statistics described previously.

In a first attempt, it is of special interest to obtain greater insight into the differences in ankle and knee joint loading between a carved ski and snowboard turn. The focus of the current study was on a carved turn since a carved turn is a common skill in both skiing and snowboarding and higher joint loadings are predicted in this kind of turn. A study of Urabe et al. [18] on skiing reported larger number of injuries at the outer leg. The outer leg might experience higher forces and moments due to its steering function. Therefore, the current study focused on the steering leg. In snowboarding steering is controlled by the rear leg.

Several biomechanical studies estimated the joint loading in skiing while turning [19–24] and on landing maneuvers after a jump [25, 26]. Also in snowboarding forces and moments have been estimated, at the boot sole with an alpine board [27] and in lower extremity joints [28]. Besides the studies by Klous et al. [23] and Krüger et al. [28], none of the previous studies performed full three-dimensional (3D) inverse dynamic analysis in skiing or snowboarding with sufficient accuracy. This is due to the complexity to collect 3D kinematic data accurately in a field experiment [20]. Recently, we developed a method to collect accurate 3D kinematic data Klous et al. [29]. Comprehensive accuracy examination of the kinematic setup, kinematic data collection, and analysis led to photogrammetric errors of 11, 9, and 13 mm in  $x$ -,  $y$ -, and  $z$ -direction, respectively. The maximum error caused by skin movement artifacts was 39 mm; similar errors have been reported in laboratory settings [30]. Together with the collected 3D kinetic data, the kinematic data served as input for inverse dynamic analysis to determine lower extremity joint loading in full 3D with sufficient accuracy.

Therefore, the main purpose of the current study was to compare three-dimensional (3D) ankle and knee joint loading between carved ski and snowboard turns in the steering leg in a real life situation with high accuracy. Based on the injury statistics and due to differences in technique, position, and equipment (hard boot versus soft boot) between skiing and snowboarding, it was hypothesized that, at the steering leg in a carved turn, ankle joint loading was greater in snowboarding and knee joint loading was greater in skiing.

## 2. Methods

**2.1. Subjects and Equipment.** Five male skilled subjects participated in the experiment, three skiers (height:  $174 \pm 5.6$  cm, weight:  $75 \pm 3.5$  kg) on an all-round carver (length: 170 cm, side cut: 34 mm, ski radius: 17 m) and two regular snowboarders (height:  $178 \pm 2.8$  cm, weight:  $66.5 \pm 4.9$  kg) on a freestyle board (length: 158 cm, binding alignment:  $25^\circ$  front,  $10^\circ$  rear binding, distance between bindings: 53 cm). Subjects were ski and snowboard teachers at national level in Austria and had no history of injuries. Subjects were wearing their own ski/snowboard boots. All subjects gave their informed consent.

**2.2. Kinematic Setup.** A detailed description of the kinematic setup can be found in Klous et al. [29]. A schematic representation of the kinematic setup is shown in Figure 1, including the course definition ((a) and (c)) and camera setup ((b) and (d)) for the ski turn ((a) and (b)) and snowboard turn ((c) and (d)). Briefly, the course was set with five gates and data were collected around the third gate. Slope inclination was  $21^\circ$  in skiing and  $23^\circ$  in snowboarding. Kinematic data were collected from edge change to the subsequent edge change (Figure 1, thick horizontal lines) with five synchronized panning, tilting, and zooming cameras (Panasonic, F15, 50 Hz).

A reference point system was set up on the hill to describe the 3D movement of the skier and snowboarder from two-dimensional (2D) video data using panning, tilting, and zooming cameras [29, 31, 32]. The positions of the camera tripods, the reference points, and the positions of the gates were measured using a theodolite. The kinematic setup allowed only one trajectory for skiing and one for snowboarding. Hence, the radii of the ski and snowboard turn were similar, but therefore the velocity of the turns varied. Approximately 100 markers were attached to a tight fitting stretch-suit on the pelvis, legs, ski/snowboard boots, and skies/snowboard. This procedure was necessary to have at least three markers per segment in sight of two successive cameras during the entire run which was required to perform 3D kinematic analysis [33].

**2.3. Kinetic Setup.** Stricker et al. [34] described in detail the kinetic setup including a thorough analysis of the accuracy of the system. Briefly, kinetic data was collected with a mobile force plate system (KISTLER, CH, 200 Hz) consisting of 4 six-component dynamometers that were mounted on the ski (two on each ski) or snowboard. The measurement error of the dynamometers was 0.3% for 3D forces ( $F > 292$  N) and ranged from 4.0% to 8.3% for 3D torques. The deviation of the calculated point of force application from its reference was 1.4 and 8.8 mm in mediolateral and anteroposterior direction, respectively. Temperature had little impact on the measurement accuracy of the dynamometers [34]. The standing height from the snow to the bottom of the ski boot was 8 cm. Four cables connected the dynamometers with the charging amplifiers in a backpack that also contained the data loggers. The additional weight of the complete measuring device was approximately 7 kg.

**2.4. Protocol.** Prior to the experiment three test runs were performed for warm-up and adjustment of measurement devices. Additionally, subjects performed quiet stance trials parallel and orthogonal to the fall line to allow definition of local coordinate systems (LCSs) for each segment. Data were collected for a carved left turn in skiing and a carved front side (right) turn in snowboarding. For both skiing and snowboarding, three runs/trials were collected in which the subject was clearly visible in all videos and the technique was performed correctly (controlled by visual inspection). To allow synchronization of the kinetic and kinematic measuring devices in the data analysis, the subject performed a jump directly after the trial that was filmed by at least one camera.

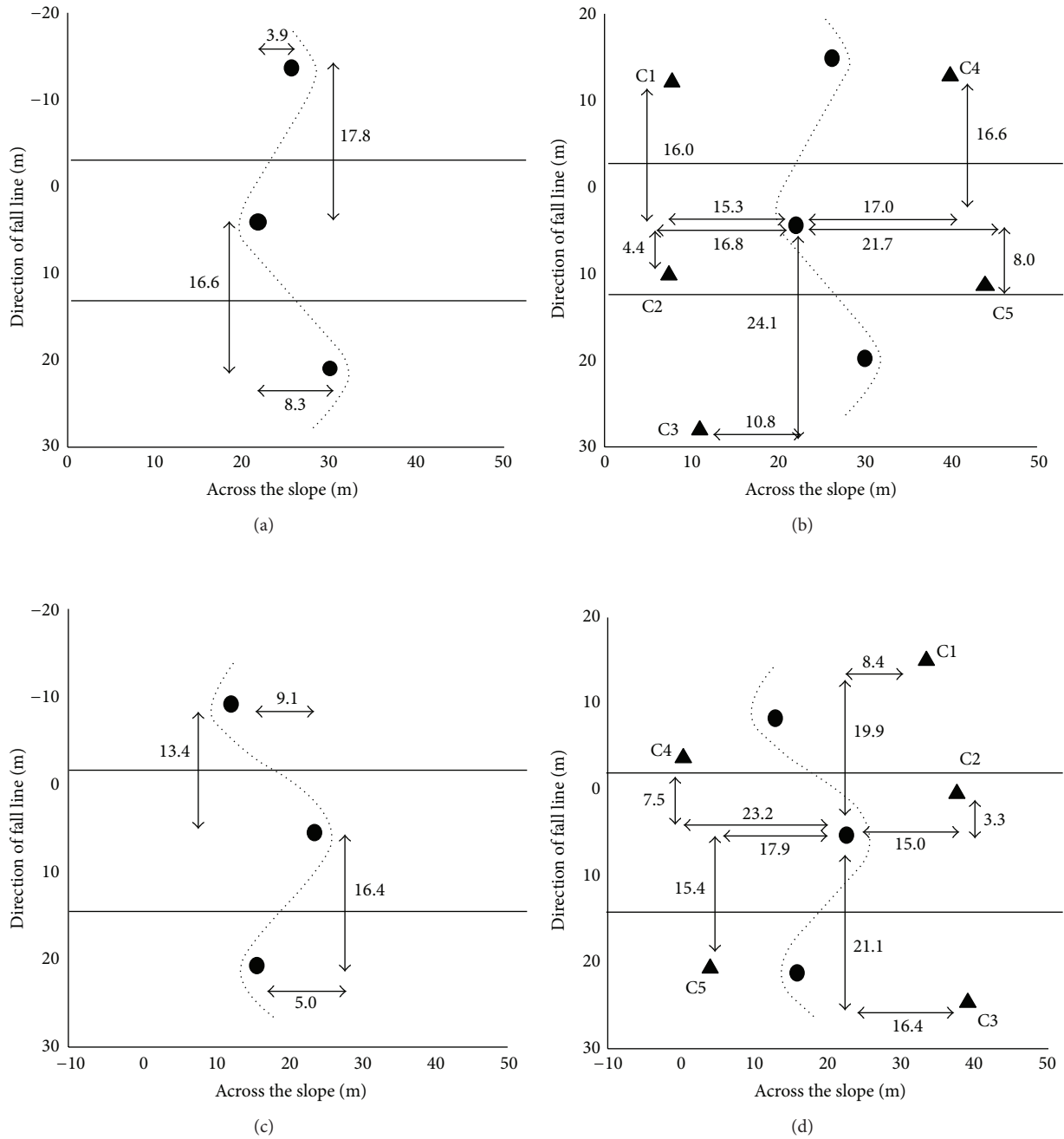


FIGURE 1: Course definition (a and c) and camera setup (b and d) for the ski turn (a and b) and snowboard turn (c and d) including gates (●), cameras (▲), and the part of the turn that is analyzed (in between the thick lines).

A second reset of the kinetic measuring device was performed after the run to control for possible drift behaviors of the system.

**2.5. Data Analysis.** Kinematic and kinetic data analyses as well as inverse dynamic calculations are described in detail in Klous et al. [29]. Briefly, 3D marker coordinates were calculated from two successive cameras after manually digitizing all visible markers for each video frame for each camera using SIMI Motion (Version 7.0, Build 242). Data were filtered and

interpolated and the position and orientation of the segments were calculated using Cardan angles with mediolateral ( $x$ ), posterior-anterior ( $y$ ), and vertical ( $z$ ) rotation sequence [35, 36] with software developed in Matlab (Version 6.5). Joint center positions were calculated using the sphere-fitting SCORE method [37]. Kinetic data of the left and right leg were synchronized and offset corrected and kinematic and kinetic data were also synchronized.

Inertial properties of the lower extremities were calculated applying the geometric model by Yeadon [38]. The

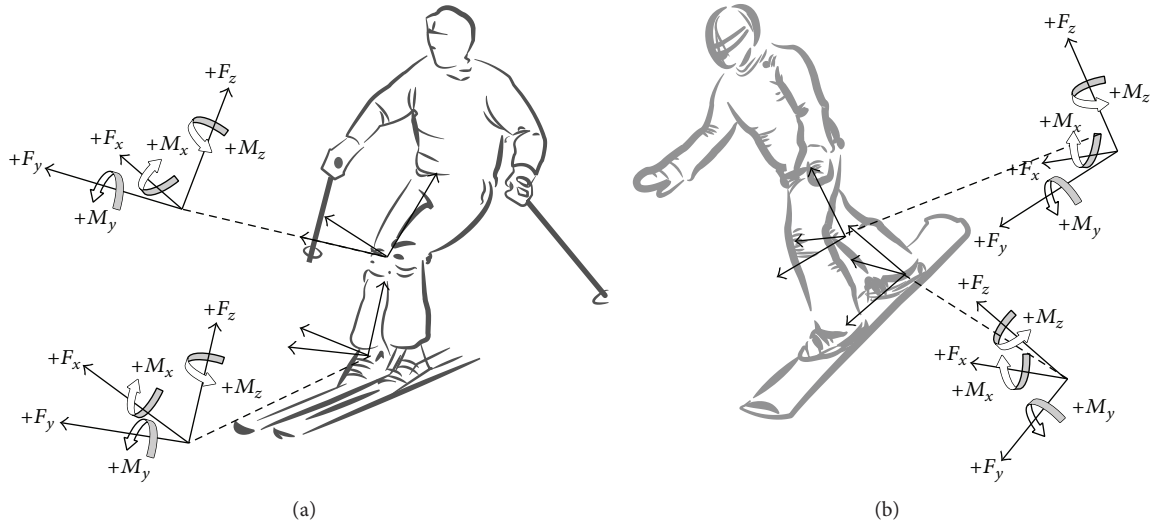


FIGURE 2: Definition of the local coordinate system (LCS) at the leg and the thigh of the steering leg in skiing (a) and snowboarding (b).

model was extended by adding ski/snowboard boots to the model. The parts of the boot below the ankle were added to the foot segment and the parts above the ankle were added to the shank segment. Density values from Dempster [39] were taken according to Yeadon [38] to calculate the inertial parameters of the segments. The experimentally determined densities for the inside and outside ski boot were  $280 \text{ kg/m}^3$  and  $1400 \text{ kg/m}^3$ , respectively. The experimentally determined densities for the inside snowboard boot were  $200 \text{ kg/m}^3$  and for the outside boot  $470 \text{ kg/m}^3$ .

Inverse dynamics analysis was applied to calculate net joint forces and moments (net joint loading) from edge changing to the subsequent one. Since high frequencies kinematic movements were not expected, the global position of the center of mass (COM) as well as the orientation of each of the segments was filtered using a 4th order zero-phase Butterworth low-pass filter with a cutoff frequency of 2 Hz. Kinematic angular and linear acceleration data were determined by numerical differentiation and kinetic and kinematic data were time-normalized to arbitrarily chosen 201 data points before entering into the inverse dynamic analysis. Net joint forces and net moments at the ankle joint and knee joint were calculated in the LCS of the calf and thigh, respectively (Figure 2). Net joint forces were normalized to body weight (BW) and net joint moments were normalized to body mass. The normalized net forces and net moments (referred to as joint forces and joint moments throughout the remaining paper) at the ankle joint represented the net forces and net moments acting from the foot at the leg calculated in the LCS of the leg. The net forces and net moments at the knee joint represented the net forces and net moments acting from the leg at the thigh calculated in the LCS of the thigh. The LCSs were defined with the  $y$ -axis in anterior-posterior direction (positive  $y$ -axis anterior), the  $z$ -axis along the length of the segment (positive  $z$ -axis proximal), and the  $x$ -axis in mediolateral direction, with the positive  $x$ -axis

pointing lateral for the steering (right) leg in both skiing and snowboarding (Figure 2).

Due to the complexity of the experimental setup and the related difficulty to collect accurate data, only in two trials a limited amount of interpolation was necessary to fulfill the requirement of three markers in sight of two successive cameras during the entire run. Therefore, in the following, one representative carved ski turn and one representative carved snowboard turn are presented comparatively. Ankle and knee joint loading in the steering leg in skiing (outside leg) and snowboarding (rear leg) were compared in the current study. Data were divided into three phases of equal duration (33%). These phases correspond approximately to the functional aspects of the turn: initiation phase, steering phase I, and steering phase II [40, 41].

A skidding angle  $\beta$  was calculated describing the skidding component in a turn [42, 43]. This angle was defined as the angle between the orientation vector (line from the front to the rear binding piece of the ski) and the velocity vector of the ankle of the skier/snowboarder's leg. In the current study an average skidding angle was calculated for skiing by averaging the positions of the rear-binding piece of both skies, the positions of the front binding piece of both skies, and the ankle joint position of the right and left leg. In snowboarding, an average ankle joint position was calculated. With the angle  $\beta$  can objectively be verified that turns were carved. Before calculating the skidding angle, position data were filtered with a 5 Hz low-pass 4th order, zero-lag Butterworth filter [23, 42].

Since only one trial for each discipline is compared only descriptive statistics are reported with means and standard deviations for each of the three phases of the turn.

### 3. Results

**3.1. Turning Technique.** A skidding angle  $\beta$  was calculated to verify the proper performance of the turning techniques (Figure 3). The average angle in skiing was  $6.1^\circ (\pm 3.2^\circ)$  and in

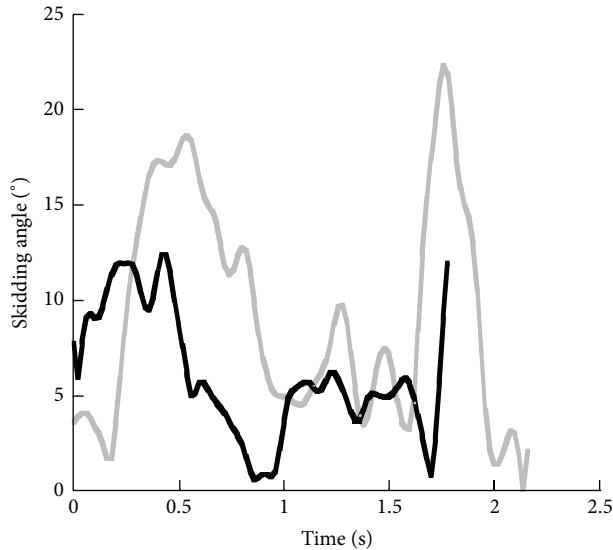


FIGURE 3: Average skidding angle  $\beta$  in a ski turn (black) and a front side snowboard turn (grey).

snowboarding  $9.2^\circ (\pm 5.9^\circ)$ . The average velocity was 13.9 m/s and 11.1 m/s in skiing and snowboarding, respectively. The maximum velocity in skiing was 16.5 m/s and in snowboarding 11.9 m/s. Note that the ski and snowboard turn were performed with similar turning radii, but different velocities.

**3.2. Ankle Joint Loading at the Steering Leg.** Time profiles of the mediolateral forces, anterior/posterior forces, and longitudinal forces at the ankle joint in skiing and snowboarding are shown in Figure 4 and Table 1. Mediolateral forces and anterior/posterior forces were clearly lower than the forces along the longitudinal axis. In both skiing and snowboarding, ankle joint forces acted in posterior and upward direction. Longitudinal forces in skiing were higher than in snowboarding. These forces increase up to 2-3 times BW at 60% of the turn in skiing, whereas in snowboarding the longitudinal force was rather consistent at approximately 1-BW. Smaller forces in posterior direction showed more variation in skiing than in snowboarding. Average ankle joint forces in mediolateral were rather similar for skiing and snowboarding in the first two phases, but higher in snowboarding in the last phase. The ankle joint forces in anterior/posterior direction were similar for the last two phases, but in the first phase the anterior/posterior force was higher in skiing. The longitudinal forces were clearly greater in skiing than in snowboarding in the first two phases and higher in longitudinal direction than in the other directions. In snowboarding the longitudinal force was more consistent throughout the phases.

During the turn predominantly an extension moment and abduction moment acted at the ankle joint in both skiing and snowboarding (Figure 5). Furthermore, an internal rotation moment acted at the ankle joint in snowboarding and an external rotation moment in skiing. Time profiles of

flexion/extension moments showed more variations in skiing than in snowboarding with fluctuations between  $-1$  and  $7$  Nm/kg, whereas the extension moment in snowboarding varied between  $2$  and  $5$  Nm/kg. Average magnitudes (Table 2) showed higher flexion/extension moments in snowboarding but larger fluctuations in skiing in the first and second phase of the turn represented by the large standard deviation (SD). A large abduction moment in skiing was observed in the second phase with peak values over  $4$  Nm/kg and an average value of  $1.7$  Nm/kg. In snowboarding the abduction moment was approximately  $0$  Nm/kg in the first and second phases (see also Table 2) but increased up to  $3$  Nm/kg and averaged  $1.6$  Nm/kg in the third phase. The internal rotation moment clearly showed larger average magnitudes in all three phases in snowboarding than in skiing (Table 2).

**3.3. Knee Joint Loading Steering Leg.** Similar time profiles were observed for the forces in anterior/posterior direction for skiing and snowboarding till approximately 70% of the turn with slightly lower values in snowboarding (Figure 6). In the third part of the turn, the force in the anterior direction is clearly higher in snowboarding than in skiing. This is confirmed by the average magnitudes for each of the three phases presented in Table 3. Anterior/posterior forces and forces along the longitudinal axis of the knee joint showed similar patterns in skiing. Until 60% of the turn, forces increased up to approximately 2-BW and then decreased. Longitudinal forces in snowboarding varied around 0-BW. Forces in medial/lateral direction showed opposite time profiles at the steering leg for skiing and snowboarding. The lateral force in skiing showed a larger increase between 50 and 75% of the turn and a smaller increase in the first 25% of the turn. In snowboarding, this increase was only observed between 50 and 75% of the turn in medial direction. Average magnitudes for medial/lateral forces for all three phases were larger in skiing than in snowboarding.

The time profiles of the moments at the knee joint were rather different for skiing and snowboarding (Figure 7). In skiing the moment varied between flexion and extension throughout the turn with magnitudes between approximately  $-2$  and  $4$  Nm/kg. In snowboarding, a flexion moment acted at the knee joint throughout the turn with magnitudes up to  $6$  Nm/kg. Average magnitudes were clearly higher in snowboarding for all three phases, but the larger SD in skiing for all three phases represented the larger fluctuations in skiing (Table 4). Furthermore, in skiing an abduction moment acted at the knee joint, whereas in snowboarding an adduction moment throughout the turn. Average magnitudes were clearly larger in skiing in phase 1 and in snowboarding in phase 3. In phase 2 average magnitudes were approximately similar, but in opposite directions (Table 4). Rather similar time profiles were observed for the internal/external rotation moment at the knee joint. Both in skiing and snowboarding acted an internal rotation moment during most of the turn. However, average magnitudes were clearly higher in snowboarding than in skiing in the first and second phases of the turn. In the third phase these magnitudes were similar (see Table 4).

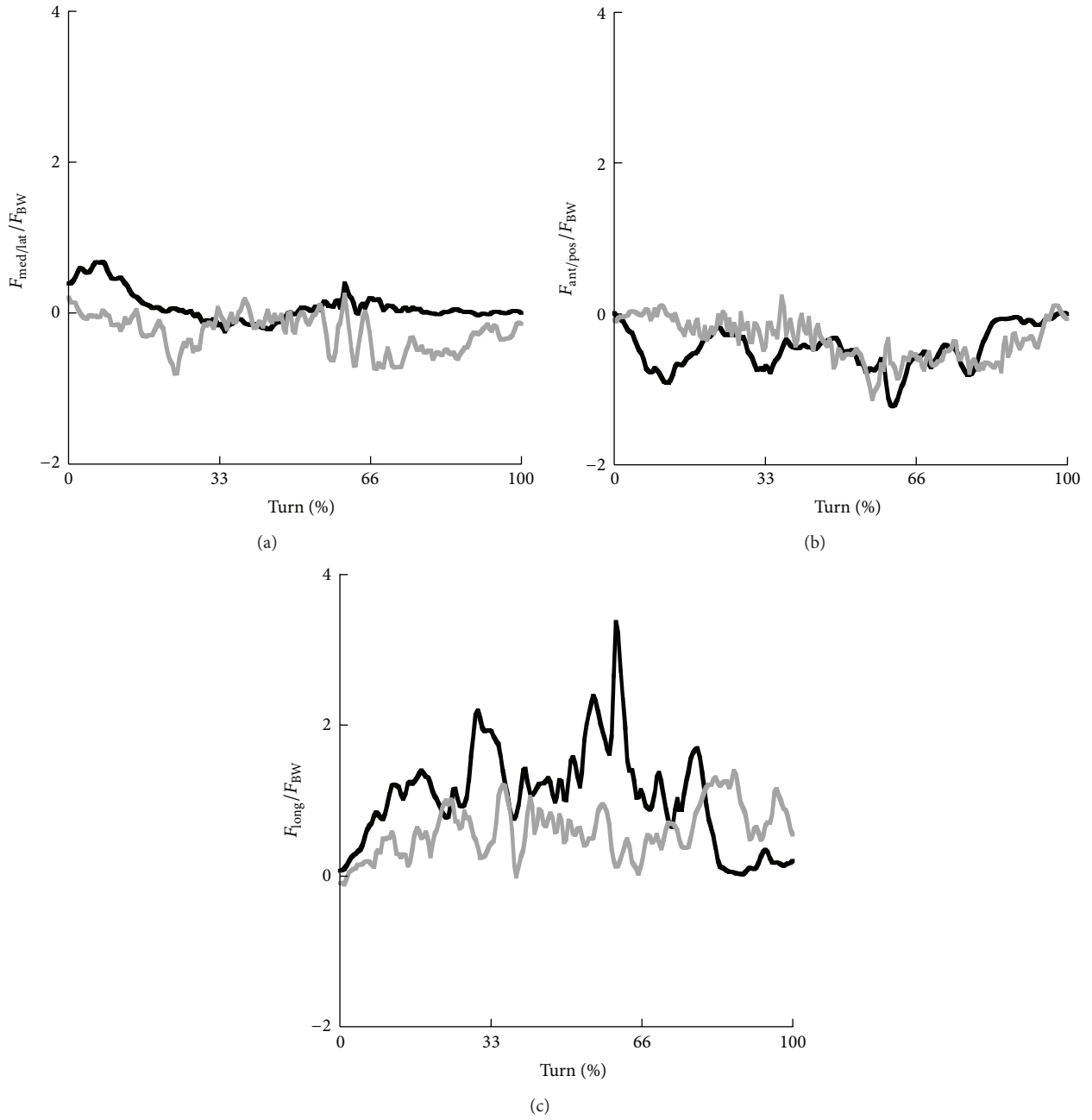


FIGURE 4: Time profiles of the net medial (-)/lateral (+) forces (a), net anterior (+)/posterior (-) forces (b), and net forces around the longitudinal axis (c) at the ankle joint for the steering leg in skiing (black) and snowboarding (grey).

TABLE 1: Average net ankle joint forces in medial (-)/lateral (+) direction ( $F_{\text{med-lat}}$ ), anterior (+)/posterior (-) direction ( $F_{\text{ant-pos}}$ ), and along the longitudinal axis ( $F_{\text{long}}$ ) and standard deviations in the steering leg in skiing and snowboarding for each of the three phases.

	$F_{\text{med-lat}}/F_{\text{BW}}$ (SD)		$F_{\text{ant-pos}}/F_{\text{BW}}$ (SD)		$F_{\text{long}}/F_{\text{BW}}$ (SD)	
	Ski	Snowboard	Ski	Snowboard	Ski	Snowboard
Phase 1	0.2 (0.3)	-0.2 (0.2)	-0.5 (0.3)	-0.1 (0.1)	1.0 (0.5)	0.4 (0.3)
Phase 2	0.0 (0.1)	-0.1 (0.2)	-0.6 (0.2)	-0.5 (0.3)	1.5 (0.6)	0.6 (0.3)
Phase 3	0.0 (0.1)	-0.4 (0.2)	-0.3 (0.3)	-0.4 (0.2)	0.6 (0.5)	0.8 (0.3)

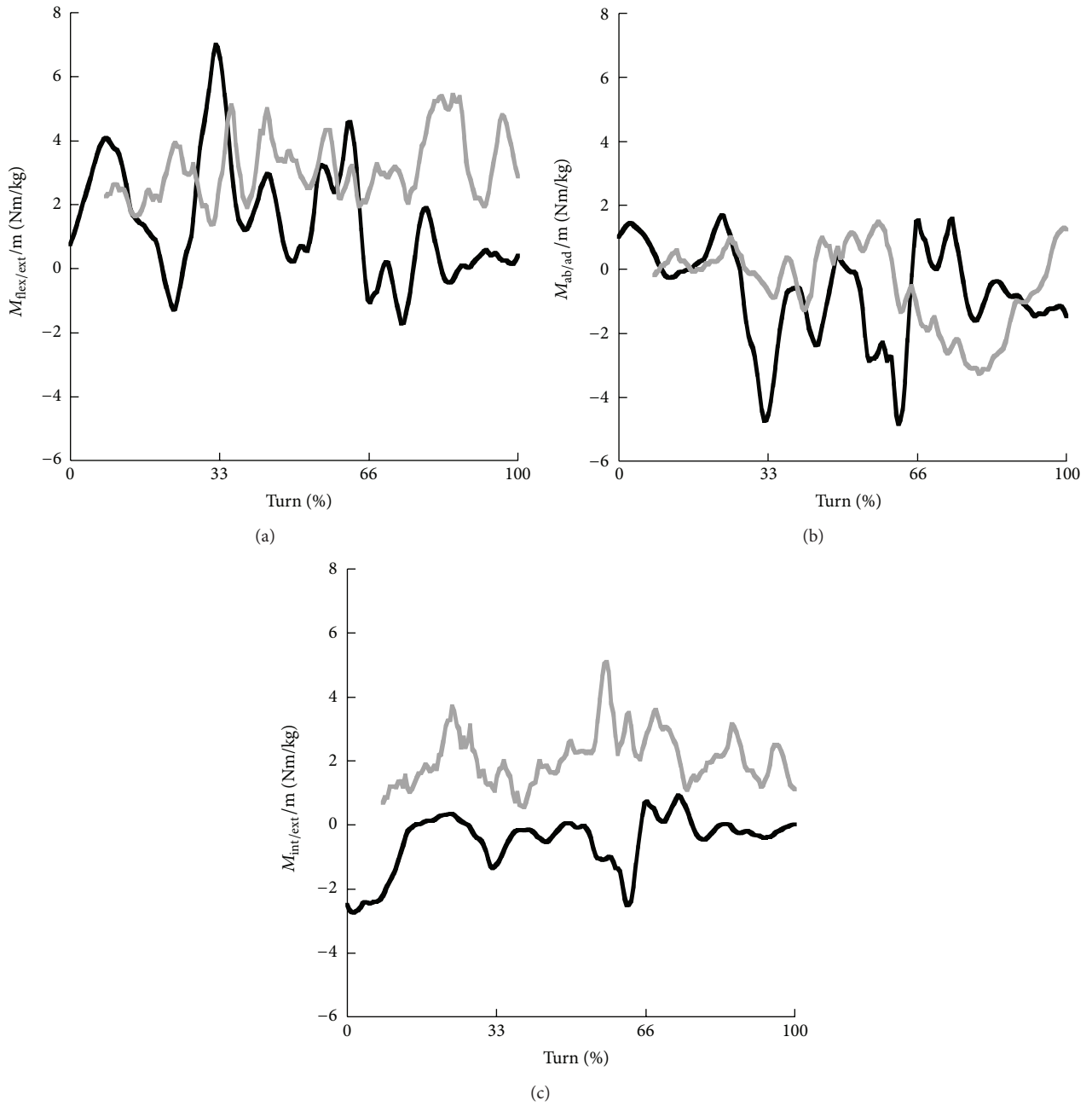


FIGURE 5: Time profiles of the net flexion (+)/extension (-) moments (a), net adduction (+)/abduction (-) moments (b), and net internal (+)/external (-) moments (c) at the ankle joint for the steering leg in skiing (black) and snowboarding (grey).

TABLE 2: Average net ankle joint flexion (-)/extension (+) moments ( $M_{\text{flex-ext}}$ ), net adduction (+)/abduction (-) moments ( $M_{\text{ad-ab}}$ ), and net internal (+)/external (-) rotation moments ( $M_{\text{int-ext}}$ ) and standard deviations in the steering leg in skiing and snowboarding for each of the three phases.

	$M_{\text{flex-ext}}/m$ (SD) (Nm/kg)		$M_{\text{ad-ab}}/m$ (SD) (Nm/kg)		$M_{\text{int-ext}}/m$ (SD) (Nm/kg)	
	Ski	Snowboard	Ski	Snowboard	Ski	Snowboard
Phase 1	2.2 (2.0)	2.5 (0.7)	0.0 (1.6)	0.2 (0.4)	-0.9 (1.1)	1.9 (0.8)
Phase 2	2.2 (1.5)	3.3 (0.8)	-1.7 (1.5)	0.1 (0.9)	-0.6 (0.7)	2.3 (1.0)
Phase 3	0.1 (0.8)	3.6 (1.1)	-0.5 (0.9)	-1.6 (1.3)	-0.0 (0.4)	2.1 (0.7)

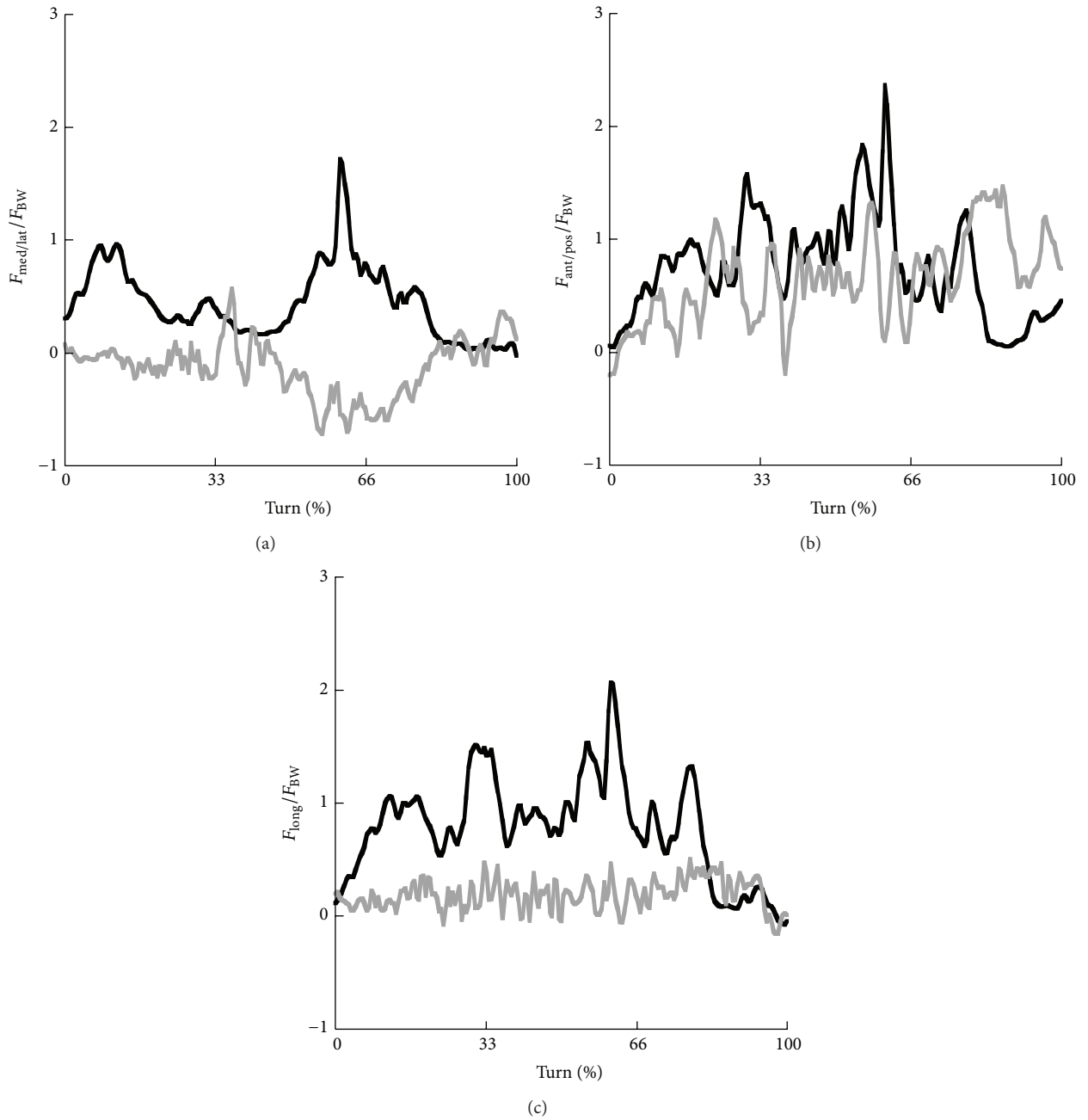


FIGURE 6: Time profiles of the net medial/lateral forces (a), net anterior/posterior forces (b), and net forces around the longitudinal axis (c) at the knee joint for the steering leg in skiing (black) and snowboarding (grey).

TABLE 3: Average net knee joint forces in medial (-)/lateral (+) direction ( $F_{\text{med-lat}}$ ), anterior (+)/posterior (-) direction ( $F_{\text{ant-pos}}$ ), and along the longitudinal axis ( $F_{\text{long}}$ ) and standard deviations in the steering leg in skiing and snowboarding for each of the three phases.

	$F_{\text{med-lat}}/F_{\text{BW}}$ (SD)		$F_{\text{ant-pos}}/F_{\text{BW}}$ (SD)		$F_{\text{long}}/F_{\text{BW}}$ (SD)	
	Ski	Snowboard	Ski	Snowboard	Ski	Snowboard
Phase 1	0.5 (0.2)	-0.1 (0.1)	0.7 (0.4)	0.4 (0.3)	0.8 (0.3)	0.2 (0.1)
Phase 2	0.5 (0.4)	-0.2 (0.3)	1.1 (0.4)	0.6 (0.3)	1.1 (0.3)	0.2 (0.1)
Phase 3	0.3 (0.2)	-0.1 (0.3)	0.4 (0.3)	0.9 (0.3)	0.5 (0.4)	0.2 (0.2)

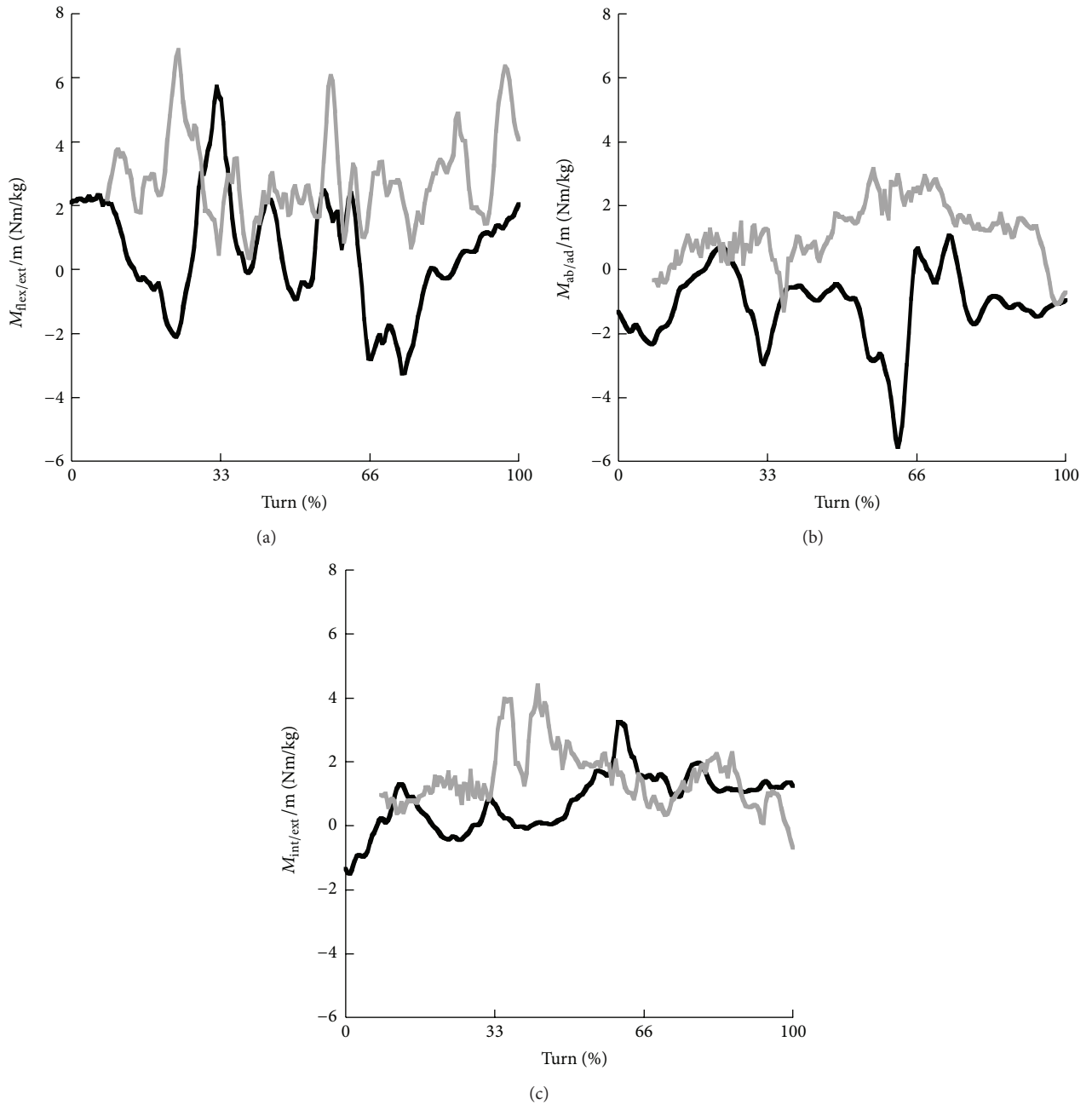


FIGURE 7: Time profiles of the net flexion (+)/extension (-) moments (a), net adduction (+)/abduction (-) moments (b), and net internal (+)/external (-) moments (c) at the knee joint for the steering leg in skiing (black) and snowboarding (grey).

TABLE 4: Average net knee joint flexion (+)/extension (-) moments ( $M_{flex-ext}$ ), net adduction (+)/abduction (-) moments ( $M_{ad-ab}$ ), and net internal (+)/external (-) rotation moments ( $M_{int-ext}$ ) and standard deviations in the steering leg in skiing and snowboarding for each of the three phases.

	$M_{flex-ext}/m$ (SD) (Nm/kg)		$M_{ad-ab}/m$ (SD) (Nm/kg)		$M_{int-ext}/m$ (SD) (Nm/kg)	
	Ski	Snowboard	Ski	Snowboard	Ski	Snowboard
Phase 1	1.1 (2.0)	3.3 (1.4)	-1.0 (1.1)	0.6 (0.5)	0.0 (0.7)	1.0 (0.3)
Phase 2	0.8 (1.4)	2.3 (1.2)	-1.6 (1.4)	1.4 (1.0)	1.0 (1.0)	2.3 (0.9)
Phase 3	-0.4 (1.5)	3.0 (1.3)	-0.8 (0.7)	1.3 (1.0)	1.3 (0.3)	1.0 (0.7)

#### 4. Discussion

The aim of this study was to compare the ankle and knee joint loading at the steering leg between a carved ski and snowboard turn. Based on reported injury statistics and due to differences in technique, position, and equipment between skiing and snowboarding, it was hypothesized that ankle joint loading was greater in snowboarding and knee joint loading was greater in skiing. However, the current study showed a different outcome. While forces were mostly similar for skiing and snowboarding, the joint moments were consistently greater during a snowboard turn, whereas in skiing much more fluctuations were observed during the turn, particularly in the first and second phase of the turn (represented by the greater standard deviation in skiing in those two phases). Moreover, forces along the longitudinal axis were higher in skiing than in snowboarding.

Results showed that the carved turn demonstrated some skidding components. The average skidding angle calculated across time was higher in snowboarding than in skiing, which could be due to the rather steep slope to perform a carved turn in snowboarding. Nevertheless, both turns were representative of a carved turn. Results were in agreement with Müller et al. [43] and Wagner [42] who reported average skidding angles for the carving technique in skiing of  $4.1^\circ$ . Knünz et al. [44] reported angles in a carved ski turn of  $1\text{--}2^\circ$  for the outer leg and  $7\text{--}8^\circ$  for the inner leg in a (purely) carved ski turn.

Forces in anterior/posterior and medial/lateral direction at the ankle joint were similar and rather low for skiing and snowboarding. As a consequence it is expected that the internal/external rotation moment is also rather low as is observed in skiing. However, in snowboarding internal rotation moments reached magnitudes of approximately  $2\text{ Nm/kg}$ . Consistent and larger values throughout the turn were also observed for the flexion/extension moment in snowboarding, whereas the force along the longitudinal axis was below  $1\text{ BW}$  and the anterior/posterior force was even lower. Krüger et al. [28] reported even larger peak values for the flexion/extension moment at the ankle joint compared to the current study but do not report if these values are a consequence of large kinetic or kinematic values. With the low forces observed in the current study, these relatively high moments must be due to kinematics, hence angular accelerations of the segments, or due to the different body positions in skiing and snowboarding which is represented by the position of the joint centres with respect to the force vector. The use of soft boots in snowboarding allowed short but fast rotational movements (i.e., kinematic parameters), whereas these movements were not possible with stiff ski boots. These equipment differences would explain the greater joint moments at the ankle joint in snowboarding. This was supported by a study of Delorme et al. [45] that compared ankle joint kinematics between stiff and soft boots in snowboarding. This study reported that the use of soft boots leads to larger average dorsi/plantar flexion angles and internal/external rotation angles, as well as larger maximum dorsi/plantar flexion angles, eversion/inversion angles, and internal/external rotation angles, larger minimal

internal/external rotation angles, and a larger range of motion in dorsi/plantar flexion.

In skiing, the time pattern of the force along the longitudinal axis at the ankle joint showed similarities with the time pattern of the flexion/extension and abduction/adduction moments, but in opposite direction. Hence, opposite to snowboarding, the large moments in skiing seemed to be a consequence of the produced forces. Note that, in skiing, the flexion/extension moment allowed the movement to the tip/tail of the ski, whereas the abduction/adduction moment places the ski at the edges (see Figure 2). Fluctuations (represented by the standard deviation) were much larger for the moments than for the forces and also much larger in skiing than in snowboarding. This might suggest that the greater number of injuries at the ankle joint is caused by the specific body position in snowboarding and the consistently high moments due to kinematic variables, rather than large fluctuation as observed in the moments in skiing.

At the knee joint both medial/lateral forces and forces along the longitudinal axis were higher in skiing, whereas the anterior/posterior forces were similar for skiing and snowboarding. However, the higher forces in skiing did not result in consistently higher moments compared to snowboarding. The flexion/extension moments in snowboarding were required to place the snowboard at the edges, just like the abduction/adduction moment in skiing. The flexion/extension moments in snowboarding were approximately  $3\text{ Nm/kg}$ , whereas the abduction/adduction moments in skiing were approximately  $1.0\text{--}1.5\text{ Nm/kg}$ . Also the flexion/extension moments in skiing were approximately  $1\text{ Nm/kg}$  as were the abduction/adduction moments in snowboarding. In general, moments were slightly lower at the knee joint than at the ankle joint in snowboarding, whereas in skiing the opposite was observed. Again, the larger moments in snowboarding seemed not to be due to the high forces but due to the soft boot allowing larger accelerations and a different body position in snowboarding than in skiing.

Even though the fluctuations were larger in snowboarding at the knee than at the ankle joint, these variations were still much lower in snowboarding than in skiing. These fluctuations represent the loading and unloading that are clearly greater in skiing than in snowboarding. In situations when a skier has to make a sudden adjustment, these peak values would increase even further. In skiing, joint moments increased in the knee joint compared to the ankle joint, whereas in snowboarding the moments decreased. Besides the knee joint forces being similar or greater in skiing than in snowboarding, also the peak forces and moments were larger in skiing than in snowboarding, except for the internal/external rotation moment. Krüger et al. [28] reported clearly lower peak values for the flexion/extension moment in snowboarding (33% less) than in the current study, which would make differences between skiing and snowboarding even more pronounced. These three aspects together could be an explanation for the larger amount of knee injuries in skiing than in snowboarding.

Even though the joint loading observed in the current study is rather high, one should realise that many other aspects can explain the injury statistics as presented in

the current study. The quality of the snow, the technical and physical capability of the skier or snowboarder, and the large number of skiers and snowboarders at the slope could explain the many injuries that occur in skiing and snowboarding. The skier and snowboarder in the current study carried additional equipment to allow measurement of ground reaction forces. This equipment influenced their weight and their standing height. With their level of expertise, the skier and snowboarder did not report any influence of this equipment. Nevertheless, the equipment might have influenced their technique and performance. Additionally, the differences in stiffness between ski and snowboard boots could have influenced the results. Due to the stiff ski boot, part of the loading might have been transferred to the boot and thereby reduced the ankle joint in skiing. Inverse dynamic calculations did not allow determining how much of the ankle joint was transferred to the ski boot. Hence, this could have caused overestimation of the ankle joint in skiing. However, where the current results showed larger ankle joint in snowboarding, the difference in ankle joint between skiing and snowboarding would have even been greater if the ankle joint in skiing was overestimated. When current results showed larger ankle joint in skiing, these differences might not have been as profound. Both situations support the research hypothesis. Also, the magnitudes of the ankle joint forces and moments in skiing might have been lower, but it is not to expect that the time patterns were influenced. Furthermore, the kinematic setup allowed a ski and snowboard turn to be performed with similar radii but different velocities. The centripetal force ( $F_c$ ) in a turn is influenced by the velocity ( $F_c = mv^2/r$ ). Although the velocity in snowboarding was lower than in skiing, the ankle and knee joint forces and moments were not consistently lower than in skiing. We speculate that if the snowboard turn was performed with higher velocities, the forces and moments at the ankle and knee joint would further increase due to an increase of the centripetal force. Furthermore, videos and data of ground reaction forces throughout the collected data were similar. Nevertheless, the findings should be interpreted with caution due to the single subject design. Additionally, even though the applied method shows a good accuracy for on-snow data collection, the results of inverse dynamic calculations depend strongly on the accuracy of the input data. As is shown by McCaw & DeVita [46] errors in the input data are propagated in the inverse dynamics procedures, thereby reducing the accuracy of the results calculated using this procedure. Finally, it is important to emphasise that we calculated forces and moments during successful turns, which are not representative of the forces and moments during unsuccessful turns that result in falling and/or injury.

## 5. Conclusion

The expected higher ankle joint loading in snowboarding and higher knee joint loading in skiing that was based on reported injury statistics in the lower extremities in skiing and snowboarding and the differences in position, technique,

and equipment (soft boot versus hard boot) could not be confirmed. Ankle joint loading was not consistently greater in snowboarding than in skiing and vice versa for the knee joint loading. When comparing skiing and snowboarding, differentiation was required between forces and moments, the direction of the forces and moments, and the phase of the turn that was considered. However, there seemed to be a trend that forces were larger in skiing and moments showed large fluctuations (loading-unloading), whereas in snowboarding high moments with a more consistent pattern were observed. In future research it is important to increase the number of participants in the study and study joint loading of various turning techniques.

## Conflict of Interests

The authors declare that there is no conflict of interests regarding the publication of this paper.

## Acknowledgments

The authors thank ski company Atomic for providing the test equipment. They appreciate the helpful discussions with Dr. Josef Kröll.

## References

- [1] K. Grabler and G. J. Stirnweis, "Wirtschaftsbericht der Seilbahnen—Trends Winter 2011-2011," WKO die Seilbahnen, 2011, [http://portal.wko.at/wk/format\\_detail.wk?angid=1&stid=621545&dstdid=329&opennavid=0](http://portal.wko.at/wk/format_detail.wk?angid=1&stid=621545&dstdid=329&opennavid=0).
- [2] R. Schönbächler and G. Schärer, *Fakten und Zahlen zur Schweizer Seilbahnbranche*, Seilbahnen Schweiz, 2012, <http://www.seilbahnen.org/de/Branche/Fakten-Zahlen/Fakten-Zahlen>.
- [3] N. Laplante, "2008-2009 Canadian Skier and Snowboarder Facts and Stats," 2009, <http://xcski.org/news/2009%20Facts%20and%20Stats%20final%20draft.pdf>.
- [4] M. Klous, *Three-dimensional joint loading on the lower extremities in alpine skiing and snowboarding [Ph.D. thesis]*, University of Salzburg, Salzburg, Austria, 2007.
- [5] S. Corra, A. Conci, G. Conforti, G. Sacco, and F. de Giorgi, "Skiing and snowboarding injuries and their impact on the emergency care system in South Tyrol: a retrospective analysis for the winter season 2001–2002," *Injury Control and Safety Promotion*, vol. 11, no. 4, pp. 281–285, 2004.
- [6] M. Langran and S. Selvaraj, "Snow sports injuries in Scotland: a case-control study," *British Journal of Sports Medicine*, vol. 36, no. 2, pp. 135–140, 2002.
- [7] S. Sulheim, I. Holme, A. Rødven, A. Ekeland, and R. Bahr, "Risk factors for injuries in alpine skiing, telemark skiing and snowboarding—case-control study," *British Journal of Sports Medicine*, vol. 45, no. 16, pp. 1303–1309, 2011.
- [8] S. Kim, N. K. Endres, R. J. Johnson, C. F. Ettliger, and J. E. Shealy, "Snowboarding injuries: trends over time and comparisons with alpine skiing injuries," *The American Journal of Sports Medicine*, vol. 40, no. 4, pp. 770–776, 2012.
- [9] M. Burtscher, M. Flatz, R. Sommersacher et al., *Österreichische Skiunfallerhebung Wintersaison 2002/2003*, Österreichischen

- Skiverbandes in Kooperation mit dem Institut für Sportwissenschaften der Universität Innsbruck, 2003.
- [10] C. Goulet, G. Régner, G. Grimard, P. Valois, and P. Villeneuve, "Risk factors associated with alpine skiing injuries in children: a case-control study," *The American Journal of Sports Medicine*, vol. 27, no. 5, pp. 644–650, 1999.
- [11] E. J. Bridges, F. Rouah, and K. M. Johnston, "Snowblading injuries in Eastern Canada," *British Journal of Sports Medicine*, vol. 37, no. 6, pp. 511–515, 2003.
- [12] D. Ishimaru, H. Ogawa, K. Wakahara, H. Sumi, Y. Sumi, and K. Shimizu, "Hip pads reduce the overall risk of injuries in recreational snowboarders," *British Journal of Sports Medicine*, vol. 46, no. 15, pp. 1055–1058, 2012.
- [13] H. Xiang, K. Kelleher, B. J. Shields, K. J. Brown, and G. A. Smith, "Skiing- and snowboarding-related injuries treated in U.S. emergency departments, 2002," *Journal of Trauma-Injury Infection & Critical Care*, vol. 58, no. 1, pp. 112–118, 2005.
- [14] C. Made and L. G. Elmqvist, "A 10-year study of snowboard injuries in Lapland Sweden," *Scandinavian Journal of Medicine and Science in Sports*, vol. 14, no. 2, pp. 128–133, 2004.
- [15] E. Aschauer, E. Ritter, and H. Resch, *Wintersport Unfallstatistik 2002/2003*, Universitätsklinik für Unfallchirurgie und Sporttraumatologie Salzburg, 2003.
- [16] T. M. Davidson and A. T. Laliotis, "Snowboarding injuries a four-year study with comparison with alpine ski injuries," *The Western Journal of Medicine*, vol. 164, no. 3, pp. 231–237, 1996.
- [17] J. Howe, *The New Skiing Mechanics*, McIntire Publishing, Waterford, UK, 2nd edition, 2001.
- [18] Y. Urabe, M. Ochi, K. Onari, and Y. Ikuta, "Anterior cruciate ligament injury in recreational alpine skiers: analysis of mechanisms and strategy for prevention," *Journal of Orthopaedic Science*, vol. 7, no. 1, pp. 1–5, 2002.
- [19] S. M. Maxwell and M. L. Hull, "Measurement of strength and loading variables on the knee during alpine skiing," *Journal of Biomechanics*, vol. 22, no. 6–7, pp. 609–624, 1989.
- [20] T. P. Quinn and C. D. Mote Jr., "Prediction of the loading along the leg during snow skiing," *Journal of Biomechanics*, vol. 25, no. 6, pp. 609–625, 1992.
- [21] C. Raschner, E. Müller, and H. Schwameder, "Kinematic and kinetic analysis of slalom turns as a basis for the development of specific training methods to improve strength and endurance," in *Science and Skiing*, E. Müller, H. Schwameder, E. Kornexl, and C. Raschner, Eds., pp. 251–261, Chapman & Hall, Cambridge, Mass, USA, 1997.
- [22] M. Brodie, A. Walmsley, and W. Page, "Fusion motion capture: a prototype system using inertial measurement units and GPS for the biomechanical analysis of ski racing," *Sports Technology*, vol. 1, pp. 17–28, 2008.
- [23] M. Klous, E. Müller, and H. Schwameder, "Three-dimensional knee joint loading in alpine skiing: a comparison between a carved and a skidded turn," *Journal of Applied Biomechanics*, vol. 28, no. 6, pp. 655–664, 2012.
- [24] F. Vaverka, S. Vodickova, and M. Elfmark, "Kinetic analysis of ski turns based on measured ground reaction forces," *Journal of Applied Biomechanics*, vol. 28, no. 1, pp. 41–47, 2012.
- [25] L. Read and W. Herzog, "External loading at the knee joint for landing movements in alpine skiing," *International Journal of Sport Biomechanics*, vol. 8, pp. 62–80, 1992.
- [26] W. Nachbauer, P. Kaps, B. Nigg et al., "A video technique for obtaining 3-D coordinates in alpine skiing," *Journal of Applied Biomechanics*, vol. 12, no. 1, pp. 104–115, 1996.
- [27] B. Knünz, W. Nachbauer, K. Schindelwig, and F. Brunner, "Forces and moments at the boot sole during snowboarding," in *Science and Skiing II*, E. Müller, H. Schwameder, C. Raschner, S. Lindinger, and E. Kornexl, Eds., pp. 242–249, Kovač, Hamburg, Germany, 2001.
- [28] A. Krüger, P. McAlpine, F. Borrani, and J. Edelmann-Nusser, "Determination of three-dimensional joint loading within the lower extremities in snowboarding," *Proceedings of the Institution of Mechanical Engineers H: Journal of Engineering in Medicine*, vol. 226, no. 2, pp. 170–175, 2012.
- [29] M. Klous, E. Müller, and H. Schwameder, "Collecting kinematic data on a ski/snowboard track with panning, tilting, and zooming cameras: is there sufficient accuracy for a biomechanical analysis?" *Journal of Sports Sciences*, vol. 28, no. 12, pp. 1345–1352, 2010.
- [30] A. Cappozzo, F. Catani, A. Leardini, M. G. Benedetti, and U. Della Croce, "Position and orientation in space of bones during movement: experimental artefacts," *Clinical Biomechanics*, vol. 11, no. 2, pp. 90–100, 1996.
- [31] V. Drenk, "Panning—Zusatzprogramm zur Behandlung schwenk- und neigbarer und in ihre brennweite variierbarer Kameras in Peak3D—Dokumentation," Institut für Angewandte Trainingswissenschaften e. V., Leipzig, Germany, 1993.
- [32] V. Drenk, "Bildmeßverfahren für schwenk- und neigbare sowie in ihrer Brennweite variierbare Kameras," *Zeitschrift für Angewandte Trainingswissenschaft*, vol. 1, pp. 130–142, 1994.
- [33] B. M. Nigg and W. Herzog, *Biomechanics of the Musculo-skeletal System*, John Wiley & Sons, New York, NY, USA, 3rd edition, 2007.
- [34] G. Stricker, P. Scheiber, E. Lindenhofer, and E. Müller, "Determination of forces in alpine skiing and snowboarding: validation of a mobile data acquisition system," *European Journal of Sport Science*, vol. 10, no. 1, pp. 31–41, 2010.
- [35] D. G. E. Robertson, G. E. Caldwell, J. Hamill, G. Kamen, and S. N. Whittlesey, *Research Methods in Biomechanics*, Human Kinetics, Champaign, Ill, USA, 2004.
- [36] V. M. Zatsiorsky, *Kinematics of Human Motion*, Human Kinetics, Champaign, Ill, USA, 1998.
- [37] R. M. Ehrig, W. R. Taylor, G. N. Duda, and M. O. Heller, "A survey of formal methods for determining the centre of rotation of ball joints," *Journal of Biomechanics*, vol. 39, no. 15, pp. 2798–2809, 2006.
- [38] M. R. Yeadon, "The simulation of aerial movement. II. A mathematical inertia model of the human body," *Journal of Biomechanics*, vol. 23, no. 1, pp. 67–74, 1990.
- [39] W. T. Dempster, "Space requirements of the seated operator," WADC Technical Report TR-55-159, Wright-Patterson Air Force Base, Wright-Patterson, Ohio, USA, 1955.
- [40] E. Müller, "Biomechanische Analysen moderner alpiner Skilauftechniken in unterschiedlichen Schnee-, Gelände- und Pistensituationen," in *Biomechanik der Sportarten, Bd2: biomechanik des alpinen skilaufs*, F. Fetz and E. Müller, Eds., pp. 1–49, Ferdinand Enke, Stuttgart, Germany, 1991.
- [41] C. Raschner, C. Schiefermüller, G. Zallinger, E. Hofer, F. Brunner, and E. Müller, "Carving turns versus traditional parallel turns—a comparative biomechanical analysis," in *Science and Skiing II*, E. Müller, H. Schwameder, C. Raschner, S. Lindinger, and E. Kornexl, Eds., pp. 203–217, Dr. Kovač, Hamburg, Germany, 2001.
- [42] G. Wagner, *Messtechnische Differenzierung von gerschnittenen und gerutschten Kurven im alpine Skilauf [M.S. thesis]*, University of Salzburg, 2006.

- [43] E. Müller, M. Klous, and G. Wagner, “Biomechanical aspects of turning techniques in alpine skiing,” in *Science and Sports: Bridging the Gap*, T. Reilly, Ed., pp. 135–142, Shaker Publishing BV, Maastricht, The Netherlands, 2008.
- [44] B. Knünz, W. Nachbauer, M. Mössner, K. Schindelwig, and F. Brunner, “Track analysis of giant slalom turns of World Cup racers,” in *Proceedings of the 5th Annual Congress of the European College of Sport Science (ECSS '00)*, pp. 399–401, Jyväskylä, Finland, 2000.
- [45] S. Delorme, S. Tavoullaris, and M. Lamontagne, “Kinematics of the ankle joint complex in snowboarding,” *Journal of Applied Biomechanics*, vol. 21, no. 4, pp. 394–403, 2005.
- [46] S. T. McCaw and P. DeVita, “Errors in alignment of center of pressure and foot coordinates affect predicted lower extremity torques,” *Journal of Biomechanics*, vol. 28, no. 8, pp. 985–988, 1995.